ADVANCES IN QUANTUM CHEMISTRY

Volume 45

Remigio Cabrera-Trujillo

ADVANCES IN

QUANTUM CHEMISTRY

VOLUME 45

ADVANCES IN
QUANTUM CHEMISTRY

THEORY OF THE INTERACTION OF SWIFT IONS WITH MATTER. PART 1

EDITORS

JOHN R. SABIN
QUANTUM THEORY PROJECT
UNIVERSITY OF FLORIDA
GAINESVILLE, FLORIDA

ERKKI BRÄNDAS
DEPARTMENT OF QUANTUM CHEMISTRY
UPPSALA UNIVERSITY
UPPSALA, SWEDEN

FOUNDING EDITOR

PER-OLOV LÖWDIN
1916–2000

GUEST EDITORS

REMIGIO CABRERA-TRUJILLO
QUANTUM THEORY PROJECT
UNIVERSITY OF FLORIDA
GAINESVILLE, FLORIDA

JOHN R. SABIN
QUANTUM THEORY PROJECT
UNIVERSITY OF FLORIDA
GAINESVILLE, FLORIDA

VOLUME 45

ELSEVIER
ACADEMIC
PRESS

Amsterdam · Boston · Heidelberg · London · New York · Oxford
Paris · San Diego · San Francisco · Singapore · Sydney · Tokyo

ELSEVIER B.V.
Sara Burgerhartstraat 25
P.O. Box 211, 1000 AE Amsterdam
The Netherlands

ELSEVIER Inc.
525 B Street, Suite 1900
San Diego, CA 92101-4495
USA

ELSEVIER Ltd
The Boulevard, Langford Lane
Kidlington, Oxford OX5 1GB
UK

ELSEVIER Ltd
84 Theobalds Road
London WC1X 8RR
UK

First edition 2004

ISBN: 0-12-034845-4
ISSN: 0065-3276

♾ The paper used in this publication meets the requirements of ANSI/NISO Z39.48-1992 (Permanence of Paper). Printed and bound in Great Britain.

Contents

Contributors

Numbers in parentheses indicate the pages where the authors' contributions can be found.

M. Alducin (223), Donostia International Physics Center (DIPC), P. Manuel de Lardizabal 4, 20018 San Sebastián, Spain

Néstor R. Arista (47), División Colisiones Atómicas, Centro Atómico Bariloche and Instituto Balseiro, Comisión Nacional de Energía Atómica, 8400 S.C. Bariloche, Argentina

A. Arnau (201), Unidad de Física de Materiales, Centro Mixto CSIC-UPV/EHU, Paseo Manuel de Lardizabal 3, 20018 San Sebastián, Spain; Donostia International Physics Center DIPC, Paseo Manuel de Lardizabal 4, 20018 San Sebastián, Spain; Departamento de Física de Materiales, Facultad de Químicas UPV/EHU, Apartado 1072, 20080 San Sebastián, Spain

Remigio Cabrera-Trujillo (1, 99), Quantum Theory Project, Department of Physics, University of Florida, Gainesville, FL, USA; Quantum Theory Project, Departments of Physics and Chemistry, University of Florida, P.O. Box 118435, Gainesville, FL 32611-8435, USA

M. J. Caturla (79), Dept. de Física Aplicada, Facultat de Ciencies, Universitat dAlacant, Apt. 99, E-03080 Alacant, Spain

R. Díez Muiño (201), Unidad de Física de Materiales, Centro Mixto CSIC-UPV/EHU, Paseo Manuel de Lardizabal 3, 20018 San Sebastián, Spain; Donostia International Physics Center DIPC, Paseo Manuel de Lardizabal 4, 20018 San Sebastián, Spain

E. Deumens (99), Quantum Theory Project, Departments of Physics and Chemistry, University of Florida, P.O. Box 118435, Gainesville, FL 32611-8435, USA

F. Flores (175), Departamento de Física Teórica de la Materia Condendada C-V, Universidad Autónoma de Madrid, E-28049 Madrid, Spain

P. L. Grande (7), Instituto de Física da Universidade Federal do Rio Grande do Sul, Avenida Bento Gonçalves 9500, 91501-970, Porto Alegre, Brazil

A. Gras Martí (79), Dept. de Física Aplicada, Facultat de Ciencies, Universitat dAlacant, Apt. 99, E-03080 Alacant, Spain

I. G. Gurtubay (247), Materia Kondentsatuaren Fisika Saila, Zientzi Fakultatea, UPV/EHU, 644 Posta Kutxatila, E-48080 Bilbo, Basque Country, Spain

J.-C. Jiménez Saez (79), Dept. de Electricidad y Electrónica, Facultad de Ciencias Físicas, Universidad Complutense, E-28040, Madrid, Spain

J. J. Jiménez-Rodríguez (79), Dept. de Electricidad y Electrónica, Facultad de Ciencias Físicas, Universidad Complutense, E-28040, Madrid, Spain

J. I. Juaristi (223), Depto. de Física de Materiales and Centro Mixto CSIC-UPV/EHU, Facultad de Química, UPV/EHU, Apartado 1072, 20080 San Sebastián, Spain

V. A. Khodyrev (125), Centro de micro-análisis de materiales, Campus de Cantoblanco – UAM, 28049 Cantoblanco, Madrid, Spain

Agustín F. Lifschitz (47), División Colisiones Atómicas, Centro Atómico Bariloche and Instituto Balseiro, Comisión Nacional de Energía Atómica, 8400 S.C. Bariloche, Argentina

Richard J. Mathar (277), Max-Planck Inst. für Astronomie, Heidelberg, Germany

E. J. McGuire (159), Ejmcguire Physics Research, 3567 Sequoia Pl NW Albuquerque, NM 87120, USA

R. C. Monreal (175), Departamento de Física Teórica de la Materia Condensada C-V, Universidad Autónoma de Madrid, E-28049 Madrid, Spain

V. U. Nazarov (247), Department of Physics and Institute of Condensed Matter Physics, Chonnam National University, Kwangju 500-757, South Korea

Y. Öhrn (99), Quantum Theory Project, Departments of Physics and Chemistry, University of Florida, P.O. Box 118435, Gainesville, FL 32611-8435, USA

M.-C. Pérez-Martín (79), Dept. de Electricidad y Electrónica, Facultad de Ciencias Físicas, Universidad Complutense, E-28040, Madrid, Spain

J. M. Pitarke (247), Materia Kondentsatuaren Fisika Saila, Zientzi Fakultatea, UPV/EHU, 644 Posta Kutxatila, E-48080 Bilbo, Basque Country, Spain; Donostia International Physics Center (DIPC) and Centro Mixto CSIC-UPV/EHU, E-20018 Donostia, Basque Country, Spain

John R. Sabin (1, 99, 277), Quantum Theory Project, Department of Physics, University of Florida, Gainesville, FL, USA; Quantum Theory Project, Departments of Physics and Chemistry, University of Florida, P.O. Box 118435, Gainesville, FL 32611-8435, USA

G. Schiwietz (7), Bereich SF, Hahn-Meitner-Institut Berlin, Glienicker Str. 100, D-14109 Berlin, Germany

S. B. Trickey (277), Quantum Theory Project, Departments of Physics and Chemistry, University of Florida, Gainesville, FL 32611-8435, USA

Preface

It will soon be a century since Niels Bohr developed the first theory of energy deposition of α-particles colliding with a material target. Although his approach was based on a harmonically bound electron and was purely classical, it provided the basis for the study of several processes which would later become important in fields such as radiotherapy, dosimetry, material modification, surface analysis, aerology, astrophysics, plasma physics, etc. Personalities such as Hans Bethe, Enrico Fermi, and Jens Lindhard, among others, laid the foundations to what now has become the study of energy deposition and energy loss in atomic and molecular collisions.

From the technological point of view, there is a quantum leap between the materials developed and the equipment used today and what was available to the original pioneers of this field.

It is not only the technological applications that have taken advantage of the study of energy deposition of ions and atoms in materials, but it has also led to greater theoretical understanding of the interaction of ions, atoms, and molecules. The introduction of new methods into the analysis of energy deposition, charge transfer and phase effects has spawned new lines of research. Among the newer methods presently used are density functional theory, montecarlo methods, and various *ab initio* methods (close-coupling, electron-nuclear dynamics, etc…), among others. Some of these methods require extensive computational resources; however, the details and the understanding that such computations led to is unprecedented. This is an aspect of the field that will evolve as faster and more powerful computers become available.

The intention of this and the next volume is to present the latest stage of the field of energy deposition as it is actually viewed by many of the major players in the arena. It is hard to incorporate all of the important players and all of the topics related to energy deposition in the limited space available to us; however, we have tried to present the state of the art as it is now.

We thank all the contributors that have spent time and dedication in the preparation of their contributions, and hope this volume will serve as a starting point to new researchers in the field, as a reference, and serve as a guide to the direction which energy deposition is taking.

Remigio Cabrera-Trujillo, John R. Sabin

Gainesville, January, 2004

The Theory and Computation of Energy Deposition Properties

Remigio Cabrera-Trujillo and John R. Sabin

Quantum Theory Project, Department of Physics, University of Florida, Gainesville, FL, USA

Contents

1. INTRODUCTION

To set the stage for this volume, let us first consider a swift ion of charge Z_1 moving with some laboratory frame velocity v through a medium. By colliding with the nuclei and electrons and thereby transferring energy to them, the projectile is slowed, and the energy loss, $\Delta E(v)$, per unit path length, Δx, is known as the stopping power $(-\Delta E(v)/\Delta x)$ of the target material. The quantity is velocity dependent and carries a negative sign so that the stopping power will be positive as the projectile slows. As simple energy and momentum conservation demand, at all but the lowest projectile velocities, the stopping power comes from collisions of the projectile with target electrons, and thus from energy transfer to the electronic structure of the target atoms, molecules, or solid.

The stopping power is generally normalized by the target scatterer density n, to produce the stopping cross-section, $S(v)$. If one removes the primary velocity dependence and constants from the cross-section, one obtains the stopping number, $L(v)$, where interesting physics is concentrated. These quantities are related as

$$-\frac{\mathrm{d}E}{\mathrm{d}x} = nS(v) = \frac{4\pi n e^4 Z_1^2 Z_2}{m_e v^2} L(v) \tag{1}$$

where e and m_e are the electron charge and mass, respectively.

ADVANCES IN QUANTUM CHEMISTRY, VOLUME 45
ISSN: 0065-3276 DOI 10.1016/S0065-3276(04)45001-1

It is convenient to expand the stopping number in a Born series

$$L(v) = \sum_{i=0}^{\infty} Z_1^i L_i(v) \tag{2}$$

in the projectile charge, Z_1. The leading term, L_0, is dominant over most of the range of commonly encountered projectile velocities [1]; however, other terms in the series become large at very low projectile velocity (L_1 and L_2) or at very high (relativistic) velocities (e.g., L_5) [2]. In fact, each term in the Born series can be again expanded in series

$$L_i(v) = \sum_{j=0}^{\infty} L_{ij}(v) \tag{3}$$

where the terms beyond L_{i0} correct for assumptions made in the derivation of L_{i0}.

The best-known example is for the first term in the expansion when the Bethe formulation is employed. In this case, the first, or Bethe–Born term in L_0 can be written, including the relativistic terms [3], as

$$L_{00} = \ln \frac{2mv^2}{I_0} - \ln(1 - \beta^2) - \beta^2 \tag{4}$$

where I_0 is the mean excitation energy or first moment of the energy weighted dipole oscillator strength distribution for the target and, as usual, $\beta = v/c$. However, the Bethe theory is developed assuming that the projectile has a much larger velocity than do the target electrons. To correct for this error, a new term, $L_{01} = -C/Z_2$, called the shell corrections, was introduced [4–7]. For the most part, terms beyond $i = 2$ and $j = 1$ have not been investigated.

It is primarily with the various methods and approaches for calculating the stopping cross-section or properties related to it, as well as the various terms in the series expansion of the stopping cross-section that many of the chapters in this volume will be concerned.

2. SOME HISTORY

Although there was early work on energy deposition using classical theory and free particle targets by Darwin [8] and Thomson [9] in 1912, the first formulation of the energy deposition problem based on the realization that the binding of electrons in a target atom is important was due to Niels Bohr in 1913 [10] and 1915 [11], when he realized the importance of

considering the target electrons to be bound. His treatment was classical, but considered the target electrons to be harmonically bound, and gave a leading term in the Born series that depends on the logarithm of v^3/ω, where ω is the characteristic frequency of the target electron. These seminal papers by Niels Bohr can be considered the beginning of energy deposition theory and since then, there has been considerable interest in the interaction and penetration of energetic ions with matter.

Following Bohr, there was significant activity (for an excellent review of the early history and an extensive list of references up to 1980, see Sections I and III of Ref. [12]). An important step was taken by Bethe in 1930 with the quantum mechanical solution of the problem in the first Born approximation, and using the dipole approximation to the oscillator strength distribution [13]. Again, as in Bohr's treatment, the leading term in the Born series was found to be proportional to the logarithm of a power of the projectile velocity over a characteristic energy, but this time it was v^2/I_0, where I_0 is again the mean excitation energy of the target. Bethe extended his treatment to the relativistic regime in 1932 [14].

In 1933, Bloch revisited the problem [15], and found that, in the dipole approximation, the odd powers in the Born series vanish, but that there is a non-negligible third term in the Born series, giving $S(v) \propto Z_1^4$. This term is now referred to as the Bloch correction and corresponds to L_2 in the Born series (equation (2)).

In 1963, Barkas noticed the difference in stopping powers when measured with positively and negatively charges projectiles [16], which implied an odd power L_1 contribution to the Born series, and the Z_1^3 contribution to the stopping cross-section is now referred to as the Barkas correction.

Higher order terms in the Born series, relevant to relativistic interactions, are seldom, but occasionally (*cf.* e.g., Refs. [2,17]) discussed.

Details of the forgoing can be found in the classic work by Livingston and Bethe [18], which contains a comprehensive review of experimental data, as well as in the extensive review papers by Fano [3], Fano and Cooper [19], Inokuti [20], Bichsel [4], and by Ahlen [12].

The preceding was developed mostly for atomic or molecular targets, and, indeed, much experimental work has been carried on gaseous samples. If one thinks along the lines of the Bragg rule [21], then one would not expect such considerations to differ much from results obtained on solid samples, and for most molecular or van der Waals solids – indeed they do not [22].

However, metals have a fundamentally different electronic structure than do atoms and molecules: the electrons are described more realistically by bands than by localized orbitals. In the early 1950s, using a density functional based theory, Lindhard [23–26] developed a successful method for treating solids directly that is still in use today.

3. THE SITUATION TODAY

During the past decade, there has been a revitalization of theoretical interest in energy deposition. This interest has been supported by the availability of extensive computational resources and stimulated by new and more accurate measurement techniques, so that details of the interactions between swift ions and materials can now be both measured and computed.

Many of the articles in this volume reflect the differences in the plan of attack on the energy deposition problem as it is presently formulated with respect to that of two decades ago. In the most general terms, the treatment of energy deposition in terms of considering each perturbation to the Bethe (or Bohr) leading term in the Born series has given way to what one might call in more avant garde terms, a more holistic approach.

Some of the contributions retain the framework of the first Born approximation, and explore ways to improve L_0 and thus gain a better understanding of some of the corrections, while others attempt to address the problem without the restriction of the Born approximation. Atomic, molecular, and solid targets are all well represented. In addition, many more details of ion-target interactions are now studied that were neglected before, due to the lack of sufficiently precise measurements and accurate theories. Channeling in solids, highly charged projectiles, chemical state and phase effects, charge changing, and dressed projectile ions are all in the accessible realm.

It is the object of this volume to present the most recent developments in a single collection, representing the state of the art in energy deposition theory.

ACKNOWLEDGEMENTS

This work has been supported in part by ONR grant No. N0014-96-1-0707 to JRS, and by and IBM SUR grant to the Quantum Theory Project. This support is gratefully acknowledged.

REFERENCES

[1] E. Bonderup, *Penetration of Charged Particles Through Matter*, 2nd edn., Fysisk Instituts Trykkeri, Aarhus Universitet, 1981.
[2] S. P. Ahlen, *Phys. Rev. A*, 1978, **17**, 1236.
[3] U. Fano, *Annu. Rev. Nucl. Sci.*, 1963, **13**, 1.
[4] H. Bichsel, Passage of charged particles through matter, in *American Institute of Physics Handbook* (ed. D. E. Gray), McGraw-Hill, New York, 1972, pp. 8.142–8.189.
[5] M. C. Walske, *Phys. Rev.*, 1952, **88**, 1283.
[6] M. C. Walske, *Phys. Rev.*, 1956, **101**, 940.
[7] E. Bonderup, *Kgl. Dan. Vidensk. Selsk.: Mat.-Fys. Medd.*, 1967, **35**.
[8] C. G. Darwin, *Phil. Mag.*, 1912, **23**, 901.

[9] J. J. Thomson, *Phil. Mag.*, 1912, **6–23**, 449.
[10] N. Bohr, *Phil. Mag.*, 1913, **25**, 10.
[11] N. Bohr, *Phil. Mag.*, 1915, **30**, 581.
[12] S. P. Ahlen, *Rev. Mod. Phys.*, 1980, **52**, 121.
[13] H. Bethe, *Ann. Phys. (Leipzig)*, 1930, **5**, 325.
[14] H. Bethe, *Z. Physik*, 1932, **76**, 293.
[15] F. Bloch, *Ann. Phys. (Leipzig)*, 1933, 285.
[16] W. H. Barkas, J. N. Dyer and H. H. Heckman, *Phys. Rev. Lett.*, 1963, **11**, 26.
[17] S. P. Ahlen, *Phys. Rev. Lett.*, 1977, **39**, 1338.
[18] M. S. Livingston and H. A. Bethe, *Rev. Mod. Phys.*, 1937, **9**, 245.
[19] U. Fano and J. W. Cooper, *Rev. Mod. Phys.*, 1968, **40**, 441.
[20] M. Inokuti, *Rev. Mod. Phys.*, 1971, **43**, 297.
[21] W. H. Bragg and R. Kleeman, *Phil. Mag.*, 1918, **10**, 305.
[22] D. I. Thwaites, *Nucl. Instrum. Methods B*, 1987, **27**, 293.
[23] J. Lindhard and M. Scharff, *Kgl. Dan. Vidensk. Selsk.: Mat.-Fys. Medd.*, 1953, **27** (15).
[24] J. Lindhard, *Kgl. Dan. Vidensk. Selsk.: Mat.-Fys. Medd.*, 1954, **28** (8).
[25] J. Lindhard, M. Scharff and H. E. Schiøtt, *Kgl. Dan. Vidensk. Selsk.: Mat.-Fys. Medd.*, 1963, **33** (14).
[26] J. Lindhard, *Kgl. Dan. Vidensk. Selsk.: Mat.-Fys. Medd.*, 1965, **34** (14).

This Page Intentionally Left Blank

Ionization and Energy Loss Beyond Perturbation Theory

P. L. Grande[1] and G. Schiwietz[2]

[1] *Instituto de Física da Universidade Federal do Rio Grande do Sul, Avenida Bento Gonçalves 9500, 91501-970, Porto Alegre, Brazil*
[2] *Bereich SF, Hahn-Meitner-Institut Berlin, Glienicker Str. 100, D-14109 Berlin, Germany*

Abstract

A review is given on the application of the coupled-channel method for the calculation of the electronic energy loss of ions as well as ionization in matter. This first principle calculation, based on the solution of the time-dependent Schrödinger equation, has been applied to evaluate the impact parameter and angular dependence of the electronic and nuclear energy losses of ions as well as the ionization due to high-power short laser pulses. The results are compared to experimental data as well as to other current theoretical models.

Contents

ADVANCES IN QUANTUM CHEMISTRY, VOLUME 45
ISSN: 0065-3276 DOI 10.1016/S0065-3276(04)45002-3

1. INTRODUCTION

The electronic energy loss has been studied for many years because of its direct application in problems concerning material damage and ion beam analysis. The theoretical treatment of the energy loss in atomic collisions has been greatly improved over the last decades and relies on an accurate treatment of target-continuum states up to high-emitted electron energies. Calculations of the electronic energy loss have been performed by using traditional methods known from atomic physics investigations such as the plane wave Born approximation (PWBA) [1,2], the high-energy solution by Bethe [3] and the semi-classical approximation (SCA) [4]. More advanced models are the Continuum-Distorted Wave Eikonal-Initial-State (CDW-EIS) [5], the classical trajectory Monte Carlo (CTMC) [6,7], the ACAM-CKLT model based on Liouville and Wigner equations in phase space [8], the Electron Nuclear dynamics (END) [9] and finally the atomic orbital coupled-channel method (AO) [10–13] that yields reliable values for the impact-parameter dependent electronic energy loss. These methods based on atomic physics calculations offer reliable ways to obtain detailed information on the energy-loss processes in gases as well as for the inner-shell electrons of solids. Of course, other approaches have to be adopted for conduction-band electrons of solid-state targets [14–17] in order to obtain an accurate description of the energy loss due to the valence electrons. Other models such as those of Refs. [18–21] have strongly enlarged our understanding of the physical processes that govern the energy loss.

In recent years we have investigated the electronic energy loss of bare and screened ions for light targets using the coupled-channel method. This first principle calculation [10–12], based on an expansion of the time dependent electronic wave function in terms of atomic orbitals, has been successfully applied to evaluate the impact-parameter and angular dependence of the electronic energy loss and the total stopping cross section of ions (antiprotons, H and He) colliding with H and He atoms at energies of 1–500 keV/amu. It has also been applied to calculate the entrance-angle dependence of the stopping force for He ions channeling along the Si main crystal directions [22,23] as well the shape of the surface peak for protons backscattered from Al under channeling and blocking conditions [24].

These benchmark calculations have also been used to check simplified models that account for the basic energy loss processes without the need of large scale calculations [25,26] and to calculate the probability of multiphoton ionization in the case of intense fs-laser pulses [27].

The chapter is organized as follows. The principle of the coupled-channel method is reviewed in detail in Section 2. The results are discussed in connection to higher order terms in Section 3. The application to multiphoton ionization is described in Section 4. Comparisons with measurements are provided in Section 5. A simple model for the electronic energy loss is

presented and compared to coupled-channel calculations in Section 6 and finally the conclusion and outlook are presented in Section 7. If not indicated otherwise, atomic units ($e = m = \hbar = 1$) will be used throughout the chapter.

2. THE COUPLED-CHANNEL METHOD

Here we will focus the attention on atomic treatments of the energy-transfer process. Thus, we will not consider solid-state effects such as intra-band transitions, collective excitations (bulk and surface plasmons) and the corresponding dynamic projectile screening.

Generally, ion–atom collision processes may be described either by first- or second-order perturbative approaches or by coupled-channel calculations. Perturbation theory often yields simple and in some cases even analytical results, but has the disadvantage of being valid only for high incident energies and low projectile charge states. In this work we will use the highest-order (coupled-channel) theory, which allows for an infinite number of interactions between projectile, target, and electron. The electron may be ionized in the first step and may be accelerated or decelerated in the second step. It is also possible that an electron, after being ionized, is 'thrown' back to the initial state. Furthermore, the probability for ionizing an electron is always less than or equal to unity. All this does not hold for perturbation theory. In the following, the basic ingredients of our model will be described.

2.1. Impact-parameter method

The theoretical formulation of atomic excitation and ionization processes is conveniently discussed by introducing the quantum-mechanical Hamilton operator. For a three-body system the Hamiltonian reads

$$\mathcal{H} = T_{\mathrm{p}}(\vec{r}_{\mathrm{p}}) + T_{\mathrm{t}}(\vec{r}_{\mathrm{t}}) + T_{\mathrm{e}}(\vec{r}_{\mathrm{e}}) + V_{\mathrm{pt}}(\vec{R}) + V_{\mathrm{te}}(\vec{r}) + V_{\mathrm{pe}}(\vec{R} - \vec{r}) \quad (1)$$

with the kinetic and potential energies denoted by T and V, respectively. The subscripts 'p', 't', and 'e' refer to the projectile ion, target core, and electron as indicated in Fig. 1. In the following we will use the impact-parameter method, i.e., it is assumed that $\vec{r}_{\mathrm{p}}$ and $\vec{r}_{\mathrm{t}}$ are given by classical paths $\vec{r}_{\mathrm{p}} = \vec{r}_{\mathrm{p}}(t, b)$, $\vec{r}_{\mathrm{t}} = \vec{r}_{\mathrm{t}}(t, b)$ (determined by the impact parameter b). This concept was first introduced by Bang and Hansteen [28]. It is well known [29] that the impact-parameter methods are valid as long as the Coulomb parameter

$$\nu_{\mathrm{i}\to\mathrm{f}} = \frac{Z_{\mathrm{p}} Z_{\mathrm{t}}}{q_{\mathrm{i}\to\mathrm{f}}} \approx \frac{Z_{\mathrm{p}} Z_{\mathrm{t}} v_{\mathrm{p}} m_{\mathrm{p}}}{\Delta E_{\mathrm{i}\to\mathrm{f}}} \quad (2)$$

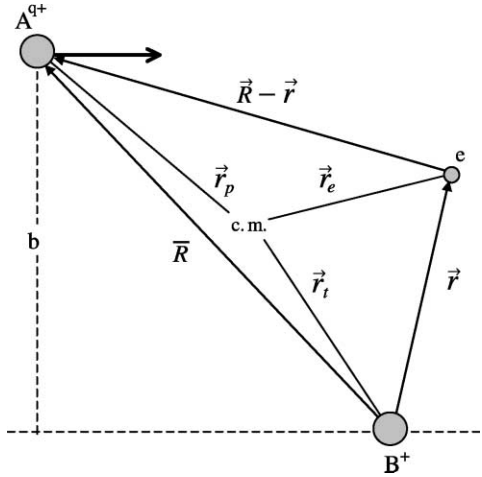

Fig. 1. Vector diagram for the projectile ion A^{q+}. the ionic target core B^+, and one active electron. The impact parameter b is indicated. $\vec{r}_p$, $\vec{r}_t$ and $\vec{r}_e$ are position vectors of projectile, target, and electron in the center-of-mass system.

is large compared to unit ($q_{i\to f}$ is the momentum transfer). This is always valid if the incident ion has at least thermal energies. If, additionally, an independent motion of the electron [30] is assumed, one may solve the time-dependent Schrödinger equation for one active electron:

$$\left(\mathrm{i}\frac{\partial}{\partial t} - \mathcal{H}_e\right)\Phi_e(t) = 0 \tag{3}$$

with

$$\mathcal{H}_e(t) = \mathcal{H}_{te} + V_{pe}(\vec{R}(t) - \vec{r}) \tag{4}$$

and

$$\mathcal{H}_{te}(t) = T_e(\vec{r}_e) + V_{te}(\vec{r}_e - \vec{r}_t(t)). \tag{5}$$

In the subsequent treatment the electron coordinate will be measured from the accelerated target nucleus and is the only dynamical variable. Thus the target system is the frame of reference [31,32]. In such a noninertial system non-Newtonian forces arise. The corresponding Hamiltonian $\mathcal{H}_{te}$ is

$$\mathcal{H}_{te} = -V_{te}(\vec{r}) + T_e(\vec{r}) + V_{recoil}(\vec{r}, \vec{r}_t(t)). \tag{6}$$

It is reasonable to neglect the last term V_{recoil}. By doing this transitions are excluded which are due to the interaction of the active electron with the recoiling target nucleus. This so-called recoil effect leads to insignificant contributions to total cross sections, but may be important for very close collisions ($b < 10^{-3}$ a.u.) [33]. Before the solution of equation (3) is

explained in detail, the classical path $\vec{R}(t)$ should be defined. Given the time-dependent electronic wave function Φ_e, a classical Hamiltonian for the heavy particles may be defined:

$$\mathcal{H}_h = T_p(\vec{r}_p) + T_t(\vec{r}_t) + V_{pt}(\vec{R}) + \langle \Phi_e | V_{pe}(\vec{R} - \vec{r}) | \Phi_e \rangle + \langle \Phi_e | V_{te}(\vec{r}) | \Phi_e \rangle. \quad (7)$$

With this Hamiltonian the classical equations of motion are solved. The last term in equation (7) was neglected because of its small influence on the motion of the target core in case of a strongly target-centered wave function Φ_e. It is emphasized that the concept defined by equation (7) introduces for the first time a dynamically curved projectile trajectory in the impact-parameter method. Thus the projectile motion is coupled to the motion of the active electron. However, since the projectile interacts with a mean electronic field, there is only approximate conservation of energy and momentum. For small projectile scattering angles this deficiency can be circumvented. In this case conservation of energy and momentum may be forced by applying the Eikonal transformation [34].

It is noted that some calculations have been performed with hyperbolic projectile paths. In this case only the first three terms in equation (7) are considered. However, most of the previous calculations have been performed for straight line paths, as given by the first two terms in equation (7). Such calculations are equivalent to quantum-mechanical solutions of the three-body Schrödinger equation with plane projectile waves. Typical examples for such quantum-mechanical three-body theories are the plane-wave Born approximation [35] and its limiting form at high incident energies, the Bethe theory [36]. However, the main advantage of the present model compared to previous stopping-power theories is the highest-order (coupled-channel) description of the electronic motion.

2.2. Independent particle model

The electronic many-body Hamiltonian in equation (1) is treated in the framework of the independent-electron frozen-core model. This means that there is only one active electron, whereas the other electrons are passive (no dynamic correlation is accounted for) and no relaxation occurs. In this model the electron–electron interaction is replaced by an initial-state Hartree–Fock–Slater potential [37]. This treatment is expected to be highly accurate for heavy collision systems at intermediate to high incident energies. The largest uncertainties of the independent-electron model will show up for low-Z few-electron systems, such as $H^0 + H^0$ and $H + He^0$ or for high multiple-ionization probabilities.

The independent-electron approximation allows for a distinction of target electrons and projectile-centered electrons which screen the projectile

nuclear charge. One of the most important dynamic correlation effects (deviations from the independent-electron approximation) is the collision of a target electron with a projectile-centered electron [38,39]. This will directly enhance the energy loss and reduce the projectile screening. It follows that a separate treatment of the different projectile charge states is important for reliable predictions of the mean energy loss for atomic targets [4,10,11,40], insulators and at higher incident energies also for metals [41].

The time-dependent Schrödinger equation may be solved by expanding $\Phi_e(\{\vec{r}\},t)$ in terms of unperturbed eigenfunctions φ_i of the target with coefficients $a_i(t) = \langle\varphi_i|\Phi_e(t)\rangle$. Thus, equation (3) is replaced by a set of coupled first-order differential equations, the so-called coupled-channel equations

$$\mathrm{i}\frac{\mathrm{d}}{\mathrm{d}t}a_i(t) = \sum_j a_j(t)\mathrm{e}^{\mathrm{i}(E_i-E_j)t}V_{j\to i}(\vec{R}(t)) \tag{8}$$

with the internuclear distance $\vec{R}$ and

$$V_{j\to i}(\vec{R}(t)) = \langle\varphi_i|V_{\mathrm{pe}}(\vec{R}(t),\vec{r})|\varphi_j\rangle. \tag{9}$$

E_i is the orbital energy associated with the target wave function φ_i. Here V_{pe} is an effective potential seen by the active electron, which contains the screening effect produced by other electrons from the medium. For bare incident ions, the active-electron projectile interaction V_{pe} is just the Coulomb potential. However, in the case where the projectile carries electrons, we use a screened potential made up of the Coulomb part due to the projectile-nuclear charge and the static potential produced by the target electrons that screen the projectile-nuclear charge

$$V_{\mathrm{pe}}(\vec{R}-\vec{r}) = -\frac{Z_{\mathrm{p}}}{|\vec{R}-\vec{r}|} + \sum_n^{\mathcal{N}}\int \mathrm{d}^3r'\,\frac{|\chi_n(\vec{r}')|^2}{|\vec{R}-\vec{r}-\vec{r}'|}, \tag{10}$$

where Z_{p} is the projectile nuclear charge, χ_n is the projectile-electron wave function and $\mathcal{N}$ is the number of projectile electrons. The wave functions χ_n for each electron n of the projectile are obtained according to the Hartree–Fock–Slater procedure [37]. Thus, we neglect dynamic screening (a time dependence of χ_n due to target induced polarization, respectively, excitation/ionization), Pauli correlation (anti-symmetrization of the projectile- and target-centered wave functions) as well as dynamic correlation effects due to the residual electron–electron interaction. It is pointed out, that the dynamic electron–electron interaction is not included in the present model since there is only one active electron.

For high projectile speeds and low projectile charge-states the transition matrix elements $V_{j\to i}$ are small. This is the domain of first-order perturbation theory (SCA, first-order Born approximation). In this case, most transitions

are governed by the direct step from the initial state j to the final i. Thus, we may drop the summation over j and use $a_j(t) = 1$ (the state j corresponds to the ground state). Hence, the time-consuming solution of the coupled-channel equations is reduced to a set of simple integrals over time within perturbation theory.

2.3. Wave functions – the basis set

The starting point of the present theory is an expansion of the time-dependent electronic wave function Φ_e in terms of single-center eigenfunctions φ_i of the target Hamiltonian $\mathcal{H}_{te}$

$$\Phi_e(\vec{r}, t) = \Phi_B(\vec{r}, t) + \Phi_C(\vec{r}, t), \tag{11}$$

$$\Phi_B(\vec{r}, t) = \sum_{n,l,m} a_{n,l,m}(t) e^{-iE_{n,l}t} \varphi_{n,l,m}(\vec{r}), \tag{12}$$

$$\Phi_C(\vec{r}, t) = \sum_{l,m} \int_0^\infty d\varepsilon \; b_{l,m}(\varepsilon, t) e^{-i\varepsilon t} \varphi_{\varepsilon,l,m}(\vec{r}). \tag{13}$$

In the above equations n, l and m are the main quantum number and the quantum numbers associated with angular momentum and angular momentum projection, respectively. The eigenfunction $\varphi_{n,l,m}(\vec{r})$ is defined in the usual way as

$$\varphi_{n,l,m}(\vec{r}) = \frac{1}{r} u_{n,l}(r) Y_{l,m}(\Omega) \tag{14}$$

and

$$E_{n,l} u_{n,l}(r) = \left(-\frac{d^2}{2\, dr^2} + \frac{l(l+1)}{2r^2} - V_t(r) \right) u_{n,l}(r), \tag{15}$$

where $E_{n,l}$ and the subscript n have to be replaced by ε for continuum states. The radial wave functions $u_{n,l}$ and $u_{\varepsilon,l}$ are calculated numerically using a Runge–Kutta method with variable step width. The bound-state wave functions $u_{n,l}$ are integrated from large r values down to zero and free wave functions are calculated from zero towards large r in order to suppress any irregular component in the wave function. The numerical uncertainty of the bound-state eigenvalues $E_{n,l}$ is about 10^{-6}. Boundary values for small r are obtained from a polynomial expansion of V_{te} and $u_{\varepsilon,l}$. The normalization of continuum states is similar to the method described by Cowan [42]. Bound-state wave functions are dimensionless whereas the continuum states are normalized per square root of energy (in a.u.). Hence it follows from equation (13) that the coefficients $b_{l,m}$ are also given per square root of energy (in a.u.). The eigenfunctions of $\mathcal{H}_{te}$ should be complete and

orthogonal. The completeness was checked by calculating the overlap matrix elements between an arbitrary target-centered wave function and Φ_e. The sum over the corresponding squared overlap matrix elements was equal to unity to within 10^{-4}. Orthogonality was verified by calculating overlap matrix elements between different eigenfunctions φ_i which are typically in the order of 10^{-5}. The infinite sums in equations (12) and (13) have to be truncated in order to perform the numerical calculation of the time-dependent wave function or the corresponding coefficients a and b. This introduces no problems for the bound states since highly excited states are generally less populated than the K, L or M shell. However, electrons captured into projectile states, as well as high-energy continuum electrons, lead to a population of high l states of target-centered wave functions. Thus partial waves exceeding orbital angular momenta of $l = 8$ often have to be considered for the continuum states. Another problem arises since the continuous energy variable of the free wave functions is not easy to handle in a numerical calculation. Therefore, the continuum is represented by a sum over a few (about 10 for each orbital angular momentum in the present work) pseudodiscrete radial wave functions $\Psi_{l,m}$:

$$\Phi_C(\vec{r},t) = \sum_{j,l,m} \frac{1}{r}\,\Psi_{l,m}(\varepsilon_j - \Delta\varepsilon_j/2, \varepsilon_j + \Delta\varepsilon_j/2, r, t) Y_{l,m}(\Omega), \qquad (16)$$

$$\Psi_{l,m}(E_1, E_2, r, t) = \int_{E_1}^{E_2} \mathrm{d}\varepsilon\; b_{l,m}(\varepsilon, t) \mathrm{e}^{-\mathrm{i}\varepsilon t} u_{\varepsilon,l}(r). \qquad (17)$$

An exact solution for $\Psi_{l,m}$ may be given in case of a pulse-like ionization process at $t = 0$. The corresponding moving wave packet is known as a Weyl packet [43,44],

$$\Psi_{l,m}(E_1, E_2, r, t) \approx \bar{b}_{l,m}(\bar{\varepsilon}, t) \int_{E_1}^{E_2} \mathrm{d}\varepsilon\; \mathrm{e}^{-\mathrm{i}\varepsilon t} u_{\varepsilon,l}(r). \qquad (18)$$

However, the numerical treatment of such explicitly time-dependent basis states would be time consuming compared to the treatment of bound states. Thus we search for a further simplification of $\Psi_{l,m}$ by investigating the asymptotic behavior of Coulomb wave functions [42]. For $r\Delta\varepsilon \ll \pi$ the radial wave function $u_{\varepsilon,l}$ is nearly independent of ε and may be considered constant for integration. For $\varepsilon t \ll \pi$ the exponential function in equation (18) is nearly independent of ε. In both cases $\Psi_{l,m}$ in equation (18) may be replaced by

$$\Psi_{l,m}(E_1, E_2, r, t) \approx \frac{\bar{b}_{l,m}(\bar{\varepsilon}, t)}{E_2 - E_1} \left(\int_{E_1}^{E_2} \mathrm{d}\varepsilon\; \mathrm{e}^{-\mathrm{i}\varepsilon t} \right) \left(\int_{E_1}^{E_2} \mathrm{d}\varepsilon\; u_{\varepsilon,l}(r) \right) \qquad (19)$$

$$\begin{aligned}\Psi_{l,m}(E_1, E_2, r, t) &= \bar{b}_{l,m}(\bar{\varepsilon}, t)\mathrm{e}^{-\mathrm{i}\bar{\varepsilon}t} F(E_2 - E_1, t) \int_{E_1}^{E_2} \mathrm{d}\varepsilon \; u_{\varepsilon,l}(r) \\ &= \frac{\bar{a}_{l,m}(\bar{\varepsilon}, t)}{\sqrt{E_2 - E_1}} \mathrm{e}^{-\mathrm{i}\bar{\varepsilon}t} F(E_2 - E_1, t) \int_{E_1}^{E_2} \mathrm{d}\varepsilon \; u_{\varepsilon,l}(r), \end{aligned} \tag{20}$$

with

$$F(\Delta E, t) \equiv \frac{2}{t\Delta E} \sin\left(\frac{t\Delta E}{2}\right). \tag{21}$$

The dimensionless coefficients $\bar{a}$ correspond to the coefficients $\bar{b}$ defined above. Except for $\bar{a}$ and the exponential function in equation (19), all quantities are real numbers and only the integral over the radial continuum wave functions needs to be calculated numerically. A damping function similar to F was introduced by Reading *et al.* [44] in order to improve the asymptotic behavior of continuum wave functions. However, the wave packets as described above are only approximate solutions for large values of t and r. It is evident that this deficiency will affect mainly those continuum states which have a considerable overlap with asymptotic projectile states. Most of these states are neglected anyway because of the finite number of target-centered partial waves ($l < 11$) taken into account. From the structure of Coulomb wave functions it is obvious that transition matrix elements involving either a high Rydberg state or a low-energy continuum state are identical when re-normalized per square root of energy [42]. Since an explicit summation over an infinite number of bound states is impossible in a numerical treatment, we have integrated these re-normalized Rydberg wave functions up to the continuum threshold. The resulting Rydberg wave packet is then added to the lowest energy continuum packet. In this way approximate completeness of the basis set is achieved.

It is noted that other authors have either neglected the damping factor F [29,43] or they used only approximate atomic wave functions in similar descriptions of the electronic motion.

From symmetry properties of the wave function and from the Coulomb matrix elements it is possible to distinguish between two classes of basis states, namely gerade (denoted by $+$) and ungerade (denoted by $-$) states. The corresponding wave functions Φ^+ and Φ^- may be obtained by replacing the spherical harmonics $Y_{l,m}$ in equation (14) by

$$Y^{\pm}_{l,|m|} = \frac{1}{\sqrt{2}}(Y_{l,|m|} \pm (-1)^m Y_{l,-|m|}), \tag{22}$$

for $m \neq 0$ and

$$Y^{+}_{l,0} = Y_{l,0}. \tag{23}$$

The projectile interaction does not lead to transitions between gerade and ungerade states. Therefore, only states with the same symmetry as the ground state have to be considered. The coupled-channel equations are solved in the present work for about 500 gerade states (including to up 50 bound states), which replace about 900 eigenstates. The gerade (or ungerade) states are chosen to yield optimum convergence for a certain regime of incident energies.

2.4. Matrix elements

In order to integrate the coupled-channel equation (8) the time as well as the impact-parameter dependence of the matrix elements (equation (9)) have to be determined. For this purpose, the matrix elements $V_{j\to i}(\vec{R}(t))$ are expanded in terms of the radial (R) and angular ($\hat{R}$) parts of the internuclear vector $\vec{R}$ according to

$$V_{j\to i}(\vec{R}(t)) = -\sum_{L=|l_i-l_j|}^{l_i+l_j} W_{L,M}^{i,j} G_L^{i,j}(R) Y_{L,M}(\hat{R}), \qquad M = m_j - m_i, \tag{24}$$

which is obtained after separating the radial and angular parts (determined by the spherical harmonics $Y_{L,M}$) of the atomic target wave function φ_i. The coefficients $W_{L,M}^{i,j}$ are given by

$$W_{L,M}^{i,j} = \left(\frac{4\pi(2l_i+1)(2l_j+1)}{2L+1}\right)^{1/2} (-1)^{m_i+M} \begin{pmatrix} l_i & l_j & L \\ 0 & 0 & 0 \end{pmatrix} \times \begin{pmatrix} l_i & l_j & L \\ -m_i & m_j & -M \end{pmatrix}. \tag{25}$$

The symbols

$$\begin{pmatrix} \cdots & \cdots & \cdots \\ \cdots & \cdots & \cdots \end{pmatrix}$$

in equation (25) represent the Wigner '3j' symbol as described in Ref. [45]. We consider only screened interaction potentials, which are spherically symmetric. In this case the function $G_L^{i,j}(R)$ can be written as

$$G_L^{i,j}(R) = \int_0^\infty \mathrm{d}r u_i^* u_j f_L(r,R), \tag{26}$$

where u_i, u_j are the radial wave functions of the states i and j, respectively. The function $f_L(r,R)$ is determined by the interaction potential and is given

by

$$f_L(r,R) = -Z_\mathrm{p}\frac{r_<^L}{r_>^{L+1}}, \tag{27}$$

for the Coulomb potential $-Z_\mathrm{p}/(|\vec{R}-\vec{r}|)$ and

$$f_L(r,R) = \lambda(2L+1)(-1)^L A_L(\lambda r_<)H_L(\lambda r_>). \tag{28}$$

for the Bohr-like screened potential

$$\frac{\exp(-\lambda|\vec{R}-\vec{r}|)}{|\vec{R}-\vec{r}|}.$$

The functions $A_L(x)$ and $H_L(x)$ are equal to the modified spherical Bessel functions $i^L j_L(ix)$ and $i^{L+1}h_L^+(ix)$, respectively [46]. The notation $r_{<(>)}$ means the smaller (larger) of the values of r and R.

The projectile-electron potential (equation (10)) is represented here by

$$V_\mathrm{pe}(\vec{R}-\vec{r}) = -\frac{Z_\mathrm{p}-n_\mathrm{p}}{|\vec{R}-\vec{r}|} + n_\mathrm{p}\sum_{n=1}^{n_\mathrm{max}}(A_n + B_n|\vec{R}-\vec{r}|)\frac{\exp(-\lambda_n|\vec{R}-\vec{r}|)}{|\vec{R}-\vec{r}|}, \tag{29}$$

where n_p is the number of bound electrons and the coefficients A_n, B_n and λ_n are obtained by fitting to the numerically determined potential from equation (10). The number of Bohr-like screened potential terms, n_max, corresponds to the number of electronic shells of each target atom. In this way, the function $f_L(r,R)$ used in equation (26) is obtained straightforwardly.

With the matrix elements from equation (24) the coupled-channel equations are solved numerically in order to obtain the coefficients a_i after the collision ($t \to \infty$). For instance, the probability of ionizing the target from the ground state to a continuum state of energy ε, angular momentum l and projection m in a collision with impact parameter b is given by

$$\frac{\mathrm{d}P_{l,m}}{\mathrm{d}\varepsilon}(b) = \lim_{t\to\infty}|a_{\varepsilon,l,m}(b,t)|^2 \tag{30}$$

and to a empty bound state n

$$P_{n,l,m}(b) = \lim_{t\to\infty}|a_{n,l,m}(b,t)|^2. \tag{31}$$

The accuracy of the present computer code when restricted to perturbation theory (SCA mode) was checked against PWBA [1,47] and SCA [29,33] results for ionization and excitation. From the comparison a relative uncertainty of less than 0.1% for probabilities and about 2% for cross sections was inferred for different final states. It is noted that the uncertainty

in the cross section calculations is mainly due to the small number of impact parameter steps and continuum energies considered in this work. The numerical transition matrix elements agree to within 10^{-4} or better with analytical solutions for transitions between the lowest bound states. Finally, the accuracy of the coupled-channel code was checked against results of the well-established two-center code (AO +) by Fritsch [48,49]. When restricted to the same 20 target-centered bound states the results of both codes agree to within two to three digits for excitation probabilities ranging from 10^{-6} to 0.15. With the present code unitarity can be preserved to within about 10^{-7} if the damping factor F in equation (21) is set to unity.

The results coming from the coupled-channel method results agree with the predictions of the first-order perturbation theory (SCA) in the case of a small perturbation. Small perturbations correspond to either fast projectiles, large impact parameters or small projectile charges. Thus, the advantages of coupled channel calculations compared to first-order theories should show up especially at intermediate incident energies and for small impact parameters. In contrast to other coupled-channel calculations we do not use pseudostates to represent the electron continuum wave functions. Instead we use a large number of continuum wave-packets that are composed of a superposition of exact continuum eigenstates (up to 500 gerade states with partial waves up to $l = 10$), since the computation of the stopping power demands high accuracy of the emitted electron energy spectrum.

2.5. Ionization/stopping/straggling cross sections

2.5.1. Electronic

Each excited or continuum state corresponds to a well-defined energy transfer ΔE_i ($= E_i - E_0$). Then the cross section for such an energy-transfer process will read

$$\sigma_i = 2\pi \int_0^\infty b \, \mathrm{d}b P_i(b) \tag{32}$$

and average electronic energy loss $\bar{Q}(b)$ is given by

$$\bar{Q}(b) = \sum_i P_i(b) \Delta E_i \tag{33}$$

with the ionization and excitation probabilities P_i from equations (30) and (31). The electronic stopping cross section S_e and energy straggling W per atom can be computed directly from:

$$S_\mathrm{e} = \sum_i \sigma_i \Delta E_i = 2\pi \int_0^\infty b \, \mathrm{d}b \, \bar{Q}(b) \tag{34}$$

and

$$W = \sum_i \sigma_i \Delta E_i^2. \tag{35}$$

It is noted that the above sums have to be replaced by integrals in the case of continuum states.

Figure 2 shows the comparison of the present coupled-channel results (solid curve) with other calculations for the total ionization cross section as well as for the electronic stopping power S_e of antiprotons on H. The dashed curve also represents coupled-channel calculations [50] using a large number of pseudostates. Both coupled-channel calculations provide similar results and are in rather good agreement with recent measurements [51] (symbols). Also displayed are results of first-order Born (PWBA) and the CDW-EIS model. As it can be seen from this figure, higher order effects become very important at low projectile energies. The PWBA calculations yield too large values of the electronic energy loss, since for antiprotons the polarization effect leads to a reduced electronic density along the ion path. In the CDW-EIS model [5] (dotted line) the initial and final states partially include the effect of the projectile potential (approximate two-center initial and final

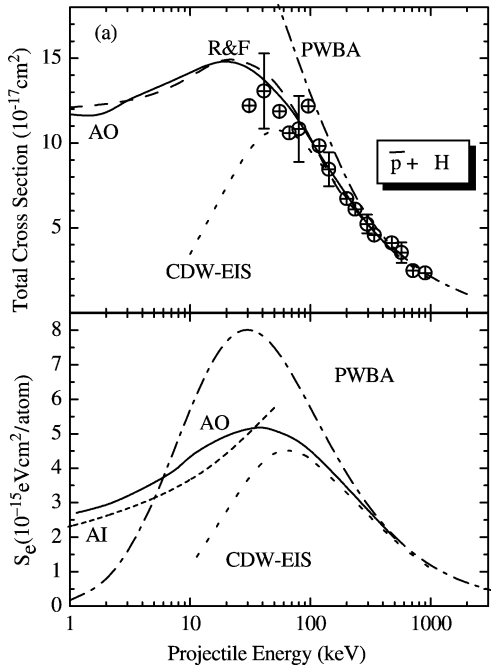

Fig. 2. Total ionization cross section and stopping power for antiprotons on hydrogen atoms.

states) and as a consequence the results at intermediate to high energies are significantly improved. However, a breakdown of this model is observed for energies below 70 keV. This is attributed to the incomplete treatment of the two-center effects and to the neglect of higher order residual projectile–target interactions in the CDW-EIS model. Furthermore, at low energies it is not able to describe the Fermi–Teller effect responsible for the slow decrease of the stopping power as a function of the projectile energy. The curve denoted by AI provides a simple model for this adiabatic ionization [52]. In this model the adiabatic potential curves for the electronic states in the field of the quasidipole formed by p and $\bar{p}$ are taken into account and a good agreement with AO results is observed for low energies.

2.5.2. Nuclear

The nuclear energy loss and the corresponding stopping cross section can also be calculated from the solution of classical equations for the projectile path. In equation (7) the interaction of the electron cloud with the residual target core was neglected. Thus, the projectile scattering angle θ is a more accurate quantity than the recoil energy in this model. Consequently, we search for a connection between the Q value, the projectile scattering angle, and the projectile energy loss. Considering conservation of energy and momentum, the kinetic energy transfer to the target atom is given by

$$T[Q] = \frac{4m_\mathrm{p}m_\mathrm{t}}{(m_\mathrm{p}+m_\mathrm{t})^2}E\left(f\,\sin^2(\theta_\mathrm{cm}/2) + \frac{1}{4}(1-f)^2\right) \tag{36}$$

with $f \equiv \sqrt{1 - Q/E(m_\mathrm{p}+m_\mathrm{t})/m_\mathrm{t}}$, E the ion initial energy, and θ_cm the projectile scattering angle in the center-of-mass system

$$\left(\tan\,\theta = \frac{\sin\,\theta_\mathrm{cm}}{\cos\,\theta_\mathrm{cm} + m_\mathrm{p}/m_\mathrm{t}}\right).$$

The nuclear stopping power per atom S_n may be computed directly from the impact-parameter integration of the nuclear energy loss.

At low incident energies the nuclear stopping process determines the slowing down of ions in the matter. Calculation with parameterized time-independent potentials have yielded stopping powers and ranges in good agreement with experimental data [53] except for some special systems [54]. These potentials correspond to static (frozen) electronic charge distributions. However, investigations of highly charged ions or negative particles require the treatment of collisional excitation processes and of the resulting dynamic target polarization. Any polarization during the collision will influence the projectile/target interaction potential. Hence, the nuclear stopping power is changed. It should be emphasized that the nuclear stopping may also be influenced by the electronic energy loss in a different fashion for

many-electron systems due to the formation of quasi-molecular orbitals that influence the excited potential [54].

We have used our atomic-orbital coupled-channel code to calculate dynamic curved projectile trajectories for protons and antiprotons in the field of polarized hydrogen atoms. According to Section 2.1, the electronic motion is treated quantum mechanically resulting in a time-dependent electronic density. The nuclear motion is determined simultaneously by Newtow's classical equation of motion and the nuclear energy transfer may directly be extracted. Figure 3 shows scaled nuclear energy loss cross sections for different incident light particles on atomic hydrogen. For fast projectiles the nuclear energy loss cross section S_n behaves roughly as $\ln(E_\mathrm{p})/E_\mathrm{p}$ and a maximum of S_n is found at about 50 eV. Thus, $S_n E_\mathrm{p}/\ln(E_\mathrm{p}/10\ \mathrm{eV})$ is nearly constant when E_p is varied from 1 to 300 keV. The lowest curve in Fig. 3 is the well-known ZBL stopping-power prediction [53]. It relies on an approximate

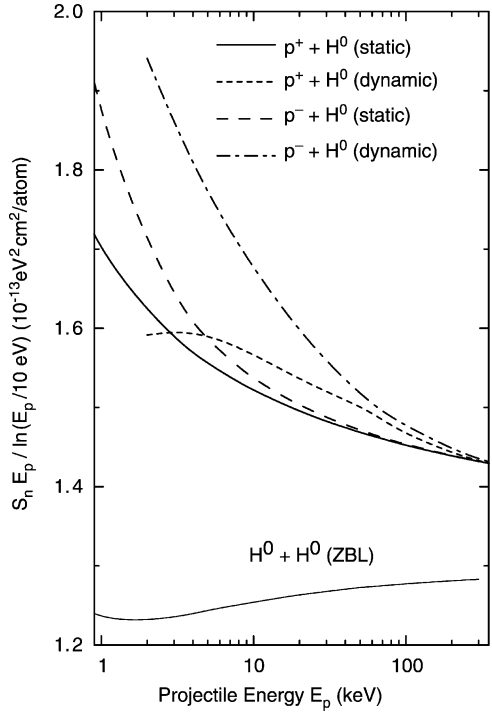

Fig. 3. Scaled nuclear stopping power as a function of the projectile energy for protons (short-dashed and thick solid line), antiprotons (long-dashed and dash-dotted lines) and neutral hydrogen incident on hydrogen atoms. Thin solid line: ZBL prediction [53] for neutral projectiles. For two of the curves (short-dashed and dashdotted) dynamic target polarization has been accounted for in the calculation.

treatment of the static interaction between a projectile and the target atom. Since both collision partners are screened in this case the results are lower than the static results for incident protons and antiprotons. For antiprotons at low velocities the static results are slightly larger than for protons because the distance of closest approach r_0 is smaller for antiprotons.

Especially at low energies, the results of dynamic calculations show a significant deviation from the static ones. At 2 keV the antiproton results with polarization lie about 20% above the static results. Furthermore, S_n clearly shows a different energy dependence for antiprotons and protons. The reason for this deviation is depicted in Fig. 4. At large impact parameters negative projectiles repel the target electron cloud and positively charged particles attract the electrons. Hence, in both cases the projectile is deflected towards to the target atom and the deflection is larger than in the static case. The situation is different for the positive ions at small impact parameters; at larger internuclear distances the projectile is attracted by the electron cloud, but at small distances the Coulomb force between the nuclei leads to a sudden projectile deflection away from the target nucleus. At low energies, this repulsion is even enhanced due to a reduction of r_0. At intermediate impact parameters, the attraction and the repulsion are of the same strength

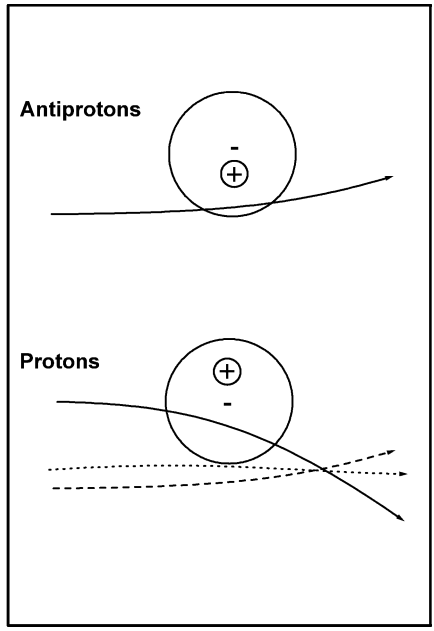

Fig. 4. Scheme showing typical projectile trajectories of protons and antiprotons in the field of polarized target atoms.

and the trajectory is nearly a straight-line. Thus, the nuclear energy transfer is strongly reduced and at a certain impact parameter it is even zero.

Finally, at low incident energies, larger impact parameters gain importance and the dynamic results exceed the static ones. On the contrary, for fast positively charged projectiles the zero-crossing of the projectile scattering angle (at impact parameters of about 2 a.u. in the case of H) leads to slightly reduced dynamic nuclear stopping cross sections.

2.6. Two-center calculations

The procedure outlined in the previous sections to solve the time-dependent Schrödinger equation should be highly accurate as long as electron capture is of minor importance. An exact description of an even single projectile-centered state would require an infinite number of target-centered states in the basis set. The use of huge basis sets of target-centered states can in fact describe, in same cases [12], the energy loss due to the capture process but in general full two-center calculations have to be performed.

The present coupled-channel calculations also allow for the inclusion of projectile-centered states according to following expansion

$$\Psi_{\mathrm{e}}(t) = \sum_n a_n(t)\phi_n(\vec{r},t), \tag{37}$$

where the wave functions $\phi_n(\vec{r},t)$ are either time-dependent target-centered states (bound or wave packet continuum states) or projectile-centered states. The coupled-channel equations are obtained from the more general matrix elements for transitions between two moving reference frames

$$\langle\phi_m(\vec{r},t)|\mathcal{H}_{\mathrm{e}} - \mathrm{i}\frac{\partial}{\partial t}|\Psi_{\mathrm{e}}(t)\rangle \tag{38}$$

and they read

$$\sum_n \langle\phi_m(\vec{r},t)|\phi_n(\vec{r},t)\rangle \mathrm{i}\frac{\mathrm{d}a_n}{\mathrm{d}t} = \sum_n a_n(t)\langle\phi_m(\vec{r},t)|\mathcal{H}_{\mathrm{e}} - \mathrm{i}\frac{\partial}{\partial t}|\phi_n(\vec{r},t)\rangle. \tag{39}$$

The matrix elements can be calculated as

$$\begin{aligned}\left\langle\phi_m(\vec{r},t)\middle|\mathcal{H}_{\mathrm{e}} - \mathrm{i}\frac{\partial}{\partial t}\middle|\phi_n^{\mathrm{P}}(\vec{r},t)\right\rangle &= \langle\phi_m(\vec{r},t)|V_{\mathrm{t}} + \mathcal{H}_{\mathrm{p}} - \mathrm{i}\frac{\partial}{\partial t}|\phi_n^{\mathrm{p}}(\vec{r},t)\rangle \\ &= \langle\phi_m(\vec{r},t)|V_{\mathrm{t}}|\phi_n^{\mathrm{p}}(\vec{r},t)\rangle\end{aligned} \tag{40}$$

and

$$\begin{aligned}
&\langle\phi_m(\vec{r},t)|\mathcal{H}_{\rm e} - {\rm i}\frac{\partial}{\partial t}|\phi_n^t(\vec{r},t)\rangle \\
&\quad = \langle\phi_m(\vec{r},t)|V_{\rm p} + \mathcal{H}_{\rm t} - {\rm i}\frac{\partial}{\partial t}|\phi_n^t(\vec{r},t)\rangle \\
&\quad = \langle\phi_m(\vec{r},t)|V_{\rm p}|\phi_n^t(\vec{r},t)\rangle,
\end{aligned}$$

for exact time-dependent target-centered states $\phi_n^t(\vec{r},t)$ or projectile-centered $\phi_n^{\rm p}(\vec{r},t)$ states.

Since the wavepackets $\phi_n^t(\vec{r},t) = {\rm e}^{-{\rm i}\bar{E}t}(\Delta E)^{-1/2}\int_{\varphi_{\rm E}}(\vec{r},t)\,{\rm d}E$ are not exact solutions of the time-dependent Schrödinger equation for the target atom, there is an extra term

$$\begin{aligned}
&\langle\phi_m(\vec{r},t)|\mathcal{H}_{\rm e} - {\rm i}\frac{\partial}{\partial t}|\phi_n^t(\vec{r},t)\rangle \\
&\quad = \langle\phi_m(\vec{r},t)|V_{\rm p}|\phi_n^t(\vec{r},t)\rangle + \langle\phi_m(\vec{r},t)|^{-{\rm i}\bar{\varepsilon}t}(\Delta E)^{-1/2}\int(\varepsilon-\bar{\varepsilon})|\varphi_\varepsilon(\vec{r},t)\rangle{\rm d}\varepsilon,
\end{aligned}$$

which is not zero in the case of capture matrix element ($\langle$projectile$|\cdots|$target$\rangle$). It is noted that this term does not appear in the case of target–target matrix elements. All matrix elements are calculated numerically for hydrogen-like projectile wave-functions.

The capture probabilities are then obtained from the coefficients a_n from the expansion (37). For the capture energy-loss, the translation factor energy $v^2/2$ has to be added to the transition energy between the target and projectile states. In conclusion, the treatment of electron capture requires to account for phase factors of the moving reference systems, for non-orthogonal states at both centers and to consider the time dependence of wave packets. Such calculations are, therefore, much more time consuming than target-centered computations.

3. HIGHER ORDER EFFECTS

The coupled-channel calculations allow for accurate calculations of higher order effects. At high energies the electronic energy loss may be expanded in terms of the projectile charge $Z_{\rm p}$ according to

$$Q(b) = q_1 Z_{\rm p}^2 + q_2 Z_{\rm p}^3 + q_3 Z_{\rm p}^4 + \cdots \tag{41}$$

The quadratic term is the leading one at high energies. It is well described by first-order Born theory and involves only direct ionization and excitation of the target atom. With decreasing ion energy higher order effects become important. They either depend on the sign of the projectile charge $Z_{\rm p}$

(polarization and binding effects) or only on the absolute value of Z_p (Magnus [55] and Bloch [19] corrections). All higher order effects (deviations from the Z_p^2 proportionality) can be related to multiple successive interactions of the active electron with the projectile and the (screened) target within a single collision. The number of these interactions increases for high projectile charges, small impact parameters and low projectile velocities. We can distinguish different higher order contributions as a function of the strength of the perturbation.

For small perturbations of outer-shell electrons the polarization of the electronic density appears first. Positively charged particles attract and negatively charged projectiles repel the electron cloud during an early stage of the collision, which leads to a change in the density around the projectile path and correspondingly to a change in the stopping power. This is a second-order effect (proportional to Z_p^3).

By decreasing the ion energy the influence of the projectile is no longer a small perturbation and effects such as saturation and binding-energy modifications will appear. In standard first-order treatments, the sum over all probabilities exceeds one since no reduction of the initial-state population is accounted for. This leads to an artificial creation of electrons (overestimated stopping power proportional to Z_p^4). The corresponding experimentally observed saturation (stopping power reduction compared to Z_p^2 for heavy ions) may roughly be described within the unitary first-order Magnus approximation [55]. A different treatment by Bloch [19] also takes into account this effect and the term proportional to Z_p^4 agrees quite well with the one from coupled-channel calculations.

For inner-shell electrons the so-called binding effect gains importance. The resulting change of the stopping power is proportional to Z_p^3 but its sign is opposite to the change induced by the polarization effect. The binding effect can be viewed as an increased binding energy of the bound electron in the vicinity of positively charged projectiles, which reduces the stopping power. It is a second-order effect (proportional to Z_p^3) that may be included in a perturbative treatment by consistently accounting for the diagonal matrix elements of the projectile/electron interaction or by including the mean binding effect in a perturbed stationary-state model [56].

Finally, at low energies the projectile represents a strong perturbation and effects such as electron capture for positive projectiles and adiabatic ionization (Fermi–Teller effect [52]) for negatively charged projectiles turn out to be very important. The electron capture may be viewed as a very strong polarization effect (target electrons are attracted by and finally travel with the projectile). If the electronic motion is described in a target-centered basis all orders of the perturbation are necessary to yield the time-dependent electron-density. In other words, the interaction between electron and projectile never stops. In the Fermi–Teller effect, collisions with negative heavy projectiles are involved. For the case of antiprotons on H, the electrons

move in the field of a transient 'quasidipole' formed by the heavy particles. The electronic states of the quasidipole experience a rapid loss of binding energy when the distance between the heavy particles decreases, and become even unbound at a certain non-zero 'critical' distance.

Besides these effects we also observe for increasing perturbations (high Z_p at low energies) a diffusion like effect in the energy spectrum of emitted electrons [7]. The first excitation step gives rise to an excitation spectrum with a maximum at low energy transfers. Successive interactions (continuum–continuum couplings) yield a broadening of the excitation spectrum. Hence, low electron energies are suppressed due to this diffusion-like process and the mean stopping power as well as the straggling are enhanced. This energy-diffusion effect may be viewed as the onset of the Fermi-shuttle effect, where multiple head-on collisions between projectile and electron in the field of target lead to extremely high electron energies.

Figure 5 shows a contour plot of the time-dependent electron density for a hydrogen atom disturbed by a positively (displayed on left) and negatively (displayed on right) charged particle at 10 keV with an impact parameter of 1 a.u. These electronic densities correspond to a cut in the collision plane and were obtained directly from the calculated transition amplitudes $a_i(t)$ according to

$$\rho(\vec{r},t) = \sum_{i,j} a_i a_j^* \, \mathrm{e}^{-\mathrm{i}(E_i - E_j)t} \varphi_i(\vec{r}) \varphi_j^*(\vec{r}) \tag{42}$$

using about 200 gerade states. An inspection of this figure shows several interesting features. First, the positively charged particle (proton) attracts the electron on the incoming path; the so-called polarization process. One may see that the electron density moves towards the projectile. The opposite effect takes place for the negatively charged particle (antiproton).

Second, for protons at the distance of closest approach, the maximum of the electron-density points to the backward direction at an angle of about 120° with respect to the beam axis. It is clearly visible that the electron density lies behind the projectile, although the proton is attracting the electron. The reason for this behavior is a delayed response of the electron cloud (the inertia due to the electron mass). Third, the proton enables electron-capture in the outgoing path of the collision and large fraction of the electron density is finally bound to and moving with the projectile. Since an antiproton repels the target-electron, the electron density near the projectile on the outgoing path of the collision is almost zero.

For collisions of antiprotons with atomic hydrogen, a quasidipole is formed during the collisions. The dipolar antiproton–proton system does not support bound states for inter-particle distances below 0.64 a.u. [52]. For finite velocities and larger impact parameters b (in the figure, $b = 1$) there is still a significant ionization contribution. As can be observed in the figure at

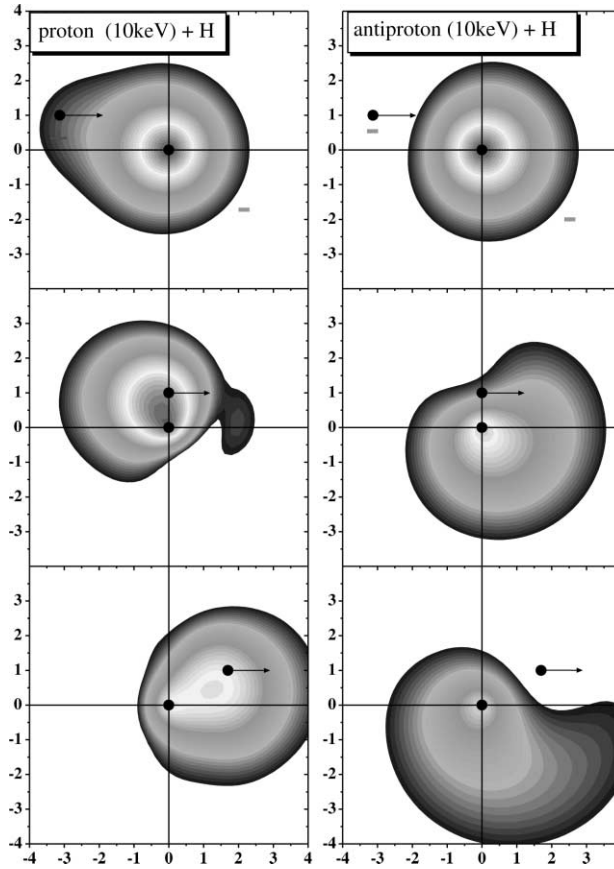

Fig. 5. Contour plot of the time-dependent electronic density of a hydrogen atom disturbed by a 10 keV proton (on left) and antiproton (on right) at $b = 1$. The plot corresponds to a cut of the density across the collision plane.

the distance of closest approach there is a high transition probability (blowing up of the density).

The electronic energy loss for proton, antiproton, helium and antihelium on H at 500 keV normalized to first-order Born (SCA) results is shown in Fig. 6 as a function of the impact parameter. Results for particles are represented by solid lines and for antiparticles by dashed lines. Deviations from the horizontal line (ratio equal to one) correspond to higher order effects. A fictitious projectile charge $Z_p = \pm 0.5$ is also displayed in order to observe the tendency of the energy loss as a function of the projectile charge. For large impact parameters the difference between the energy loss for particles and antiparticles is due to the polarization effect. The energy loss

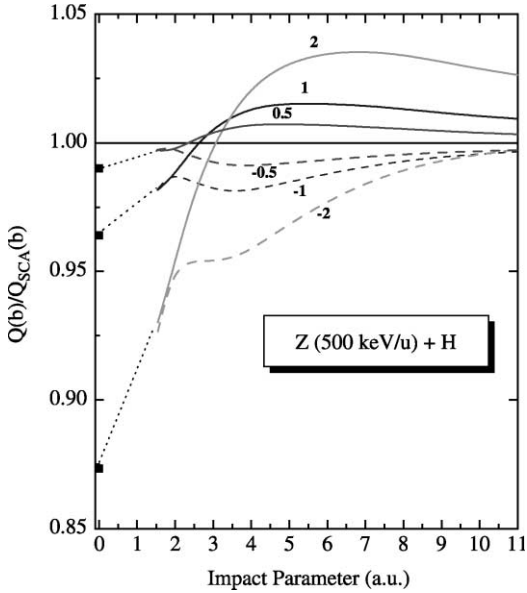

Fig. 6. The electronic energy loss normalized to first-order Born results for bare projectiles with $Z_p = \pm 0.5, \pm 1$ and ± 2 at 500 keV/u on hydrogen. Results for positively charged particles are represented by solid lines and for negatively charged ones by dashed-lines. The squares at $b = 0$ represent a calculation with improved accuracy. The dotted lines indicate the transition between the two AO calculations.

for positively charged particles is larger than for negatively charged particles and the difference is nearly symmetrical for low Z_p.

For small impact parameters one may see an overall reduction of the energy loss as a function of $|Z_p|$. This corresponds to Z_p^4 effects overshadowing the Z_p^3 ones (polarization and binding effects). The binding effect can enhance or reduce the probability to excite or ionize the target atom. It always leads to a significant reduction of the polarization effect at small impact parameters. It should be noted that although the overall numerical uncertainties are about 2%, they can be much larger for impact parameters smaller than 2 a.u. For central collisions ($b \rightarrow 0$), we can, however, strongly increase the size of the basis set by using only states with angular momentum projection m equal to zero due to the azimuthal symmetry of the time-dependent electronic wave function. Calculations performed with almost 150 of these states show that the Barkas effect, the difference between the energy loss for positively and negatively charged particles, is nearly zero (to within the numerical uncertainties) for unscreened projectiles. This result seems to be independent of the target potential since it is also observed for a harmonic-oscillator target [57].

4. PHOTON VS. CHARGED-PARTICLE IONIZATION

Here we apply the coupled-channel method to calculate photo ionization of atomic hydrogen by short (femtosecond) laser pulses at high power densities (up to 5×10^{14} W/cm^2). A classical electro-dynamical field approximates the laser/atom interaction, according to (in the Coulomb gauge)

$$V_{\text{laser}}(t) = -\vec{r}\cdot\vec{E}(t) \tag{43}$$

with

$$E(t) = E_0 \exp\left(-\frac{t^2 4 \ln 2}{\Delta t^2}\right)\cos(\omega t). \tag{44}$$

The time dependent shape of this field is given by a cos-function with amplitude E_0 enveloped by a Gaussian centered at the time $t = 0$ with full width at half maximum (FWHM) Δt representing the laser pulse length.

The transition matrix elements are non-vanishing if the dipole selection rules are fulfilled. The dipole approximation is valid, since the wavelength of the laser is large in comparison to the atomic radius. For a linear polarized laser beam, with the electrical field in the z-direction, this means $\Delta l = \pm 1$ and $\Delta m = 0$. The coupled-channel method is used to determine the coefficients of the wave function by solving the system of coupled-channel equation (3) for 764 eigenstates of the target. These consist of 45 bound states up to $n = 9$ and wave packets up to continuum energies of 18 eV and $l = 9$, all coupled by the corresponding dipole matrix elements for linearly polarized light. Although we have performed large-scale computations, there will be an upper limit for the laser-pulse width Δt_{p}, since the corresponding energy broadening ΔE_{p} should exceed the energy difference of neighboring continuum states. Furthermore, there will be a maximum possible power density I related to the upper limit of electron energies and partial waves l in the calculation. These two computational limits have been explored here.

As a result of the calculations we obtain the differential probability dP of ionizing an atom in an energy interval dε depending on the electron energy. Figure 7 represents such an ionization probability calculated for hydrogen atoms excited with a wavelength of 260 nm and a pulse duration of 10 fs. The probability is enhanced at integer multiples of the photon energy ($nh\nu$ where the minimum number n is given by the multiple at which the ionization limit is exceeded (in case of hydrogen $n = 3$). Sometimes a small shift of the harmonics is observed which is caused by second-order terms in the perturbation theory like Stark effect and ponderomotive force [58]. The differential probability is increased with a high power of the laser intensity. This is seen in the broadening and increase of the ionization peak structures with increasing laser intensity in Fig. 7. The broadening results from

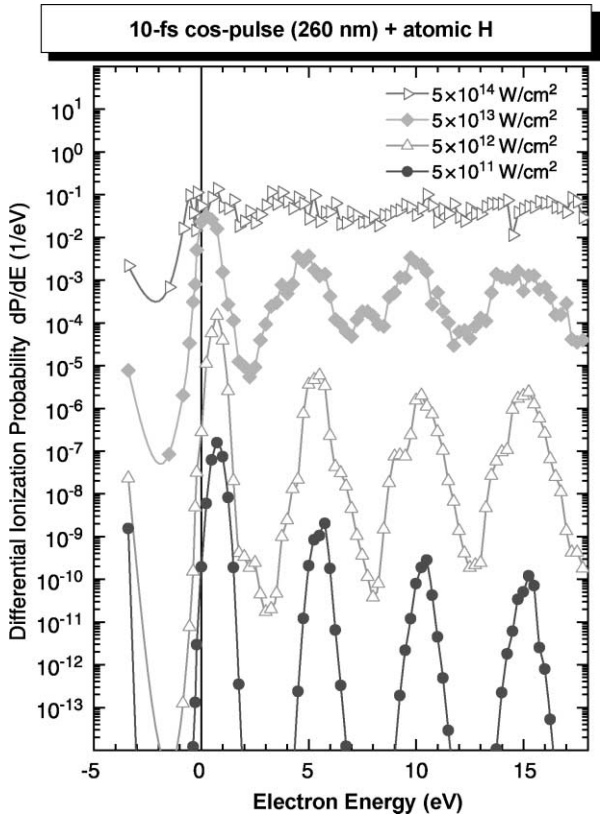

Fig. 7. Differential ionization probability of hydrogen at 260 nm calculated for four laser intensities.

a reduced effective interaction time, since the ground state may be depopulated on a sub-femto second time scale for high laser intensities.

Resonant and also non-resonant multiphoton transitions are well reproduced with the program. This was tested by changing the wavelength from 200 to 260 nm.

Figure 8 displays the corresponding 3-photon ionization cross sections $\sigma^{(3)}/I^2$ in comparison with literature values [59]. The corresponding N-photon cross sections in units of $\mathrm{cm}^{2N}/\mathrm{W}^{N-1}$ are defined as

$$\sigma^{(N)}/I^{N-1} = P/F/I^{N-1}/\tau_{\mathrm{eff}}(N), \tag{45}$$

where P is the ionization probability, F is the flux in photons/cm^2/s and I is the power density in W/cm^2. The effective interaction time $\tau_{\mathrm{eff}}(N)$ is equal to the width of the light-pulse Δt_{p} divided by $1.33N^{\,0.5}$ for a long Gauss packet.

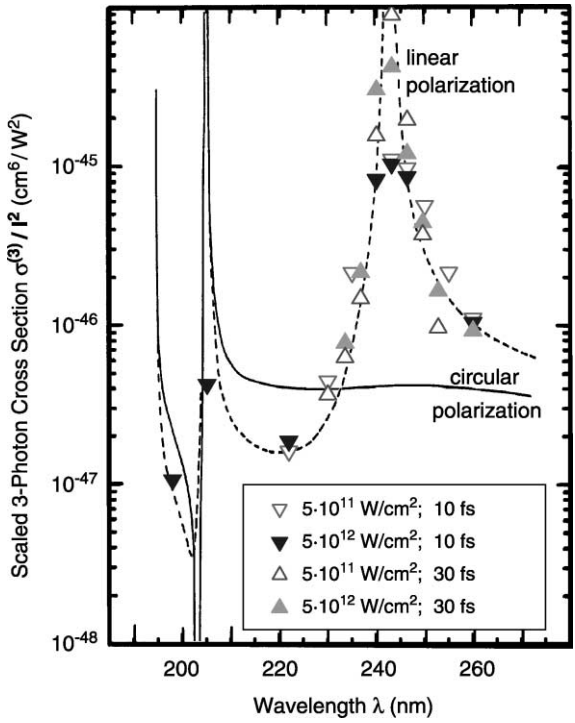

Fig. 8. Scaled 3-photon ionization cross sections $\sigma^{(3)}/I^2$ as a function of the wavelength λ for two power densities I and two-pulse lengths Δt_p. Standard results for asymptotically long times and asymptotically low power densities are taken from Ref. [59] and shown as dashed (linear polarization) and solid (circular polarization) curves.

For light with linear polarization 3 overlapping Fano-peak profiles are visible in Fig. 8. These peaks correspond to resonance ionization with the intermediate bound states 2s (at 243 nm), 3s/3d (at 205 nm) and 4s/4d (at 195 nm). It is seen that our coupled-channel results (symbols) are in good agreement with the results of third-order perturbation theory [59]. We predict a broadening of the 2s-resonance maximum due to the short pulse durations of only 10 and 30 fs. For the 30 fs-pulses there is a clear indication for non-perturbative effects as the cross section for $I = 5 \times 10^{12}$ W/cm^2 is suppressed (due to induced photon emission) in comparison with the one for 5×10^{11} W/cm^2 at the center of the peak. For a wavelength of 253 nm at the lower power density we find a significant deviation between our results and the reference curve. This deviation is most likely due to the finite numerical energy steps of 0.25 eV that exceed the photo-ionization peak-width of 0.17 eV for this case.

Figure 9 displays the integrated ionization probability of H after pulsed optical excitation as a function of the maximum cycle-averaged laser-power density. Calculations have been performed for wavelengths between 80 and 590 nm and for pulse lengths between 10 and 30 fs (Fig. 8). All results (symbols and fitted thin curves) show a monotonous increase as a function of the power density I and nearly 100% ionization is reached for $I = 5 \times 10^{14}$ W/cm^2. At low power densities the curves are proportional to I^N, in agreement with perturbation theory.

The following restrictions have been found to the application of coupled-channel calculations for the computation of pulsed-laser ionization. The dipole approximation restricts the photon energy to < 1 keV in the current treatment. This, however, does not pose a strict condition since a partial-wave expansion of the laser field may be used, similar to as in the case of screened Coulomb potentials. In comparison to ion/atom collisions, typical photon/atom interaction times are extremely long. An upper limit of the pulse width $\Delta t_p = 100$ fs at intermediate laser-power densities follows from the numerically restricted density of continuum states.

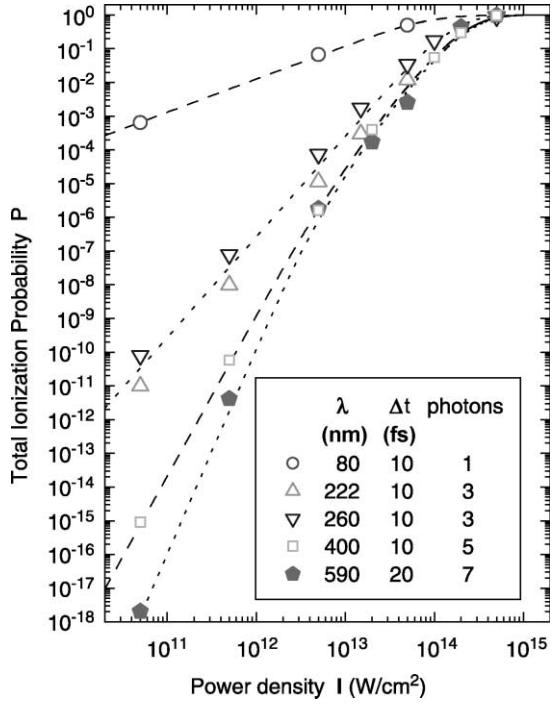

Fig. 9. Total ionization probability of H as function of the power density I for different non-resonant laser wave lengths and pulse widths.

High power densities ($\gg 10^{14}$ W/cm^2) and small laser frequencies ($\lambda > 600$ nm) are related to extremely high orders of perturbation theory. This requires basis sets extending to high values of ($l \gg 15$) and high ejected-electron energies ($\varepsilon \gg 20$ eV). With the help pf P/Q space methods [60] the range of validity of coupled-channel calculations may be extended in this case.

5. COMPARISON WITH MEASUREMENTS

The first coupled-channel calculations for total and differential energy losses were performed for very simple systems such as H on H, He [11,12,61]. Later theses calculations have been extended to more complex systems such as the inner-shells of Al and Si [22,24]. Good agreement with experimental data has been found and the remaining discrepancies have been attributed to multielectron processes.

5.1. Gas targets

5.1.1. Angular dependence

A direct measurement of the electronic energy loss as a function of the impact parameter is a hard task to be performed from the experimental point of view and only a few experiments have been performed for fast light ions. Experiments in gas targets under single collision condition provide a more direct and precise comparison of the theoretical results with the experimental data. Here we compare the results of the coupled-channel method for collisions of protons with He as a function of the projectile scattering angle.

Winter and Auth [61,62] have directly measured the energy loss of protons impinging on gas targets as a function of the final projectile scattering angle. For helium targets they have observed a peak structure (with a width of about 0.6 mrad) in the mean energy loss at scattering angles around 0.5 mrad. The angular dependence of the energy loss for 200 keV is shown in Fig. 10. The peak can be related to the so-called binary process: if the projectile interacts with a free electron initially at rest, each final electron energy corresponds to a well-defined impact parameter and projectile scattering angle. Small but non-zero impact-parameter collisions between proton and electron give rise to a maximum projectile-scattering angle of 0.5 mrad for this case. The angle is given by the mass ratio of an electron and the projectile.

The scattering of a proton with a He atom is at least a three-body problem involving the projectile–active-electron and the projectile–target-core interaction (the four-body problem is reduced to a three-body problem by application of the independent-electron frozen-core model). Therefore, the conversion from impact parameter to projectile-scattering angle should be done carefully. For incident energies above a few hundred eV/amu and for

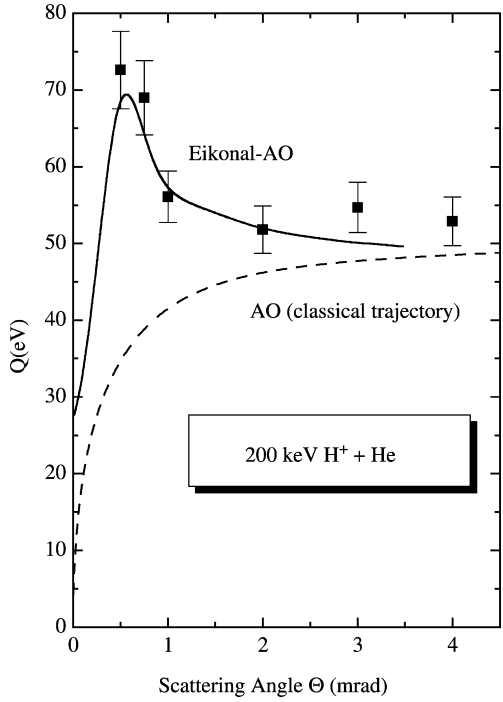

Fig. 10. Mean electronic energy loss for H^+ incident on He at 200 keV as a function of the projectile scattering angle. Closed squares with error bars: experimental results from Ref. [61]. Solid line: (three-body) Eikonal-AO results; dashed-line: (two-body) AO results for mean-field projectile trajectories.

small projectile scattering angles, this transformation can be performed employing the Eikonal method [34]. Basically, the transition amplitude as a function of projectile scattering angle is obtained from the impact parameter dependent amplitudes $a_i(b)$ by a Hankel transformation. The two-electron amplitude can then be obtained from the product of two single-electron amplitudes. The differential scattering amplitude for a small projectile scattering-angle Θ, in the Eikonal approximation [34], reads

$$f_{n_1,l_1,m_1;n_2,l_2,m_2}(\Theta) = i^{m_1+m_2} K \int_0^\infty b\,\mathrm{d}b J_{|m_1+m_2|}(K\Theta b) \times \left(a_{n_1,l_1,m_1}(\infty,b) a_{n_2,l_2,m_2}(\infty,b) \exp\left(-\mathrm{i} \int \mathrm{d}t \frac{Z_\mathrm{p} Z_\mathrm{t}}{R} \right) - \delta_{1,2;\mathrm{GS}} \right)$$

for a bare projectile with charge Z_p and for a target nuclear-charge Z_t. The principal quantum number is denoted n_i and l_i, m_i are quantum numbers associated with the angular momentum and angular momentum projection of

the ith electron. $\delta_{1,2;\mathrm{GS}}$ is equal to one only when both electrons are in the ground state, otherwise it is zero and $J_m(z)$ are Bessel functions of integer order. K is the momentum of the projectile in the laboratory frame. The above transformation accounts for the combined influence of the target nuclear potential and individual electronic transitions on the projectile motion. Then, the mean electronic energy-transfer can be directly computed from

$$Q(\Theta) = \frac{\sum_i |f_i(\Theta)|^2 \Delta E_i}{\sum_i |f_i(\Theta)|^2} \tag{46}$$

since each two-electron state i (specified by $n_1, l_1, m_1; n_2, l_2, m_2$) corresponds to a well-defined energy transfer $\Delta E_i = E_i - E_0$ (E_0 is the initial state energy).

Figure 10 displays the results of our mean energy loss calculations for protons incident on helium at 200 keV as a function of the projectile scattering angle by using the Eikonal transformation (solid line) in comparison with the experimental data of Winter and Auth (closed squares). The dashed lines represent results that are also based on AO calculations but the conversion to projectile-scattering angle was performed by solving the classical Hamilton equations for an averaged heavy-particle Hamiltonian (see equation (7)) that is computed from the time-dependent electron density. This mean-field trajectory treatment goes beyond models that use predetermined straight-line or hyperbolic trajectories. In fact, the averaged potential used in the definition of the average trajectory is unable to account for the kinematics of a violently ionizing collision in contrast with the eikonal method. These violent collisions enhance the mean energy transfer by a factor of about two for this case. Deviations between mean-field and Eikonal-AO results extend up to $\Theta \approx 3$ mrad and point to the importance of three-body effects. Further details may be found in Ref. [61].

5.1.2. Stopping cross section

Figure 11 shows our coupled-channel (atomic orbital) results for the electronic stopping cross sections corresponding to hydrogen beams penetrating He gas. In order to calculate the equilibrium mean stopping power we must consider the charge state distribution of the projectile and the fact that we are restricted to only one active electron. Then, we have to calculate the energy loss in three reaction classes:

(1) $H^+ + He^0 \rightarrow H^+ + He^*$ or (electron capture)
(2) $H^0 + He^0 \rightarrow H^0 + He^*$
(3) $He^0 + H^0 \rightarrow He^0 + H^*$

where $*$ includes excitation and ionization as well. For case 1 we have evaluated the electronic energy loss due to the electron capture process.

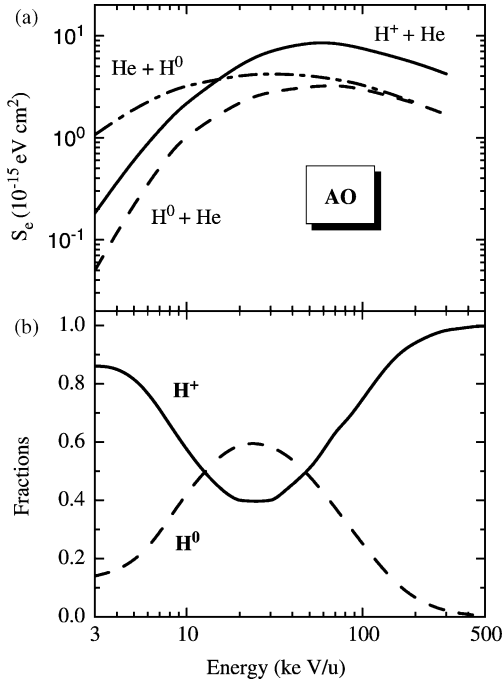

Fig. 11. (a) Coupled-channel results for the electronic stopping cross section of H^+ and H^0 beams incident on He vs. incident energy (solid and dashed lines). Ionization and excitation of projectiles, in the case of the H^0 charge-state fraction, is accounted for by considering the collision system $He + H^0$ (dot-dashed line). (b) Experimental equilibrium fractions for hydrogen beams in helium gas, from Ref. [63].

Ionization and excitation of the target electrons have been computed for 1 and 2. Case 3 provides the energy dissipation by projectile electron loss and projectile excitation. The energy loss involving neutral collision-partners ($H^0 + He$ and $He + H^0$) is basically due to target or projectile ionization. Excitation of the target or the projectile is of minor importance. The same holds true for collisions between H^+ and He at high energies ($E > 100$ keV). However, the main contribution at low projectile energies stems from the capture of target electrons into the projectile 1s state. From Fig. 11 we can see that the partial electronic stopping power for bare hydrogen is dominant at high energies whereas excitation and ionization of the projectile yield the highest partial cross section at low velocities. Nevertheless, the projectile ionization leads to an enhancement of the H^+ charge-state fraction at low velocities and consequently the contribution of H^0 to the stopping processes is reduced. The experimental equilibrium fraction [63] for hydrogen beams in He gas

are shown in Fig. 11. The H^+ fraction increases for high and low energies as well. The neutral fraction is only significant for intermediate ion velocities. This means that the $H^+ + He$ collisions dominate the low energy part of the stopping power. For energies around 30 keV/u, all reaction classes are equally important.

In Fig. 12 the equilibrium mean total stopping cross section per atom for $H + He$ collisions is presented in comparison with experimental data of different groups [64–69]. The solid curve represents the values of Fig. 11 weighted with the corresponding charge-state fractions (also displayed in Fig. 11, the contribution due to H^- can be neglected [63]). Special attention should be drawn to the low energy stopping power data which was recently measured by Golser and Semrad [69]. At energies below 10 keV experimental and theoretical results agree within 5% or better.

At 30 keV/u we find the largest deviation between the measured stopping power and our calculated values of about 12%. This may be attributed to an overestimation of cross sections for multielectron processes because of the use of the independent particle model. We emphasize that the present calculation does not properly take into account events in which more than one electron is actively involved, e.g., double target ionization or excitation and simultaneous projectile and target ionization.

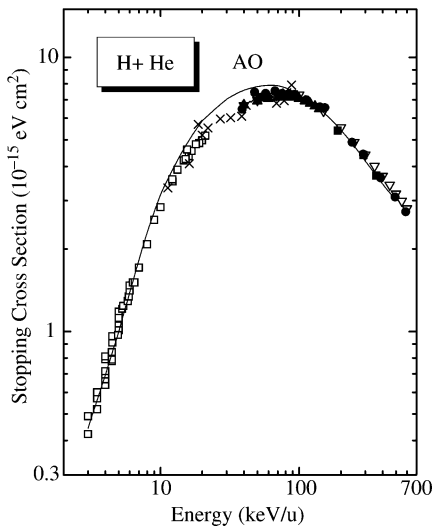

Fig. 12. Equilibrium mean stopping cross section per atom for hydrogen beams penetrating He gas. Present atomic orbital (AO) calculation (solid line). Experimental values: open triangles [64,65], closed squares [66], closed triangles [67], closed circles [68], open squares [69].

5.2. Solid targets

Here, we briefly describe a comparison with experimental channeling energy loss data for He ions in Si [22,23]. Coupled-channel calculations were performed for He^+ and He^{2+} on the Si inner shells. The energy-loss term associated with the Si-valence electrons was obtained from the experimental stopping cross section of Ref. [70] by subtracting the calculated contributions involving Si inner-shell and He electrons. The He charge-state distribution was taken from experimental results under channeling conditions from Ref. [71] (see insert in Fig. 13) and the sum of the energy loss for each Si atom located across the channel was averaged according to the ion flux distribution [22]. Further details of the solid-state energy-loss treatment maybe found in Ref. [22].

Figure 13 shows the stopping power of He ions moving through the Si crystalin the $\langle 100 \rangle$ channeling direction. The symbols correspond to recent experimental data [22,72] for the channeled energy-loss and the solid line represents accurate experimental stopping values for a random direction [70]. Experiments at 800 keV with He^+ and He^{2+} ions show that charge equilibrium is reached at a depth of about 50 Å. We expect this distance to increase by an order of magnitude for 5 MeV He ions. Since the mean charge state of fast ions is close to two and the measurements above 1000 keV were performed with He^{2+} ions there should be no significant deviation from the assumed equilibrium charge-distribution.

The results of the AO calculations (dashed-line) for the projectile-energy dependence of the electronic stopping power under channeling conditions agree with the data to within the experimental uncertainty. For ion energies above 1.2 MeV (see insert in Fig. 13 for the He charge-state fractions), the He^{2+} fraction is dominant and the main physical process responsible for the reduction of the energy loss under channeling conditions compared to random directions is the suppressed inner-shell ionization (L-shell) of Si atoms.

The energy region from 1.2 up to 5 MeV is close to the maximum of the stopping cross section due to Si L-shell electrons and only non-perturbative calculations (including many higher order terms) are reliable in this energy region. By comparing the AO results with first-order ones at 2 MeV we obtain a difference of about 40% for $b = 1.3$ Å (middle of $\langle 100 \rangle$ channel). For energies below 1.2 MeV, the influence of charge-changing processes begins to be significant. The present energy-loss results as a function of the projectile energy are most sensitive to the computation of the inner-shell contribution at random directions, since under channeling conditions they are determined by the contribution of the valence excitations. The inner-shell contribution under channeling condition is suppressed by 75% at 5 MeV). Thus, a comparison with the angle dependent energy-loss data provides more information about the impact-parameter dependence of the energy loss [22].

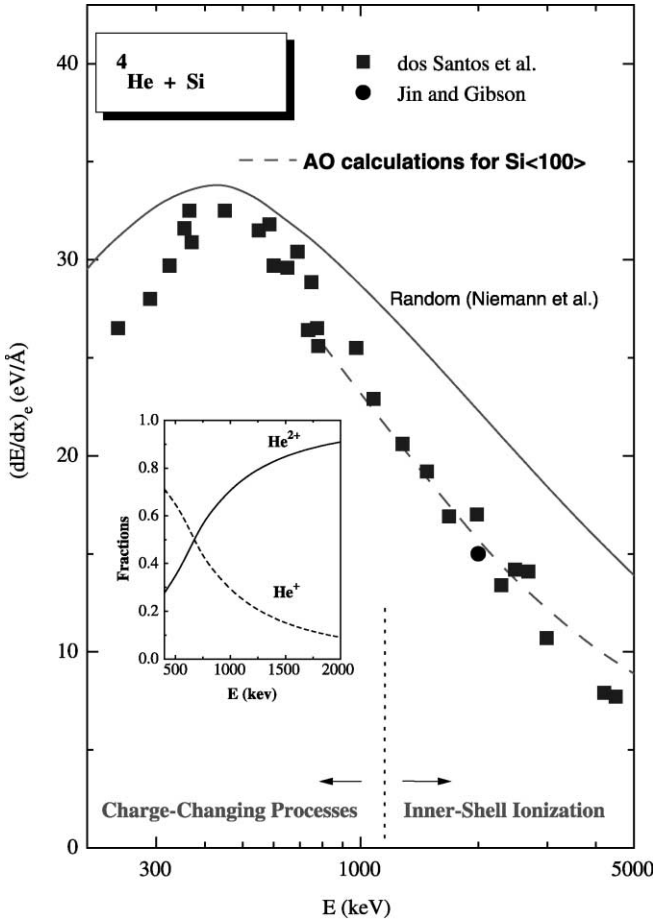

Fig. 13. Electronic stopping power as a function of the ^{4}He energy for the Si ⟨100⟩ direction.

6. SIMPLE MODELS FOR THE ENERGY LOSS

The coupled-channel calculations are used as benchmark results to check simple models of the impact parameter dependence of the electronic energy loss. A detailed description of such models (convolution approximation) may be found elsewhere [25,26]. Here we present only a short outline of the method. The electronic energy loss involves a sum over all final target states for each impact parameter. Usually this demands a computational effort that precludes its direct calculation in

a computer simulation code. Therefore, we search for an approximate solution without the necessity of performing a large-scale calculation.

In recent works [25] we have proposed a simple formula for $Q(b)$ (called PCA) that virtually reproduces SCA results for all impact parameters for bare and also for screened projectiles.

The following simple formula

$$Q(b) = \int \mathrm{d}^2 r_\mathrm{T} \mathcal{K}(\vec{b} - \vec{r}_\mathrm{T}) \int \mathrm{d}z \rho(\vec{r}_\mathrm{T}, z) \tag{47}$$

with

$$\mathcal{K}(b) = \frac{2Z^2}{v^2 b^2} h(2vb/\eta) \sum_i f_i g\left(\frac{\omega_i b}{v}\right) \tag{48}$$

joins smoothly all regions of impact parameters b for which two-body ion-electron (small b) and dipole (large b) approximations are valid. The function $h(2vb)$ [25] approaches zero for $b \ll 1/v$ (relative impact parameter smaller than the electron de Broglie wavelength in the projectile frame) and it reaches 1 for large values of b. The first two terms in equation (48) resemble the classical energy transfer to a statistical distribution of electrons at rest and describe violent binary collisions. The last term, involving the g function [25] and the oscillator strengths f_i, accounts for the long ranged dipole transitions. The first integral $\int \mathrm{d}^2 r_\mathrm{T} \cdots$ in equation (47) describes a convolution with the initial electron density also outside the projectile path and yields nonlocal contributions to the energy loss. It is noted that these nonlocal contributions are neglected in most previous simple energy loss models. With the parameter η equal to one, this formula mimics the first-order Born approximation very well [25]and it is denoted PCA (perturbative convolution approximation). For increasing projectile-charge first-order calculations (on which PCA is based) break down. They do not take in account, for instance, that each electronic transition gives rise to an increased final-state population and a corresponding reduction of the initial state population. It is clear that the ionization probability cannot increase indefinitely with the strength of the perturbation (the so-called saturation effect). Since these ionization processes come mostly from small impact parameters, we have introduced in Ref. [26], a scaling parameter η in the function h that enforces unitarity in accordance with the Bloch model [19].

Figure 14 displays calculated scaled energy losses (Q/Z_p^2) as a function of the projectile charge Z_p for a small impact parameter ($b = 0.2$ a.u.) compared to the He 1s-shell radius ($r_0 = 0.6$ a.u.). The SCA results show up as a horizontal dashed line, since they scale with Z_p^2. The AO results for positively (open circles) and negatively charged projectiles (solid squares) are shown separately in this plot. The error bars of the AO results for positive bare ions are estimated from the numerical convergency and

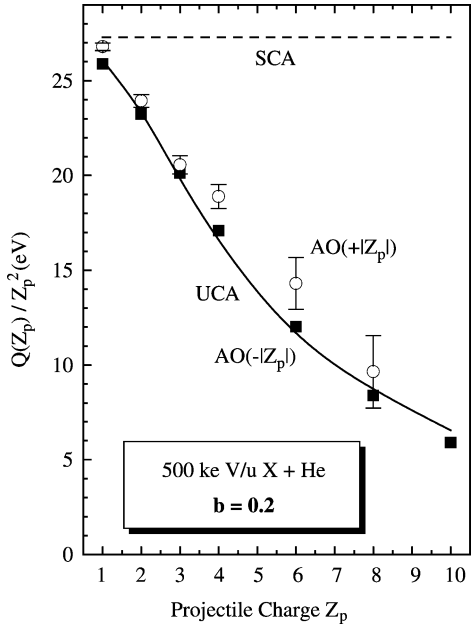

Fig. 14. Non-perturbative results for the energy loss at a small impact parameter in 500 keV/u $X^{Z_p+} + He$ collisions, compared to the values from first-order perturbation theory (SCA, dashed line). Atomic orbital (AO) coupled-channel results for positively charged particles (open circles) and for anti-nuclei (closed squares). Results using the UCA model: solid curve.

integration properties and are mainly related to the accuracy of the capture matrix elements. The uncertainties for the antiparticle energy losses are only 3%, since a large basis set of target-centered states is sufficient for accurate AO calculations. AO calculations for positive ions at 500 keV/u were performed with an explicit consideration of 10 bound projectile states, for an improved treatment of electron capture, in addition to 210 target states. It is clearly evident from this figure that the deviations between results for heavy particles and antiparticles is much smaller than the deviation from the SCA.

Thus, the even orders of an Z_p expansion, as included in the unitary convolution approximation (UCA), dominate the non-perturbative effects. The present UCA results are plotted as a solid curve. This curve lies close to the average of the AO results for particles and antiparticles. Hence, although the present UCA does not include sign-of-charge effects it perfectly describes the majority of the energy transfer processes (dominated by ionization) of fast heavy particles at small impact parameters.

7. WHAT HAVE WE LEARNED FROM COUPLED-CHANNEL CALCULATIONS

Virtually all non-trivial collision theories are based on the impact-parameter method and on the independent-electron model, where one active electron moves under the influence of the combined field of the nuclei and the remaining electrons frozen in their initial state. Most theories additionally rely on much more serious assumptions as, e.g., adiabatic or sudden electronic transitions, perturbative or even classical projectile/electron interactions. All these assumptions are circumvented in this work by solving the time-dependent Schrödinger equation numerically exact using the atomic-orbital coupled-channel (AO) method. This non-perturbative method provides full information of the basic single-electron mechanisms such as target excitation and ionization, electron capture and projectile excitation and ionization. Since the complex populations amplitudes are available for all important states as a function of time at any given impact parameter, practically all experimentally observable quantities may be computed.

Huge-basis set calculations have been performed with hundreds of states, including bound atomic orbitals of the target and target-centered continuum wave-packets. If necessary bound projectile states are included as well. These calculations involve solutions of the Schrödinger equation for each impact parameter and for all important projectile charge-states weighted with the corresponding charge-state fraction. Thus, not only the screened target potential (in most cases a self-consistent Hartree–Fock–Slater potential) but also screened projectile potentials have to be considered.

In recent years, the model was applied to the light atomic targets H and He and a few selected solids (C, Al and Si) for projectile nuclear charges between -10 and $+10$. Total cross section, mean energy transfers, energy-loss and straggling cross sections, electron energy and angular distributions, and projectile-angle dependent energy-loss spectra have been computed with the AO model and compared to experimental results. As shown in this work, also a treatment of multiphoton ionization beyond perturbation theory is possible with the same model. Here we have found numerical limitations concerning the laser power-density, pulse-width and frequency.

So far we found no serious limitations for the treatment of collision processes concerning the projectile nuclear charge (comparable to the case of high laser power-densities). At low projectile velocities, however, the calculations require the use of basis sets with extremely dense energy grids. High orders of the perturbation series often dominate the ionization probabilities for this case and high computation times are thus needed. This situation is similar to the case of long laser pulses with low frequencies and intermediate to high power densities.

We have applied our code to kinetic projectile energies of up to a few hundred keV per nucleon. In most cases good agreement with experimental

data was found. The remaining cases could be traced back to a breakdown of the independent electron model. For light targets, di-electronic transitions and for heavy targets collective dynamic screening effects modify the mean electronic motion and lead to uncertainties of up to about 20% for the electronic energy loss. Especially for slow heavy particles in the molecular-orbital regime, electron-exchange and dynamic mean-field effects are important and have to be incorporated in the treatment. At small impact parameters a simple united-atom treatment is usually sufficient, but a more general solution would be a time-dependent Hartree–Fock (TDHF) treatment as it is often applied to nuclear collision processes.

Another problematic point appears in the treatment of electron loss due to heavy (neutral) targets. In this case, unrealistic capture processes come into play where the projectile electron is transferred into populated bound target states. In principle, this problem may be circumvented by using the multielectron anti-symmetrization method, where the Pauli exclusion principle is enforced for the transitions amplitudes. Thus, an explicit and time-consuming treatment of these occupied bound states would then be necessary.

In most cases, however, for atoms, insulators or inner shells of conductors accurate stopping cross sections may be computed (including excitation, ionization and electron capture) using the AO coupled-channel method. This is a time-consuming task, since it has to be done for each subshell, each impact parameter and each projectile charge-state separately. On the other hand, it provides full information about all single-electron transitions. In general, at low projectile energies target excitation or electron capture give rise to the largest transition probabilities and cross sections. Since, quasi-molecular effects are important, the impact-parameter dependence may even show an oscillating behavior. At high projectile velocities (compared to the mean electron-orbital velocity) ionization dominates the electronic energy loss and the energy transfer is typically a smoothly decaying function of the impact parameter.

The AO results may also be used for benchmark tests of simpler models. In this context we have also checked a simple non-perturbative model, the UCA. This model includes the main features of fast heavy-ion stopping, as is shown by comparison with large-scale AO results for the impact-parameter dependent electronic energy transfer. The computation of the energy loss within the UCA is much simpler and by many orders of magnitude faster than the full numerical solution of the time-dependent Schrödinger equation.

ACKNOWLEDGEMENTS

Part of this work (the photoionization section) was performed in collaboration with Melanie Roth (HMI, Berlin). We would also like to

acknowledge R.C. Fadanelli for the final revision of the manuscript. This work was partially supported by CAPES-PROBRAL Project 121/00, by CNPq and by the Alexander-von-Humboldt foundation.

REFERENCES

[1] D. R. Bates and G. Griffing, *Proc. Phys. Soc.*, 1953, **A66**, 961.
[2] E. J. McGuire, *Phys. Rev. A*, 1971, **3**, 267; E. J. McGuire, *Phys. Rev. A*, 1983, **28**, 2096; E. J. McGuire, *Phys. Rev. A*, 1998, **57**, 2758.
[3] H. Bethe, *Ann. Phys.*, 1930, **5**, 325.
[4] N. M. Kabachnik, V. N. Kondratev and O. V. Chumanova, *Phys. Status Solidi (b)*, 1988, **145**, 103.
[5] P. D. Fainstein, V. H. Ponce and A. E. Martinez, *Phys. Rev. A*, 1993, **47**, 3055.
[6] R. E. Olson, *Radiat. Effects Defects Solids*, 1989, **110**, 1.
[7] P. L. Grande and G. Schiwietz, *J. Phys. B: At. Mol. Opt. Phys.*, 1995, **28**, 425.
[8] G. Maynard, K. Katsonis, C. Deutsch, *et al*., *Nucl. Instrum. Methods*, 2001, **A464**, 86; G. Maynard, G. Zwicknagel, C. Deutsch, *et al*., *Phys. Rev. A*, 2001, **63**, 2903.
[9] R. Cabrera-Trujillo, Y. Ohrn, J. R. Sabin and E. Deumens, *Phys. Rev. A*, 2002, **65**, 024901; R. Cabrera-Trujillo, Y. Ohrn, E. Deumens and J. R. Sabin, *Phys. Rev. A*, 2000, **62**, 052714.
[10] G. Schiwietz, *Phys. Rev. A*, 1990, **42**, 296.
[11] P. L. Grande and G. Schiwietz, *Phys. Rev. A*, 1991, **44**, 2984.
[12] G. Schiwietz and P. L. Grande, *Nucl. Instrum. Methods*, 1992, **B69**, 10; P. L. Grande and G. Schiwietz, *Phys. Rev. A*, 1993, **47**, 1119.
[13] P. L. Grande and G. Schiwietz, *Nucl. Instrum. Methods*, 1997, **B132**, 264.
[14] N. R. Arista, *Nucl. Instrum. Methods*, 2002, **B195**, 91; A. F. Lifschitz and N. R. Arista, *Phys. Rev. A*, 1998, **57**, 200; J. E. Valdes, P. Vargas and N. R. Arista, *Phys. Rev. A*, 1997, **56**, 4781.
[15] I. Campillo, J. M. Pitarke and A. G. Eguiluz, *Phys. Rev. B*, 1998, **58**, 10307.
[16] J. J. Dorado and F. Flores, *Phys. Rev. A*, 1993, **47**, 3092.
[17] P. M. Echenique, R. M. Nieminem and R. H. Ritchie, *Solid State Commun.*, 1981, **37**, 779; P. M. Echenique, R. M. Nieminem, J. C. Ashley and R. H. Ritchie, *Phys. Rev. A*, 1986, **33**, 897.
[18] N. Bohr, *Phil. Mag.*, 1913, **25**, 10; N. Bohr, *Phys. Rev.*, 1941, **59**, 270.
[19] F. Bloch, *Ann. Physik*, 1933, **16**, 285.
[20] P. Sigmund and U. Haagerup, *Phys. Rev. A*, 1986, **34**, 892; H. H. Mikkelsen and P. Sigmund, *Phys. Rev. A*, 1989, **40**, 101; H. H. Mikkelsen, *Nucl. Instrum. Methods*, 1991, **B58**, 136.
[21] P. Sigmund and A. Schinner, *Eur. Phys. J. D.*, 2000, **12**, 425; P. Sigmund and A. Schinner, *Phys. Scripta*, 2001, **T92**, 222.
[22] J. H. R. dos Santos, P. L. Grande, M. Behar, H. Boudinov and G. Schiwietz, *Phys. Rev. B*, 1997, **55**, 4332.
[23] P. L. Grande and G. Schiwietz, *Nucl. Instrum. Methods*, 1998, **B136–138**, 125.
[24] P. L. Grande, A. Hentz, G. Schiwietz, W. H. Schulte, B. W. Busch, D. Starodub and T. Gustafsson, *Phys. Rev. B*, 2004.
[25] P. L. Grande and G. Schiwietz, *Phys. Rev. A*, 1998, **58**, 3796.
[26] G. Schiwietz and P. L. Grande, *Nucl. Instrum. Methods*, 1999, **B153**, 1.
[27] ISL Annual Report, HMI-B587, p. 20, 2001.
[28] J. Bang and J. M. Hansteen, *Kgl. Dan. Vidensk. Selsk. Mat. Fys. Medd.*, 1959, **31** (13); L. Wilets and S. J. Wallace, *Phys. Rev.*, 1968, **169**, 84; M. R. Flannery and K. J. MacCann, *Phys. Rev. A*, 1973, **8**, 2915.

[29] G. Baur, M. Pauli and D. Trautmann, *Nucl. Phys.*, 1974, **A211**, 333.
[30] J. H. McGuire and L. Weaver, *Phys. Rev. A*, 1977, **16**, 41.
[31] L. Kocbach, J. U. Andersen, E. Laegsgaard and M. Lund, in *Proceedings of the 10th International Conference on the Physics of Electronic and Atomic Collisions*, Paris, (ed. G. Watel), North-Holland, Amsterdam, 1977, p. 42.
[32] M. Kleber and K. Unterseer, *Z. Phys. A*, 1979, **292**, 311.
[33] F. Rösel, D. Trautmann and G. Bauer, *Nucl. Instrum. Methods*, 1982, **192**, 43.
[34] L. Wilets and S. J. Wallace, *Phys. Rev.*, 1968, **169**, 84; R. Mc Carrol and A. Salin, *J. Phys.*, 1968, **B1**, 163; M. R. C. Mc Dowell and J. P. Coleman, *Introduction to the Theory of Ion–Atom Collisions*, North-Holland, Amsterdam, 1970.
[35] S. T. Manson, L. H. Toburen, D. H. Madison and N. Stolterfoht, *Phys. Rev. A*, 1975, **12**, 60.
[36] M. Inokuti, *Rev. Mod. Phys.*, 1971, **43**, 297.
[37] F. Herman and S. Skillmann, *Atomic Structure Calculations*, Prentice-Hall, Englewood Cliffs, NJ, 1963.
[38] J. H. McGuire, N. Stolterfoht and P. R. Simony, *Phys. Rev. A*, 1981, **24**, 97.
[39] E. C. Montenegro, W. E. Meyerhof and J. H. McGuire, *Adv. At. Mol. Opt. Phys.*, 1994, **34**, 249.
[40] A. Dalgarno and G. W. Griffing, *Proc. R. Soc.*, 1955, **A232**, 423.
[41] A. Arnau, *Nucl. Instrum. Methods*, 1996, **B115**, 2.
[42] R. D. Cowan, *The Theory of Atomic Structure and Spectra*, University of California Press, London, 1981.
[43] U. Heinz, W. Greiner and B. Müller, *Phys. Rev. A*, 1979, **20**, 130.
[44] J. F. Reading, T. Bronk, A. L. Ford, L. A. Wehrman and K. A. Hall, *J. Phys. B: At. Mol. Opt. Phys.*, 1997, **30**, L189.
[45] A. Messiah, *Quantum Mechanics*, North-Holland/Interscience, Amsterdam/New York, 1963, Vol. 2.
[46] M. Abramowitz and I. Stegun, *Handbook of Mathematical Functions*, Dover, New York, 1970.
[47] A. Salin, private communication.
[48] W. Fritsch and C. D. Lin, *J. Phys. B*, 1982, **15**, 1225; W. Fritsch and C. D. Lin, *Phys. Rev. A*, 1983, **27**, 3361.
[49] Fritsch, private communication.
[50] J. F. Reading, T. Bronk, A. L. Ford, L. A. Wehrman and K. A. Hall, *J. Phys. B: At. Mol. Opt. Phys.*, 1997, **30**, L189.
[51] H. Knudsen, U. Mikkelsen, K. Kirsebom, S. P. Moeller, E. Uggerhoef, J. Slevin, M. Charlton and E. Morenzoni, *Phys. Rev. Lett.*, 1995, **74**, 4627.
[52] G. Schiwietz, U. Wille, R. Diez Muiño, P. D. Fainstein and P. L. Grande, *J. Phys. B: At. Mol. Opt. Phys.*, 1996, **29**, 307.
[53] F. Ziegler, J. P. Biersack and U. Littmark, *The Stopping and Range of Ions in Solids*, Pergamon Press, London, 1985, ISBN 0-08-021603.
[54] P. L. Grande, F. C. Zawislak, D. Fink and M. Behar, *Nucl. Instrum. Methods*, 1991, **B61**, 282.
[55] H. Ryufuku and T. Watanabe, *Phys. Rev. A*, 1978, **18**, 2005; H. Ryufuku and T. Watanabe, *Phys. Rev. A*, 1979, **19**, 1538; U. Wille, *J. Phys. B: At. Mol. Phys.*, 1983, **16**, L275.
[56] L. L. Balashova, N. M. Kabachnik and V. N. Kondratev, *Phys. Status Solidi (b)*, 1991, **161**, 113.
[57] H. H. Mikkelsen and H. Flyvbjerg, *Phys. Rev. A*, 1990, **42**, 3962.
[58] D. Charalambidis, D. Xenakis, C. J. G. J. Uiterwaal, P. Maragakis, J. Zhang, H. Schröder, O. Faucher and P. Lampropoulos, *J. Phys. B: At. Mol. Opt. Phys.*, 1997, **30**, 1467.
[59] F. H. M. Faisal, Germany Book Series: *Physics of Atoms and Molecules*, Kluwer Academic/Plenum Press, London, 1987.

[60] H. J. Lüdde, A. Henne, A. Salin, A. Toepfer and R. Dreizler, *J. Phys. B: At. Mol. Opt. Phys.*, 1993, **26**, 2667.
[61] G. Schiwietz, P. L. Grande, C. Auth, H. Winter and A. Salin, *Phys. Rev. Lett.*, 1994, **14**, 2159.
[62] C. Auth and H. Winter, *Phys. Lett.*, 1993, **A176**, 3055.
[63] S. K. Allison, *Rev. Mod. Phys.*, 1958, **30**, 1137.
[64] H. K. Reynolds, D. N. F. Dunbar, W. A. Wenzel and W. Whaling, *Phys. Rev.*, 1953, **92**, 742.
[65] J. A. Phillips, *Phys. Rev.*, 1953, **90**, 532, d and t projectiles were used for incident energies below 40 keV.
[66] P. K. Weyl, *Phys. Rev.*, 1953, **91**, 289.
[67] J. T. Park and E. J. Zimmermann, *Phys. Rev.*, 1963, **131**, 1611.
[68] F. Besenbacher, H. H. Andersen, P. Hvelplund and H. Knudsen, *Mat. Fys. Medd. Dan. Vid. Selsk.*, 1979, **40** (3).
[69] R. Golser and D. Semrad, *Phys. Rev. Lett.*, 1991, **66**, 1831.
[70] D. Niemann, P. Oberschachtsiek, S. Kalbitzer and H. P. Zeindl, *Nucl. Instrum. Methods*, 1993, **B80/81**, 37.
[71] R. J. Petty and G. Dearnaley, *Phys. Lett.*, 1974, **50A**, 273.
[72] H. S. Jin and W. M. Gibson, *Nucl. Instrum. Methods*, 1986, **B13**, 76.

Non-Linear Approach to the Energy Loss of Ions in Solids

Néstor R. Arista and Agustín F. Lifschitz

División Colisiones Atómicas, Centro Atómico Bariloche and Instituto Balseiro, Comisión Nacional de Energía Atómica, 8400 S.C. Bariloche, Argentina

Abstract

The present work includes the discussion of three main aspects in the area of the energy loss of ions in solids. First we review some of the main features contained in the historical Bohr, Bethe and Bloch theories, and related models based on them. Then we analyze new developments in this area based on a non-linear formulation of the energy loss of ions in a free electron gas. As a final question, we reconsider, from the new perspective of the non-linear approach, some long-standing problems concerning the charge state of ions moving in solids and its relationship with the effective charge concept.

Contents

ADVANCES IN QUANTUM CHEMISTRY, VOLUME 45
ISSN: 0065-3276 DOI 10.1016/S0065-3276(04)45003-5

1. INTRODUCTION

The basic theoretical models to describe the interaction of ionized particles with matter were developed early in the 20th century by Bohr [1,2], Bethe [3] and Bloch [4] (BBB). These models provide the general framework to almost any consideration on the energy loss of swift particles in matter. The first two of these models are based on widely different assumptions, the Bohr description is fully classical, representing the atomic electrons by classical oscillators, while the Bethe model is based on quantum perturbation theory (first-order Born approximation).

The fact that the two formulations produced different results was the stimulus for the study by Bloch, published shortly after Bethe's one, and solving the discrepancy between the two earlier results. The comprehensive study carried out by Bloch was based on a time-dependent description of the collision, based on Schrödinger equation, considering the distortion of the electronic wave function produced by the passing charge. The relevant parameter in Bloch's formulation is the dimensionless quantity $\eta = Z_1 e^2/\hbar v$, where $Z_1 e$ is the particle charge and v its velocity. Bloch's description bridged the gap between the Bohr and Bethe models, which may be obtained as opposite limits of his description, corresponding to the cases $\eta \gg 1$ and $\eta \ll 1$, respectively.

The characteristic application ranges and the wide coverage of these theoretical models is illustrated in Fig. 1 in terms of the main parameters, Z_1 and v. The ranges of applicability of the Bohr and Bethe theories pertain mostly to high energies, since a common assumption in these formulations is the condition of bare ions (point charges).

The original ideas of Bohr where further explored by many people and were the point of reference for numerous advances in the area. Further developments were based on statistical approaches considering slow ions [5,6], while others made use of effective-charge models [7,8] for swift ions. All of them have been widely used to analyze a large number of experimental results, and to systematize a body of data covering nearly all possible projectile–target combinations and a wide energy range [9]. But the physical basis of these approaches is not always clear, and moreover, there are additional evidences that indicate that the physics involved in these models is not complete enough to describe important features of the slowing down process. The limitations of the old models became evident when new measurements with heavy ions, in the low-energy range, revealed an oscillatory dependence of the stopping power, when plotted as a function of the ion atomic number Z_1 [10]. The quantum non-perturbative nature of these effects was soon demonstrated. The region where these effects turn out to be of greatest importance is represented in the lower part of Fig. 1 by the indication 'non-linear quantum region'.

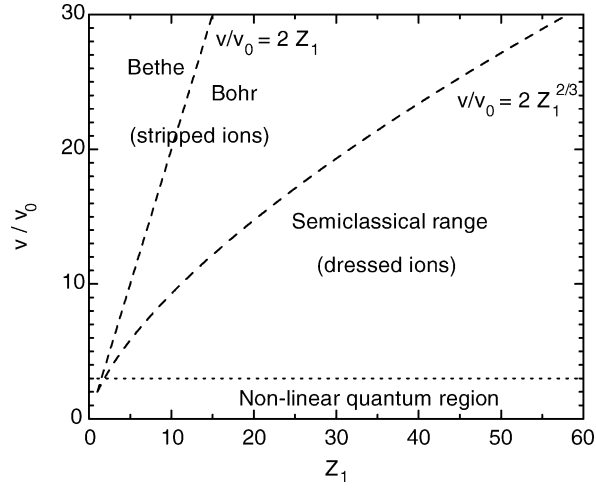

Fig. 1. Relevant regions of interest to characterize the interaction of ions with solids, in terms of the ion velocity v and atomic number Z_1. The line $v/v_0 = 2Z_1^{2/3}$ is indicative of the intermediate region between weakly and strongly ionized atoms; the line $v/v_0 = 2Z_1$ shows the limits of applicability of the Bohr and Bethe models. The transition across this line is given by the Bloch model. The lower region is the domain of low and intermediate velocities where non-linear quantum effects are dominant.

On the other hand, following different lines of research, alternative models were developed by considering the stopping medium as a dispersive dielectric medium. This line was developed by numerous authors, particularly by Fermi [11], Pines [12], Lindhard [13], and Ritchie [14]. The dielectric function (DF) developed by Lindhard [13] has become a standard approach in studies of the interaction of charged particles with conduction or valence electrons in solids, usually represented as a degenerate electron gas. The dielectric formulation is a form of *linear* response model, and considers the excitations in the medium within a perturbative approximation. This method has the convenience of a closed formulation based on analytical functions. The model incorporates the velocity distribution of target electrons (according to the electron gas description) and contains a self-consistent treatment of screening effects (not included in the atomistic formulations), which are of relevance for dense media. This model may be extended in a straightforward way to the case of partially stripped ions by introducing appropriate form factors [15]. Calculations using this approach will be considered in Section 3.

Various review papers have described and updated many of the developments and applications emerging from the Bethe theory [16–20],

while other developments have explored alternative descriptions using kinetic theory [21–24] and the harmonic-oscillator model [25].

On the other hand, the Bohr model has been extended recently by Sigmund *et al.* [26] obtaining a new theoretical framework based on semiclassical concepts (the so-called Binary Theory). Other recent developments [27–29] have formulated non-perturbative quantum models which apply at intermediate and high energies [27,28] as well as at low energies [29].

As indicated before, the strongest quantum effects are observed with slow ions, and produce an oscillatory structure of the low velocity stopping powers. A nice account of this phenomenon was given by Briggs and Pathak [30] who considered the interaction between slowly moving ions and the individual electrons of the medium considered as an electron gas (representing the conduction or valence electrons in the solid) and applied the methods of quantum-scattering theory.

An essential difference between this method and the BBB scheme is the evaluation of quantum effects in an exact way (by numerical solutions of the Schrödinger equation). This type of approach is indicated as a *non-linear* stopping calculation, due to its non-perturbative character (and to distinguish it from studies based on perturbative or *linear* approximations).

Further developments for slow ions included the application of the density functional theory (DFT) by Echenique *et al.* [31–33], which yields a more sophisticated (and also non-linear) treatment of many-body effects in dense media. This theory explains also the oscillatory behavior of the stopping powers in the range of low velocities ($v < v_0$, v_0 being the Bohr velocity). But the question of extending the DFT calculations to intermediate or large velocities is still a complicated numerical problem.

An alternative approach proposes to treat both screening and scattering effects in a self-consistent way, by the introduction of parametric scattering potentials which may be adjusted by an appropriate self-consistent procedure [34,35]. An important criterion that may be used for this optimization is provided by the Friedel sum rule, which expresses in a general way the condition of overall charge neutrality for an ion immersed in a metallic environment. The original formulation of this method was also restricted to low velocities (nearly static ions). But a more recent development along this line provides an extension of the Friedel sum rule to moving ions [36] (the extended Friedel sum rule, EFSR). This opens the possibility of carrying out calculations for various incident ions on a wide energy range. Previous calculations for light ions [37,38] (He^+, protons and antiprotons) showed good agreement with experiments. An extension of this method to the case of heavy ions has also been proposed [39].

We analyze in this chapter recent developments in the area of ion–solid interactions, describing in particular the non-linear method to study the energy loss of ions in solids. We consider the non-perturbative scheme provided by quantum scattering theory, using self-consistent methods to

optimize the screening of moving ions. These methods are the basis of the non-linear approach to the current energy loss studies.

2. BOHR–BETHE–BLOCH: THE STANDARD RESULTS FOR BARE IONS

As it was mentioned before, the Bohr model considers the interaction between a fast moving particle, with charge Ze, and a classical oscillator with frequency ω_0 (which represents the motion of the electron attached to the target atom) and calculates the energy loss of the projectile after separating the interaction domain in two regions: the range of close collisions, which are treated as binary electron–ion collisions (neglecting the binding force acting on the electron), and a range of distant collisions, where the perturbation of the oscillator is approximated by the dipole-term expansion of the field of the moving particle.

On the other hand, the Bethe theory considers an inelastic scattering process using the first-order Born approximation where the projectile states are represented by incident and outgoing plane waves (delocalized description). The ranges of close and distant collisions are replaced here by the regions of large and small momentum transfers, respectively. In the high energy limit, analytical approximations can be obtained for both contributions.

Finally, the Bloch theory uses a semiclassical approach where the moving particle is described classically (impact parameter method) and the excitation of the atom is described using time dependent perturbation theory. The evolution of the electronic wave function is analyzed and asymptotic conditions are imposed. As in the Bohr model, the use of an impact parameter description gives the possibility of separating the two relevant regions of close and distant interactions. But in this case, the region of close collisions is described more accurately using appropriate Coulomb wave functions. This part of the solution is the one that contains the previous classical and perturbative (plane wave) approximations as opposite limits in terms of a single parameter, $\eta = Ze^2/\hbar v$.

A well-known common feature of the BBB theories is the coincidence of the dominant term in the final stopping power expressions derived from them, which are all of the form

$$S \equiv -\left\langle \frac{\mathrm{d}E}{\mathrm{d}x} \right\rangle = \frac{4\pi n Z^2 e^4}{mv^2} L(v) \tag{1}$$

where n is the density of electrons, Ze is the ion charge and v its velocity. The function $L(v)$ is the so-called *stopping logarithm*, a non-trivial quantity that absorbs all the intricate details of the stopping process.

The common forefactor $4\pi nZ^2e^4/mv^2$ is associated to the Rutherford scattering cross section, whose validity includes the classical as well as the perturbative and the full quantal formulations. Hence, the differences between these approaches are contained in the stopping logarithm. The value of this function is determined essentially by the characteristics of the interactions in the limiting cases, i.e., in the short and in the long-range limits. For swift ions, $L(v)$ has the form of a logarithmically divergent integral which represents the contribution of Coulomb interactions taking place in an infinite range of distances. But in a more detailed analysis, there are various competing factors that control the interaction process at short and long distances and suppress the unphysical divergencies.

The explanation is formally different in the classical and in the quantal pictures, since the former is established in terms of impact parameters and the latter in terms of momentum transfers. So each case requires some particular considerations.

In the classical picture, the short range interaction is described by the classical Rutherford scattering theory, which is parameterized in terms of $b/b_{\rm cl}$, b being the impact parameter and $b_{\rm cl} = Ze^2/mv^2$ the classical collision radius. Instead, in the quantum perturbation theory, the short-range behavior is related to high momentum transfers. In the Bethe and Lindhard theories the upper limit in the momentum transfer, for fast particles, is $\hbar k_{\rm max} \cong 2mv$, which, by a complementarity argument [16] may be assimilated to a lower limit in the definition of the impact parameter, $b_{\rm QM} = \hbar/2mv$. The fact that $b_{\rm cl}$ and $b_{\rm QM}$ differ is the origin of the discrepancy between the Bohr and Bethe results. The discrepancy is solved by the Bloch formulation, where, in the final result, it is the largest of these two values the one that prevails.

On the other hand, the upper cut off in the long-range behavior has to do with specific target properties. In the classical Bohr model, the cut off is generated by an adiabatic behavior in distant interactions. In this description, the relevant quantities are the interaction time, $\sim b/v$, in relation to the natural oscillation time $\sim \omega_0^{-1}$, (where ω_0 is the harmonic oscillator frequency), and, from the matching of these quantities, the adiabatic impact parameter becomes $b_{\rm ad} = v/\omega_0$. So, for impact parameters $b > b_{\rm ad}$ the energy transfer $\Delta E(b)$ becomes vanishingly small, and the energy loss integral converges. The final classical result is expressed by a logarithmic function which depends on the ratio $b_{\rm ad}/b_{\rm cl} = mv^3/Ze^2\omega_0$.

In the Bethe formulation, the long-range behavior is connected, by the complementarity argument, with low momentum transfers. The energy transfer $\Delta E_{ij} = E_j - E_i$ corresponding to a given transition, $i \rightarrow j$, determines a minimum value of momentum transfer $\hbar k_{\rm min} = \Delta E_{ij}/v$. Hence in this theory the logarithmic term depends on the ratio $k_{\rm max}/k_{\rm min} = 2mv^2/\Delta E_{ij}$.

The dielectric formulation by Lindhard is basically consistent with the Bethe theory, but still requires some particular comments. The energy loss in the electron gas model is decomposed in individual and collective

excitations. The individual excitations are responsible for the maximum momentum transfers (close interactions) and are characterized, as in the Bethe theory, by a limiting value $k_{\max} \cong 2mv/\hbar$. The collective excitations, on the other hand, are delocalized interactions and they determine the behavior in the long-range limit (or low momentum transfers). These excitations have a characteristic frequency $\omega_P = (4\pi ne^2/m)^{1/2}$ (plasma frequency), and therefore, they determine a minimum wavevector $k_{\min} = \omega_P/v$. This may be explained either in classical or in quantum terms. The classical explanation is that a particle moving with velocity v has a Fourier spectrum (in the $\omega - k$ plane) restricted to the region $\omega \leq kv$, hence the resonance at ω_P may be excited only if $k \geq \omega_P/v$. The quantum explanation is similar to the one in Bethe's theory: the collective oscillations are quantized in modes of energy $\hbar\omega_P$, then the minimum momentum transfer should be $\hbar k_{\min} = \hbar\omega_P/v$. The logarithmic term in this model depends on the ratio $k_{\max}/k_{\min} = 2mv^2/\hbar\omega_P$.

Finally, the derivation of the Bloch model for the electron gas, which provides the connection between the classical (Bohr) and quantal (Bethe) results, may also be carried out in a closed way, although various mathematical details should be taken into account. A detailed derivation is given in Ref. [40].

Since we consider here the interaction of projectile ions with a free electron gas, we summarize the standard results for this system as follows (some appropriate numerical factors are included here for better precision).

(a) Classical formulation (Bohr model):

$$L_{\text{Bohr}}(v) \approx \ln\left(\frac{1.123mv^3}{Z\omega_P}\right) \tag{2}$$

(b) Perturbative dielectric-function formulation (Bethe–Lindhard model):

$$L_{\text{Bethe-Lindhard}}(v) \approx \ln\left(\frac{2mv^2}{\hbar\omega_P}\right) \tag{3}$$

(c) Semiclassical formulation (Bloch model):

$$L_{\text{Bloch}}(v) \approx \ln\left(\frac{2mv^2}{\hbar\omega_P}\right) - \text{Re}[\psi(i\eta)] - \gamma \tag{4}$$

where $\eta = Ze^2/\hbar v$ and $\gamma = 0.5772$.

These equations show only the approximate results in the high velocity limit, $v \gg v_F$, where v_F is the Fermi velocity of the electron gas. Usually,

v_F is of the order of the Bohr velocity $v_0 \equiv e^2/\hbar$, for realistic electron gas densities in metals.

The function $\psi(x)$ in equation (4) is de digamma function [41], and it has the virtue of leading to both the previous (Bohr and Bethe) expressions in the appropriate limits. Thus, for $\eta \gg 1$, one gets $\mathrm{Re}[\psi(\mathrm{i}\eta)] \to \ln(\eta)$, and equation (2) is obtained, whereas for $\eta \ll 1$, $\mathrm{Re}[\psi(\mathrm{i}\eta)] \to -\gamma$, and equation (3) if retrieved. A very accurate representation of the function $\mathrm{Re}[\psi(\mathrm{i}\eta)]$ is the following [40]: $\mathrm{Re}[\psi(\mathrm{i}\eta)] \cong -\gamma + \frac{1}{2}\ln(1 + \Gamma^2\eta^2)$, with $\Gamma = \exp(\gamma) = 1.781$. With this approximation the Bloch formula may be written in the more convenient form

$$L_{\mathrm{Bloch}}(v) \approx \ln\left(\frac{2mv^2}{\hbar\omega_P}\right) - \frac{1}{2}\ln(1 + \Gamma^2\eta^2) \tag{5}$$

with $\eta = Zv_0/v$.

As mentioned earlier, these formulations are applicable to structureless particles (bare ions). The only one of them that may be easily extended to complex ions is the perturbative formulation, either in the form of Bethe's theory for atomic targets or Lindhard's theory (dielectric formalism, DF) for the electron gas model. In addition, a comprehensive semiclassical approach, which extends the Bohr model to complex ions, has been developed more recently by Sigmund *et al.* [26].

In the following we will consider the energy loss of ions using two formulations: the 'linear' formulation based on the DF (i.e., a perturbative approach), and the 'non-linear' (or non-perturbative) formulation, which will be extensively applied in the rest of the work.

3. ENERGY LOSS FORMULATIONS

3.1. Dielectric formulation

The DF is adequate to describe the interaction of ions with the valence electrons in a solid, provided that the perturbation induced by the presence of the external particle is not very large. In this approximation the response of the system (induced density or electric field) is *linear* in the magnitude of the perturbation. In practice this assumption applies to fast but not highly charged ions.

The properties of the target are described by its dielectric function $\varepsilon(k, \omega)$, where $\hbar k$ and $\hbar\omega$ represent the momentum and energy transfer to the system in an elementary inelastic process. This approach has the possibility of describing in a condensed way the screening of the intruder ions as well as the excitations of valence electrons in the solid, including both collective and single-particle (or electron–hole) excitations [13,14]. The stopping power in

the DF is given by

$$S_{\mathrm{DF}}(v) = \frac{2e^2}{\pi v^2} \int_0^\infty \frac{\mathrm{d}k}{k} |f(k)|^2 \int_0^{kv} \mathrm{d}\omega\, \omega\, \mathrm{Im}\left[\frac{-1}{\varepsilon(k,\omega)} \right], \tag{6}$$

where $f(k)$ is the form factor of the incident ion – which we consider spherically symmetric – defined in terms of its charge distribution (nuclear and electronic) $\rho_{\mathrm{ion}}(\vec{r})$, by

$$f(k) = \int \mathrm{d}^3 r\, \exp(\mathrm{i}\vec{k}\cdot\vec{r})\rho_{\mathrm{ion}}(\vec{r}). \tag{7}$$

A practical way to handle the calculations by a unified approach comprising all ions was proposed by Brandt and Kitagawa [15]. In this approach the structure of the ion is represented by a statistical model (of Thomas–Fermi type), and $f(k)$ is analytically expressed as

$$f_{\mathrm{BK}}(k) = Z_1 \frac{(q/Z_1) + k^2\Lambda^2}{1 + k^2\Lambda^2} \tag{8}$$

which depends on the ion charge q and atomic number Z_1. Here Λ is the screening radius of the ion (which depends also on q and Z_1). The simplest case of bare nuclei corresponds to $f(k) = Z_1$.

The analysis of the properties of the linear theory to be considered in the following will make use of this formulation, using for $\varepsilon(k, \omega)$ the dielectric function obtained by Lindhard [13].

3.2. Non-linear energy loss formulation

As indicated before, the non-linear approach to the energy loss of ions in solids is based on the following methods: (a) the transport cross section (TCS) method, and (b) the extended Friedel sum rule (EFSR). In addition, particular models will be used to represent the scattering potential by a sum of (i) the ion potential and (ii) the screening potential. The scattering potential will be adjusted in a self-consistent way, for each ion velocity, by the constraint of the EFSR.

We describe now the basic ingredients used in this approach, and in Section 4 we consider the determination of the scattering potential.

3.2.1. Transport cross section method

In this method, one considers the scattering of target electrons in the field of an incident ion with nuclear charge $Z_1 e$ (dressed by its electronic cloud), and calculates the TCS, defined by

$$\sigma_{\mathrm{tr}} \equiv \int (1 - \cos\theta)\mathrm{d}\sigma \tag{9}$$

Using the quantum mechanical formulation, based on the partial-wave analysis, the TCS may be expressed as

$$\sigma_{\rm tr}(k) = \frac{4\pi}{k^2} \sum_{l=0}^{\infty} (l+1)\sin^2[\delta_l(k) - \delta_{l+1}(k)]. \tag{10}$$

where $\delta_l(k)$ denotes the phase shift corresponding to the scattering of wave components with angular momentum $l = 0,1,\ldots$, and $k = mv_{\rm r}/\hbar$ is the wave vector corresponding to target electrons having relative velocities $v_{\rm r}$ with respect to the scattering center (center of mass frame).

In the following we consider an electron gas of uniform density n, where the Fermi velocity $v_{\rm F}$ is related to the electron gas parameter $r_{\rm s}$ through $r_{\rm s} = 1.919/v_{\rm F} = 0.621n^{-1/3}$ (in a.u.).

3.2.2. Extended Friedel sum rule

The generalization of the Friedel sum rule to finite (non-zero) velocities was developed in Ref. [36]. It is based on the general property that the screening of an impurity in a free electron gas is complete, and this applies to a moving ion as well as to a fixed one. However, the scale of distances required to screen the external field varies with velocity.

In the case of static impurities, the usual Friedel sum rule for an ion with atomic number Z_1 which carries a number of bound electrons $N_{\rm e}$ has the form

$$\frac{2}{\pi} \sum_{l=0}^{\infty} (2l+1)[\delta_l(v_{\rm F}) - \delta_l(0)] = Z_1 - N_{\rm e}, \tag{11}$$

where $q = Z_1 - N_{\rm e}$ is the net charge of the ion, which should be compensated by the screening cloud. The screening charge is a result of the distortion in the wavefunctions of the scattered electrons, so that each term in this sum represents the contribution of the l-wave component of scattered electrons to the accumulation of screening charge around the impurity.

The extended sum rule for an ion with velocity v, atomic number Z_1, and $N_{\rm e}$ bound electrons, may be written in a similar way

$$\frac{2}{\pi} \sum_{l=0}^{\infty} (2l+1) G_l(v, v_{\rm F}) = Z_1 - N_{\rm e}, \tag{12}$$

where $v_{\rm F}$ is the Fermi velocity of the solid. The functions $G_l(v, v_{\rm F})$ take into account the contribution of each l-wave component to the screening charge, and may be expressed as integrals over a displaced Fermi sphere (DFS) of the corresponding phase-shift contribution, as follows

$$G_l(v, v_{\rm F}) = \frac{1}{4\pi} \int_{\rm DFS} \left[\frac{{\rm d}\delta_l(k)}{{\rm d}k} \right] {\rm d}\Omega \, {\rm d}k = \int_{k_{\rm min}}^{k_{\rm max}} \left[\frac{{\rm d}\delta_l(k)}{{\rm d}k} \right] g(k, v) {\rm d}k, \tag{13}$$

where $k_{\min} = \max\{0, v - v_F\}$ and $k_{\max} = v + v_F$. The function $g(k, v)$ takes into account the angular part of the integration over the DFS, and the expressions for the cases $v < v_F$ and $v > v_F$ were given in Ref. [36]. The phase shift $\delta_l(k)$ is a function of the wave vector k corresponding to the relative electron–ion motion ($k = mv_r/\hbar$, where $\vec{v}_r = \vec{v}_e - \vec{v}$). The derivative $[d\delta_l(k)/dk]$ gives the contribution of each l-wave component to the accumulation of screening charge around the intruder ion. It may be shown from these expressions that one retrieves the usual Friedel sum rule in the low-velocity limit ($v < v_F$), and a perturbative form of the sum rule for high velocities ($v > v_F$) [42].

In the following we will use atomic units, so that the variables k and v_r may be used indistinctly.

In order to obtain self-consistency, the screening potential is modeled by an analytical expression containing a few parameters. In our calculations we have used two alternative forms of screening potentials: a Yukawa potential (with a single parameter α), and a Hydrogenic potentials (with two parameters α and β). Then, the self-consistency condition of equation (12) may be achieved by the variation of the screening parameters. This process has to be repeated for each ion velocity of interest, so that the screening parameters (and the scattering potential) become a function of the ion velocity v.

Finally, we use the phase shift values to calculate the TCS, from equation (10), which takes now the form

$$\sigma_{tr}(k, v) = \frac{4\pi}{k^2} \sum_{l=0}^{\infty} (l + 1)\sin^2[\delta_l(k, v) - \delta_{l+1}(k, v)]. \tag{14}$$

We note that the phase shifts δ_l and the TCS in equation (14) depend now on the ion velocity v and on the relative electron–ion velocity, with $k = |\vec{v}_r|$.

3.2.3. Stopping power integration

After the TCS is evaluated for a wide range of relative velocities v_r, we calculate the stopping power $S = -\langle dE/dx \rangle$ by integrating σ_{tr} over the distribution of electron velocities in a Fermi sphere ($0 \le v_e \le v_F$) and over the range of relative velocities v_r (with $|v - v_e| \le v_r \le v + v_e$) [36]. This integration is performed in a closed form using the expression (in atomic units)

$$S(v) = \frac{1}{4\pi^2 v^2} \int_0^{v_F} v_e \, dv_e \int_{|v-v_e|}^{|v+v_e|} dv_r \, v_r^4 \sigma_{tr}(v_r, v) \left[1 + \frac{v^2 - v_e^2}{v_r^2} \right], \tag{15}$$

where $\sigma_{tr}(v_r, v)$ is calculated from equation (14).

4. THE SCATTERING POTENTIAL

Since the purpose of this study to describe partially stripped ions, the scattering potential will be represented by a sum of two components: (a) an ionic core potential $V_{\rm ion}(r)$, which includes the atomic screening provided by the bound electrons carried by the ion, and (b) the outer screening potential $V_{\rm s}(r)$, which is produced by the target valence electrons in order to neutralize the net charge of the ion. The assumption of spherical symmetry of the potential is one of the main assumptions of this model, and may be considered to represent the spherical average of the real potential. We introduce screening functions $\phi_{\rm ion}(r)$ and $\phi_{\rm s}(r)$ corresponding to each of these potentials, so that the total electron–ion scattering potential may be expressed as follows:

$$V_{\rm total}(r) = V_{\rm ion}(r) + V_{\rm s}(r) = -\frac{N_{\rm e}e^2}{r}\phi_{\rm ion}(r) - \frac{qe^2}{r}\phi_{\rm s}(r) \qquad (16)$$

where $N_{\rm e}$ is the number of bound electrons and q is the charge of the ion.

A basic difference between both potentials, $V_{\rm ion}(r)$ and $V_{\rm s}(r)$, is that while the ionic component remains essentially frozen when the ion velocity increases (besides possible changes due to the increased stripping), the outer screening component changes with velocity since the electrons readjust themselves in a dynamical way to the field of the moving ion.

This property is included in our approach, where the screening component $V_{\rm s}(r)$ is adjusted for each velocity in order to satisfy the extended sum rule.

4.1. Ion model

In a previous study [39] various ion models were tested and a new model was proposed, which was called the 'Molière-ion potential'. Due to its simplicity and good comparison with other models (including Dedkov's model for ions [43] and Molière and Thomas–Fermi models for neutral atoms [44]) we have used this model throughout this study.

In this model, the ionic component, $V_{\rm ion}(r) = -(N_{\rm e}e^2/r)\phi_{\rm ion}(r)$, is determined by the 'Molière-ion function' $\phi_{\rm Mi}(r)$ (i.e., $\phi_{\rm ion} \equiv \phi_{\rm Mi}$) which – following the form of the original Molière function – is expressed as

$$\phi_{\rm Mi}(r) = C\sum_{j=1}^{3} A_j \exp(-\alpha_j r/a_{\rm TF}), \qquad (17)$$

with $a_{\rm TF} = 0.8853/Z_1^{1/3}$ and $C = (A_1 + A_2 + A_3)^{-1} = Z_1/N_{\rm e}$. In the case of neutral atoms ($q = 0$) the normal values of the coefficients are used, namely [44]: $A_j = (0.1, 0.55, 0.35)$ and $\alpha_j = (6, 1.2, 0.3)$; so that in this case one retrieves from equation (16) the Molière-atom potential given by $V_{\rm total}(r) = -(Z_1e^2/r)\phi_{\rm M}(r)$, $\phi_{\rm M}(r)$ being the usual Molière screening function.

To represent ions with increasing degrees of ionization $i = q/Z_1$, the coefficients in $\phi_{Mi}(r)$ are modified as follows: first the value of the third coefficient A_3 is decreased (until it eventually becomes zero, for $i = 0.35$); for higher ionization ($0.35 < i < 0.9$) a similar reduction is done on the value of A_2; and finally (if $i > 0.9$) the value of A_1 is decreased (until complete ionization is reached). In any case (i.e., for a given velocity), the sum of these coefficients should correspond to the actual ionization degree q/Z_1, namely, $A_1 + A_2 + A_3 = N_e/Z_1 = 1 - q/Z_1$.

4.2. Screening potential

In these calculations we have used a screening potential $V_s(r) = -(qe^2/r)\phi_s(r)$, considering two alternative forms of the screening function $\phi_s(r)$: (a) a simple Yukawa potential, $\phi_s(r) = \exp(-\alpha r)$, using a single parameter α, and (b) a hydrogenic potential, $\phi_s(r) = (1 + \beta r)\exp(-\alpha r)$, containing two parameters, α and β.

In the EFSR approach, the value(s) of the screening parameter(s) are adjusted in a self-consistent way for each velocity v using equation (12). This requires a significant time of computation, since for each step of the iteration the phase shifts $\delta_l(k)$ are calculated by numerical integration of the Schrödinger equation. Two alternatives that may be used to speed up the calculations are the following: (1) for $l > 30$ the phase shifts may be evaluated using appropriate semiclassical approximations [36]; (2) an additional recourse is to interpolate the values of the screening parameters between the low and the high-velocity limits. We have found this procedure to be accurate enough for most practical purposes. Further details of the calculation methods have been given elsewhere [36–39].

5. ILLUSTRATIVE CALCULATIONS

To illustrate the basic and qualitative differences between the linear and non-linear approaches we will show first a set of calculations for simple systems, where these differences may be analyzed in a clear way.

First, we show calculations for bare ions, using the following methods: (i) the linear response formalism described in Section 3.1, based on the exact Lindhard's dielectric function $\varepsilon(k, \omega)$, and (ii) following the non-linear approach described in Section 3.2.

We show in Fig. 2 a couple of examples for bare ions with $Z_1 = 1$ and 7. The figure illustrates important differences between linear (or perturbative) and non-linear calculations. For $Z_1 = 1$ we note important quantitative differences at low and intermediate energies. The non-linear results exceed those of the linear theory by about 60% at low velocities. Thus, in the case of protons the non-linear theory predicts a significant enhancement of

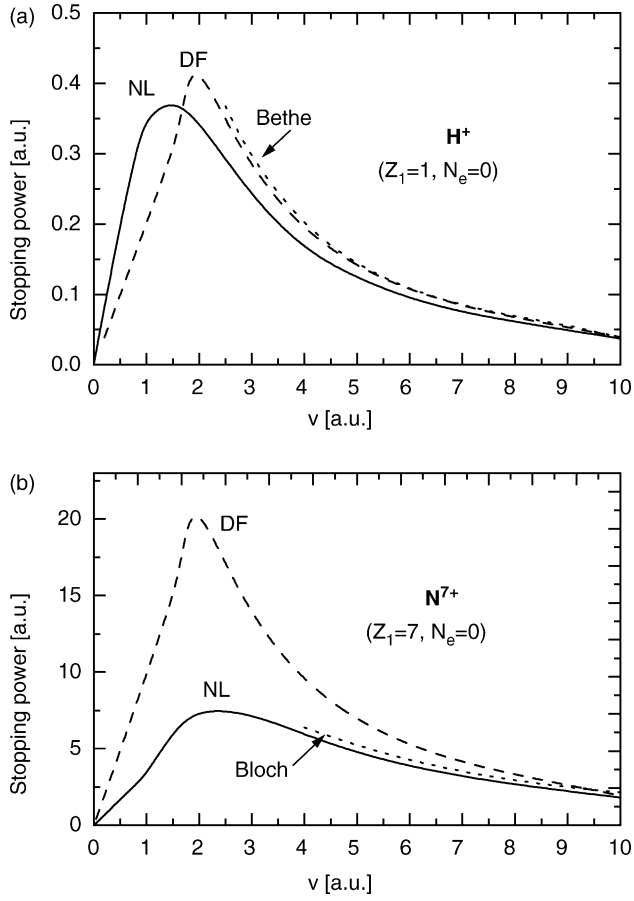

Fig. 2. Stopping power calculations for bare ions, H^+ and N^{7+}, according to the linear (DF) and non-linear (NL) formulations described in the text, for a medium with $r_s = 1.6$. The asymptotic Bethe and Bloch limits are also indicated.

the stopping power values in this energy range. This non-linear effect has been noted long ago and is in excellent agreement with a large number of experimental results [45].

On the other hand, in the case $Z_1 = 7$ we observe a different behavior. Here the non-linear values lie well below those of the linear calculation on the whole velocity range. The interpretation of these results is also very revealing. The results obtained from the dielectric calculation increase by a whole factor 49 when going from $Z_1 = 1$ to $Z_1 = 7$ – as expected from a linear formalism. Instead, the non-linear results increase by a much smaller factor (a ratio about 20 between both maxima). This may be interpreted as a 'saturation' in the energy loss process, i.e., the values increase by a much

smaller proportion than expected from a Z_1^2 scaling. We also note that the Bloch model yields a good representation of the high-energy side of the stopping curve. This indicates that, at least for the case of bare ions, the saturation effect may be understood by considering the behavior of the terms in the simplified Bloch analysis. It turns out that the reason for this effect stems basically from the behavior of the energy transfer mechanism in the range of close impact parameters, according to the semiclassical representation of the collision process. The dominant term in this range is the classical collision radius, $b_{\mathrm{cl}} = Z_1 e^2/mv^2$. Then, as Z_1 increases so does the value of b_{cl}, and hence the relevant interaction range ($b_{\mathrm{cl}} < b < b_{\mathrm{ad}}$) shrinks. Therefore, the comparative reduction of the energy loss (with respect to the Z_1^2 scaling) may be explained in this case by the saturation of the energy transfer in the range of impact parameters $b < b_{\mathrm{c}}$, and, as shown by this explanation, is an effect of classical origin.

Another interesting result for energetic bare ions is illustrated in Fig. 3. Here we show the values of the stopping logarithm, obtained from the non-linear calculations of the energy loss, $\mathrm{d}E/\mathrm{d}x$, and using the relation $L = -(\mathrm{d}E/\mathrm{d}x)/(Z_1 e\omega_{\mathrm{P}}/v)^2$. The calculations correspond to an energy

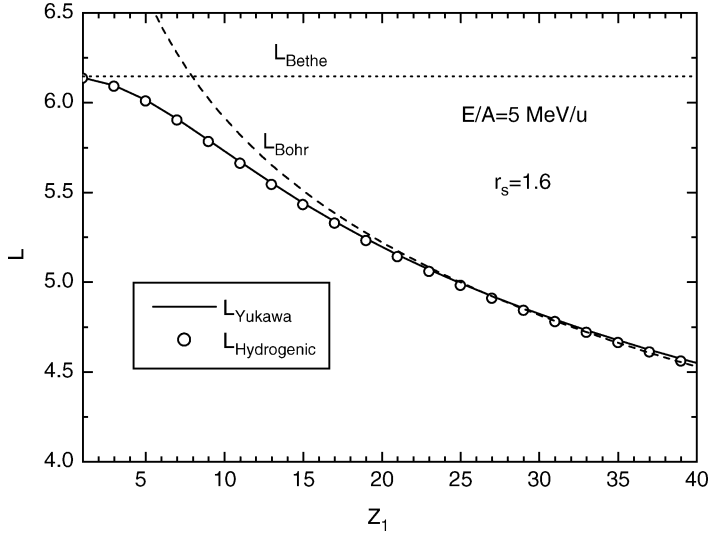

Fig. 3. High-velocity limit of the non-linear model for bare ions, for a velocity $v = 14.1$ a.u. (energy $E/A = 5$ MeV/u), *versus* the ion charge number Z_1. The figure shows the values of the stopping logarithm $L(v)$ in equation (1), calculated using two different screening models: Yukawa and Hydrogenic potentials, with parameters fixed by the condition of the extended Friedel sum rule. The results of both models are in excellent agreement, and the approach to the Bohr and Bethe limits – in the corresponding ranges of applicability – is observed.

$E/A = 5$ MeV/u (i.e., a fixed ion velocity $v = 14.1$ a.u.), and different ion atomic numbers Z_1. The simple predictions from the Bohr and Bethe theories for $v \gg v_F$, equations (2) and (3), are shown by dashed and dotted lines. We also show the results of numerical integrations using the non-linear approach considering two assumptions for the screening potential: Yukawa (solid line) and Hydrogenic (circles). As it may be observed, there is an almost exact coincidence between both screening models on the whole range (it should be noted that this agreement is found only after the parameters of the screening potentials are optimized according to the EFSR).

Moreover, for low-Z values ($\eta \ll 1$, in terms of the Bloch parameter $\eta = Z_1 e^2/\hbar v$) the numerical results converge to those predicted by the Bethe–Lindhard theory, $L \cong \ln(2mv^2/\hbar\omega_P)$, which is independent of the charge, whereas for high-Z values ($\eta \gg 1$) they converge to the predictions of the Bohr model.

Hence, in the high energy limit the non-linear calculations for bare ions reproduce the corresponding limits of the BBB theory.

The simplicity of this picture is broken when one considers partially ionized projectiles. To illustrate this point we show in Fig. 4 calculations for N^{3+} ions, considering frozen charge state conditions. The dashed lines in this figure are the results of the Bloch model for point charges Z, for the values

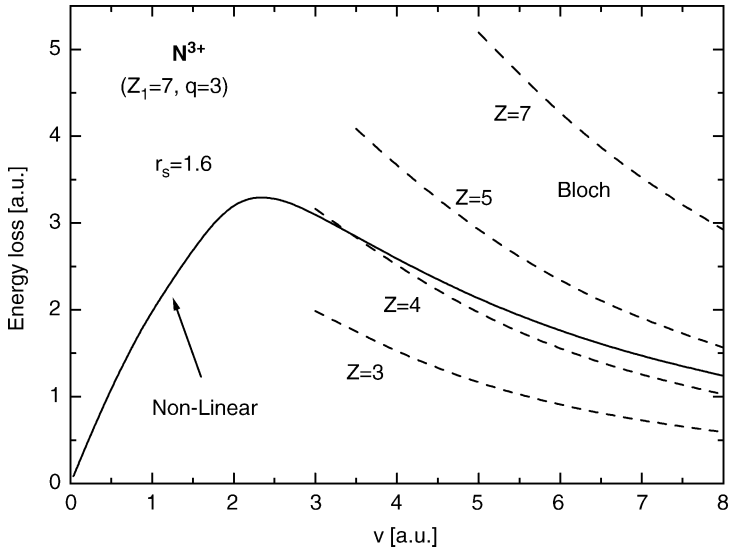

Fig. 4. Energy loss of N^{3+} ions (assuming frozen charge state conditions) as a function of the ion velocity v. The solid line is the result of the non-linear calculation for partially dressed ions ($Z_1 = 7$, $N_e = 4$). The dashed lines are the predictions of the Bloch model for bare ions with various charges Z, as indicated.

$Z = 3, 4, 5$ and 7. We observe that the extreme assumptions of using either the ion charge, $Z = q = 3$, or the nuclear charge $Z = Z_1 = 7$, give very bad results. We note instead that the high-energy side of the curve may be roughly approximated by equivalent Bloch particles with charges in the range 4–5. This is physically reasonable since the electrons scattered in close collisions will 'see' an effective charge Z within the range $q < Z < Z_1$. It is also reasonable that the most adequate value of Z increases weakly with ion velocity (*cf.* Fig. 4), but it should be noted that since the ion charge is frozen the effective charge corresponding to *large* impact parameter collisions will remain close to the ion charge q at all velocities. Hence, the effective charge value Z that would be required for a simplified Bloch estimation actually represents a whole average of all types of collision processes.

6. STOPPING POWER CALCULATIONS

We have shown in Section 5 that the non-linear approach yields a good representation of the energy loss in the high-energy region, showing a connection with the BBB models for bare ions, and extending the possibilities of calculations to all types of ions.

In the case of light ions, this approach has been applied to calculate the energy loss for the following systems: (i) helium ions in aluminum targets [37], and (ii) protons and antiprotons in various solids [38] (with particular evaluation of the Barkas effect). In all these cases the agreement with experimental results was very good.

Now we will show more extensive calculations following this approach, including light and heavy ions, and the corresponding comparisons with experimental results.

6.1. Slow ions

As it was mentioned, one remarkable feature of the low-energy stopping phenomenon is the oscillatory dependence on the ion atomic number Z_1. The question of representing this structure constitutes an important test for the theoretical descriptions.

In Fig. 5 we show, with solid line, the non-linear calculations of the stopping power of carbon for all ions with atomic numbers in the range $1 \leq Z_1 \leq 40$, and with a fixed velocity $v = 0.8$ a.u., together with experimental results from various authors [10,46,47]. We also show the theoretical results obtained from the DFT [32] (which, for the electron density of carbon targets, are available only in the range $Z_1 \leq 17$), and the calculations according to the Brandt–Kitagawa model (BK) [15]. This model is based on linear theory and includes a statistical model for the ion structure as well as

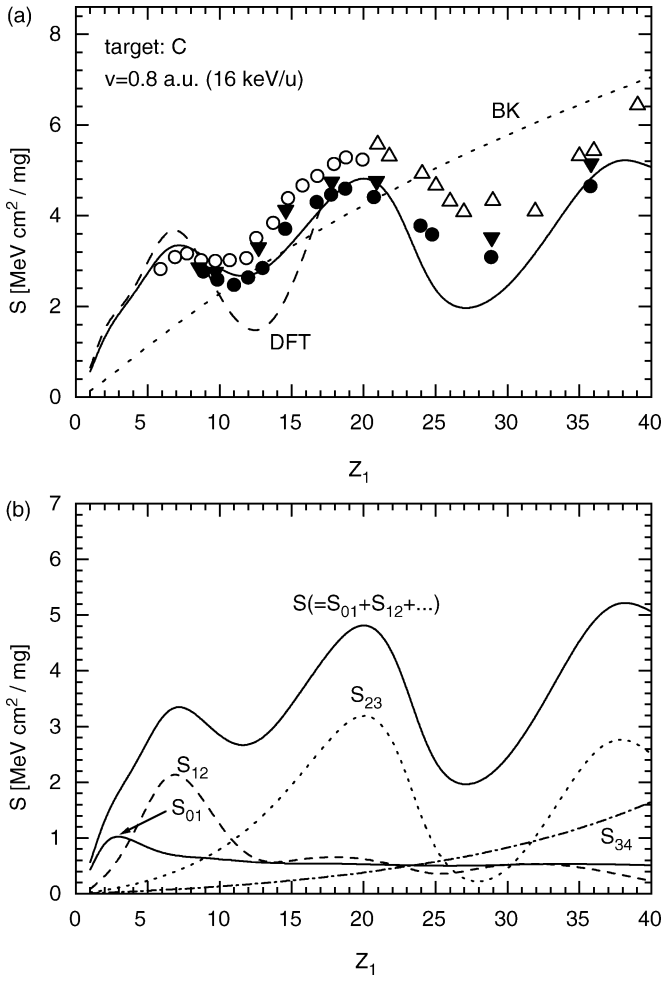

Fig. 5. (a) Stopping power of carbon targets (with $r_s = 1.6$) for slow ions with velocity $v = 0.8$ a.u. ($E/A = 16$ keV/u). The solid line is the result of the present non-linear calculations for $1 \leq Z_1 \leq 40$; the dashed line shows the result of the density functional theory (DFT) for $1 \leq Z_1 \leq 17$ (with $r_s = 1.5$); the dotted line shows the result of the Brandt–Kitagawa model. The symbols show the experimental results from various authors [10,46,47]. (b) Contributions of the main partial wave components, $l = 0, 1, \ldots, 4$, to the total stopping power shown in part (a).

for the mean equilibrium charge $\bar{q}_{\mathrm{BK}}$ (*cf.* Fig. 7); it yields an average representation of the stopping power, but of course it does not represent the oscillatory structure, since it is based on statistical assumptions. The DFT accounts for the first part of the oscillations, although it shows some deviations from the experimental data. Our model yields a fairly good

description on the whole range, but still shows some deviations for Z_1 values between 25 and 32.

To illustrate the physical origin of this structure, we show in panel (b) of this figure the decomposition of the total stopping $S = S_{01} + S_{12} + S_{23} + \cdots$, where each term $S_{l(l+1)}$ is the contribution of partial wave components l, $l+1$, corresponding to the terms $(l+1)\sin^2[\delta_l - \delta_{l+1}]$ in equation (14). Hence, the participation of p and d electrons in the structure of these oscillations is clearly shown. The physics of the Z_1 structure has been discussed in the previous work from two (related) points of view: the relation with the well-known Ramsauer–Townsed resonances in low-energy electron scattering [30] and the occurrence of resonances close to the Fermi surface ($v_{\text{res}} \approx v_{\text{F}}$) for certain impurity ions in metals [31].

It may be shown, moreover, that the reason for the great amplitude of these oscillations is the fact that, at these low energies, the TCS is determined by only few phase shifts ($l = 0, 1, \ldots, 4$). If the energy is increased, more and more phase shifts are required and then the amplitude of the oscillations gradually decreases [39]. So, at larger energies a uniform dependence of the stopping power with Z_1 is observed [9].

6.2. Swift ions

Having analyzed the behavior of the stopping power in the low-energy range, we now take a view to the case of swift ions. For this purpose, we include in Fig. 6 a sample of calculations and experimental results for ions with atomic numbers from 6 to 92, in carbon targets. Here the results cover a wide range of energies, showing the transition from the low to the high-energy sides of the stopping curve.

An important question that should be mentioned here is the value of the ion charge inside the solid, since the calculated stopping power values depend of course very much on the ion charge value. This question will be discussed in detail in Section 7, but we should indicate that the calculations shown in these figures have been made assuming conditions of charge equilibrium (in correspondence with the experimental conditions), and considering a mean ion charge, $\bar{q}$, whose value was set equal to the empirical mean charge value measured after the ions emerge from the solid into vacuum ($\bar{q} \cong \bar{q}_{\text{exit}}$). Hence, the comparison with experiments is also a test of this assumption.

In addition, since we are considering higher energies, one should include a correction due to the excitation of the inner shells of the target atoms (additional contributions due to excitation or ionization of the projectile electrons are estimated to be less relevant [26,48] and they have been neglected). In the chosen case of carbon, however, the required correction is comparatively small, involving only the contribution of the two K-shell electrons which are tightly bound, with binding energy $E_{\text{K}} \approx 300$ eV.

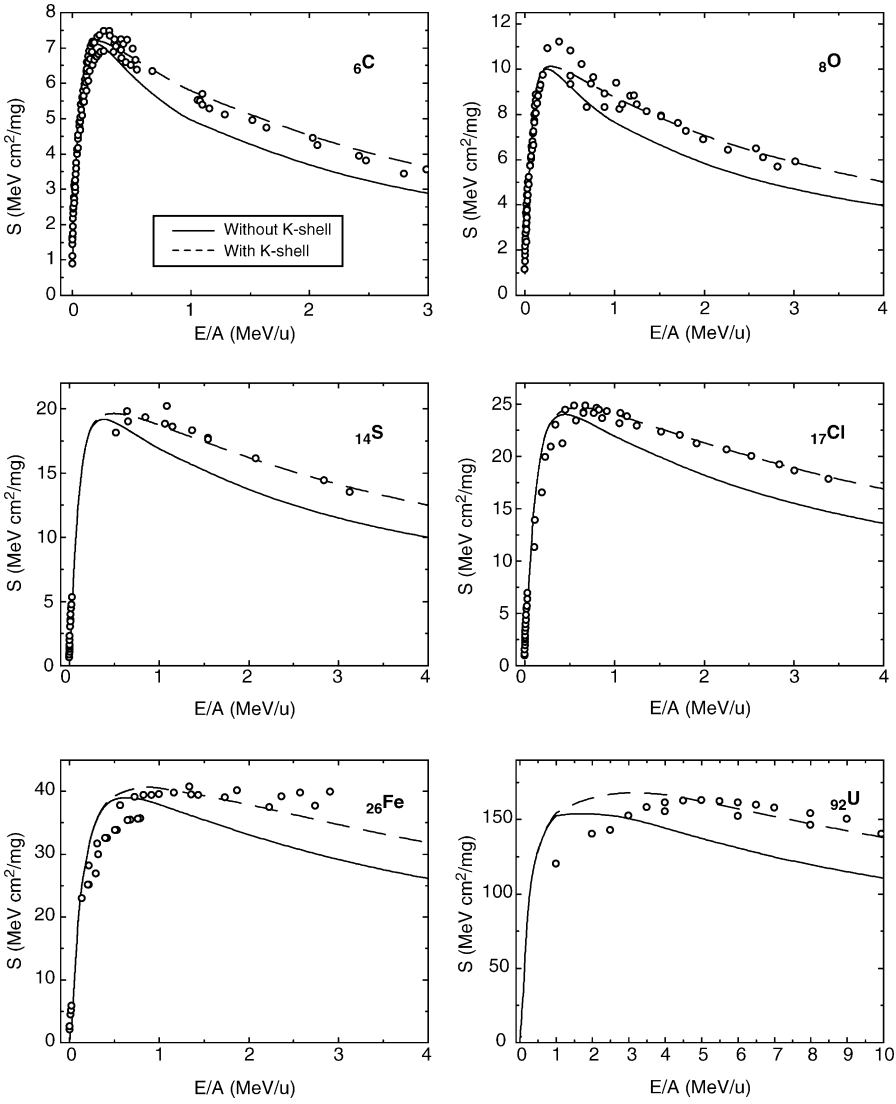

Fig. 6. Calculations and experimental results of carbon stopping powers for ions with atomic numbers from 6 to 92. The solid lines show the contribution of valence electrons (with $r_s = 1.6$) calculated with the non-linear approach. The dashed lines show the total stopping, including the K-shell contribution.

Moreover, since this effect is important only in the high-energy range, we estimated its contribution using a simple Bethe–Bloch approximation.

The results in Fig. 6 show the contribution of valence electrons, calculated with the non-linear approach (shown with solid lines), and the total (valence

plus K-shell correction), shown with dashed lines. The final results compare fairly well with the available experimental data. Some discrepancies are observed, particularly for the heaviest ions, in the energy range around the stopping maximum, but the general view is very good.

7. AN OLD QUESTION REVISITED: THE EQUILIBRIUM CHARGE OF IONS IN SOLIDS

The final problem that we will discuss here refers to a basic aspect of the interaction of swift ions with solids, which is the relation between the charge state of ions moving *inside* a solid and the 'effective charge' values deduced from stopping power measurements. This question has been analyzed recently in Refs. [49,50], based on different non-linear models and reaching similar results. Hence, the approach provides a convenient framework to clarify some seeming contradictions which have been under discussion for many years.

The problem of the charge state of ions penetrating matter is one of the most relevant questions for studies on the interaction of ions with solids. It is known that after some penetration distance the ions reach a state of charge equilibrium determined by the competition between capture and loss processes [2,7]. As a result of this equilibrium the ions acquire a mean ionization charge $\bar{q}$, as well as a stationary distribution of charge states around $\bar{q}$.

In the case of solid targets a direct determination of $\bar{q}$ is not possible, since only the charge state after emerging from a foil can be measured. From these types of experiments, the mean equilibrium charge state of the emerging ions $\bar{q}_{\text{exit}}$ may be determined.

To illustrate the current situation concerning different ion charge estimations we show in Fig. 7 several representative reference values. The lines indicated ND and SG refer to empirical fitting expressions for the average charge state of *emerging* ions (after penetrating solid foils) given by Nikolaev–Dmitriev [55], and by Schiwietz–Grande [56], respectively. The line indicated as BK is a calculation of the ionization state of ions moving inside the solid, according to the Brandt–Kitagawa model [15] (using a statistical stripping criterion), and the line ZBL is the equilibrium ionization value proposed by Ziegler *et al.* [9].

On the other hand, a second method to infer (indirectly) the charge state of the ions inside the solid is from its energy loss. This leads to the concept of the 'effective charge' [7–9]. In the original papers by Bohr and others [2,51] this term was used in the sense of the real equilibrium charge of the ion (i.e., the present $\bar{q}$ value). However, a different definition was introduced later [52]. According to perturbation theory, the stopping power of a bare ion with nuclear charge Z and velocity v is proportional to Z^2. By a simple analogy, the effective charge Z_{eff} of an ion with atomic number Z_1 and velocity v was

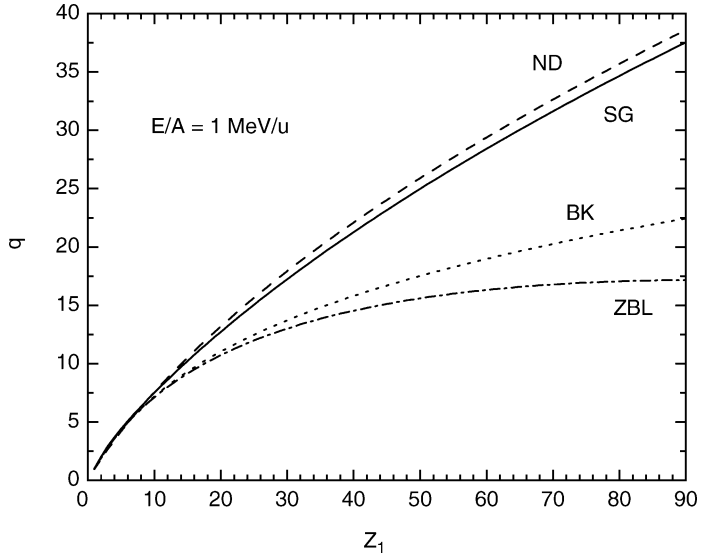

Fig. 7. Different estimation of the mean charge state of ions in carbon foils. The lines indicated ND and SG show the empirical fitting expressions for the average charge state of ions crossing solid foils given by Nikolaev–Dmitriev [55] and Schiwietz–Grande [56], respectively. The line BK is the Brandt–Kitagawa model [15] for the equilibrium charge of ions moving inside solids. The line ZBL is the equilibrium ionization value proposed by Ziegler *et al*. [9].

operationally defined through the stopping power ratio

$$\frac{Z_{\text{eff}}}{Z'_{\text{eff}}} = \left[\frac{S_{\text{exp}}(Z_1, v)}{S_{\text{exp}}(Z'_1, v)} \right]^{1/2} \tag{18}$$

where $S_{\text{exp}}(Z_1, v)$ is the experimental stopping power of the ion Z_1 and $S_{\text{exp}}(Z_1{}', v)$ is the corresponding stopping of a chosen reference ion with atomic number Z'_1 (usually hydrogen or helium ions) with the same velocity v. Using the stopping of bare protons, S_{p}, as the reference value, this relation may be written simply as $Z_{\text{eff}} = [S_{\text{ion}}/S_{\text{p}}]^{1/2}$. However, we should note that this unfortunate definition of the effective charge marks a serious discrepancy with the original Bohr concept [2]. It seems that this double use of the same word explains in part the confusion that pervades the literature in the area. Other authors have also noted the problems arising from this definition [53,54].

The relationship between $\bar{q}$ and Z_{eff} is not clear. At low energies, where the ions may be assumed to be nearly neutral, it is obvious that $Z_{\text{eff}} > \bar{q}$, but at high energies the situation has been for many years a point of discussion. In fact, it has been determined long ago that, in experiments

with solid targets, the values of $\bar{q}_{\mathrm{exit}}$ for swift ions exceed those of Z_{eff} for the same situation, whereas in the case of gas targets the corresponding values of $\bar{q}_{\mathrm{exit}}$ and Z_{eff} are much closer, being also close to the values of Z_{eff} for solid targets [7]. This observation gave rise to two different models on the charge state of ions in solids: the Bohr–Lindhard [57] and the Betz–Grodzins [58] models.

The Bohr–Lindhard (BL) model [57] considers that the fast sequence of collisions experienced by the ion within a solid produces an enhancement in the excitation and ionization probabilities, leading to an increased equilibrium charge. The effect of the exit surface is considered to be not very relevant, due to the high velocity condition, and so the exit charge $\bar{q}_{\mathrm{exit}}$ is expected to be close to $\bar{q}$. In this way the BL model explains the relatively higher values of the ion charge measured after a foil. But the remaining open question is how to explain according to this view the larger values of $\bar{q}$ as compared to the effective charges Z_{eff} determined experimentally from energy loss measurements.

The Betz–Grodzins (BG) model [58], instead, claims that the effect of repeated collisions within the solid produces ions with several excited electrons in outer shells, but those electrons remain mostly attached to the ion until it emerges into vacuum and, after this, the ion decays to the ground state by giving up its excess energy by electron emission through Auger processes. According to this model, the ion charge state $\bar{q}$ inside the solid would be close to Z_{eff} and the higher value of $\bar{q}_{\mathrm{exit}}$ would be determined at the exit surface. Hence, the model predicts a significant number of emitted electrons in the case of swift heavy ions. From the empirical $\bar{q}_{\mathrm{exit}}$ and Z_{eff} values [7], the number of such electrons, $\Delta N \cong \bar{q}_{\mathrm{exit}} - Z_{\mathrm{eff}}$, may be as high as 4–16 electrons for heavy ions with energies in the range 0.1–10 MeV/u (similar, and even larger differences may be observed between q_{SG} and q_{ZBL} in Fig. 7). These multiple emission processes have been sought for many years, but the number of electrons actually observed was much lower than the predictions.

The problem of the ion charge state may be studied from the point of view of the energy loss process, since the calculated stopping values depend very much on the assumed value of $\bar{q}$. Following the methods of the non-linear approach already explained we have calculated the energy loss of swift ions, in the range of energies where the discrepancy between the BL and BG models is greater; the results are shown in Fig. 8, and they are compared with empirical values [59,60]. In these calculations we have tried two different assumptions: (i) that the internal ion charge value $\bar{q}$ is coincident with the measured exit charge values, using in this case the SG fitting [56], $\bar{q} \cong \bar{q}_{\mathrm{exit}} = q_{\mathrm{SG}}$, and (ii) that the value of $\bar{q}$ is instead given by the expression proposed by Ziegler *et al.* [9], $\bar{q} = q_{\mathrm{ZBL}}$ (*cf.* equations (3)–(39) of this reference).

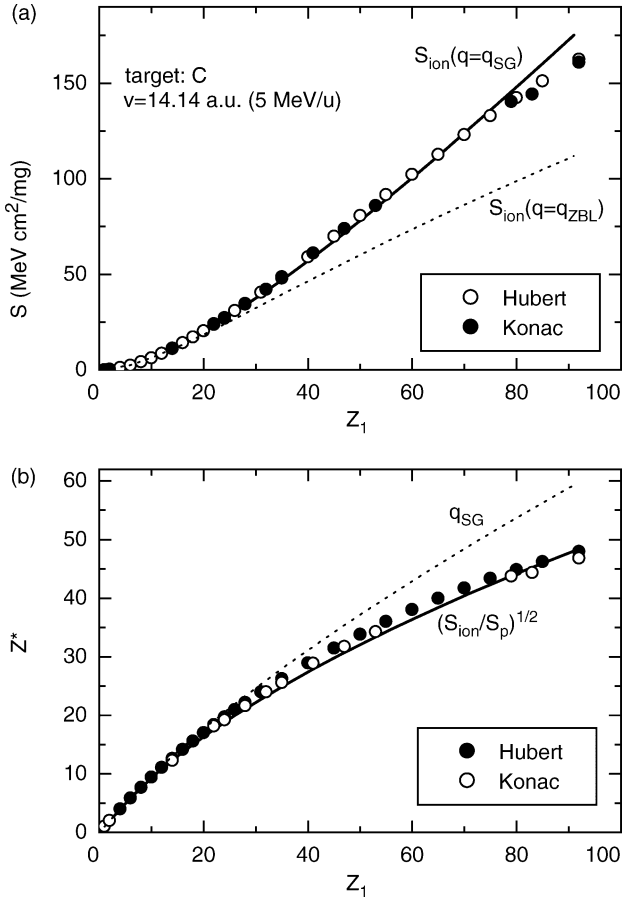

Fig. 8. (a) Calculations and empirical values [59,60] of carbon stopping powers for ions with atomic numbers $1 \leq Z_1 \leq 92$ and velocity $v = 14.14$ a.u. ($E/A = 5$ MeV/u). Solid line: calculations assuming $\bar{q} = q_{\mathrm{SG}}$; dotted line: calculations with $\bar{q} = q_{\mathrm{ZBL}}$. (b) The same results are plotted in the form of an equivalent effective charge, $Z^* = (S_{\mathrm{ion}}/S_{\mathrm{p}})^{1/2}$. The calculated results (with $\bar{q} = q_{\mathrm{SG}}$) are shown by the solid line. The input charge value, $\bar{q} = q_{\mathrm{SG}}$, is shown only for comparison.

The results of Fig. 8(a) show that the non-linear stopping power calculations are consistent with the first assumption, and in clear discrepancy with the second.

To show the relationship with the effective charge, we show in Fig. 8(b) the same results scaled with the proton stopping power at the same velocity, S_{p} (calculated with the same approach), in the form of equation (18). This yields a theoretical 'effective charge' $Z^* = [S_{\mathrm{ion}}(q = q_{\mathrm{SG}})/S_{\mathrm{p}}]^{1/2}$, shown

by the solid line, which compares very well with the empirical Z_{eff} values shown by symbols. The input charge value, $\bar{q} = q_{\text{SG}}$, is shown here only for comparison.

Another important test of the theory is provided by the well-known *scaling* property of the empirical effective charge, which makes it a very practical and widely used quantity. This scaling is obtained by representing the whole collection of experimental stopping power values, according to equation (18), versus the reduced velocity $v/Z_1^{2/3}$. When this is done, the universe of experimental points cluster around a narrow region which may be approximated by the fitting formula [9]

$$Z_{\text{eff}} = Z_1(1 - \exp(-0.92v/Z_1^{2/3})) \tag{19}$$

To test this property, we have condensed in Fig. 9 the results of numerous calculations using the present non-linear method [50], for ions with atomic numbers in the range $1 \leq Z_1 \leq 92$, and assuming always $\bar{q} \cong \bar{q}_{\text{exit}} \cong \bar{q}_{\text{SG}}$. In this figure the calculated results, in the form of an equivalent 'effective

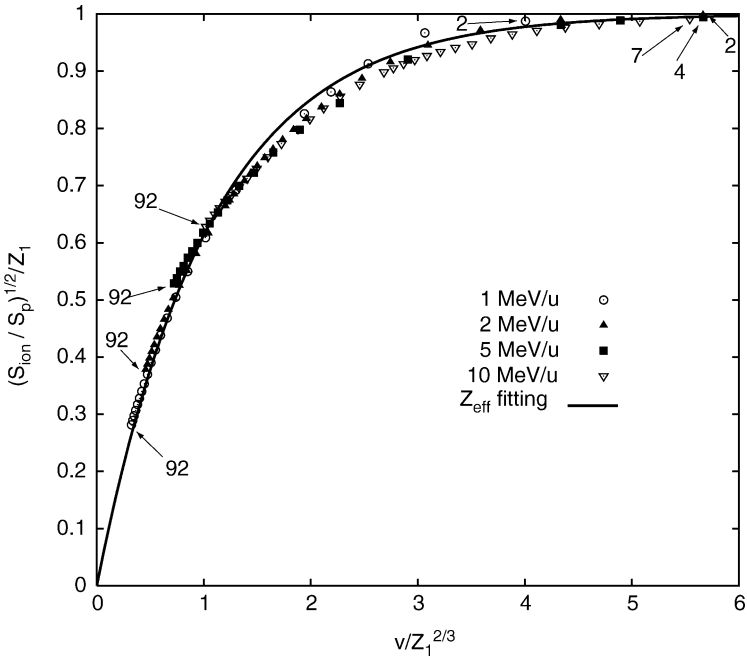

Fig. 9. General scaling of the 'effective charge' values $Z^* = [S_{\text{ion}}(v)/S_{\text{p}}(v)]^{1/2}$ obtained from the non-linear calculations for all the ions with $1 \leq Z_1 \leq 92$ in carbon targets, with energies $E/M = 1$, 2, 5, and 10 MeV/u, assuming $\bar{q} = q_{\text{SG}}$. Here the calculated values are shown by symbols, while the solid line shows the empirical fitting to Z_{eff} given by equation (19).

charge ratio', $[S_{ion}/S_p]^{1/2}$, are shown by symbols, whereas the line is the empirical fitting curve to Z_{eff} of equation (19), which represents all the existing experimental values for swift ions with velocities $v > 3$ a.u. (the fitting expression is accurate within 10%, according to Ref. [9]).

We find that the values for the different energies (ranging from 1 to 10 MeV/u) converge on a same strip, satisfying the scaling property, and being in excellent agreement of the empirical fitting curve. This agreement gives significant support to the non-linear method together with the assumption on the ion charge $\bar{q}$.

The striking discrepancy between the $\bar{q}$-values used in the present non-linear approach and the frequently used ZBL values (Fig. 7) may be explained as follows. The fitting expression for $\bar{q}$ given in Ref. [9] was obtained from a very extensive analysis of stopping power data performed within the framework of a linear approach [15]. But, as we have shown, the linear models overestimate the stopping of heavy ions. Hence, the lower $\bar{q}$-values obtained by this procedure compensate the excessive stopping of the linear approach.

In summary, the results shown here lead to two main conclusions concerning swift heavy ions: (a) the calculations show a clear relationship between the charge state of ions emerging from solids and the effective charge values determined from stopping power measurements, solving a seeming contradiction between these values; (b) the non-linear stopping analysis is consistent with the assumption of nearly equal values of the mean ion charges inside solids and those of emerging ions; this rules out the BG model which predicts large differences for swift heavy ions.

7.1. The relation between $\bar{q}$ and Z_{eff}

All the results shown in Figs. 8 and 9 pertain to the domain of swift highly ionized projectiles and correspond to the regime where $\bar{q} > Z_{eff}$. This is a rather unexpected result, since all the models based on perturbation, or linear, theory would indicate the opposite, namely, $Z_{eff} > \bar{q}$.

To understand the basic difference arising from the linear and non-linear models with respect to the deduced effective charge values, we have performed energy loss calculations for partially stripped ions with two models: (i) the linear DF model, and (ii) the present non-linear theory (NL). The linear calculations have been performed using equation (6) and using the DF obtained by Lindhard [13]. The electronic structure of the ions in both calculations was represented by the same Molière-ion function.

In Fig. 10 we show the calculations for two cases: N^{2+}, and Kr^{10+}, assuming conditions of frozen charge state (constant q values) for all velocities. The stopping values are shown in the form of 'effective charge fractions', $Z^* = [S_{ion}(v)/S_p(v)]^{1/2}$. The horizontal dotted line separates the ranges of $Z^* > q$ and $Z^* < q$.

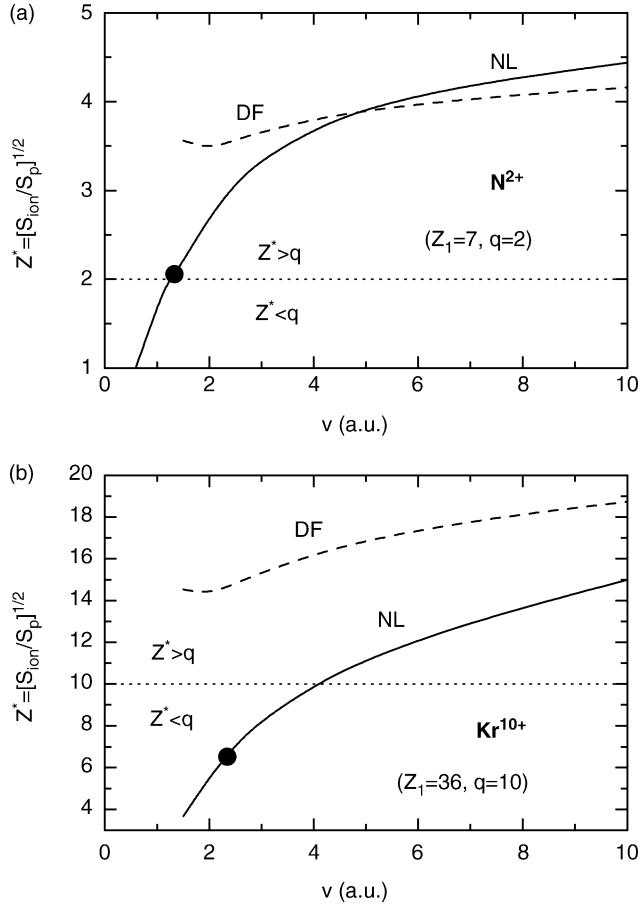

Fig. 10. 'Effective charge' values, $Z^* = [S_{\rm ion}(v)/S_{\rm p}(v)]^{1/2}$ for N^{2+} and Kr^{10+} ions in carbon targets, obtained from energy loss calculations using the dielectric function (DF) and the non-linear (NL) models described in the text. The dotted lines separate the regions where $Z^* > q$ and $Z^* < q$.

In the case of weakly ionized N^{2+} ions we observe that in most of the range the two methods yield values $Z^* > q$, although the NL line shows a crossing from the region $Z^* < q$ to $Z^* > q$, at a velocity $v_{\rm c} \sim 1.2$ a.u. However, for higher ionization (Kr^{10+}) the NL line shows a larger discrepancy with the DF result and the crossover (from $Z^* < q$ to $Z^* > q$) occurs at $v_{\rm c} \sim 4$ a.u., whereas the DF calculation yields always $Z^* > q$. The DF results may be explained in rather simple terms: the form factor $f(k)$ in equation (6) has values in the range between q and Z_1, corresponding

to the limiting cases of small and large k values (in a classical analogy, those electron whose trajectories approach the ion 'see' an effective charge in the range between q and Z_1). The stopping integral, equation (6), scales with the square of the form factor. Therefore, according to this picture, effective charge values always larger than the actual ion charge q are expected. This is for instance one well-known property of the Brandt–Kitagawa model [15].

The reason why this behavior is broken in the non-linear picture has to do again with the previously mentioned 'saturation' effect. When the ion charge becomes large (so that $q/v > 1$ a.u.) the non-linear stopping values cannot increase in the same proportion as the perturbative values. Therefore, the increase in the stopping ratio $S_{\rm ion}(v)/S_{\rm p}(v)$ cannot follow in the same way the increase of the ion charge. As a consequence, there is a relative decrease of this ratio with respect to the q value. We note, incidentally, that the crossings of the $Z^* = q$ line in the NL results in the figures occur for velocities such that $q/v \sim 2$.

As mentioned, these calculations have been made assuming frozen charge conditions, which is not always experimentally realizable. So, to obtain a more realistic picture, we also show in Fig. 10 by solid symbols the velocities at which (according to the $q_{\rm SG}$ formula) the respective ions would have an equilibrium charge value $\bar{q}$ equal to the one assumed in the calculations (2 and 10 in these examples). These points mark the realistic situations of experimental measurements in conditions of charge equilibrium. We find that in the case of N^{2+} the point is very close to the condition $Z^* = q$, while for the Kr^{10+} ion the experimental point lies in the range where $Z^* < q$ (the non-perturbative region). This analysis may be extended to all the calculations shown in the previous figures, and explain the reason for the results with $Z^* < q$ previously obtained.

In summary, the ranges where $Z^* < q$ are indicative of non-linear (saturation) effects, and include the cases of highly ionized ions shown here. But on the other hand, one may also have strong non-linear regions where instead $Z^* > q$ (like the Z_1-oscillations regime at low velocities). From a more detailed study of different cases we find that the range where perturbative models apply (showing the 'normal' behavior $Z^* > q$ [15]) is constrained to swift weakly ionized projectiles.

8. SUMMARY AND OUTLOOK

The present review has dealt with some recent developments, as well as some old questions, related to the energy loss of ions in solids. We have summarized the most relevant aspects of the process according to the standard Bohr–Bethe–Bloch picture, and have paid special attention to

those questions that cannot be accounted for by straightforward extensions of these models.

The non-linear formulation discussed here provides a new approach to the problem. The model considers the interaction process at a fundamental level, avoiding the usual perturbative expansions or semiclassical approximations. It is based on two main building blocks: the quantum transport cross-section method, and the use of self-consistent models to describe the ion screening by the electron gas.

The model describes the strong quantum effects that dominate the stopping of ions in the low-velocity range, and converges in a natural way to the semiclassical and perturbative models that apply at high energies.

The present method contains a free electron gas assumption, quite appropriate for metallic targets, but in practice may be extended to describe the excitation of valence electrons in most solid targets. These are the electrons that dominate the stopping at low energies, and also the ones that produce the strongest non-linearities. Hence, the model is particularly appropriate to take into account the main non-linear contributions. This was clearly illustrated in the case of carbon targets considered here. For heavier targets, the relevance of inner shell excitations becomes important at energies close to and above the stopping maximum. At these larger velocities other non-perturbative models for inner-shell ionization are available and could be combined readily with the present model of valence electron excitations. Further studies of this type would be useful.

In addition, there are still some aspects of the present approach that could deserve future consideration, and where various improvements could presumably be made. This may include a revision of the interaction potentials used for partially stripped ions, and perhaps the use of non-spherical potentials for the screening component.

The non-linear scheme described in this work is implemented in the computer program Histop (Heavy Ions Stopping), which is freely available from the web page indicated in Ref. [61].

The final question analyzed in this work was the application of the non-linear formulation to swift heavy ions, with the purpose of clarifying the connection between various quantities related to the ion charge values, namely, the equilibrium charge-state of ions moving inside solids, as compared to that of emerging ions, and the connection with the ‘effective charge’ parameter (actually, not a charge but a stopping ratio). The non-linear approach was found to be consistent with the predictions of the Bohr–Lindhard model, and in clear discrepancy with the alternative Betz–Grodzins model. In addition, the non-linear approach is in disagreement with other ion-charge parametrizations (like the ZBL one) which are generally used in the context of linearized representations of the stopping power.

ACKNOWLEDGEMENTS

Financial support from ANPCYT (PICT 0303579) is acknowledged. The authors are grateful to J. C. Eckardt and G. H. Lantschner for many useful comments.

REFERENCES

[1] N. Bohr, *Phil. Mag.*, 1913, **25**, 10; N. Bohr, *Phil. Mag.*, 1915, **30**, 581.
[2] N. Bohr, *Kgl. Danske Videnskab. Selskab., Mat.-Fys. Medd.*, 1948, **18/8**, 1.
[3] H. Bethe, *Ann. Phys. (Leipzig)*, 1930, **5**, 325.
[4] F. Bloch, *Ann. Phys. (Leipzig)*, 1933, **16**, 285.
[5] J. Lindhard and M. Scharff, *Phys. Rev.*, 1961, **124**, 128.
[6] O. B. Firsov, *Sov. Phys. JETP*, 1959, **9**, 1076.
[7] H.-D. Betz, *Rev. Mod. Phys.*, 1972, **44**, 465.
[8] B. S. Yarlagadda, J. E. Robinson and W. Brandt, *Phys. Rev. B*, 1978, **17**, 3473.
[9] J. Ziegler, J. P. Biersack and U. Littmark, *The Stopping and Range of Ions in Solids*, Pergamon Press, New York, 1985.
[10] J. H. Ormrod and H. E. Duckworth, *Can. J. Phys.*, 1963, **41**, 1424; J. H. Ormrod, J. R. Macdonald and H. E. Duckworth, *Can. J. Phys.*, 1965, **43**, 275.
[11] E. Fermi, *Phys. Rev.*, 1940, **57**, 485.
[12] D. Pines and D. Bohm, *Phys. Rev.*, 1952, **85**, 338; D. Pines, *Plasma Phys.*, 1961, **2**, 5.
[13] J. Lindhard, *K. Dan. Vidensk. Selsk. Mat. Fys. Medd.*, 1954, **28**, 8; J. Lindhard and A. Winther, *K. Dan. Vidensk. Selsk. Mat. Fys. Medd.*, 1964, **34**, 4.
[14] R. H. Ritchie, *Phys. Rev.*, 1959, **114**, 644.
[15] W. Brandt and M. Kitagawa, *Phys. Rev. B*, 1982, **25**, 5631.
[16] U. Fano, *Annu. Rev. Nucl. Sci.*, 1963, **13**, 1.
[17] M. Inokuti, *Rev. Mod. Phys.*, 1971, **43**, 297; M. Inokuti, Y. Itikawa and J. E. Turner, *Rev. Mod. Phys.*, 1978, **50**, 23.
[18] I. A. Akhiezer and L. N. Davydov, *Sov. Phys. Usp.*, 1979, **22**, 804.
[19] S. P. Ahlen, *Rev. Mod. Phys.*, 1980, **52**, 121.
[20] P. M. Echenique, F. Flores and R. H. Ritchie, *Solid State Phys.*, 1990, **43**, 229.
[21] P. Sigmund, *Phys. Rev. A*, 1982, **26**, 2497.
[22] J. R. Sabin and J. Oddershede, *Phys. Rev. A*, 1982, **26**, 3209.
[23] J. Oddershede and J. R. Sabin, *At. Data Nucl. Data Tables*, 1984, **31**, 275.
[24] D. E. Metzler, J. R. Sabin and S. B. Trickey, *Phys. Rev. A*, 1990, **41**, 220.
[25] P. Sigmund and U. Haagerup, *Phys. Rev. A*, 1986, **34**, 892; H. H. Mikkelsen and P. Sigmund, *Phys. Rev. A*, 1989, **40**, 101.
[26] P. Sigmund and A. Schinner, *Eur. Phys. J. D*, 2000, **12**, 425; P. Sigmund and A. Schinner, *Nucl. Instrum. Methods B*, 2002, **195**, 64.
[27] P. L. Grande and G. Schiwietz, *Phys. Rev. A*, 1991, **44**, 2984; P. L. Grande and G. Schiwietz, *Phys. Rev. A*, 1993, **47**, 1119; P. L. Grande and G. Schiwietz, *Nucl. Instrum. Methods B*, 2002, **195**, 55.
[28] G. Maynard, C. Deutsch, K. Dimitriou, K. Katsonis and M. Sarrazin, *Nucl. Instrum. Methods B*, 2002, **195**, 188.
[29] R. Cabrera Trujillo, J. R. Sabin, Y. Ohrn and E. Deumens, *Phys. Rev. A*, 2000, **61**, 032719; R. Cabrera Trujillo, J. R. Sabin, Y. Ohrn and E. Deumens, *Phys. Rev. A*, 2000, **62**, 052714.
[30] J. Briggs and A. Pathak, *J. Phys. C*, 1973, **6**, L153; J. Briggs and A. Pathak, *J. Phys. C*, 1974, **7**, 1929.

[31] P. M. Echenique, R. M. Nieminen and R. H. Ritchie, *Solid State Commun*, 1981, **37**, 779; P. M. Echenique, R. M. Nieminen, J. C. Ashley and R. H. Ritchie, *Phys. Rev. A*, 1986, **33**, 897.
[32] M. J. Puska and R. M. Nieminen, *Phys. Rev. B*, 1983, **27**, 6121.
[33] P. M. Echenique and M. E. Uranga, in *Interaction of Charged Particles with Solids and Surfaces* (eds A. Gras-Martí, H. M. Urbassek, N. R. Arista and F. Flores), NATO ASI Series, Plenum, New York, 1991, Vol. B271, p. 39.
[34] T. L. Ferrell and R. H. Ritchie, *Phys. Rev. B*, 1977, **16**, 115.
[35] B. Apagyi and I. Nagy, *J. Phys. C*, 1987, **20**, 1465; B. Apagyi and I. Nagy, *J. Phys. C*, 1998, **21**, 3845.
[36] A. F. Lifschitz and N. R. Arista, *Phys. Rev. A*, 1998, **57**, 200.
[37] A. F. Lifschitz and N. R. Arista, *Phys. Rev. A*, 1999, **58**, 2168.
[38] N. R. Arista and A. F. Lifschitz, *Phys. Rev. A*, 1999, **59**, 2719; N. R. Arista and A. F. Lifschitz, *Nucl. Instrum. Methods B*, 2002, **193**, 8.
[39] N. R. Arista, *Nucl. Instrum. Methods B*, 2002, **195**, 91, Note: the normalization constant *C* in the Molière ion functionis missing in equation (14) of this reference; this was corrected in the erratum: *Nucl. Instrum. Methods B*, 2003, **207**, 232.
[40] L. de Ferrariis and N. R. Arista, *Phys. Rev. A*, 1984, **29**, 2145.
[41] M. Abramowitz and I. A. Stegun, *Handbook of Mathematical Functions*, Dover, New York, 1970.
[42] I. Nagy and A. Bergara, *Nucl. Instrum. Methods*, 1996, **115**, 58.
[43] G. H. Dedkov, *Soviet Phys. Uspekhi*, 1995, **38** (8), 877.
[44] M. A. Kumakhov and F. F. Komarov, *Energy Loss and Ion Ranges in Solids*, Gordon & Breach, New York, 1981.
[45] A. Mann and W. Brandt, *Phys. Rev. B*, 1981, **24**, 4999.
[46] B. Fastrup, P. Hvelplund and C. A. Sautter, *Kgl. Danske Videnskab. Selskab., Mat.-Fys. Medd.*, 1966, **35**, 10; P. Hvelplund and B. Fastrup, *Phys. Rev.*, 1968, **165**, 408.
[47] W. N. Lennard, H. Geissel, D. P. Jackson and D. Phillips, *Nucl. Instrum. Methods B*, 1986, **13**, 127.
[48] J. S. Dolado, R. Diez Muiño and A. Arnau, *Nucl. Instrum. Methods B*, 1998, **146**, 101.
[49] G. Maynard, M. Chabot and D. Gards, *Nucl. Instrum. Methods B*, 2000, **164–165**, 139.
[50] A. F. Lifschitz and N. R. Arista, *Phys. Rev. A*, 2004, **69**, 012902.
[51] J. Neufeld, *Phys. Rev.*, 1954, **95**, 1128; J. Neufeld, *Phys. Rev.*, 1954, **96**, 1470.
[52] L. C. Northcliffe, *Ann. Rev. Nucl. Sci.*, 1963, **13**, 67.
[53] L. E. Porter, *Phys. Rev. B*, 1977, **16**, 1812.
[54] P. Sigmund and A. Schinner, *Nucl. Instrum. Methods B*, 2001, **174**, 535.
[55] V. S. Nikolaev and I. S. Dmitriev, *Soviet Phys. JETP*, 1965, **20** (2), 409; V. S. Nikolaev and I. S. Dmitriev, *Phys. Lett.*, 1968, **28A**, 277.
[56] G. Schiwietz and P. L. Grande, *Nucl. Instrum. Methods B*, 2001, **175–177**, 125.
[57] N. Bohr and J. Lindhard, *Kgl. Danske Videnskab. Selskab., Mat.-Fys. Medd.*, 1954, **28**, 7.
[58] H. D. Betz and L. Grodzins, *Phys. Rev. Lett.*, 1970, **25**, 903.
[59] F. Hubert, R. Bimbot and H. Gauvin, *At. Data Nucl. Data Tables*, 1990, **46**, 1.
[60] G. Konac, Ch. Klatt and S. Kalbitzer, *Nucl. Instrum. Methods*, 1998, **146**, 106.
[61] http://cabcat1.cnea.gov.ar/~colato/grupos/stop/index.html.

This Page Intentionally Left Blank

Molecular Dynamics Simulations of Energy Deposition in Solids

M. J. Caturla,[1] A. Gras Martí,[1] J. J. Jiménez-Rodríguez,[2]
J.-C. Jiménez Saez,[2] and M.-C. Pérez-Martín[2]

[1] *Dept. de Física Aplicada, Facultat de Ciencies, Universitat dAlacant, Apt. 99, E-03080 Alacant, Spain*
[2] *Dept. de Electricidad y Electrónica, Facultad de Ciencias Físicas, Universidad Complutense, E-28040, Madrid, Spain*

Abstract

Molecular dynamics (MD) simulations have been used since the early 1960s to study the interaction of energetic particles (up to 100s of keV) with solids for a large variety of applications. In this article we briefly describe the MD methodology for the particular case of atomic collisions in solids. As examples of systems and processes that can be studied using this technique we present three results, related to relevant industrial applications. First we describe how MD can be used to study defects produced during implantation of dopants in semiconductors, and how these results can be used to develop models for the semiconductor technology. Secondly we present an overview of radiation damage effects in metals relating them to the degradation of their mechanical properties. Finally, a recent field of research has emerged that promises important changes in the field of materials, the so-called nanotechnology. MD is particularly useful to describe the processes occurring at the atomic scale and therefore it is widely used to study effects at the nanoscale. We present an application of MD for the case of nanocluster interfaces. To conclude, a few remarks are made regarding the future of this technique to study collisions in solids.

Contents

ADVANCES IN QUANTUM CHEMISTRY, VOLUME 45
ISSN: 0065-3276 DOI 10.1016/S0065-3276(04)45004-7

1. INTRODUCTION

While Bohr said in the first paragraph of his 1948 paper that "The phenomenon of the scattering and stopping of high speed atomic particles in passing through matter and the accompanying ionization and radiation effects have […] been one of the most important sources of information regarding the constitution of atoms", we might add that the interaction of charged particles with matter has led to a much better understanding of the behavior of solids under irradiation. He was well aware that [loc. cit., cf. page 5]: "…many penetration phenomena depend essentially on the forces acting between the individual constituents of the atoms and may even be influenced by the interaction of neighboring atoms in the stopping material…" [1].

Starting from Bohr's seminal work in the period 1913–1948, and thanks to the contributions of the Danish School, particularly his disciple J. Lindhard, a few decades followed when analytic transport theory of atomic collisions in solids was thoroughly developed. However, from the early 1960s a new approach started to develop quickly in this field: computer simulations. Modern applications based upon the use of accelerated ions interacting with solids require simulation methods to investigate the complexity of the underlying phenomena, and to guide or analyze the experiments required to address the detailed questions that need to be answered.

By application of the MD technique one can directly calculate the contributions of collisional, thermal and chemical processes to the induced atomic relocations. It is important to state, however, that two basic assumptions of Bohr's work – the applicability of classical mechanics and the separation between elastic and inelastic losses in atomic collisions in solids – are still assumed in most present-day simulations.

Molecular dynamics (MD) simulations have been used to model the production of defects in an energy range where the binary collision approximation is no longer valid, since many-body interactions in the solid are expected [2]. These simulations started with the work of Vineyard *et al.* in the 1960s at Brookhaven [3] and have continued since, modeling radiation effects in metals [4–9], semiconductors [10,11] and ceramics [12,13]. The number of publications in this subject is very large and we will not attempt in this paper to make a review of all of them. We will, however, describe the methodology used in MD to study collisions in solids, and we will present three applications of these types of simulations related to the interaction of energetic particles with matter. We will show how MD can be used to

understand processes relevant to the semiconductor technology, and in particular to silicon doping. Studies of damage production in metals during irradiation, topic of the first simulations by Vineyard, will be reviewed, as well as how the presence of defects produced during irradiation induce degradation of the mechanical properties of the material. Finally, we will present results of MD simulations applied to nanotechnology, in particular to nanocluster interfaces.

2. MOLECULAR DYNAMICS SIMULATION METHODOLOGY

MD allows the study of the time evolution of an N-body system of interacting particles. The approach is based on a deterministic model of nature, and the behavior of a system can be computed if we know the initial conditions and the forces of interaction. For a detail description see Refs. [14,15]. One first constructs a model for the interaction of the particles in the system, then computes the trajectories of those particles and finally analyzes those trajectories to obtain observable quantities. A very simple method to implement, in principle, its foundations reside on a number of branches of physics: classical nonlinear dynamics, statistical mechanics, sampling theory, conservation principles, and solid state physics.

Newton's second law relates the motion of a particle to the force acting on it. If we have N molecules, then Newton's second law yields $3N$ second-order, ordinary differential equations. For an isolated system of particles with position vectors $\mathbf{r}_i$, and momentum $\mathbf{p}_i$ the total energy of the system (potential energy plus kinetic energy) will be conserved. The total energy of the system will take the form:

$$H(\mathbf{r}^N, \mathbf{p}^N) = \frac{1}{2m} \sum_i \mathbf{p}_i^2 + U(\mathbf{r}^N) = E \tag{1}$$

The potential energy U describes the molecular interactions. The equations of motion for N particles in an isolated system are then

$$\mathbf{F}_i = m\ddot{\mathbf{r}}_i = \frac{-\partial H}{\partial \mathbf{r}_i} = \frac{-\partial U}{\partial \mathbf{r}_i} \tag{2}$$

The goal of MD is to obtain the trajectories of a set of N molecules interacting through a potential function U by solving the above equations of motion. The key component in this technique is, therefore, the interatomic potential, since it defines the properties of our system.

2.1. Interatomic potentials

Let us briefly review some of the basic interatomic potential functions used in the literature. An interatomic potential $U(\mathbf{r}^N)$ can be approximated by a sum ranging from two-body to N-body contributions of the form

$$U(\mathbf{r}^N) = \sum_i u_1(\mathbf{r}_i) + \sum_{\substack{i,j \\ i<j}} u_2(\mathbf{r}_i, \mathbf{r}_j) + \sum_{\substack{i,j,k \\ i<j<k}} u_3(\mathbf{r}_i, \mathbf{r}_j, \mathbf{r}_k) + \cdots \tag{3}$$

where the first term represents external forces, and the rest are interactions among target constituents. The most important term in usual applications of MD is the second term: the pair potential, which depends only on the separation between two molecules, r_{ij}.

In 1924, Lennard-Jones [16] introduced a model for a soft-sphere pair potential of the form

$$u_2(r_{ij}) = k\varepsilon\left[\left(\frac{\sigma}{r_{ij}}\right)^n - \left(\frac{\sigma}{r_{ij}}\right)^m\right] \tag{4}$$

containing a short-range, repulsive force and a longer range attractive force. The short-range force prevents the system from collapsing and the long-range attractive interaction maintains the structure bonded. The usual parameter choices are $m = 6$ and $n = 12$.

This potential is a good representation of interactions occurring in noble gases and it has also been used for metals. For example in the case of copper the parameters are $\sigma = 2.3151$ Å and for $\varepsilon = 0.167$ eV. Figure 1 shows the potential energy in reduced units ($u^* = u/\varepsilon$ and $r^* = r/\sigma$) for a Lennard-Jones potential.

For the case of metals, an interatomic potential introduced by Daw and Baskes in 1984 [17] is still widely used with some success particularly for the case of fcc metals. This potential considers that a metallic bond occurs due to the immersion of an ion in a free electron gas. Under this assumption, the energy of N atoms is given by

$$U(r^N) = \sum_{\substack{i,j \\ i<j}} \phi(r_{ij}) + \sum_i F(\rho_i) \tag{5}$$

This so-called 'embedded atom potential' consists of two terms. The first term is a two-body potential that represents the repulsion between the ion and the rest of the ions in the system. The second term is a many-body function that represents the energy to embed an atom in the position i, where there is an electron density ρ_i that comes from the linear superposition of spherically averaged atomic electron densities.

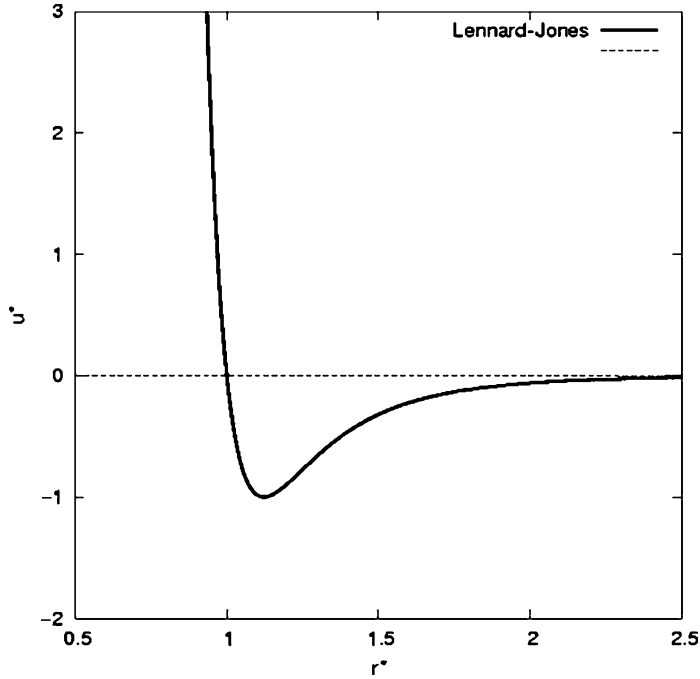

Fig. 1. Lennard-Jones interatomic potential in reduced units.

One of the advantages of this potential is that it is environmental dependent, since a change in coordination of an atom will result in a different electron density and therefore it will change the bond energy. The embedding function, the electron density and the pair potentials can be obtained either from *ab initio* calculations or from fitting to experimental properties, such as the atomic volume, the elastic constants or the ground state structure, using advanced many-body potentials [18, 19]. This formalism also allowed for the development of interatomic potentials for alloys [19].

When angular-dependent interactions contribute significantly to the bonding, pair potentials like those described above are not sufficient and three-body or higher order terms must be included in the potential energy. That is the case of covalently bonded systems like silicon or transition metals. For the case of silicon two interatomic potentials are widely used: the one developed by Stillinger and Weber [20] and the one developed by Tersoff [21]. Other empirical potentials have been developed to include the angular dependence such as the modified embedded atom method (MEAM) [22].

Despite the limitations of empirical potentials, for the last three decades computer simulations have improved the knowledge on physical properties of metals and alloys. In particular, due to the development of empirical interatomic potentials [18,19], it has become possible to describe by the MD technique a great number of solid properties such as recrystallization, structural relaxation, energetic barriers and mixing [23]. The EAM developed by Foiles *et al.* [18] has successfully described bulk properties of metal and alloys and some surface relaxation and reconstruction features [17,18,24,25], and the empirical potential developed by Ackland and Vitek has been applied successfully to investigate the structure of the noble metal alloys [19] and the deposition of Cu clusters on Au (111) [26] and of Cu and Au clusters on Cu (001) surfaces [27].

2.2. Integration algorithms, boundary conditions and neighbor lists

As mentioned above, the goal of MD is to compute the phase-space trajectories of a set of molecules. We shall just say a few words about numerical technicalities in MD simulations. One of the standard forms to solve these ordinary differential equations is by means of a finite difference approach and one typically uses a predictor–corrector algorithm of fourth order. The time step for integration must be below the vibrational frequency of the atoms, and therefore it is typically of the order of femtoseconds (fs). Consequently the simulation times achieved with MD are of the order of nanoseconds (ns). Processes related to collisions in solids are only of the order of a few picoseconds, and therefore ideal to be studied using this technique.

The boundary conditions are of importance in MD simulations. Even with the most powerful computers only a relatively small number of molecules can be followed, and those molecules on the surface of the simulation cell will experience forces which are very different from the ones in the bulk. If we are considering a short-range interatomic potential, i.e., if we define a cut-off radius such that for distances further apart than a given cut-off the interaction between particles is zero, we can make use of periodic boundary conditions to compute the interaction between the particles of the principal simulation box and all the surrounding images. We then model an infinite system and avoid the problem of surfaces. If the interatomic potential is not short-ranged then this approximation cannot be used unless the total contribution of all the images is included. Such is the case of Coulombic interatomic potentials. Periodicity, however, can be a problem for modeling amorphous systems. Moreover, with periodic boundary conditions the occurrence of long wavelength fluctuations is inhibited, as no density wave with a wavelength larger than the box length will exist, which could have an effect on some dynamic properties [15]. Although periodic boundary conditions seem to have very little effect on the equilibrium thermodynamics

properties of solids it is important to check their influence by changing the system size.

Another technical issue in MD simulations is neighbor lists. To compute the forces over a set of N atoms we have to loop over the j neighbors of each particle i for all N particles, considering a short-range potential. If the distance between those two particles is smaller than the cut-off of the interatomic potential then we go to the next atom. This implies a total of N^2 calculations. There are several methods to reduce the number of calculations, one of the most popular being the Verlet neighbor list [14]. Another method commonly used in MD considers linked cells that reduce significantly the number of computations, from N^2 to $27NN_c$ where N_c is the number of atoms in the cell [28,29].

We should mention one feature that makes MD simulations particularly efficient. That is the calculations can be distributed among many processors working in parallel, achieving good scalability with the number of processors used. Many parallel MD codes have been implemented and simulations with up to one billion atoms have been possible using the most powerful supercomputers [30]. This feature allows for an increase in the number of atoms, or the simulation size. However, parallelization does not help with the maximum simulation time that can be achieved using MD. This time is still of the order of nanoseconds. There are, however, active computational groups implementing new algorithms to overcome this limitation [31].

2.3. Modeling energetic collisions with molecular dynamics

The standard MD methodology described in the sections above has to be modified to simulate the collisions of energetic atoms in a solid. In particular, the interatomic potentials mentioned above must often be adjusted to describe the interactions at the shortest range, or high energies. The standard procedure consists of a fit between the pair part of the interatomic potential considered and the Universal potential [32]. The Universal potential obtained by Ziegler *et al.* [33] gives a more accurate description of the interaction between atoms at short distances. However, there is no clear cut-off for the validity range of one potential *versus* the other. Quite arbitrarily, this range is chosen between a few eV for the potential function. The two functions are fitted, with the constrains that both the potential and the first derivative of the potential are smooth functions.

On the other hand, and as already mentioned in Section 1, modeling of atomic collisions using MD is based on Bohr's assumption of a partition between elastic and inelastic energy loss. Most of the simulations of energetic particles in solids using MD do not include an energy loss due to inelastic collisions since the energies are usually low (a few keV) and the contribution of inelastic collisions is assumed to be negligible. However, in a few cases the inelastic energy loss has been included through a friction force

using the Lindhard model of stopping [34]. This is particularly significant when modeling collisions of light projectiles. For example, for boron in silicon, the maximum nuclear stopping occurs at an energy of only 3 keV, while for As it happens at approximately 70 keV [11].

Due to the size constrains of the simulations special boundary conditions are used in many cases to dissipate the energy produced by the high-energy particle. The method employed in most of the simulations is a thermal bath at the boundary of the simulation box. This thermal bath is forced to keep a constant temperature, and several techniques can be used for such purpose, for example, rescaling the velocities of those atoms in the thermal bath, or applying Langevin dynamics to those atoms at the boundary.

Finally, a topic of controversy on the simulation methodology of collision cascades is the dissipation of the deposited energy through electron conduction. In fact, most of the simulations of high-energy particles with MD neglect this aspect. However, several attempts have been made to include the electronic heat conduction in MD simulations [35–37], revealing significant differences when this term is included. The expected effect of this process is a faster cooling rate of the cascade and therefore a lower number of residual defects for the case of systems with strong electron–phonon coupling.

3. APPLICATIONS OF MOLECULAR DYNAMICS TO IRRADIATION EFFECTS IN MATERIALS

With a view to presenting the state of the art and the capabilities of MD of atomic collisions in solids, we shall briefly discuss some examples. The emphasis will be on theoretical aspects of the simulations, rather that on their relation to experimental results.

3.1. Semiconductor technology: shallow boron dopant on silicon

The continuous shrinking of the electronic technology demands a detailed understanding of the microscopic mechanisms that undoubtedly affect the design and performance of the new devices. Particularly, the study of damage induced by ion implantation is of major relevance to silicon technology. Shallow boron profiles are needed, which implies lower energy and higher doses, to form pn junctions. Besides, these profiles are strongly affected by structural defects. A recommendation of The Technology Road-Map for Semiconductor is the developing of improved models for damage formation. Reliable pictures of the microscopic mechanisms governing dopant diffusion properties can only be provided by atomistic simulations.

The process of semiconductor doping consists normally of two steps: implantation of the dopant and annealing, to eliminate those defects created

during the implantation and activate the dopant. The energy of the implanted dopant, and the annealing time and temperature control the final dopant concentration depth profile. Different models have been proposed to study the configuration, distribution and diffusion of defects in implanted samples [38,39]. The energetic of point and complex defects and also their diffusion barriers have been studied by first-principles simulations [40,41], the distribution of these defects following the implantation is known by MD simulations [42–44], whereas annealing requires kinetic Monte Carlo models [40,45,46].

The enhanced diffusivity of boron observed after implantation and annealing, also known as transient enhanced diffusion (TED) has been demonstrated to be controlled by those point defects produced during the implantation. Knowledge of the types of point defects is desirable since they have different behavior relating to complex defect diffusion and creation, which finally affects the performance of the device. The aim of modeling is the characterization of the boron implant (range and channeling), as well as the identification of the configuration of the implanted species and surroundings (substitutional and interstitial).

Low-energy boron bombardment of silicon has been simulated at room temperature by MD. Tersoff potential *T*3 was used in the simulation and smoothly linked up with the universal potential. The boron–silicon interaction was simulated according to Tersoff potential for SiC but modified to account for the B–Si interaction. Silicon crystal (Si-c) in the (001) direction, with (2×1) surface reconstruction, was bombarded with boron at 200 and 500 eV. Reasonably good statistics are obtained with 1000 impact points uniformly distributed over a representative surface area. The simulation size was $16 \times 16 \times 14$ unit cells. Periodic boundary conditions were applied laterally. The temperature was kept at 300 K with a thermal bath applied to the more external cells in the crystal except the top surface. In these conditions the crystal was relaxed during 19 ps. In order to avoid direct channeling, the incidence was inclined 7° out of the normal, as usual in experiments, with random azimuthal direction.

One of the key issues in a MD simulation is extracting relevant information from the large amount of data obtained, since the outcome of these simulations is the space trajectory of all the particles considered. Therefore, we must develop methodologies to identify, in this particular case, those defects produced by the implantation of boron. We have to determine which atoms remain in perfect lattice sites and those that are displaced from ideal locations. Figure 2 shows the distribution of atoms as a function of the distance to a perfect lattice site after irradiation. Three regions may be distinguished in this case. Atoms closer than 0.7 Å to a perfect lattice site are considered occupying that site; consequently none of them are defects. For such distances, the lattice points are considered to be occupied by either the atom that initially was at such

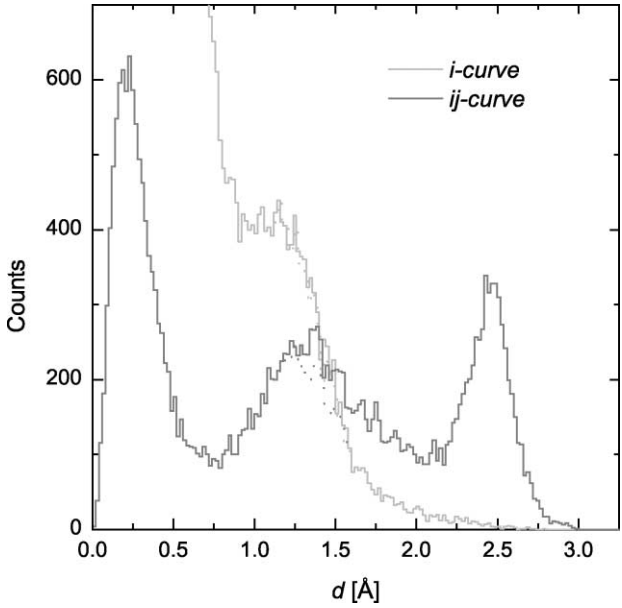

Fig. 2. Distributions of the nearest neighbors to a lattice point as a function of the distance to such a point.

a site and that has suffered a very short displacement (*i*-curve), or by another atom coming from another site which lies close to a previously emptied lattice point (*ij*-curve). In both cases, these short separations from the perfect lattice are due to relatively low damaged environment and/or thermal vibrations, driving to a maximum in the distribution around 0.3 Å (not shown in the *i*-curve). Besides quantifying the total number of defects produced by the irradiation, it is also possible, using MD to characterize the geometry of those defects produced, depending on the environment of the defect. One may identify the interstitials as one of the known self-interstitial configurations: tetrahedral or T-type interstitial, Si^T, Hexagonal or H-type, Si^H, and ⟨110⟩ or ⟨100⟩ Dumbbells, Si^D.

When we have a system with more than one species, as in the case of boron implantation in silicon, it is also important to identify the final location of the implanted atom, critical in this particular example, since the activation of the dopant will depend on this configuration. The different possibilities for a stable configuration of boron in a silicon lattice, together with their occurrence probability are shown in Table 1. It must be emphasized with high probability that a boron atom has to occupy a substitutional site, called B^S.

Table 1. Relative frequency of boron final configuration(s)

Energy (eV)	Reflected (sputtered) (%)	Substitutional (%)	Interstitial(s) (%)	Ad-atom(s) (%)
200	9.6	66.6	21.2	2.6
500	5.4	67.2	27.1	0.3

The unique two H-type interstitials found were for boron atoms. A more complex structure composed by a silicon T-type interstitial and a substitutional boron, $B^S + Si^T$, has been identified. It is depicted in Fig. 3 and it corresponds to the lower energy configuration. This result is corroborated by other authors in the literature [41,47].

3.2. Radiation damage effects in metals

As mentioned above, Vineyard's group at Brokhaven was the first one to use computer simulations for radiation damage studies [3]. Their simulations showed that Frenkel pairs are produced in metals as a result of replacement collision sequences (RCS), where one atom replaces its neighbor in a chain of events that results in a separation of a few atomic distances between the vacant site and the interstitial atom.

The development of powerful computers a few years after these pioneer calculations resulted in a more detailed picture of the processes occurring in a collision cascade [48]. These simulations showed that there are two main stages in the process of transferring energy from the energetic atom to the lattice. In the first stage, called the ballistic or collisional phase, the energy is

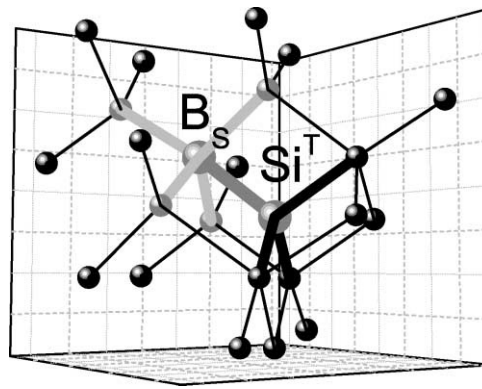

Fig. 3. Configurations of implanted boron atoms in silicon Complex $B^S + Si^T$.

transferred to several atoms in the lattice and a highly disordered region is created. This stage lasts of the order of one picosecond (ps). It is during this stage when most of the atomic mixing occurs. The number of atoms displaced at this point is higher than the values obtained using a binary collision approximation model. The second stage consists of the cooling or thermal spike regime, where most of the atoms return to perfect lattice sites and only a few defects are left behind. This stage lasts of the order of tens of ps. The number of displaced atoms after the cooling phase is smaller than the number predicted by the modified Kinchin-Pease model, or NRT model [49]. As an example, we present in Fig. 4 the evolution of a collision cascade in Cu produced by a 20 keV Cu atom and for different times. The light spheres represent the location of interstitial atoms while dark ones represent the location of vacancies. This picture clearly shows the large displacement of atoms during the first stage of the collision cascade and the recrystallization produced during the thermal spike, resulting in a few vacancies and interstitials.

After the system has gone back to equilibrium, defects are left in the lattice. One of the great advantages of MD simulations is the possibility of studying the size, shape and distributions of the defects produced by these collision events. In metals, it has been found that most of the vacancies remain in the center of the collision cascade, while the interstitials are in the periphery. Moreover, important differences are observed among different metals, although the origin of these differences are not clearly identified or explained yet. Figure 4 shows the final defects produced in our 20 keV Cu in Cu example. In this particular case the total number of defects produced is 65 (32% efficiency with respect to the NRT model, considering a threshold displacement energy for Cu of 40 eV). From these 12% of the vacancies and only 10% of the interstitials are isolated, while the rest of the defects are forming clusters. The largest vacancy cluster size is 50 vacancies, while the largest interstitial size is 21 interstitials. Although this is the result

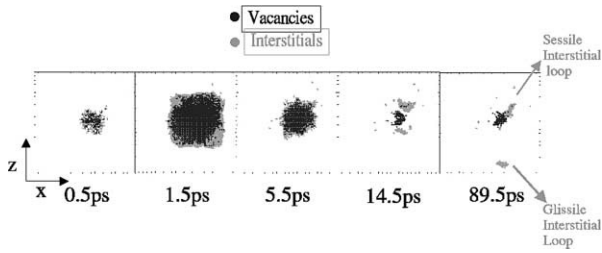

Fig. 4. Evolution of a cascade produced by a 20 keV energetic Cu atom in Cu at 300 K for different times. Light circles are the location of self-interstitials while dark ones are vacancy sites.

of a single event, qualitatively all cascades in Cu at these energies present the same features, with a high number of vacancies and interstitials in clusters.

Other metals, such as W, do not present this tendency of the vacancies to cluster, and at the end of the collisional cascade most of the vacancies are isolated. Such observation can be clearly seen in Fig. 5 where we present the result of those defects produced in W by a 30 keV W atom. This lack of vacancy clustering is observed for energies as high as 100 keV, where already sub-cascade formation occurs. The level of clustering in a system has been attributed to the rate of recrystallization during the thermal spike [50]. However, an exhaustive study for fcc and bcc systems regarding this issue has not been done to date.

The interaction of these defects produced during irradiation with impurities, dislocations, grain boundaries and other microstructural features, can alter significantly the mechanical properties of the material [51]. For example, metals exposed to irradiation can undergo a volume change [52], and this phenomena is attributed to the interaction between defects (vacancies) with impurities such as He, creating voids and bubbles, together with the diffusion of interstitials to sinks (such as surfaces, grain boundaries or dislocations) and inducing void swelling [53,54]. Other important effect of the interaction of defects produced during irradiation with the microstructure is the loss of ductility of metals, known as irradiation hardening and irradiation-induced embrittlement [51,55]. This phenomenon has traditionally been associated to the defects produced during irradiation acting as barrier for dislocations motion. Understanding these fundamental processes is of great importance to the development of models of metals under irradiation.

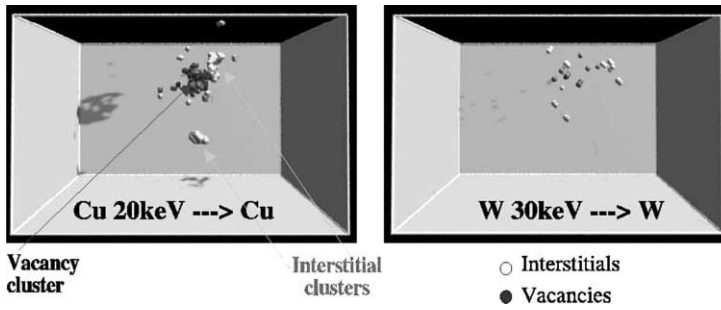

Fig. 5. Vacancies (dark circles) and self-interstitials (light circles) produced by irradiation in Cu by a 20 keV Cu atom and W by a 30 keV W atom. Notice the lack of clustering in the W case.

3.3. Molecular dynamics applied to nanotechnology: metallic nanocluster interfaces

A final example of the capabilities of MD simulations is given in this section. Nanotechnology is a fast growing research area that requires powerful models to explain the new regimes that appear when system sizes are reduced to nanometers. In this respect MD is one of such powerful techniques. We examine in this example how MD can be applied to study nanocluster interfaces.

One may study the misfit of metallic nanocluster interfaces. For example, atomic distances and deformations in two metallic interfaces, Au/Cu (001) and Ni/Cu (001) have been analyzed. We study the behavior of the atomic distances at the interface of two crystals with a considerable difference between their lattice parameters like Au and Cu (12.8%) and with a small difference like Ni and Cu (2.6%). In both the cases, the growing thin film–substrate interface is strained, and the relaxation of the different structures on an atomic scale is followed. In Ni/Cu, the fcc lattice becomes tetragonal (fct) at the interface as a result of the structural matching. This effect gives rise to interesting magnetic properties, such as the perpendicular magnetic anisotropy (PMA). In Cu/Au, only the pseudomorphic growth is possible when the system is a Cu cluster on top of an Au substrate. In the opposite case, Au on Cu, the system relaxes generating a network of dislocations.

The correct characterization of the structural matching at a metal-on-metal interface is an area of great interest for material science due to a great variety of technological applications. One needs a better understanding of the correlation between the size of the grown overlayer and the formation of defects.

3.3.1. Relaxation process in Ni/Cu systems

Figure 6 shows the relaxation undergone by a two Ni monolayer system of (10×10) surface size with AA interface (AA means that the Ni atoms are initially on top of Cu atoms in the surface). The stress field due to the misfit

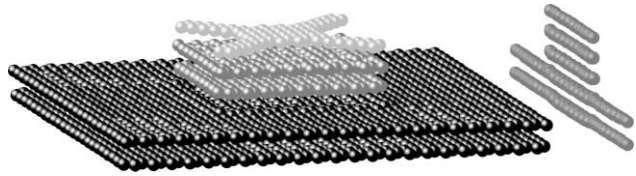

Fig. 6. Structural relaxation of a $(10 \times 10 \times 1)$ Ni crystal (2 ML) on top of a $(23 \times 23 \times 12)$ Cu substrate with AA interface. Adatoms begin the formation of the adlayer along the $\langle 110 \rangle$ directions at the surface. Besides the 3D image, the *yz*-projection is also shown. Only the two upper Cu monolayers are shown.

generated in the central region of the interface extracts atoms equally from the two Ni monolayers and locates them at the surface forming an adlayer. This lack of atoms helps to structural relaxation of the interface and to the consequent adaptation of the in-plane lattice parameters of both the structures. It can be observed in Fig. 6 that Ni atoms form this adlayer locating along the ⟨110⟩ directions at the surface. Identical process has been observed for the case of 1 ML with AA interface. These two simulations clearly show the tendency of the Ni(001) crystals to form adlayers along ⟨110⟩ directions. This directionality also appears in magnetic phenomena. In fact, the directions of the easy magnetization axes in Ni are along the ⟨110⟩ directions. This anisotropic arrangement of Ni has also been experimentally observed in other structures such as Au/Ni(110) [56]. Related to the flux of atoms towards the surface are the periodic ejections in Ni(111) of ⟨110⟩ Ni

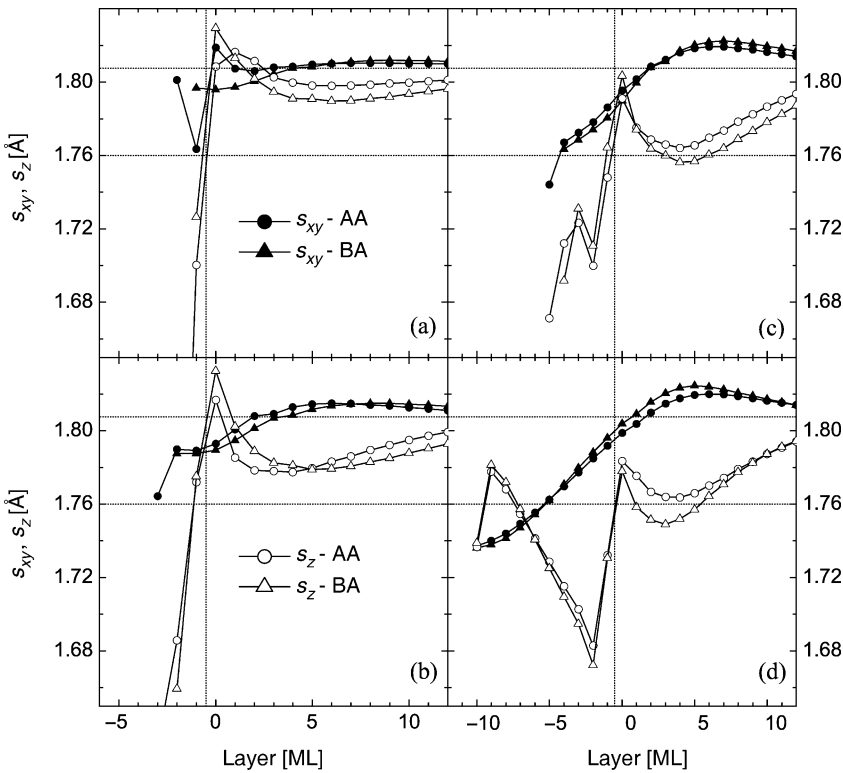

Fig. 7. (200) spacing, s_{xy}, (solid symbols) and (002) spacing, s_z, (open symbols) as a function of the number of the layer ((002) plane) for AA (atoms in the two surfaces overlapping) and BA (nonoverlapping of atoms in the surfaces) interfaces. The relaxed systems are Ni crystals of (10 × 10) surface size and (a) 1, (b) 2, (c) 4 and (d) 10 ML on top of a (23 × 23 × 12) Cu substrate.

surface rows to relieve the stress due to the excess density induced by the absorption of sulfur atoms [57].

We are interested in quantifying the degree of matching of the atomic distances at the interface. We calculate the spacings between (002) and (200) planes, latter equivalent to (020) due to the symmetry, as a function of the layer ((002) plane) for different systems. Figure 7 shows these distances as a function of the layer ((002) plane). Ni layers are set on the left (negative values) and Cu layers on the right (positive values including zero). The vertical line at -0.5 represents the end of a material and the beginning of the other. We describe the distance between planes (200) perpendicular to the interface as s_{yz} and those parallel to the interface as s_z. Initially, both s_{xy} and s_z magnitudes have the same value of 1.76 Å in the Ni crystal and of 1.81 Å in the Cu crystal (horizontal lines) except $s_z(-1)$ that takes the value of 2.16 Å corresponding to the initial separation between the Cu and Ni crystals. Far from the interface, s_{xy} and s_z tend toward their ideal values (bulk values) due to the boundary conditions. However, closer to the interface important deviations can be observed: normal planes increase their separation (always relative to the ideal value) while parallel planes come closer. One may similarly discuss their behavior in the Ni crystal.

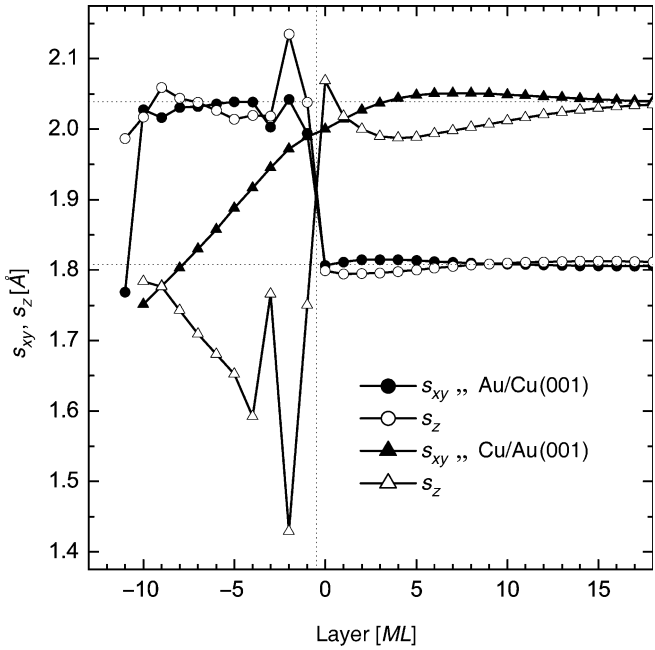

Fig. 8. s_{xy} (solid symbols) and s_z (open symbols) spacings in two $(10 \times 10 \times 5)/(38 \times 38 \times 12)$ systems built initially with gradual interface. One of them is an Au/Cu (001) interface and the other is a Cu/Au (001) interface.

3.3.2. Atomic distances in Au/Cu systems

Figure 8 shows the s_{xy} and s_z spacings for the Au/Cu (001) system with initial gradual interface. Cluster layers are set on the left (negative values) and substrate layers on the right (positive values including zero). The vertical line, set at 0.5, represents the end of a material and the beginning of the other. Initially, both magnitudes, s_{xy} and s_z, have the same value of 2.04 Å in the Au crystal and 1.81 Å in the Cu crystal, except $s_z(-1)$ whose value is 2.16 Å corresponding to the separation between the Au and Cu crystals. These ideal values are depicted in Fig. 8 by horizontal dotted lines as a reference. The graph shows that there is a discontinuity in both magnitudes at the interface. Therefore, the relaxation of a system initially with a gradual change in the s_{xy} and s_z magnitudes gives rise to a system with a steep variation of both magnitudes at the interface. The main conclusion is that in the Au/Cu (001) system it is corroborated that there is no quantitative adaptation of the atomic distances at the interface and therefore, nonmatching takes place. Simulations with clusters of lower number of monolayers also confirm this result.

4. CONCLUSIONS

The deposition of energy in a solid at the lowest energy levels (a few keV) can be studied using MD. Simulations of atoms with energies up to 100 keV have been possible with the use of powerful supercomputers and with several million atoms in the simulation box. These computer simulations reveal effects in the energy deposition that cannot be captured by other models such as the binary collision approximation, due to the presence of multiple collisions at the lowest energies. For example, coherent displacements of atoms during ion irradiation have been observed using MD [58]. Moreover, MD can determine the type, size and distribution of those defects created by the irradiation, since it tracks the location of all the atoms in the particular simulation box.

However, MD can only reach, even with the most powerful supercomputers, systems sizes of millions of atoms, and therefore cannot model efficiently those processes with energies higher than a few keV. Moreover, these higher energy regimes are well described within a binary collision model, and more efficiently. There have been some attempts to connect within a single simulation code Monte Carlo models using the binary collision approximation and MD; however, its efficiency is expected to remain low due to the computational demands of MD. An approach used more systematically has been to obtain a database of cascades in different materials and use those as input data for other simulations, such as modeling defect diffusion [59,60]. This same database can also be used to calculate the

total number of defects produced by high-energy particles (photons, electrons, protons, neutrons, etc.). In this particular case the initial distribution of energetic particles in the target produced by such projectiles must be obtained from other models used in high-energy physics like FLUKA, MCNP, SPECTER and others [61–63]. Such approach has been used to study the effect of neutron irradiation in different metals [7,9], proton irradiation in Cu and W [64] and others.

As mentioned above, the processes simulated using MD always make use of the approximation of Bohr where there is a division between elastic and inelastic collisions. Interestingly there are not many studies devoted to those regimes where these two energies compete and simulations including inelastic energy losses have also been very limited. We foresee an increasing number of studies in this area as the computer power increases and higher energies can be approached with this simulation method.

REFERENCES

[1] N. Bohr, The penetration of atomic particles through matter, Mat-Fys, 1948.
[2] R. S. Averback and M. Ghaly, *Nucl. Instrum. Meth. B*, 1997, **127/128**, 1.
[3] J. M. Gibson, A. N. Goland, M. Mulgram and G. H. Vineyard, *Phys. Rev.*, 1960, **120**, 1229.
[4] J. R. Beeler, Jr., *Radiation Effects Computer Experiments*, North-Holland, Amsterdam, 1983.
[5] T. Diaz de la Rubia and M. W. Guinan, *Phys. Rev. Lett.*, 1991, **66**, 2766.
[6] D. J. Bacon and T. Diaz de la Rubia, *J. Nucl. Mater.*, 1994, **216**, 275.
[7] R. Stoller, G. R. Odette and B. D. Wirth, *J. Nucl. Mater.*, 1997, **251**, 49.
[8] K. Nordlund, M. Ghaly, R. S. Averback, M. J. Caturla, T. Diaz de la Rubia and J. Tarus, *Phys. Rev. B*, 1998, **57**, 7556.
[9] N. Soneda and T. Diaz de la Rubia, *Phil. Mag. A*, 1998, **78**, 995.
[10] T. Diaz de la Rubia and G. H. Gilmer, *Phys. Rev. Lett.*, 1995, **74**, 2507.
[11] M. J. Caturla, T. Diaz de la Rubia and G. H. Gilmer, *Phys. Rev. B*, 1996, **54**, 16683.
[12] F. Gao and W. J. Weber, *Phys. Rev. B*, 2000, **63**, 54101.
[13] A. Kubota, M.-J. Caturla, J. Stolken, B. Sadigh, S. Reyes, T. Diaz de la Rubia and J. F. Latkowski, *Nucl. Instrum. Meth. B*, 2003, **202**, 88.
[14] M. P. Allen and D. J. Tildesley, *Computer Simulation of Liquids*, Oxford Science Publications, Oxford, 1986.
[15] J. M. Haile, *Molecular Dynamics Simulation. Elementary Methods*. Wiley Professional Paperback Series, 1997.
[16] J. E. Lennard-Jones, *Proc. R. Soc. London A*, 1924, **106**, 441.
[17] M. S. Daw, *Surf. Sci.*, 1986, **166**, L161; S. M. Foiles, *Surf. Sci.*, 1987, **191**, L779.
[18] S. M. Foiles, M. I. Baskes and M. S. Daw, *Phys. Rev. B*, 1986, **33**, 7983.
[19] G. J. Ackland and V. Vitek, *Phys. Rev. B*, 1990, **41**, 10324.
[20] F. H. Stillinger and T. A. Weber, *Phys. Rev. B*, 1985, **31**, 5262.
[21] J. Tersoff, *Phys Rev. B*, 1989, **39**, 5566.
[22] M. I. Baskes, *Phys. Rev. Lett.*, 1987, **59**, 2666.
[23] J. Dominguez-Vazquez, E. P. Andribet, A. M. C. Perez-Martin and J. J. Jimenez-Rodriguez, *Radiation Effects Defects Solids*, 1997, **142**, 115.
[24] F. Ercolessi, E. Tosatti and M. Parrinello, *Phys. Rev. Lett.*, 1986, **57**, 719.

[25] B. W. Dodson, *Phys. Rev. B*, 1986, **35**, 880.
[26] H. L. Lei, Q. Hou and M. Hou, *J. Phys. Condens. Matter*, 2000, **12**, 8387.
[27] Y. Xu, Z. Y. Pan and Y. X. Wang, *Modern Phys. Lett. B*, 2001, **15**, 455.
[28] B. Quentrec and C. Brot, *J. Comput. Phys.*, 1975, **13**, 430.
[29] R. W. Hockney and J. W. Eastwood, *Computer Simulation Using Particles*, McGraw-Hill, New York, 1981.
[30] F. Abraham, *Philos. Trans. R. Soc. London, Ser. A, Math. Phys. Engng Sci.*, 2002, **360**, 367.
[31] A. E. Voter and M. R. Sorensen, *Materials Research Society Symposium Proceedings Series Multiscale Modelling of Materials Symposium*, 1999, 427.
[32] K. Gärtner, D. Stock, B. Weber, G. Betz, M. Hautala, G. Hobler, M. Hou, S. Sarite, W. Eckstein, J. J. Jiménez-Rodríguez, A. M. C. Pérez-Matín, E. P. Andribet, V. Konoplev, A. Gras-Marí, M. Posselt, M. H. Shapiro, T. A. Tombrello, M. H. Urbassek, H. Hensenl, Y. Yamamura and W. Takeuchi, *Nucl. Instrum. Meth. B*, 1995, **102**, 183.
[33] J. F. Ziegler, J. P. Biersack and U. Littmark (ed. J. F. Ziegler), *The Stopping and Range of Ions in Solids*, Pergamon Press, New York, 1985, Vol. 1, p. 85.
[34] J. Lindhard and M. Scharff, *Phys. Rev.*, 1961, **124**, 128.
[35] C. P. Flynn and R. S. Averback, *Phys. Rev. B*, 1988, **38**, 7118.
[36] M. W. Finnis, P. Agnew and A. J. E. Foreman, *Phys. Rev. B*, 1991, **44**, 567.
[37] A. Caro and M. Victoria, *Phys. Rev. A*, 1989, **40**, 2287.
[38] A. La Magna, P. Alippi, L. Colombo and M. Strobel, *Comput. Mater. Sci.*, 2003, **27**, 10.
[39] G. Hobler and G. Otto, *Mater. Sci. Semicond. Process*, 2003, **6**, 1.
[40] B. Sadigh, T. J. Lenosky, S. K. Theiss and M.-J. Caturla, *Phys. Rev. Lett.*, 1999, **83**, 4341.
[41] M. Hakala, M. J. Puska and R. M. Nieminen, *Phys. Rev. B*, 2000, **61**, 8155.
[42] A. M. C. Prez-Martn, J. Domnguez-Vzquez and J. J. Jimnez-Rodrguez, *Nucl. Instr. Meth. B*, 2000, **164/165**, 431.
[43] G. Otto, G. Hobler and K. Gärtner, *Nucl. Instrum. Meth. B*, 2003, **202**, 114.
[44] T. Aoki, J. Matsuo, G. Takaota, N. Toyoda and I. Yamada, *Nucl. Instrum. Meth. B*, 2003, **206**, 855.
[45] M. J. Caturla, *Comp. Mater. Sci.*, 1998, **12**, 319.
[46] M. Jaraiz, G. H. Gilmer, J. M. Poate and T. Diaz de la Rubia, *Appl. Phys. Lett.*, 1996, **68**, 409.
[47] P. Alippi, L. Colombo and P. Ruggerone, *Comput. Mater. Sci.*, 2001, **22**, 44.
[48] M. W. Guinan and J. H. Kinney, *J. Nucl. Mater*, 1981, **103/104**, 1319.
[49] M. J. Norgett, M. T. Robinson and I. M. Torrens, *Nucl. Engng Des.*, 1975, **33**, 50.
[50] T. Diaz de la Rubia, R. S. Averback, H. Horngming and R. Benedek, *J. Mater. Res.*, 1989, **4**, 579.
[51] B. N. Singh, *J. Nucl. Mater.*, 1998, **258–263**, 18.
[52] L. K. Mansur, *J. Nucl. Mater.*, 1994, **216**, 97.
[53] H. Trinkaus, B. N. Singh and C. H. Woo, *J. Nucl. Mater.*, 1994, **221**, 18.
[54] F. A. Garner and W. G. Wolfer, *J. Nucl. Mater.*, 1984, **122**, 201.
[55] R. E. Stoller, M. K. Miller, G. R. Odette and B. D. Wirth, *Trans. Am. Nucl. Soc.*, 2003, **88**, 539.
[56] L. P. Nielsen, F. Besenbacher, I. Stensgaard, E. Laegsgaard, C. Engdahl, P. Stoltze, K. W. Jacobsen and J. K. Norskov, *Phys. Rev. Lett.*, 1993, **71**, 754.
[57] L. Ruan, I. Stensgaard, F. Besenbacher and E. Lgsgaard, *Phys. Rev. Lett.*, 1993, **71**, 2963.
[58] K. Nordlund, J. Keinonen, M. Ghaly and R. S. Averback, *Nature*, 1999, **398**, 49.
[59] H. L. Heinisch, *Radiat. Effects Defects Solids*, 1990, **113**, 53.
[60] B. D. Wirth, M. J. Caturla, T. Diaz de la Rubia, T. Khraishi and H. Zbib, *Nucl. Instrum. Meth. B*, 2001, **180**, 23.

[61] A. Fasso, A. Ferrari and P. R. Sala, Electron–photon transport in FLUKA: status (eds A. Kling, F. Barao, M. Nakagawa, L. Tavora, P. Vaz), *Proceedings of the Monte Carlo 2000 Conference*, Lisbon, October 23–26 2000, Springer, Berlin, 2001, pp. 159–164.
[62] J. F. Biresmeister, *MCNP – A General Monte-Carlo N-Particle Transport Code*, Version 4B, LA-12625-M, 1997.
[63] L. R. Greenwood and R. K. Smither, *SPECTER: Neutron Damage Calculations for Materials Irradiations*, ANL/FPP-TM-197, 1985.
[64] M. J. Caturla, R. Diaz de la Rubia, M. Victoria, R. K. Corzine, M. R. James and G. A. Greene, *J. Nucl. Mater.*, 2001, **296**, 90.

Dynamical Processes in Stopping Cross Sections

R. Cabrera-Trujillo, J. R. Sabin, E. Deumens, and Y. Öhrn

Quantum Theory Project, Departments of Physics and Chemistry, University of Florida, P.O. Box 118435, Gainesville, FL 32611-8435, USA

Abstract

When a projectile collides with a target, several processes are involved, depending on the projectile energy. However, there is no single model that can treat all processes for the whole range of projectile energies without resorting to approximations, the accuracy of which depends on the projectile energy. In this work, we present an account of the efforts toward the solution of this problem by considering the time evolution of the collision for all the projectile energies. For that, we use the Electron-Nuclear Dynamics (END) approach to solve the time-dependent Schrödinger equation. A quantum mechanical Lagrangian formulation is employed to approximate the Schrödinger equation, via the time-dependent variational principle, by a set of coupled first-order differential equations in time for the END. We obtain the final wavefunction of the system as a function of the projectile energy, allowing us to determine collisional properties of interest. We discuss the relevance of the time-dependent description of the energy loss process by presenting our results for electron capture, threshold effects, projectile energy gain and quantum effects in the scattering processes.

Contents

ADVANCES IN QUANTUM CHEMISTRY, VOLUME 45
ISSN: 0065-3276 DOI 10.1016/S0065-3276(04)45005-9

1. INTRODUCTION

It has been almost a century since Niels Bohr approached for the first time the problem of energy loss by ions interacting with matter by means of a classical approach [1,2]. Later, in 1930, Hans Bethe proposed a quantum mechanical treatment of the problem based on the First Born approximation [3]. Both of these treatments are valid for high energy projectiles. In 1953, Lindhard and Scharff approached the problem by considering a dielectric description of the target [4]. Although, Lindhard's model provides a correct description of the energy loss at low and high energies, the treatment in the intermediate region lacks the proper description of the charge exchange process. Other models for the low energy region have been proposed. In 1947, Fermi and Teller proposed a model for the energy loss of negative mesotrons based in a degenerate electron gas model [5]. Firsov, in 1959, assumed that the energy loss was due to frictional effects in the interaction of projectiles with matter. Although the low energy models predict an energy loss proportional to the projectile velocity, these models lack a proper description of the quantum mechanical process at low projectile energies, mostly those involving bonding and chemical reactions.

Furthermore, these previous treatments either assume a rigid projectile electronic structure or a bare projectile for all projectile energies. Although there have been some attempts to include the projectile electronic structure or projectile charge state in the treatment, the problem has been stalled by lack of a way to treat charge exchange effects. In 1955, Dalgarno and Griffing used the electron capture and electron loss cross section of the projectile to determine the fractional charge in a beam when colliding with a target [6]. The effective charge approach has also been utilized broadly, e.g., Yarlagadda *et al.* proposed a description of the projectile effective charge by means of the Bohr criterion for stripping ions [7]. Later Brandt and Kitagawa extended the model based on the Thomas–Fermi model of the atom [8]. However, all these models are based on a time-independent approach to the problem of energy deposition.

Although each of these models work well in its region of validity, there is no model that deals with the many-body character of the interactions valid for all energy ranges of the projectile. Furthermore, for a proper description of the interaction, any model should incorporate dynamical effects such as electron transfer, rotations and vibrations, nuclear displacement, bond breaking and bond making (chemical reactions), photon emission and absorption, electronic excitations, and ionization.

This implies that any theoretical and computational study of atomic and molecular collisions over a range of energies from a fraction of an eV to many MeV should incorporate accessible electronic states of the system and non-adiabatic coupling terms, explicitly or implicitly.

The proper approach to this problem is through the time-dependent solution of the Schrödinger equation for a Hamiltonian that incorporates all the interactions of the many-body system. There have been some attempts at calculating the energy loss processes. Schiwietz proposed in 1990 a coupled-channel approach to the calculation of stopping cross section for light swift ions penetrating atomic H and He targets [9]. Schiwietz assumed straight projectile trajectories consistent of one active electron, thus, valid only in the high energy region and suited for small systems only. A more general model is required to describe energy loss processes suitable at all projectile energies and requires a direct, non-adiabatic approach. The Electron-Nuclear Dynamics (END) theory [10] offers such a general approach.

The END theory was proposed in 1988 [11] as a general approach to deal with time-dependent non-adiabatic processes in quantum chemistry. We have applied the END method to the study of time-dependent processes in energy loss [12–16]. The END method takes advantage of a coherent state representation of the molecular wave function. A quantum mechanical Lagrangian formulation is employed to approximate the Schrödinger equation, *via* the time-dependent variational principle, by a set of coupled first-order differential equations in time to describe the END.

In Section 2, we provide a précis of stopping power theory and its connection to the END approach for which we outline the salient features in Section 3. In Section 3.2, we discuss the treatment of the END trajectories and their connection to the differential cross section and energy loss. In Section 4, we present some simple applications and results of our approach. In Section 5, we discussed future directions on the END approach to stopping cross section. Finally, Section 6 contains our conclusions.

2. STOPPING POWER

2.1. Definition

According to Bohr [17], the energy deposited by an ion beam when transiting a target of thickness Δx and density n_2 is given by

$$-\Delta E = \sum_{i}^{N} \Delta E_i n_2 \sigma_i \Delta x \tag{1}$$

where ΔE_i is the kinetic energy deposited by the projectile (energy loss) for each collision i in the path length Δx with a cross section σ_i. The minus

sign in the LHS of equation (1) assures a positive energy loss. In the limit when $\Delta x \rightarrow 0$, the energy loss per unit path length (stopping power) for a projectile is

$$-\frac{\mathrm{d}E}{\mathrm{d}x} = n_2 \int \Delta E \, \mathrm{d}\sigma = n_2 \int \Delta E \frac{\mathrm{d}\sigma}{\mathrm{d}\Omega} \mathrm{d}\Omega \tag{2}$$

Thus, the energy loss per unit path length per scattering center, the so-called, stopping cross section, is then

$$S = -\frac{1}{n_2}\frac{\mathrm{d}E}{\mathrm{d}x} = \int \Delta E \frac{\mathrm{d}\sigma}{\mathrm{d}\Omega} \mathrm{d}\Omega \tag{3}$$

In order to calculate a reliable stopping cross section, one must obtain accurate energy losses ΔE and scattering cross sections $\mathrm{d}\sigma/\mathrm{d}\Omega$ for the collision.

In a time-independent approach based on the First Born approximation, the scattering cross section is usually obtained through Fermi's golden rule. The kinetic energy loss of the projectile is obtained as the energy gained by the target (if charge exchange is neglected) by conservation of energy in the collision.

In our case, to include non-adiabatic effects, e.g., charge exchange, we require a time-dependent analysis of the binary collision.

2.2. Scattering cross section

For calculation of the stopping cross sections, an accurate, scattering cross section, valid for all the projectile energies, is a crucial ingredient of equation (3). The classical differential cross section for a particular channel with probability P_f is given by [18]

$$\frac{\mathrm{d}\sigma_\mathrm{f}(E,\theta,\varphi)}{\mathrm{d}\Omega} = \sum_i P_\mathrm{f}(b_i,E,\varphi)\frac{b_i}{\sin\theta|\mathrm{d}\Theta/\mathrm{d}b_i|}, \tag{4}$$

where the sum runs over all impact parameters that lead to the same scattering angle (θ,φ). Here, $\Theta(b)$ is the deflection function of the projectile and is defined as the angle between the final and initial projectile momenta. The deflection function contains information concerning the attractive and repulsive regions of the interaction between projectile and target.

In order to remedy the recognized deficiencies of equation (4) for the scattering cross section, such as unphysical discontinuities at $\theta = 0$, the so-called glory angle [19], and at angles where $\mathrm{d}\Theta/\mathrm{d}b = 0$, called rainbow angles [19], as well as the lack of the interference between the various trajectories in the sum of equation (4), semiclassical corrections such as the uniform Airy or Schiff [20] approximations can be included.

A classical integral cross section is obtained by integrating the differential cross section over scattering angles or equivalently by mapping the scattering angle to the impact parameter space through the deflection function to obtain

$$\sigma_{\mathrm{f}}(E) = \int_0^{\infty} \mathrm{d}b \int_0^{2\pi} \mathrm{d}\varphi b P_{\mathrm{f}}(b, E, \varphi). \tag{5}$$

This expression has been successfully applied for reactive scattering down to energies of a fraction of an eV [21].

Introducing the definition for the classical differential cross section into equation (1) for the stopping cross section, one can rewrite it as

$$S = \int \Delta E b \, \mathrm{d}b \, \mathrm{d}\varphi \tag{6}$$

and where we have assumed $P_{\mathrm{f}} = 1$ in equation (4) as required by the direct differential cross section.

Furthermore, as the projectile penetrates the target, multiple collisions will occur with a fraction of the beam consisting of ions and neutralized atoms. For example, for the case of protons, one needs to obtain the fraction of protons and hydrogens in the beam by following the equilibrium charge-state approach as devised by Dalgarno and Griffin [6]. The fractions of protons and hydrogens in the beam are given by

$$f^{+} = f(\mathrm{H}^{+}) = \frac{\sigma_{01}}{(\sigma_{10} + \sigma_{01})} \tag{7}$$

and

$$f^{0} = f(\mathrm{H}^{0}) = \frac{\sigma_{01}}{(\sigma_{10} + \sigma_{01})} \tag{8}$$

Thus, the mean stopping cross section can be calculated as

$$S = \sum_i f(\mathrm{H}^{\mathrm{i}}) S^{\mathrm{i}} \tag{9}$$

where 'i' stands for protons (+) or neutral (0) projectile contributions of the beam. Here we have assumed that the probability of forming H^{-} is negligible.

In Section 3, we make the connection between equations (3), (4), and (6) and a dynamical description of the process *via* the END model.

3. MINIMAL ELECTRON-NUCLEAR DYNAMICS

3.1. Definition of the model

END theory develops the equations of motion starting from the quantum mechanical action

$$A = \int_{t_1}^{t_2} L(\psi^*, \psi)\mathrm{d}t, \tag{10}$$

in terms of the quantum mechanical Lagrangian

$$L(\psi^*, \psi) = \langle\psi|\mathrm{i}\hbar\frac{\partial}{\partial t} - H|\psi\rangle/\langle\psi|\psi\rangle, \tag{11}$$

where H is the Hamiltonian in a laboratory system of Cartesian coordinates for the entire system of electrons and nuclei.

The principle of least action, $\delta A = 0$ for a particular choice of system state vector $|\psi\rangle$, yields the equations that describe the system dynamics. In the case of a state vector that can explore the entire Hilbert space, the stationarity of the action yields the time-dependent Schrödinger equation. For any approximate family of state vectors this procedure yields an equation that approximates the time-dependent Schrödinger equation in a manner that is variationally optimal for the particular choice of state vector form.

Various choices of families of approximate state vectors are characterized by sets of time-dependent parameters, which serve as dynamical variables as the system of electrons and atomic nuclei evolves in time. Such parameters are, for example, molecular orbital coefficients, the coefficients of the various configurations in a multi-configurational electronic state vector, average nuclear positions and momenta, etc. Minimal END is characterized by the state vector

$$|\psi\rangle = |z, R, P\rangle|R, P\rangle, \tag{12}$$

where

$$\langle X|R, P\rangle = \prod_k \exp\left(-\frac{1}{2}[(\mathbf{X}_k - \mathbf{R}_k)/w]^2 + \mathrm{i}\mathbf{P}_k\cdot(\mathbf{X}_k - \mathbf{R}_k)\right) \tag{13}$$

is the wavefunction for distinguishable nuclei with $\mathbf{R}_k$ and $\mathbf{P}_k$ being the average position and momentum vectors, respectively, of the kth nucleus. The common parameter w, which is related to the width of the traveling Gaussian wave packets is chosen not to depend on the time parameter t. The electron dynamics is described in terms of the Thouless determinant [22]

$$\langle x|z, R, P\rangle = \det\{\chi_i(x_j)\} \tag{14}$$

where the dynamical spin orbitals for N electrons are

$$\chi_h = u_h + \sum_{p=N+1}^{K} u_p z_{ph} \tag{15}$$

which are expressed in terms of the spin orbital basis $\{u_i\}$ of rank K and consisting of Gaussian orbitals with translation factors centered on the average nuclear positions $\mathbf{R}_k$ and moving with them. The molecular orbital coefficients $\{z_{ph}\}$ are complex to ensure that the electrons maintain proper momentum.

With this state vector the system Lagrangian is formed in the limit of narrow Gaussian wave packets, i.e., for $w \to 0$. The Euler–Lagrange equations

$$\frac{\mathrm{d}}{\mathrm{d}t}\frac{\partial L}{\partial \dot{q}} = \frac{\partial L}{\partial q} \tag{16}$$

with the dynamical variables $q = z,\ z^*,\ \mathbf{R}_k$, and $\mathbf{P}_k$, then yield the END equations of motion for the minimal form of the theory [10] with the following matrix representation

$$\begin{bmatrix} \mathrm{i}\mathbf{C} & \mathbf{0} & \mathrm{i}\mathbf{C}_R & \mathrm{i}\mathbf{C}_P \\ \mathbf{0} & -\mathrm{i}\mathbf{C}^* & -\mathrm{i}\mathbf{C}_R^* & -\mathrm{i}\mathbf{C}_P^* \\ \mathrm{i}\mathbf{C}_R^\dagger & -\mathrm{i}\mathbf{C}_R^{\mathrm{T}} & \mathbf{C}_{RR} & -\mathbf{I}+\mathbf{C}_{RP} \\ \mathrm{i}\mathbf{C}_P^\dagger & -\mathrm{i}\mathbf{C}_P^{\mathrm{T}} & \mathbf{I}+\mathbf{C}_{PR} & \mathbf{C}_{PP} \end{bmatrix} \begin{bmatrix} \dot{\mathbf{z}} \\ \dot{\mathbf{z}} \\ \dot{\mathbf{R}} \\ \dot{\mathbf{P}} \end{bmatrix} = \begin{bmatrix} \partial E/\partial \mathbf{z}^* \\ \partial E/\partial \mathbf{z} \\ \partial E/\partial \mathbf{R} \\ \partial E/\partial \mathbf{P} \end{bmatrix}, \tag{17}$$

where the *dynamical metric* contains the coupling elements

$$(C_{XY})_{ik;jl} = -2\,\mathrm{Im}\frac{\partial^2 \ln S}{\partial X_{ik}\partial Y_{jl}}\bigg|_{R'=R,P'=P}, \tag{18}$$

$$(C_{X_{ik}})_{ph} = (C_X)_{ph;ik} = \frac{\partial^2 \ln S}{\partial z_{ik}^*\partial X_{ik}}\bigg|_{R'=R,P'=P}, \tag{19}$$

$$C_{ph;qg} = \frac{\partial^2 \ln S}{\partial z_{ph}^*\partial z_{qg}}\bigg|_{R'=R,P'=P}. \tag{20}$$

In equation (17) S is defined as the overlap of two electronic determinantal wave functions $S = \langle z, R', P'|z, R, P\rangle$ and the energy is $E = \sum P_l^2/2M_l + \langle z, R, P|H_{\mathrm{elec}}|z, R, P\rangle/\langle z, R, P|z, R, P\rangle$. This level of theory can be characterized as fully non-linear time-dependent Hartree–Fock for quantum electrons and classical nuclei. It has been applied to a great variety of problems involving ion–atom [12,14,15,23–25], and ion–molecule reactive collisions

[26], intramolecular electron transfer [10], and solitonic charge transfer in polymeric chains [27].

The solution to equations (17) in its minimal representation, are implemented into the *ENDyne* package [28].

3.2. END trajectories

For the case of scattering energy loss, let us consider a binary collision between a projectile and a target. The target is initially at rest with its center of mass at the origin of the laboratory cartesian coordinate system. The projectile is placed 20 a.u. from the target in the z-direction, with an impact parameter b, sufficiently distant so that the initial interaction between projectile and target is considered negligible, and moving towards the target with an initial momentum commensurate with the collision energy of interest. A given initial electronic state for each system, normally the ground state, is chosen and from that an initial Thouless determinant for the system is constructed in a particular basis. An initial relative orientation of projectile and target is chosen for the case of molecular projectiles and/or targets.

Once the initial configuration of the system has been set, equation (17) for the dynamics of the collision are integrated until a time when the product species are sufficiently separated that there are no further interaction among the products. Depending on the system and on the collision energy, a variety of processes may take place. Each set of initial conditions, such as collision energy, relative orientation of reactants, and impact parameter, b, of the projectile, leads to a particular set of product species and states. The simplest situation is that where the projectile is simply scattered into a solid angle $\mathrm{d}\Omega$, with concomitant capture or loss of electrons from/to the target, and being either slowed in the collision (energy loss) or accelerated (energy gain) in the collision.

At the end of each trajectory, we obtain the position $\mathbf{R}_k$ and momentum $\mathbf{P}_k$ for the kth atom, and the final wave function $|\psi\rangle$ of the system.

In these cases, various final electronic states of the total system are calculated in the same basis and projected against the final evolved wave function to yield a transition probability $P_{\mathrm{fo}}(b, E, \varphi) = |\langle f|\psi\rangle|^2$, which depends on collision energy E and on relative initial orientation 'o' of the colliding species and scattering angles (θ, φ) or equivalently impact parameter (b, φ).

4. RESULTS

A variety of properties of the collision can be determined from the final wave-function, e.g., excitations, chemical rearrangement, vibrations,

rotations, charge exchange, and energy loss, to mention but a few. In this section, we present a review of our results regarding energy loss processes.

4.1. Impact parameter dependence of the projectile energy loss

Once all the projectile impact parameter grid has been generated as described in Section 3.2, one obtains the projectile center of mass kinetic energy loss for each trajectory as

$$\Delta E(b, E_{\mathrm{p}}) = K_{\mathrm{p}}^{\mathrm{f}}(b, E_{\mathrm{p}}) - K_{\mathrm{p}}^{\mathrm{i}} \tag{21}$$

where

$$K_{\mathrm{p}}^{\mathrm{s}} = \frac{\left(\mathbf{P}_{\mathrm{p}}^{\mathrm{s}} + \sum_{i=1}^{N_{\mathrm{e}}} \mathbf{p}_{\mathrm{e}}^{\mathrm{s}}\right)^2}{2\left(M_{\mathrm{p}}^{\mathrm{s}} + \sum_{i=1}^{N_{\mathrm{e}}} m_{\mathrm{e}}^{\mathrm{s}}\right)}. \tag{22}$$

Here s = i, f label the initial and final states of the system. K^{s} is the kinetic energy of the projectile, $\mathbf{P}_{\mathrm{p}}^{\mathrm{s}}$ is the average momentum of the projectile nuclei, $\mathbf{p}_{\mathrm{e}}^{\mathrm{s}}$ is the average momentum of the projectile electrons, $M_{\mathrm{p}}^{\mathrm{s}}$ is the projectile nuclear mass, and $\sum_{i=1}^{N_{\mathrm{e}}} m_{\mathrm{e}}^{\mathrm{s}}$ is the total mass of electrons associated with the projectile.

We should note that the final number of electrons in the projectile is a function of the impact parameter and the projectile energy due to charge

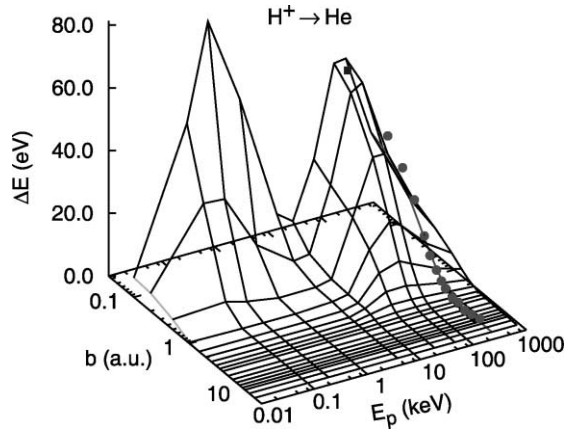

Fig. 1. Projectile energy loss for protons colliding on He atoms as a function of the projectile impact parameter and initial kinetic energy. The symbols ● are the theoretical data of Grande and Schiwietz [29]. The isolated point (■) is from Ref. [30].

exchange. In our description, the final electronic population of the projectile is calculated using the Mulliken population [15,31–33].

In Fig. 1, we present the projectile energy loss as a function of impact parameter and projectile energy for protons colliding with helium atoms. In the same figure we compare to the results obtained by Schiwietz and Grande for the case of protons at $E_p = 300$ keV. Note the two maxima in the $\Delta E(b)$ surface. One in the low projectile energy region at $E_p \sim 200$ eV, the so-called nuclear energy loss, and the second in the high energy region at $E_p \sim 100$ keV, the so-called electronic energy loss. Furthermore, the largest energy loss occurs at small impact parameter, close to the head-on collision. However, as we will see later, the dominant contribution to the stopping cross section originates from the intermediate values of the impact parameter due to the fact that $\Delta E(b)$ is weighted by the impact parameter b (equation (6)).

4.2. Angular dependence of projectile energy loss

From the deflection function, one can map the energy loss as a function of the impact parameter to a function of the scattering angle. In Fig. 2, we show the

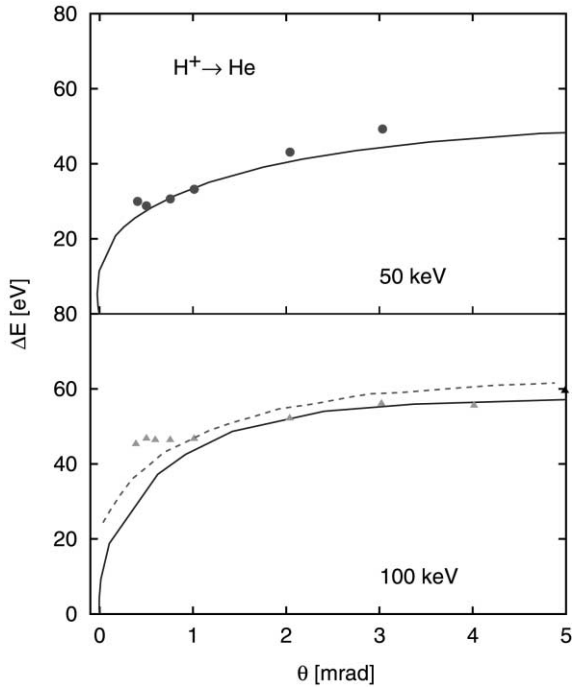

Fig. 2. Projectile energy loss for protons colliding with helium as a function of the scattering angle for proton energies of 50 and 100 keV.

projectile energy loss as a function of the projectile scattering angle. The solid line is our work and the dashed line is the coupled channel calculation of Schiwietz *et al.* [34]. The experimental points are from Auth and Winter [35]. Although the agreement is good at large scattering angles, quantum effects become important in the small scattering angle region due to forward peak character of the scattering process where the attractive and repulsive regions of the interaction play a larger role. As mentioned above, for scattering angles close to the rainbow angle, there are several projectile trajectories that will have the same scattering angle, thus interference between these nuclear wave functions is required to account for the energy loss at that angle.

4.3. Electron capture and loss

We now turn our attention to the calculation of the total electron capture, σ_{01}, and electron loss, σ_{10}, cross sections as calculated from equation (4).

In Fig. 3, we show the results for the orientationally averaged total electron capture and electron loss cross sections for protons and neutral hydrogen projectiles colliding with H_2 for projectile energies in the range of

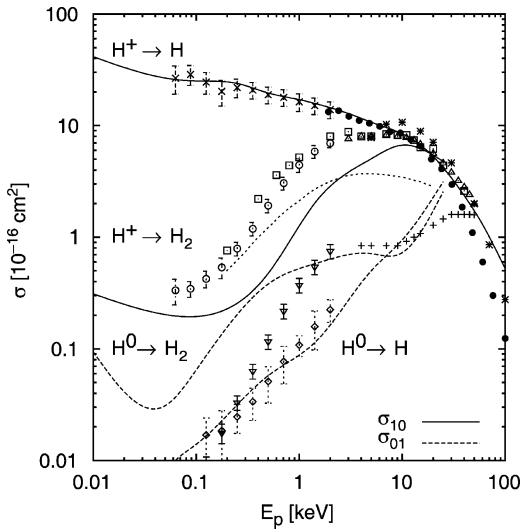

Fig. 3. Orientationally averaged electron capture, σ_{10}, and electron loss, σ_{01}, cross sections for H^+ and H colliding with H_2. For comparison we show the results for σ_{10} obtained for the atomic case [12]. The experiment data are from Ref. [36] ($\times$), Ref. [37] (●) for $H^+ \rightarrow H$; Ref. [36] (◇) for $H^0 \rightarrow H$; Ref. [36] (○), Ref. [38] (□), Ref. [39] (△), Ref. [40] ($*$) for $H^+ \rightarrow H_2$; Ref. [41] (+), Ref. [36] (▽) for $H^0 \rightarrow H_2$. For comparison, we also show the results of Kimura [42] for $H^+ \rightarrow H_2$ (short-dashed line).

10–25 keV/amu, and compare with various experimental data [36–41]. For comparison, we also present our results for the atomic hydrogen target reported in Ref. [12].

We note that for the molecular case, our results give a good description of the electron capture and electron loss for the collision. For $H^+ \rightarrow H_2$ our results are proportionally lower that those reported by Gealy *et al.* [36] which were normalized to 6.95×10^{-16} cm^2 at $E_p = 2.0$ keV. If we use the same normalization, our results agree well with the experiment. We also note that for the molecular case, the lower the energy of the projectile, the smaller the electron capture cross section, contrary to the atomic case where there is resonant electron transfer. This is a molecular effect, since the closed shell of molecular hydrogen is more stable than the open shell in the atomic case, and thus the electron capture cross section for $H^+ \rightarrow H_2$ is not one half that for $H^+ \rightarrow H$. In the same figure, we also present the results of Kimura [42] for the total electron capture obtained by the DIM method for $H^+ \rightarrow H_2$.

4.4. Projectile beam fractional charge

Before proceeding to calculate the stopping cross section, we calculate the fraction of protons, $f(H^+)$, and the fraction of neutral hydrogens, $f(H)$, in the beam during the collision according to equation (9). With the calculated values obtained for the electron capture and loss cross sections as shown in Fig. 3, we present in Fig. 4 the fraction of H^+ and H^0 in the hydrogen beam

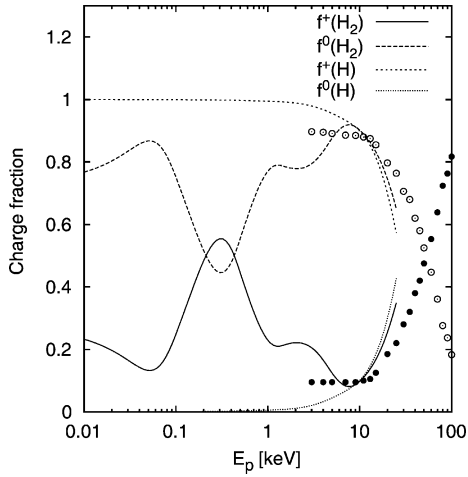

Fig. 4. Fraction of protons and neutral hydrogen projectiles in a hydrogen beam when colliding with atomic and molecular hydrogen targets as a function of the projectile energy. The experimental points are from Allison and Garcia-Munoz [43].

when colliding with atomic and molecular hydrogen as a function of the projectile energy E_p. In the same figure, we compare with the experimental data of Allison and Garcia-Munoz [43].

For projectile energies $E_p > 10$ keV, the fraction of protons and neutral hydrogen in the beam is similar for both atomic and molecular targets. However, at lower energies, discrepancies appear due to the molecular target effect. At these low energies, the projectile beam, when colliding with atomic hydrogen, has been neutralized, while for the molecular case, there is still a reasonable fraction of protons surviving. This can be understood from Fig. 3 where we note that the electron capture is resonant for protons on atomic hydrogen, thus neutralizing the beam.

4.5. Atomic stopping cross section

When we separate the projectile total energy loss into electronic and nuclear contributions, equation (6) can be written as

$$S_x(v) = 2\pi \int_0^\infty \Delta E_x(b) b \, \mathrm{d}b, \tag{23}$$

where the x labels the total, electronic, nuclear, or ro-vibrational contribution to the energy loss, ΔE. In Fig. 5, we show the total, electronic, and nuclear

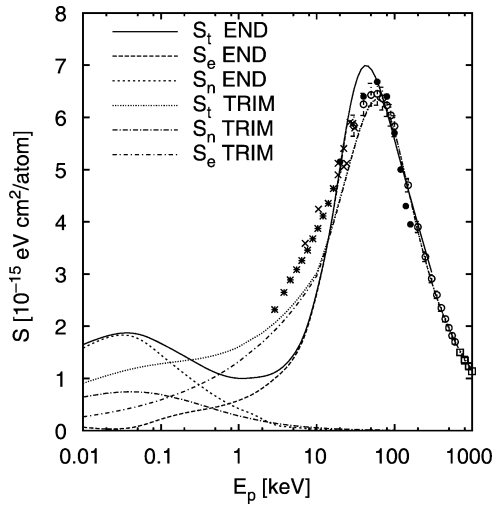

Fig. 5. Stopping cross section for proton incident on atomic hydrogen as a function of the projectile energy. The lines labeled with END are the results of this work with electronic (e), nuclear (n), and total (nuclear + electronic = t) contribution. The experiments are $*$ [44]; ○ [45]; ● [46]; □ [47]; and × [48]. Also, for comparison, we present the results obtained by TRIM-99 [49].

stopping cross sections for protons colliding with atomic hydrogen from energies ranging from a few eV to hundreds of keV, and compare with the available experimental data [44–48]. We see fair agreement between theory and experiment, principally for energies from the maximum of the stopping curve and higher. However, for lower energies, there are some discrepancies, due principally to the charge exchange processes, since the lower the energy the more screened the projectile is (Fig. 3). We also note that our results were obtained for atomic hydrogen, while the experimental data were obtained for the hydrogen molecule, and thus contain chemical bond effects.

In Figs. 6 and 7, we show the results for protons colliding with atomic helium and neon targets as a function of the projectile energy, and compare with available experimental data [44,45,50,51].

From Figs. 5–7, it seems apparent that there is a low velocity threshold below which there is no electronic stopping cross section. This threshold is a consequence of the quantum behavior of the momentum transfer and the molecular states of the system during the collision (*vide infra*).

In Fig. 8, we present the total, S_t, electronic, S_e, and nuclear, S_n, contributions to the stopping cross section as a function of the initial projectile velocity, for the case of He^+ colliding with atomic Ne. In the same figure we compare with the experimental data of Chu and Powers [52], of Fukuda [53], and of Baumgart *et al.* [54]. For the case of $He \rightarrow Ne$, and following the Dalgarno approach, we require the cross section for electron capture and loss for He^{2+}, He^+, and He in order to determine the fractional

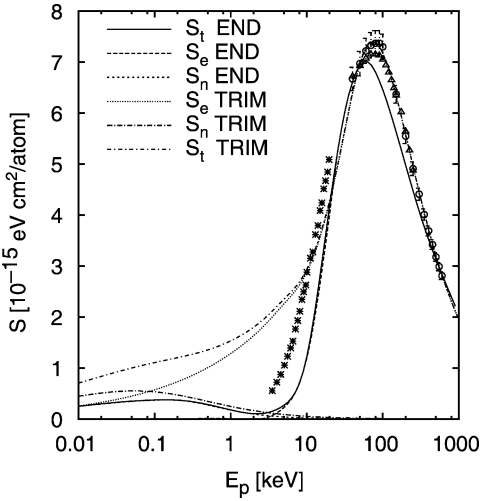

Fig. 6. Stopping cross section for proton incident on atomic helium as a function of the projectile energy. The labels are the same as in Fig. 5. The experimental data △ is from Ref. [50]. Note the threshold in the electronic energy loss at low energies.

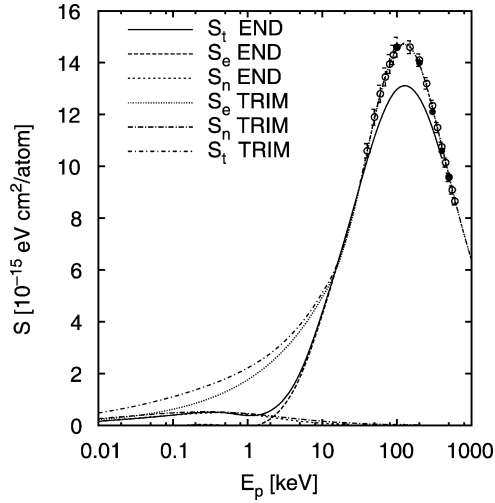

Fig. 7. Stopping cross section for proton incident on atomic neon as a function of the projectile energy. The labels are the same as in Fig. 5. The experimental data ▽ is from Ref. [51]. Note the threshold in the electronic energy loss at low energies.

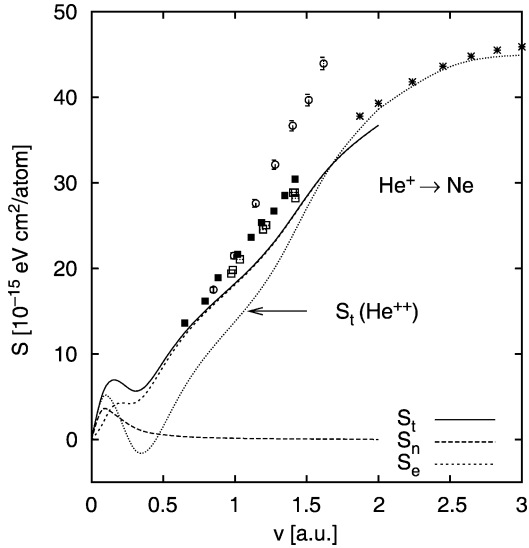

Fig. 8. Stopping cross section for He^+ projectiles colliding with atomic neon. Continuum line: total stopping cross section; long-dashed line: nuclear stopping cross section; short-dashed line: electronic stopping cross section. The experimental data are ∗ [52]; ○, ■ [53]; □ [54]. Also for comparison we show the total calculated cross section for He^{2+} ions colliding with atomic neon (dotted line).

charge for helium ions in the beam when colliding with Ne. These studies are work in progress and will be reported elsewhere. The comparison of this single channel with the experiment shows a good agreement.

4.6. Threshold effects

As mentioned above, we observe a low energy threshold in the electronic energy loss of the projectile. The explanation of this effect is simple and goes as follows. For a binary collision, the minimum momentum transferred during a collision, obtained through energy conservation, is given by [55]

$$q_{\min} = \frac{\mu v}{\hbar}\left[1 - \sqrt{1 - \frac{2(E_n - E_{n_0})}{\mu v^2}}\right], \tag{24}$$

where μ is the reduced mass of the projectile–target system, v, the projectile incoming speed, and $E_n - E_{n_0}$ the electronic energy absorbed by the target (transition energy from the initial state n_0 to the final state n). In order that this momentum transfer be enough for an electronic transition, it is necessary that

$$\frac{\hbar^2 q_{\min}^2}{2m_e} \geq (E_n - E_{n_0}). \tag{25}$$

Solving for the projectile incoming energy in the laboratory system for which the threshold occurs, one finds the condition that for an electronic transition to occur

$$E_p^{th} \geq \frac{\mu^2}{4M_1 m_e}(E_k - E_{k_0})\left[1 + \frac{m_e}{\mu}\right]^2 \tag{26}$$

where M_1 is the projectile mass. Consider the cases shown in Figs. 5–7. For helium the lowest transition is $1s^2(^1S_0) \rightarrow 1s2s(^3S)$, with an excitation energy of 18.7 eV, as calculated with *ENDyne* (19.72 eV [56]). Therefore, the threshold for the electronic stopping cross section for a proton colliding with helium should be at approximately $E_p^{th} \sim 8$ keV, which is close to the result shown in Fig. 6. For the case of neon, the lowest excitation is $1s^2 2s^2 2p^6(^1S_0) \rightarrow 1s^2 2s^2 2p^5(^2P_{1\frac{1}{2}})3s^1$ with an excitation energy of 14.9 eV, as calculated with *ENDyne* (16.5 eV [56]), such that the projectile energy threshold is expected to be near $E_p^{th} \sim 7$ keV. Note that equation (26) has been obtained assuming that there are no charge exchange processes involved during the collision. For helium and neon atoms, this is a good assumption, as they have small charge exchange cross sections (see Fig. 3 in Ref. [12]). The hydrogen target is more complicated due to the charge exchange processes, and the quasi-molecular states formed during the collision.

4.7. Acceptance angle

The results from the previous sections were obtained by integration of equation (6) for all impact parameters b considered, or equivalently, by integration over all possible projectile scattering angles θ, namely the entire solid angle of 4π. However, since all measurements are made using an apparatus with a fixed exit window, corresponding to measurement over only a subset of possible scattering angles, the acceptance angle, some care must be taken when comparing calculated results to experiment.

Since the projectile energy loss is a function of the scattering angle, θ, thus, it is possible to define a stopping cross section as a function of the possible or allowed energy losses or scattering angles within a solid angle Ω_a, i.e., $S_a(\Omega_a)$.

$$S_a = \int_{\Omega_a} \Delta E \frac{d\sigma}{d\Omega} d\Omega \tag{27}$$

In Fig. 9, we present the stopping cross section for protons on atomic and molecular hydrogen targets, S_a^+, as a function of acceptance angle as described by equation (27), for projectile energies of 0.5, 1.5, 5.0, 10.0, and 25.0 keV. Note that for high projectile energies, the largest contributions to

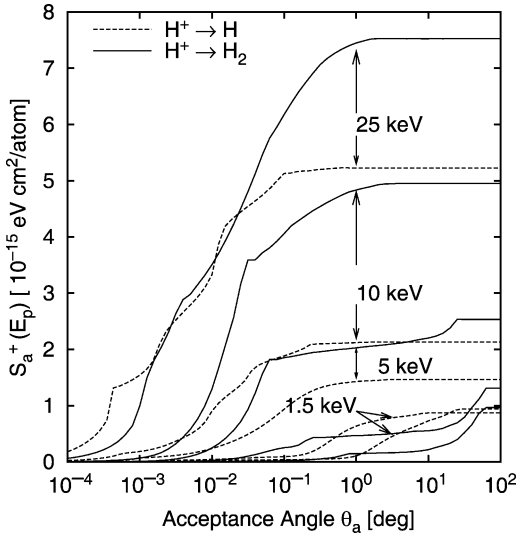

Fig. 9. Stopping cross section per atom for proton projectiles colliding with atomic and molecular hydrogen targets as a function of the acceptance angle θ_a for projectiles energies of 0.5, 1.5, 5.0, 10.0, and 25.0 keV. Note the nuclear plus rovibrational contributions when large scattering angles are taken into account.

the stopping cross section comes from scattering angles $\theta_a < 1°$. At lower projectile energies, larger acceptance angles are necessary to saturate the stopping cross section. Thus, for projectile energies of 1.5 keV, we note that at $\theta_a \simeq 1°$, equation (27) predicts a 30% contribution to S_a^+. For $\theta_a \simeq 1°$, and a projectile energy of $E_p = 0.5$ keV, the stopping cross section is only 10% of that when integrating over all the scattering angles. We also note that for the molecular case, a high contribution to S^+ arises for large angles ($\theta_a > 90°$) due to nuclear and ro-vibrational contributions. For the atomic case, we note a similar behavior at large acceptance (scattering) angles. Also, for the atomic case, we note that S_a^+ is smaller than for the molecular case for projectile energies of 5, 10, and 25 keV. For projectiles energies of 0.5 and 1.5 keV, the atomic case gives a higher contribution for large angles.

4.8. Projectile energy gain: acceleration effects

In Fig. 10, we show the acceptance angle-dependent stopping cross section for N^{4+} colliding with H. Here we observe some interesting behavior. For small acceptance angles we observe that the particles detected will be accelerated, i.e., will gain energy for large projectile energies. This happens up to an acceptance angle of around $\theta_a \sim 2°$. For low projectiles energies, where we have seen that larger angles become more important, the energy

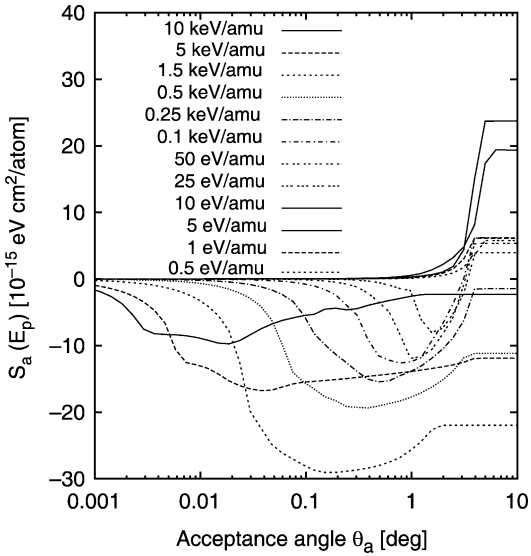

Fig. 10. Acceptance angle *vs.* stopping cross section for the reaction $N^{4+} + H \rightarrow N^{3+} + H^+$ as a function of the acceptance angle of the exit window θ_a for several projectile energies.

loss is still negative for small acceptance angles, but then at large angles, the particles lose energy, reaching saturation (zero slope) for energy loss at large acceptance angles.

The explanation of this effects is simple if one considers the effect of the charge transfer during the collision. Acceleration of the projectile during the collision requires that the change in the projectile kinetic energy $\Delta K(b, E_\mathrm{p}) > 0$. By conservation of energy, it implies that the change in the internal projectile energy $\Delta E^\mathrm{p}(b, E_\mathrm{p})$, target internal energy $\Delta E^\mathrm{t}(b, E_\mathrm{p})$, and target kinetic energy $\Delta K^\mathrm{t}(b, E_\mathrm{p})$ fulfill the following condition

$$\Delta E^\mathrm{p}(b, E_\mathrm{p}) < -\Delta E^\mathrm{t}(b, E_\mathrm{p}) - \Delta K^\mathrm{t}(b, E_\mathrm{p}) \tag{28}$$

If the target is originally in its ground state, then $\Delta E^\mathrm{t}(b, E_\mathrm{p}) > 0$ and $\Delta K^\mathrm{t}(b, E_\mathrm{p}) > 0$, therefore, $\Delta E^\mathrm{p}(b, E_\mathrm{p}) < 0$ (Fig. 11). The internal energy of the projectile must decrease its internal energy. This occurs only by de-excitation or when the projectile captures one or more electrons from the target, leading to a lower electronic energy for the projectile. For the case of electron capture, there must be a proper relation between the projectile electron affinity and target ionization barrier. The electron must overcome the ionization potential barrier in the target and be captured into a lower lying orbital in the projectile. Thus

$$E^\mathrm{t}_\mathrm{f}(b, E_\mathrm{p}) \geq E^\mathrm{t}_0 + I^\mathrm{t} \tag{29}$$

where I^t is the target ionization potential. For the projectile, we require that

$$E^\mathrm{p}_\mathrm{f}(b, E_\mathrm{p}) \geq E^\mathrm{p}_i - A^\mathrm{p} \tag{30}$$

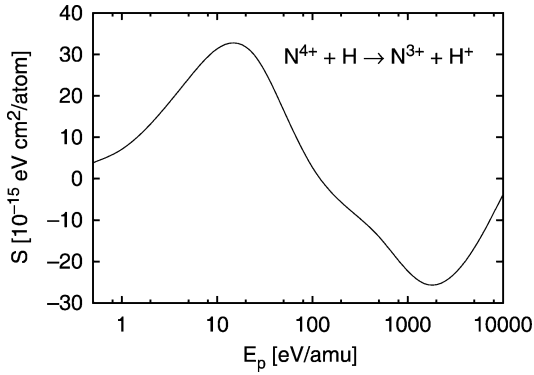

Fig. 11. Stopping cross section as a function of the projectile energy for N^{4+} ions colliding with neutral hydrogen. Note the energy gain for projectile energies $E_\mathrm{p} \geq 100$ eV/amu.

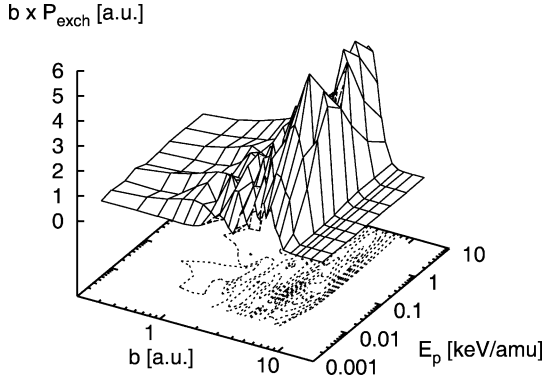

Fig. 12. Charge exchange probability times the impact parameter, for $N^{4+} \rightarrow H$ as a function of the projectile initial energy and impact parameter. Note the region where the highest exchange occurs. For an explanation, see the text.

where A^{p} is the electron affinity of the projectile while in an initial electronic configuration with energy E_i^{p}. Thus, equation (28) implies

$$A^{\mathrm{p}} > K_{\mathrm{f}}^{\mathrm{t}}(b, E_{\mathrm{p}}) + I^{\mathrm{t}}. \tag{31}$$

Therefore, "A projectile with electron affinity larger than the ionization potential of the target may, under the proper dynamical conditions of impact parameter and incident projectile energy, capture a target electron which accelerates its motion and increases its kinetic energy".

From the dynamics of the collision we can visualize the previous results. In Fig. 12 we show the probability for electron capture by the N^{4+} from atomic hydrogen as a function of the projectile energy and impact parameter, as reported in Ref. [57]. One notes that for impact parameters in the range $3 \leq b \leq 7$ the charge exchange has the highest probability and it is in agreement with the largest energy gain of the projectile, as reported in Ref. [57], thus correlating the highest charge exchange with the largest energy gain. Furthermore, due to the small core of the $N^{4+}(1s^2 2s)$, the electron captured forms a hollow atom [58] since the electron captured is mostly in the 4s and high Rydberg states.

4.9. Molecular stopping cross section: Bragg's rule

The previous examples were concerned with atomic targets, however, one of the advantages of the END formulation is the ability to deal with many-atom systems. In this section we present a review of molecular stopping cross sections *a la* END.

The many-body character of the molecular interaction introduces additional channels in the description of the molecular stopping cross

section, e.g., vibrations, rotations, bond breaking and bond making, chemical rearrangement, etc. These difficulties have resulted in a simplified treatment of molecular energy loss. In 1918, Bragg [59] found experimental evidence for an atomic addition of the molecular energy loss, i.e.,

$$S_{\mathrm{mol}} = \sum_i c_i S_i \tag{32}$$

where S_i is the stopping cross section for the ith atom type, present c_i times in the molecule.

Equation (32), known as the Bragg's rule, neglects rotational, vibrational and chemical effects which should be considered in a sophisticated treatment for the molecular stopping cross section, particularly for the low projectile energy where these effects are predominant.

In Fig. 13, we present the orientationally averaged target total, (S_t), electronic, (S_e), ro-vibrational, (S_{rv}) and nuclear, (S_n), contributions to the stopping cross section as a function of the initial projectile velocity, for the case of H^+ colliding with C_2H_6 as obtained by the END model. In the same figure, we present the theoretical core and bond results of Oddershede and Sabin [60] and the FSGO model [61] for the projectile higher energies. We note several trends in our results: the correct limit at high energies, where S_t matches the predictions of the OS and FSGO models for the total stopping cross section; a bump for projectile energies around 3 keV which is a result of the electronic and ro-vibrational contribution to $S_t(E_p)$; the ro-vibrational

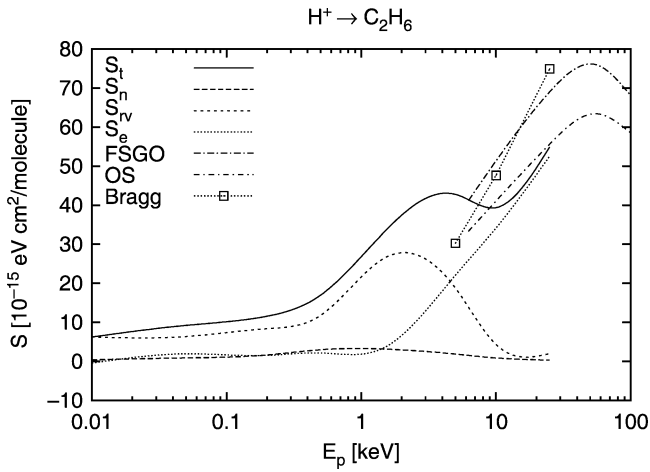

Fig. 13. Molecular stopping cross section for H^+ colliding with C_2H_6 as a function of the projectile energy. For completeness we compare with the theoretical results of Oddershede and Sabin [60] and of the FSGO model [61], as well as the Bragg's rule results when atomic values from END are used for C and H targets (see text).

stopping cross section, S_{rv} has a maximum around $E_p \sim 2.0$ keV, and as the projectile kinetic energy decreases it becomes the largest component of $S_t(E_p)$; the electronic stopping cross section, S_e presents a threshold for projectile kinetic energies $E_p \sim 1.0$ keV. This threshold effect is a consequence of the discrete energy levels of the target electronic structure [12] (*vide supra*), and thus the projectile requires a minimum kinetic energy to excite the target electronic structure and lose energy by electronic excitations. The nuclear stopping cross section has a small contribution, with a maximum around 0.7 keV due to the large mass of the target.

Also, in the same figure we compare our calculated molecular stopping to that obtained using the Bragg's rule (equation (32)). Here we calculate the atomic stopping cross section for H and C using the same method and basis sets as used for the molecular stopping. The resulting Bragg's rule stopping cross section is given by the short dashed line with squares. We see that deviations from the Bragg's rule are of the order of 20%, consistent with previous findings [62].

That the Bragg's rule is not fulfilled can be attributed to several things. First, our molecular calculations contain dynamic ro-vibrational contributions, which are missing in most calculations of Bragg's rule deviations, such as the OS and FSGO results shown in Fig. 13. As shown in Fig. 13, these effects are largest at lower energies, and are included in experimental determinations of deviations from Bragg's rule.

In addition, the atoms have large manifolds of excited states which are not present in the molecule. Thus the possibilities for energy absorption is greater in the atoms, leading to deviations from the Bragg's rule.

Regarding molecular collision, we have also considered protons colliding with H_2 [16,24], N_2 [25], and C_2H_2 [63].

5. WHAT IS NEXT?

We have been interested in extending the set of atomic and molecular systems to analyze within the time-dependent approach END.

As preliminary results, we have considered the collision of antiprotons colliding with hydrogen, a benchmark to study ionization processes. In Fig. 14, we present the preliminary results for antiprotons colliding with atomic hydrogen for projectile energies from 10 eV up to 1 MeV, and compare with the available experimental data [64]. Also, for comparison, we show the results for protons colliding with atomic hydrogen as reference. Note that at low antiproton energies, the energy loss increases dramatically, as observed experimentally. Although this is produced by annihilation of the antiproton–hydrogen system, in our case, it is produced by the strong Coulumbic interaction of the antiproton–proton–electron system at low

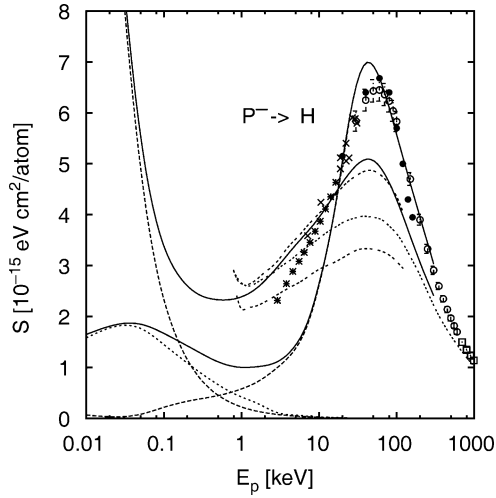

Fig. 14. Comparison of antiproton and proton stopping cross section in atomic hydrogen as a function of the projectile energy. The upper and lower dashed lines are the region of acceptable behavior for the antiproton with the central line being the average fit to the experimental data [64]. The results for protons on hydrogen are identical to Fig. 5.

energies as observed in the electronic contribution to the energy loss (dotted line).

In order to apply the END model to higher energies, we need to include a better description of the continuum states (ionization process) than the discretized version provided by the present implementation of TDHF like theory. This work is in progress.

Furthermore, we are working on the visualization of the physical effects as obtained by the END model. From the time-dependent solution to the system wave function, one can provide a visual representation (snap-shots) of the density, bond breaking, rotations and vibrations during the collision.

In Fig. 15, we present a snap-shot of the electronic density for protons colliding with atomic hydrogen as a function of time.

Initially, the projectile is not associated with any electronic density (frame 1), as it approaches the hydrogen target, it acquires some electron density (frames 2–8), then it leaves the system with a probability for electron transfer. One interesting effect of the collision is that the projectile collides with an energy of 10 keV (projectile velocity of $v = 0.6328$ a.u. close to the velocity of the electron around the target hydrogen $v_t = 1$ a.u. thus in close resonance with it). This will produce polarization effects in the electronic structure during the exchange process (frames 2–6). This polarization of the electronic density is not observed for lower projectile

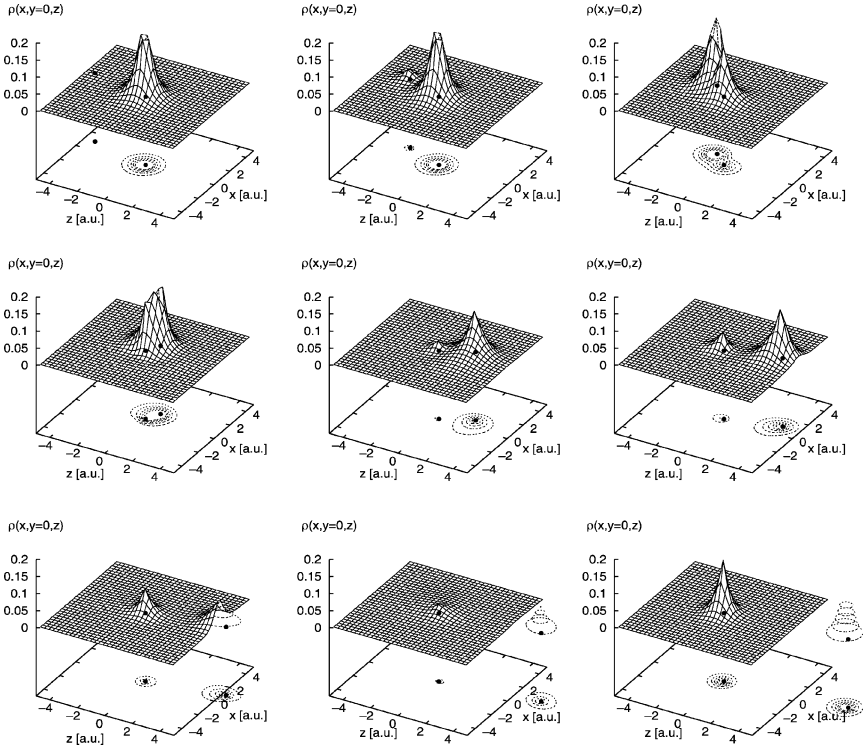

Fig. 15. Snap-shot for the electronic density on the plane of the collision for the collision of protons with hydrogen at $e_p = 10$ keV and an impact parameter of $b = 1.0$ a.u.

velocities where the electron density of the target has time to re-adapt to the incoming perturbation produced by the projectile.

We are extending this type of representation to more sophisticated colliding systems.

6. CONCLUSIONS

A proper description of the dynamics in a collision is required to obtain stopping cross sections that compare well with experimental results over a wide range of projectile energies and that include all the channels available during the collision. Here we have shown that the END approach fulfills this requirement. The proper inclusion of non-adiabatic effects, even at the minimal level of END, provides trajectories for the projectile suitable for the calculation of scattering problems. We have

seen that the charge exchange process plays an important role at low projectile energies, particularly in energy gain processes.

Inclusion of rotational, vibrational, nuclear, bond breaking and bond making within the same framework make the END model suitable for descriptions of sophisticated systems with possibilities to obtain absolute results valid over a wide range of energies.

ACKNOWLEDGEMENTS

This work was supported in part by Grants from the Office of Naval Research (Grant No. N0014-86-1-0707 to JRS and Grant No. N00014-03-1-0332, NYO).

REFERENCES

[1] N. Bohr, *Phil. Mag.*, 1913, **25**, 10.
[2] N. Bohr, *Phil. Mag.*, 1915, **30**, 581.
[3] H. A. Bethe, *Ann. Phys. (Leipzig)*, 1930, **5**, 325.
[4] J. Lindhard and M. Scharff, *Kgl. Dan. Vidensk. Selsk. Mat. Fys. Medd.*, 1953, **27**, 15.
[5] E. Fermi and E. Teller, *Phys. Rev.*, 1947, **72**, 399.
[6] A. Dalgarno and G. W. Griffing, *Proc. R. Soc. London A*, 1955, **232**, 423.
[7] Y. S. Yarlagadda, J. E. Robinson and W. Brandt, *Phys. Rev. B*, 1978, **17**, 3473.
[8] W. Brandt and M. Kitagawa, *Phys. Rev. B*, 1982, **25**, 5631.
[9] G. Schiwietz, *Phys. Rev. A*, 1990, **42**, 296.
[10] E. Deumens, A. Diz, R. Longo and Y. Öhrn, *Rev. Mod. Phys.*, 1994, **66**, 917.
[11] E. Deumens and Y. Öhrn, *J. Phys. Chem.*, 1988, **92**, 3181.
[12] R. Cabrera-Trujillo, J. R. Sabin, Y. Öhrn and E. Deumens, *Phys. Rev. Lett.*, 2000, **84**, 5300.
[13] R. Cabrera-Trujillo, E. Deumens, Y. Öhrn and J. R. Sabin, *Nucl. Instrum. Methods*, 2000, **168**, 484.
[14] R. Cabrera-Trujillo, Y. Öhrn, E. Deumens and J. R. Sabin, *Phys. Rev. A*, 2000, **62**, 052714.
[15] R. Cabrera-Trujillo, J. R. Sabin, E. Deumens and Y. Öhrn, *AIP Conf. Proc.*, 2001, **576**, 3.
[16] R. Cabrera-Trujillo, Y. Öhrn, E. Deumens and J. R. Sabin, *J. Chem. Phys.*, 2002, **116**, 2783.
[17] N. Bohr, *Mat. Fys. Medd. Dan.*, 1948, **18**, 8.
[18] H. Goldstein, *Classical Mechanics*, 2nd edn, Addison-Wesley, Reading, MA, 1980.
[19] K. W. Ford and J. A. Wheeler, *Ann. Phys. (NY)*, 1959, **7**, 259.
[20] L. I. Schiff, *Phys. Rev.*, 1956, **103**, 443.
[21] Y. Öhrn, J. Oreiro and E. Deumens, *Int. J. Quantum Chem.*, 1996, **58**, 583.
[22] D. J. Thouless, *Nucl. Phys.*, 1960, **21**, 225.
[23] R. Cabrera-Trujillo, J. R. Sabin, Y. Öhrn and E. Deumens, *Phys. Rev. A*, 2000, **61**, 032719.
[24] R. Cabrera-Trujillo, Y. Öhrn, J. R. Sabin and E. Deumens, *Phys. Rev. A*, 2002, **65**, 024901.
[25] R. Cabrera-Trujillo, Y. Öhrn, E. Deumens, J. R. Sabin and B. G. Lindsay, *Phys. Rev.*, 2003, **A66**, 042712.
[26] M. Coutinho-Neto, E. Deumens and Y. Öhrn, *J. Chem. Phys.*, 2002, **116**, 2794.

[27] B. Champagne, E. Deumens and Y. Öhrn, *J. Chem. Phys.*, 1997, **107**, 5433.
[28] E. Deumens, T. Helgaker, A. Diz, H. Taylor, J. Oreiro, J. A. Morales and R. Longo, *ENDyne version 2.7 Software for Electron Nuclear Dynamics*, Quantum Theory Project, University of Florida, 1998.
[29] P. L. Grande and G. Schiwietz, *Phys. Rev. A*, 1998, **58**, 3796.
[30] B. Skogvall and G. Schiwietz, *Phys. Rev. A*, 1992, **46**, 5687.
[31] R. S. Mulliken, *J. Chem. Phys.*, 1955, **23**, 1833.
[32] R. S. Mulliken, *J. Chem. Phys.*, 1955, **23**, 1841.
[33] R. S. Mulliken, *J. Chem. Phys.*, 1962, **36**, 3428.
[34] G. Schiwietz, P. L. Grande, C. Auth, H. Winter and A. Salin, *Phys. Rev. Lett.*, 1994, **72**, 2159.
[35] C. Auth and H. Winter, *Nucl. Instrum. Methods B*, 1994, **93**, 123.
[36] M. W. Gealy and B. Van-Zyl, *Phys. Rev. A*, 1987, **36**, 3091.
[37] G. W. McClure, *Phys. Rev.*, 1966, **148**, 47.
[38] J. B. Hasted, *Proc. R. Soc. (London)*, 1955, **A227**, 466.
[39] R. K. Curran and T. M. Donahue, *Technical Report ONR-8*, Office of Naval Research, unpublished.
[40] M. E. Rudd, R. D. DuBois, L. H. Toburen, C. A. Ratcliffe and T. V. Goffe, *Phys. Rev. A*, 1983, **28**, 3244.
[41] P. M. Stier and C. F. Barnett, *Phys. Rev.*, 1956, **103**, 896.
[42] M. Kimura, *Phys. Rev. A*, 1985, **32**, 802.
[43] S. K. Allison and M. Garcia-Munoz, in *Atomic and Molecular Processes* (ed. D. R. Bates), Pure and Applied Physics, Academic Press, New York, 1962, Vol. 13, p. 721.
[44] R. Golser and D. Semrad, *Nucl. Instrum. Methods B*, 1992, **69**, 18.
[45] H. K. Reynolds, D. N. Dunbar, W. A. Wenzel and W. Whaling, *Phys. Rev.*, 1953, **92**, 742.
[46] S. K. Allison, J. Cuevas and M. Garcia-Munoz, *Phys. Rev.*, 1962, **127**, 792.
[47] G. Reiter, N. Kniest, E. Pfaff and G. Clausnitzer, *Nucl. Instrum. Methods B*, 1990, **44**, 399.
[48] J. A. Phillips, *Phys. Rev.*, 1953, **90**, 532.
[49] J. F. Ziegler, J. P. Biersack and U. Littmark, *The Stopping and Range of Ions in Solids*, Pergamon Press, New York, 1985, For a thorough description of the most recent version of this program, see http://www.srim.org.
[50] J. T. Park and E. J. Zimmerman, *Phys. Rev.*, 1963, **131**, 1611.
[51] A. Schiefermüller, R. Golser, R. Stohl and D. Semrad, *Phys. Rev. A*, 1993, **48**, 4467.
[52] W. K. Chu and D. Powers, *Phys. Rev. B*, 1971, **4**, 10.
[53] A. Fukuda, *J. Phys. B: At. Mol. Opt. Phys.*, 1999, **32**, 153.
[54] H. Baumgart, H. Berg, E. Huttel, E. Pfaffe, G. Reiter and G. Clausnitzer, *Nucl. Instrum. Methods*, 1983, **215**, 319.
[55] M. Inokuti, *Rev. Mod. Phys.*, 1971, **43**, 297.
[56] R. F. Bacher and S. Goudsmit, in *Atomic Energy States* (ed. F. K. Richtmyer), McGraw-Hill, New York, 1932.
[57] R. Cabrera-Trujillo, J. R. Sabin, Y. Öhrn and E. Deumens, *Int. J. Quantum Chem.*, 2003, **94**, 215.
[58] H. Winter and F. Aumayr, *J. Phys. B: At. Mol. Opt. Phys.*, 1999, **32**, R39.
[59] W. H. Bragg and R. Kleeman, *Phil. Mag.*, 1918, **10**, 305.
[60] J. Oddershede and J. R. Sabin, *Nucl. Instrum. Methods*, 1989, **B42**, 7.
[61] R. Cabrera-Trujillo, S. Cruz and J. Soullard, *Nucl. Instrum. Methods*, 1994, **B93**, 166.
[62] D. I. Thwaites, *Radiat. Res.*, 1983, **95**, 495.
[63] S. A. Malinovskaya, R. Cabrera-Trujillo, J. R. Sabin, E. Deumens and Y. Öhrn, *J. Chem. Phys.*, 2002, **117**, 1103.
[64] A. Adamo, M. Agnello, F. Balestra, G. Belli, G. Bendiscioli, A. Bertin, P. Boccaccio, G. C. Bonazzola, T. Bressani, M. Bruschi, M. P. Bussa, L. Busso, D. Calvo and M. Capponi, *Phys. Rev. A*, 1993, **47**, 4517.

The Treatment of Energy Loss in Terms of Induced Current Density

V. A. Khodyrev[1]

Centro de micro-análisis de materiales, Campus de Cantoblanco – UAM, 28049 Cantoblanco, Madrid, Spain

Abstract

It is proved that the energy loss can be presented as a convolution of the electric force of the charged projectile with the density of the current induced in stopping media. This provides new possibilities in analysis and also in development of realistic models of the phenomenon. These possibilities are demonstrated in treatment of energy loss to free electrons. Particularly, the method provides a picture of spatial localization of the quantum effects. This helps to clear the origin of the higher order Barkas and Bloch corrections. The dielectric approach for a gas of interacting electrons can be also reformulated in terms of induced current. The combination of the two models permits to take into account simultaneously the higher order effects and the screening of the projectile field. Using additionally the approximation of local response, the method can be applied to describe the energy loss in ion–atom collisions. Finally, we discuss the features of electron dynamics which could result in significant correlation between the energy loss and the angle of deflection of the projectile.

Contents

[1] On leave from the Institute of Nuclear Physics, Moscow State University, Moscow 119899, Russia.

ADVANCES IN QUANTUM CHEMISTRY, VOLUME 45
ISSN: 0065-3276 DOI 10.1016/S0065-3276(04)45006-0

1. INTRODUCTION

In the present chapter, the current density approach for treatment of energy loss in heavy projectile–atom collisions is described. The general basis of the theoretical approach is presented in Refs. [1–3].

The approach is based on the fact that the energy loss to any multi-electron system can be presented as

$$\Delta E = \int \mathrm{d}t \int \mathrm{d}^3\mathbf{r}\mathscr{E}(\mathbf{r},t)\mathbf{j}(\mathbf{r},t), \tag{1}$$

where $\mathscr{E}(\mathbf{r},t) = -\nabla V(\mathbf{r},t)$ is the electric force acting on electrons due to the field of the projectile and $\mathbf{j}(\mathbf{r},t)$ the density of electron current induced due to the perturbation. We underline the following advantages of this approach:

- It can be shown that expression (1) presents the energy loss *exactly* provided, of course, that the current density $\mathbf{j}(\mathbf{r},t)$ is known.
- The current density has a clear physical meaning and this facilitates the construction of phenomenological approaches. In addition, expression (1) itself is, in fact, familiar. It reproduces the Joule–Lentz rule of classical electrodynamics for energy dissipation in a medium when an electric field is applied.
- The representation as a spatial distribution of energy deposition provides new possibilities in the analysis of the phenomenon.
- The current density $\mathbf{j}(\mathbf{r},t)$ is defined equivalently in both classical and quantum mechanics. Thus, the picture presented in this approach displays, in particular, the spatial localization of quantum effects and their significance.
- The treatment in terms of induced current is in the mainstream of modern development of the time-dependent density functional theory (TDDFT). Moreover, the current density formalism has been proposed [4] as a variant of TDDFT. The evolution of current density presents properly the response of electrons on an external field. In general words, such a strong basis is promising for a theoretical treatment of many aspects of ion interactions with atoms, molecules and solids.

In the present chapter the following issues are addressed and described. In Section 2 the basic equation for energy transport is derived. Formula (1) is then obtained as the integral of the source term in this equation. In Section 3 this basis is applied to treat the model of uniform electron gas. One of the outcomes of this analysis is a clear interpretation of the origin of the Bloch correction. The Lindhard dielectric approach [5] for a gas of interacting electrons is reformulated in terms of current density. Combining this model with the exact description of energy loss to free electrons, we arrive at the general description where both the higher order effects and the screening of the ion field are taken into account. This model augmented with the local response approximation is presented in Section 4 and this permits to consider realistic cases of atomic substances. In Section 5 the related problem of the correspondence between impact parameter and angle of deflection in ion–atom collision is considered. The principal significance of such information is recognized during interpretation of experimental data for the impact-parameter dependence of energy loss. The analysis is carried out using the distorted-wave Born approach (DWBA). The principal ingredient in the performed analysis is the ion motion described quasiclassically. This is done using a specific transformation of the DWBA expression for the scattering amplitude. The usage of the quasiclassical approach facilitates to a large extent the calculations in the DWBA approach.

Unless stated otherwise, atomic units are used throughout.

2. EVOLUTION OF ENERGY DENSITY DISTRIBUTION

2.1. Classical approach

The energy absorption in a stopping media and its transport can be described analogously in the classical and quantum-mechanical approaches. As an instructive case and for further reference we first consider the classical gas of N interacting electrons, the system described by the Hamiltonian

$$H = T + U + W + V = H_0 + V, \tag{2}$$

where H_0 is its unperturbed part, $T = \sum_i \mathbf{p}_i^2/2$ is the kinetic energy of electrons, $U = \sum_i U(\mathbf{r}_i)$ and $W = 1/2 \sum_{i \neq j} 1/|\mathbf{r}_i - \mathbf{r}_j|$ are, respectively, the interaction of electrons with an atomic nucleus and the electron–electron interaction, $V = \sum_i V(\mathbf{r}_i, t)$ is the perturbation due to the projectile field. In the statistical description, the state of electrons is presented by the distribution in phase space $f(X, P, t)$ where X and P denote the sets of coordinates and momentums of all electrons. The evolution of this distribution is described by

the equation

$$\frac{\partial f}{\partial t} = -\{H,f\} = -\sum_i \{H,f\}_i = -\sum_i \left(\frac{\partial H}{\partial \mathbf{p}_i} \frac{\partial f}{\partial \mathbf{r}_i} - \frac{\partial H}{\partial \mathbf{r}_i} \frac{\partial f}{\partial \mathbf{p}_i} \right). \quad (3)$$

To clarify the general procedure we will first consider a system consisting of only one electron ($N = 1$, $W = 0$). The general case can be treated analogously although this needs a more complicated procedure. By a simple transformation equation (3) can be rewritten as

$$\frac{\partial f}{\partial t} = -\frac{\partial}{\partial \mathbf{r}} \left(\frac{\partial H_0}{\partial \mathbf{p}} f \right) + \frac{\partial}{\partial \mathbf{p}} \left(\frac{\partial H_0}{\partial \mathbf{r}} f \right) + \frac{\partial V}{\partial \mathbf{r}} \frac{\partial f}{\partial \mathbf{p}}. \quad (4)$$

Taking the integral over $\mathbf{p}$ of both sides of this equation we arrive at the continuity equation in ordinary space

$$\frac{\partial \rho}{\partial t} = -\frac{\partial \mathbf{j}}{\partial \mathbf{r}}, \quad (5)$$

where the electron density $\rho(\mathbf{r}, t)$ and the current density $\mathbf{j}(\mathbf{r}, t)$ are determined by the expressions

$$\rho(\mathbf{r}, t) = \int \mathrm{d}\mathbf{p}\, f(\mathbf{r}, \mathbf{p}, t); \qquad \mathbf{j}(\mathbf{r}, t) = \int \mathrm{d}\mathbf{p}\, \mathbf{p} f(\mathbf{r}, \mathbf{p}, t). \quad (6)$$

Next, multiplying both sides of equation (4) by H_0 we obtain the equation for the evolution of the energy distribution in phase space (the change of H_0 averaged over the distribution $f(\mathbf{r}, \mathbf{p}, t)$ presents the energy deposited in the system):

$$\frac{\partial H_0 f}{\partial t} = -\frac{\partial}{\partial \mathbf{r}} \left(H_0 \frac{\partial H_0}{\partial \mathbf{p}} f \right) + \frac{\partial}{\partial \mathbf{p}} \left(H_0 \frac{\partial H_0}{\partial \mathbf{r}} f \right) + \frac{\partial V}{\partial \mathbf{r}} H_0 \frac{\partial f}{\partial \mathbf{p}} \quad (7)$$

Note that, at $V = 0$, the divergence type of the right-hand side of this equation ensures the conservation of total energy. Again, the integration over $\mathbf{p}$ results in the equation

$$\frac{\partial \rho_E}{\partial t} = -\frac{\partial \mathbf{j}_E}{\partial \mathbf{r}} - \frac{\partial V}{\partial \mathbf{r}} \mathbf{j}, \quad (8)$$

where $\rho_E(\mathbf{r}, t)$ and $\mathbf{j}_E(\mathbf{r}, t)$ are defined as

$$\rho_E(\mathbf{r}, t) = \int \mathrm{d}\mathbf{p}\, H_0 f(\mathbf{r}, \mathbf{p}, t); \qquad \mathbf{j}_E(\mathbf{r}, t) = \int \mathrm{d}\mathbf{p}\, H_0 \mathbf{p} f(\mathbf{r}, \mathbf{p}, t). \quad (9)$$

In the general case of interacting electrons the same equations (5) and (8) can be derived where the densities $\rho(\mathbf{r}, t)$ and $\rho_E(\mathbf{r}, t)$ are defined as

$$\rho(\mathbf{r}, t) = \sum_i \rho_i(\mathbf{r}, t) = \sum_i \int \mathrm{d}X\, \mathrm{d}P\, \delta(\mathbf{r}_i - \mathbf{r}) f(X, P, t), \quad (10)$$

$$\rho_E(\mathbf{r},t) = \sum_i \rho_{E,i}(\mathbf{r},t) = \sum_i \int \mathrm{d}X\, \mathrm{d}P\, \delta(\mathbf{r}_i - \mathbf{r}) H_{0i} f(X,P,t), \quad (11)$$

where

$$H_{0i} = \frac{\mathbf{p}_i^2}{2} + U(\mathbf{r}_i) + \frac{1}{2}\sum_{j\neq i} \frac{1}{|\mathbf{r}_i - \mathbf{r}_j|}. \quad (12)$$

The definition for the current densities $\mathbf{j}(\mathbf{r},t)$ and $\mathbf{j}_E(\mathbf{r},t)$ is obtained by inclusion of an additional factor $\mathbf{p}_i$ under the integrals in equations (10) and (11).

The last term in the right-hand side of equation (8) has a simple meaning. It describes the effect of acceleration of electrons under the action of the projectile. Thus, the momentary rate of energy deposition is straightforwardly related to the current density at a given point; the further development of the electron state is due to the internal dynamics of the system and this is presented by the divergence terms in equations (5) and (8).

2.2. Quantum approach

Turning to the quantum-mechanical description we introduce electron density in the reduced coordinates $\mathbf{r}$:

$$\rho(\mathbf{r},t) = N \int \mathrm{d}\mathbf{r}_2 \cdots \mathrm{d}\mathbf{r}_N |\Psi(\mathbf{r},\mathbf{r}_2,\ldots,\mathrm{d}\mathbf{r}_N,t)|^2, \quad (13)$$

where wave function Ψ is considered to be antisymmetric. The evolution of Ψ is described by the Schrödinger equation

$$\mathrm{i}\frac{\partial \Psi}{\partial t} = H\Psi. \quad (14)$$

The evolution of density in the configuration space of all electrons is then determined by the equation

$$\frac{\partial |\Psi|^2}{\partial t} = \frac{1}{\mathrm{i}}(\Psi^* \cdot H\Psi - H\Psi^* \cdot \Psi) = \frac{1}{2\mathrm{i}} \sum_i \frac{\partial}{\partial \mathbf{r}_i}\left(\Psi^* \frac{\partial \Psi}{\partial \mathbf{r}_i} - \frac{\partial \Psi^*}{\partial \mathbf{r}_i}\Psi\right), \quad (15)$$

where the second equality has been obtained by a simple rearrangement of derivatives over $\mathbf{r}_i$. Integration over all $\mathbf{r}_i$ except $\mathbf{r}_1$ ($= \mathbf{r}$) converts equation (15) into the continuity equation (5) with the density $\rho(\mathbf{r},t)$ given by equation (13) and the current density

$$\mathbf{j}(\mathbf{r},t) = N \int \mathrm{d}\mathbf{r}_2 \cdots \mathrm{d}\mathbf{r}_N \frac{1}{2\mathrm{i}}(\Psi^* \cdot \nabla\Psi - \nabla\Psi^* \cdot \Psi), \quad (16)$$

where $\nabla = \partial/\partial\mathbf{r}$.

An analogous procedure results in the continuity equation (8) for the energy density

$$\rho_E(\mathbf{r},t) = N\int \mathrm{d}\mathbf{r}_2\cdots\mathrm{d}\mathbf{r}_N\ \Psi^* H_0\Psi. \tag{17}$$

The density of energy current $\mathbf{j}_E(\mathbf{r},t)$ is determined as

$$\mathbf{j}_\mathbf{E}(\mathbf{r},t) = N\int \mathrm{d}\mathbf{r}_2\cdots\mathrm{d}\mathbf{r}_N \frac{1}{2\mathrm{i}}(\Psi^*\cdot\nabla H_0\Psi - \nabla\Psi^*\cdot H_0\Psi). \tag{18}$$

Notice that the definitions (17) and (18) do not necessary lead to real values of ρ_E and $\mathbf{j}_\mathbf{E}$. This is not critical, however, because, due to the hermiticy of the Hamiltonian, imaginary parts will vanish after integration over $\mathbf{r}$. Also, both variables become real when the classical limit is approached and, in case of significant quantum effects, the concept of local densities itself becomes inconsistent. Thus, without serious consequences, the imaginary parts of ρ_E and $\mathbf{j}_\mathbf{E}$ can be excluded from consideration.

For finite systems the divergence term in equation (8) does not contribute to the integral over $\mathbf{r}$. Thus, this equation of energy transport permits to express the energy loss through the current density $\mathbf{j}(\mathbf{r},t)$.

3. UNIFORM ELECTRON GAS

3.1. Non-interacting electrons

3.1.1. Current density distribution

If the time-dependent wave function of electrons $\Psi(t)$ is known, the current density approach outlined in Section 2 can be used directly to calculate the energy loss and also to analyze the spatial distribution of related effects. This is the case when the energy loss to a free electron is considered. Assuming that the electron is initially at rest, we can describe its state in the projectile frame as a state of scattering in the projectile Coulomb field. The wave function Ψ in the laboratory frame is then given by the expression

$$\Psi^+(\mathbf{r}) = \exp\left(-\frac{\pi}{2}\eta\right)\Gamma(1+\mathrm{i}\eta)\Phi(-\mathrm{i}\eta,1;\mathrm{i}(vr+\mathbf{vr})), \tag{19}$$

where $\Phi(\alpha,\beta;z)$ is the confluent hyper-geometric function. The normalization factor is defined so that the electron density in the unperturbed plane wave is equal to unity. $\Psi(\mathbf{r})$ is written for $t=0$, the moment when ion crosses the origin. The parameter $\eta = -Z_1/v$ where v is the projectile velocity may be positive or negative (we define it to be positive in the case of repulsive interaction).

With the wave function (19), equation (16) for the current density can be transformed to the form

$$\mathbf{j}(\mathbf{r},t) = -\frac{2\pi\eta}{(\mathrm{e}^{2\pi\eta}-1)}\,\frac{1}{2}(\Phi\,\Phi'^{*} + \Phi^{*}\Phi')\,\frac{v\mathbf{r}+r\mathbf{v}}{r}, \tag{20}$$

where $\Phi' = \partial\Phi(\alpha,\beta,z)/\partial z$. In case of an infinite electron wave, equation (1) describes the stationary energy loss

$$\Delta E = \int \mathrm{d}t\; v\left(-\frac{\mathrm{d}E}{\mathrm{d}x}\right) \tag{21}$$

(x is the coordinate along the projectile velocity $\mathbf{v}$). With $\mathscr{E} = -Z_1\mathbf{r}/r^3$ and $\mathbf{j}$ determined by equation (20), the specific energy loss can be written as

$$-\frac{\mathrm{d}E}{\mathrm{d}x} = -\frac{Z_1}{2v}\,\frac{2\pi\eta}{\mathrm{e}^{2\pi\eta}-1}\int \mathbf{d}^3\mathbf{r}\,\frac{vr+\mathbf{vr}}{r^3}(\Phi\,\Phi'^{*} + \Phi^{*}\Phi'). \tag{22}$$

After the integration over the longitudinal coordinate $r_{\|}$, this equation acquires a familiar form

$$-\frac{\mathrm{d}E}{\mathrm{d}x} = \int \mathrm{d}^2\mathbf{r}_{\perp}\;\delta E(r_{\perp}), \tag{23}$$

where $\delta E(r_{\perp})$ is the density of energy deposition at a given distance $r_{\perp}$ from the projectile trajectory during the total time of interaction. In this approach the integral (23) presents the energy loss analogously as in the classical integration of the energy transfer $\delta E(s)$ over impact parameter s. Clearly $\delta E(r_{\perp})$ has an identical meaning when the classical impulse approach is applicable. The divergence of the integral (23) at large $r_{\perp}$ is to be eliminated by the adiabatic effects.

Using the transformation

$$\Phi'(-\mathrm{i}\eta,1,\mathrm{i}u) = -\mathrm{i}\eta\Phi(1-\mathrm{i}\eta,2;\mathrm{i}u) \tag{24}$$

and the functional relations for the hyper-geometric functions [6], we obtain:

$$\Phi\,\Phi'^{*} + \Phi^{*}\Phi' = \eta u\Phi(1-\mathrm{i}\eta,2;\mathrm{i}u)\Phi(1+\mathrm{i}\eta,2;-\mathrm{i}u). \tag{25}$$

The change of integration variables in equation (22) to $u = vr + \mathbf{vr}$ and $\mathbf{r}_{\perp}$ results in the expression

$$\delta E(r_{\perp}) = 2Z_1^2\,\frac{2\pi\eta}{\mathrm{e}^{2\pi\eta}-1}\int_0^{\infty}\frac{\mathrm{d}u\;u^3}{(u^2+v^2r_{\perp}^2)^2}\,|\Phi(1-\mathrm{i}\eta,2;\mathrm{i}u)|^2. \tag{26}$$

Expression (26) permits to perform a detailed analysis of the energy transfer to a free electron as a function of the 'impact parameter' $r_{\perp}$. The hyper-geometric function, entering in this equation, can be expressed

through the so-called Coulomb wave function of zero momentum F_0 [6]

$$\Phi(1 - \mathrm{i}\eta, 2; \mathrm{i}u) = \frac{2}{C_0(\eta)} \frac{\mathrm{e}^{\mathrm{i}u/2}}{u} F_0\left(\eta, \frac{u}{2}\right), \tag{27}$$

where $C_0^2(\eta) = 2\pi\eta/(\exp(2\pi\eta) - 1))$. The function $F_0(\eta, z)$ satisfies the radial Schrödinger equation with zero angular momentum,

$$\frac{\partial^2 F_0}{\partial z^2} + \left(1 - \frac{2\eta}{z}\right) F_0 = 0, \tag{28}$$

for the boundary conditions $F_0(\eta, 0) = 0$ and $F_0(\eta, z) = \sin(z + \Delta\varphi)$ at large z, where $\Delta\varphi$ is the scattering phase. After substitution of equation (27) into equation (26), equation (23) can be written as

$$-\frac{\mathrm{d}E}{\mathrm{d}x} = \frac{2Z_1^2}{v^2} \int \frac{\mathrm{d}^2\mathbf{r}_\perp}{r_\perp^2} Q(\eta, \xi), \tag{29}$$

where

$$Q(\eta, \xi) = 4 \int_0^\infty \frac{\mathrm{d}w\, w}{(1 + w^2)^2} F_0^2\left(\eta, \frac{\xi w}{4}\right), \tag{30}$$

ξ is the reduced transverse coordinate, $\xi = 2vr_\perp = 2r_\perp/\lambda$, where $\lambda = 1/v$ is the deBroglie wave length for an electron of velocity v. At $Q = 1$ equation (29) reproduces the classical impulse result; so the factor Q accounts for insufficiencies of the classical impulse approach and, simultaneously, for the quantum effects.

The main result of this treatment, equations (29) and (30), can be used, particularly, to present the perturbation and classical results as corresponding approximations for the corrective factor $Q(\eta, \xi)$. In the former approach, the parameter η in equation (30) should be taken to be zero. Then, the energy loss (equation (29)) will be proportional to Z_1^2. To derive the expression for $Q(0, \xi)$, we just replace the Coulomb wave function F_0 in equation (30) by the solution of equation (28) for $\eta = 0$:

$$F_0(0, z) = \sin(z). \tag{31}$$

As a result, the first-order perturbation approach is obtained as

$$Q_{\mathrm{pert}}(\eta, \xi) = Q(0, \xi) = \xi\left[\mathrm{e}^{-(\xi/2)}\mathrm{Ei}\left(\frac{\xi}{2}\right) - \mathrm{e}^{\xi/2}\mathrm{Ei}\left(-\frac{\xi}{2}\right)\right], \tag{32}$$

where $\mathrm{Ei}(z)$ is the exponential–integral function. The same result, though in a different form, has been obtained in Ref. [7] where, from the outset, the problem is treated in the perturbation approach.

The corresponding classical phenomenon can be described using the quasiclassical solution of equation (28),

$$F_0(\eta, z) = \frac{1}{\left(1 - \dfrac{2\eta}{z}\right)^{1/4}} \sin \Theta(z), \tag{33}$$

where $\Theta(z)$ is the quasiclassical phase. Remind that $\eta > 0$ corresponds to the repulsive projectile–electron interaction (a negatively charged projectile). In this case, the value of $F_0(\eta, z)$ at $z < 2\eta$ (the region not achievable for electrons) should be taken as zero. As usual, substituting equation (33) into equation (30), we may replace $\sin^2 \Theta$ by its mean value. As a result the classical expression for $Q(\eta, \xi)$ is obtained

$$Q_{cl}(\eta, \xi) = 2 \int_{w_{\min}}^{\infty} \frac{\mathrm{d}w\, w}{(1 + w^2)^2} \frac{1}{\sqrt{1 - \dfrac{8\eta}{\xi w}}}, \tag{34}$$

where $w_{\min} = \max(0, 8\eta/\xi)$. In fact, equation (34) defines $Q_{cl}(\eta, \xi)$ as a function of one variable $\xi/\eta = r_\perp/a$ where $a = Z_1/v^2$ is the classical collisional diameter. This is just a reflection of the invariance of motion in a Coulomb potential (analogous scaling is seen in the angle of scattering, $\Theta = 2 \arctan(a/s)$).

Figure 1 illustrates how the factor $Q(\eta, \xi)$, with η as a parameter, depends on ξ. The quasiclassical results, equation (34), are also shown. It is seen from

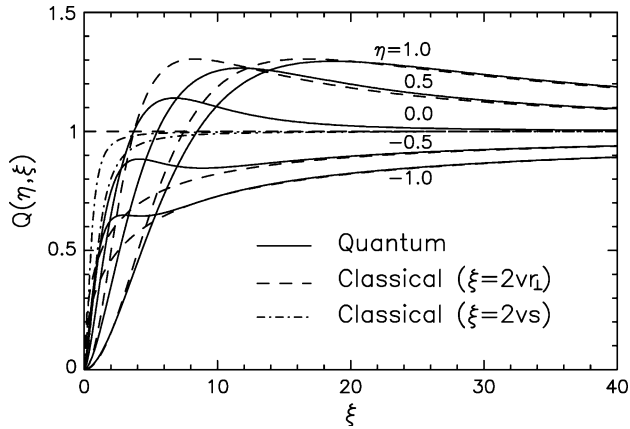

Fig. 1. The factor $Q(\eta, \xi)$ for the indicated values of η. The solid curves show the exact quantum results (30), the classical results (34) are shown as dashed curves. The dot-dashed curves present the classical results in terms of the reduced impact parameter s, $\xi = 2vs$ (equation (35)).

the figure that, at large ξ, the classical description reproduces well the exact quantum results, the quantum effects become significant at $\xi < 1$. We should notice that this kind of relation between quantum-mechanical and classical descriptions is not equivalent to the commonly accepted Bohr's criterion [8] establishing that for classical description to be applicable the parameter $|\eta|$ should be small. Really, as it is seen in Fig. 1, the classical behavior is realized at large ξ even if $|\eta| < 1$ and, inversely, at small ξ the quantum effects are significant also at large values of $|\eta|$. This circumstance is discussed in Section 3.1.3 where the role of quantum effects in energy loss is analyzed and conditions for applicability of the classical approach are derived. At large ξ, all curves in Fig. 1 approach unity demonstrating the applicability of the classical impulse approach for distant collisions.

For comparison, we present in Fig. 1 also the results of the classical description in terms of the impact parameter s (equation (41)) (to underline the similarity of s and $r_\perp$, the same notation is used for the reduced variable $\xi = 2vs$). In this case the factor Q is given by the expression

$$Q_{cl}{}'(\eta, \xi) = \frac{\xi^2}{\xi^2 + 4\eta^2}. \tag{35}$$

It seems that this representation should reflect the same picture as that obtained in the quasiclassical approach (equation (34)). However, the data in Fig. 1 may cause confusion. At large ξ, the factor $Q_{cl}{}'(\eta, \xi)$ converges rapidly to unity ($Q_{cl}{}' \approx 1 - 4\eta^2/\xi^2$). Seemingly, this implies that the electron displacement during collision is negligible (the condition for applicability of the classical impulse approach). However, if this is the case, also the variables s and $r_\perp$ should be equivalent and $Q_{cl}(\eta, \xi)$, likewise, should converge fast to unity. Yet, the factor Q_{cl} reveals much slower convergence ($Q_{cl} \approx 1 + 2\pi\eta/\xi$). This difference can be explained in the following way. In terms of electron trajectories, the electron displacement reveals itself as a modification of the effective impact parameter, the transverse displacement, and also as a shorter effective time of collision due the longitudinal acceleration of electrons. In case of the Coulomb interaction, these two effects almost cancel each other, so the deviation of $Q_{cl}{}'$ from unity does not reflect the actual inaccuracy of the impulse approach. On the other hand, when the energy loss is treated in terms of the induced current, the picture looks differently. The longitudinal acceleration results in a corresponding contribution to the induced current and this effect does not depend on what kind of terms we use. At the same time, the quantum-mechanical picture is associated with a flux of scattering electrons and the simultaneous transverse displacements of electrons do not produce an equivalent compensating effect. It can be said that the effect is concentrated at small ξ: the transverse displacements result in increased (decreased for $Z_1 < 0$) electron density in the region behind the moving projectile. In Fig. 1 this shows up as

an inversion at small ξ of the relative vertical position of curves $Q_{cl}(\eta, \xi)$ for negative and positive projectiles.

3.1.2. The Bloch correction

At large $r_\perp$, one may expect convergence of $\delta E(r_\perp)$ to the first-order perturbation result ($\eta = 0$). Hence, its subtraction from equation (26) should result in convergence of the integral over $r_\perp$ which will present the total effect of nonlinear response of electrons. If the adiabatic effect takes place at large distances, the upper limit in this integral can be taken as infinity. The higher order correction can be written in the standard form:

$$\Delta\left(-\frac{\mathrm{d}E}{\mathrm{d}x}\right) = \frac{4\pi Z_1^2}{v^2}\rho\Delta L(\eta), \tag{36}$$

where ρ is the unperturbed electron density (taken before as being equal to unity). Using equation (26) we obtain

$$\Delta L(\eta) = \frac{1}{2}\int_0^\infty \mathrm{d}u\, u e^{-\delta u}\left[\frac{2\pi\eta}{\mathrm{e}^{2\pi\eta}-1}|\Phi(1-\mathrm{i}\eta, 2; \mathrm{i}u)|^2 - |\Phi(1, 2; \mathrm{i}u)|^2\right]. \tag{37}$$

The exponential factor with infinitesimal δ is included here to provide the convergence in the integration of the separate terms in square brackets. These integrals can be taken using the method proposed in Ref. [9]:

$$\Delta L(\eta) = \frac{1}{2(1+\delta^2)}\left[\frac{2\pi\eta}{\mathrm{e}^{2\pi\eta}-1}\left(\frac{\delta+\mathrm{i}}{\delta-\mathrm{i}}\right)^{-\mathrm{i}\eta} F\left(1-\mathrm{i}\eta, 1+\mathrm{i}\eta; 2; \frac{1}{1+\delta^2}\right) - F\left(1, 1; 2; \frac{1}{1+\delta^2}\right)\right]. \tag{38}$$

Straightforward use of the asymptotic form of the hyper-geometric function $F(\alpha, \beta; \alpha+\beta; z)$ for $z \to 1^-$ [6],

$$F(\alpha, \beta; \alpha+\beta; z) \approx \frac{\Gamma(\alpha+\beta)}{\Gamma(\alpha)\Gamma(\beta)}[2\psi(1) - \psi(\alpha) - \psi(\beta) - \ln(1-z)], \tag{39}$$

where $\psi(z)$ is the logarithmic derivative of the Γ-function, results in the expression

$$\Delta L(\eta) = -\mathrm{Re}(\psi(1+\mathrm{i}\eta) - \psi(1)). \tag{40}$$

This formula has been derived in the famous paper by Bloch [10] using more complicated procedure. The formalism of the transport cross-section approach also provides such a possibility [11]. As a function of the

parameter η, the Bloch correction bridges the results of the first perturbation approach (small $|\eta|$) and the Bohr's classical result which is obtained at the asymptotics of large $|\eta|$.

3.1.3. Qualitative interpretation

The treatment of energy loss presented in the previous two sections can be supplied with qualitative analysis permitting to perceive the underlying physics in more detail. In particular, the reason for seeming inconsistency with the transport cross-section approach [11] can be recognized and origin of the higher order correction can be cleared.

The key point in the interpretation of the analytical results is the relation between the classical and quantum approaches. In this analysis we will follow the same line of reasoning which Bohr used in his analysis of the Rutherford scattering [8]. In the classical description, the energy loss to an electron in a collision with an impact-parameter s is determined as

$$T(s) = \frac{2Z_1^2}{v^2(s^2 + a^2)}, \tag{41}$$

where $a = Z_1/v^2$ is the collisional diameter. The higher order effects show up here explicitly (the adiabatic distance $s_{\mathrm{ad}} = v/\omega$, where ω is the characteristic frequency of electrons, is independent of Z_1).

The condition of applicability of the classical approach can be derived considering the energy loss to the electron wave packet. The uncertainty in transferred energy is due to uncertainty of the impact parameter s and it is determined by the width of the wave packet δs. At $s > a$ when the classical impulse approach is applicable ($T = 2Z_1^2/v^2s^2$), the resulting relative uncertainty $\delta T/T \sim \delta s/s$. On the other hand, one should also take into account that, due to the spreading of the wave packet, its width increases during the collision. The spread is determined by the dispersion of the transverse velocity (momentum) in the wave packet, $\delta p_s \sim 1/\delta s$, and by the time of collision $\tau \sim s/v$: $\delta s_{\mathrm{spr}} \sim \delta p_s \tau \sim s/v\delta s$. This results in an additional uncertainty of the energy transfer $\delta T/T \sim \delta s_{\mathrm{spr}}/s \sim 1/v\delta s$. The desired condition is a small total uncertainty of T:

$$\left(\frac{\delta s}{s}\right)^2 + \left(\frac{1}{v\delta s}\right)^2 \ll 1. \tag{42}$$

Choosing for δs the value $s_0 = (s/v)^{1/2}$ which minimizes the left-hand side of equation (42), we arrive at the condition

$$\xi = 2vs = 2s/\lambda \gg 1. \tag{43}$$

The criterion (43) differs significantly from the Bohr's criterion [8], $\eta \gg 1$, which ensures a small quantum uncertainty of the angle of electron

deflection $\Theta \approx 2Z_1/v^2 s$. Estimating the uncertainty of Θ, we should take into account an additional feature, the diffraction of the wave packet: $\delta\Theta_{\text{diffr}} = \delta p_s/v \sim 1/v\,\delta s$. Bohr's criterion is obtained from the condition that, together with the uncertainty of the impact parameter δs, this should not result in significant total uncertainty of the scattering angle Θ. It is clear, however, that the diffraction has no direct relation to the energy loss. Thus, a small value of δT can be realized simultaneously with a large $\delta\Theta$. It can be mentioned also that, in the picture of quasiclassical approach, the variable ξ can be associated with the quantum-mechanical angular momentum l of electron. Thus, the condition (43) can be considered as a condition for large effective quantum numbers l, the natural condition for applicability of the quasiclassical approach. This justifies, particularly, the classical treatment of adiabatic effects in terms of the quantum number l as it is made in Ref. [11].

Another puzzling problem can be recognized here. It is clear that, in conditions when $\delta\Theta$ is small, the energy loss can also be treated classically. According to the Bohr's criterion, this should happen simultaneously for all ξ. However, the condition (43) does not exclude significant quantum effects at small ξ, even if η is large. The data in Fig. 1 seem suggesting that this is really the case. The resolution of this contradiction is found in the above analysis of quantum effects. Really, the spreading of wave packet, considered as a source of uncertainty of energy loss, can also contribute in the uncertainty of Θ. Requiring again for small value of total uncertainty of Θ, one can easily obtain the following modification of the Bohr's criterion:

$$\sqrt{\frac{1}{v^2 s^2} + \frac{1}{\eta^2}} \ll 1. \tag{44}$$

This condition implies that, even when η is large, the classical terms are not suitable to describe the scattering on large angles. In case of Rutherford scattering this is not very important because the classical and quantum-mechanical cross-sections coincide.

Now, knowing the role of quantum effects, we can imagine how the picture of quantum perturbation approach is converted into the classical picture when the value of the parameter η increases. At large projectile velocity ($vs_{\text{ad}} = v^2/\omega \gg 1$), the adiabatic effects can be treated classically. In the pure classical description, the stopping number L is determined by the integration of equation (41)

$$L(v) = \int_0^{v/\omega} \frac{s\,\mathrm{d}s}{s^2 + a^2} \approx \ln\frac{v^3}{Z_1\omega} \tag{45}$$

($s_{\text{ad}} = v/\omega$ is assumed to be large relative to a). The collisional diameter a sets an effective lower limit in the integration (45). One may speculate, however, that at $\lambda > a$ the lower limit is determined by the quantum effects,

$s_{\min} \sim \lambda$. Therefore,

$$L(v) \approx \int_{\lambda}^{v/\omega} \frac{\mathrm{d}s}{s} = \ln \frac{v^2}{\omega}, \tag{46}$$

what coincides with the Bethe's result. Thus, it is clear that the higher order effects originate, of course, from the region of strong interaction, the close collisions in classical terms. The Bloch correction describes, in fact, in what degree the interaction in this region is modified due to the quantum spreading. It turns out that, in case of extremely large spreading (the 'ultra-quantum' limit, so to say), this spreading results in elimination of the higher order effect. In this respect, the Bethe's formula can be also seen as an ultra-quantum result (large $\hbar$) for the energy loss and the Bloch correction, as a correction to this formula, describes the emergence of classical features in the picture of dominating quantum effect.

To finish this analysis, we should also answer the question how the features described above are reproduced in the picture of the transport cross-section approach. In this approach, the energy loss in a gas of free electrons is determined by the expression

$$-\frac{\mathrm{d}E}{\mathrm{d}x} = mv^2 \rho_0 \int \mathrm{d}o \frac{\mathrm{d}\sigma_{\mathrm{tr}}^{(1)}}{\mathrm{d}o}, \qquad \frac{\mathrm{d}\sigma_{\mathrm{tr}}^{(1)}}{\mathrm{d}o} = \frac{\mathrm{d}\sigma}{\mathrm{d}o}(1 - \cos \Theta), \tag{47}$$

where ρ_0 is electron density and $\mathrm{d}\sigma/\mathrm{d}o$ the Rutherford cross-section which describes the scattering of electrons in the projectile field. Formula (47) may cause confusion [11] because, seemingly, the only dependence on Z_1 herein is the factor Z_1^2 in the Rutherford cross-section. Moreover, this does not depend on how we treat the Rutherford scattering, in quantum mechanics or classically. In the classical description, the origin of this paradox can be recognized easily: additional dependence on Z_1 appears when we take into account the adiabatic effect. This results in a lower limit in the integral (47) $\Theta_{\min} = \Theta_{\mathrm{ad}}$, where Θ_{ad} is the angle of deflection in a collision with impact parameter $s = s_{\mathrm{ad}}$, $\Theta_{\mathrm{ad}} = 2Z_1/v^2 s_{\mathrm{ad}} = 2Z_1\omega/v^3$. With this additional dependence on Z_1 we receive again the classical formula (45). However, the classical picture of scattering can be modified significantly due to diffraction of the electron wave. The angle of diffraction is estimated as $\delta\Theta_{\mathrm{diff}} \sim \delta p_s/v$, where $p_s \sim 1/s$ is the dispersion of transverse momentum. When $\delta\Theta_{\mathrm{diff}} \gg \Theta_{\mathrm{ad}}$, the effective lower limit in the integral (47) is determined by the value of $\delta\Theta_{\mathrm{diff}}$. In contrast to the classical case, this limit does not depend on Z_1 and the energy loss is determined by the Bethe's formula (46). In the case of Coulomb interaction, the inverse condition for classical treatment $\Theta_{\mathrm{ad}} \gg \Theta_{\mathrm{diff}}$ results again in Bohr's criterion $\eta \gg 1$.

The picture of the transport cross-section approach could cause serious misleading. First, it creates an illusion that the higher order effects originate from the distant collisions. In fact, as a result of the nonlinear transformation

of the impact-parameter scale ($\Theta = 2\arctan(a/s)$) the higher order effects reside now at small angles Θ. Additionally, one cannot specify with certainty at what angular range the quantum effects are localized. In fact, when η is small they are effective in the whole range of scattering angles Θ. As a result, such a treatment does not provide a definite conclusion on origin of the Bloch correction [12].

3.2. Uniform plasma of interacting electrons

3.2.1. Linear response in terms of induced currents

For our goal, the dielectric approach [5,13] is to be reformulated in terms of the induced current density $\mathbf{j}(\mathbf{r}, t)$. This can be done starting from the expression for the induced potential

$$\phi_{\text{ind}}(\mathbf{r}, t) = \frac{Z_1}{2\pi^2} \int \frac{\mathrm{d}^3\mathbf{k}}{k^2} \left(\frac{1}{\varepsilon(\mathbf{k}, \mathbf{kv})} - 1 \right) \mathrm{e}^{\mathrm{i}\mathbf{k}(\mathbf{r} - \mathbf{v}t)}, \tag{48}$$

where $\varepsilon(\mathbf{k}, \omega)$ is the dielectric function for the wave vector $\mathbf{k}$ and frequency ω of the external field. It follows from the Maxwell equations that, in order to obtain the current density, we should add an additional factor $\omega\mathbf{k}/4\pi = (\mathbf{kv})\mathbf{k}/4\pi$ in every Fourier-component of the potential (48):

$$\mathbf{j}(\mathbf{r}, t) = \frac{Z_1}{8\pi^3} \int \mathrm{d}^3\mathbf{k} \frac{(\mathbf{kv})\mathbf{k}}{k^2} \left(\frac{1}{\varepsilon(\mathbf{k}, \mathbf{kv})} - 1 \right) \mathrm{e}^{\mathrm{i}\mathbf{k}(\mathbf{r} - \mathbf{v}t)}. \tag{49}$$

Taking in equation (1) the integral over t, we arrive at the following expression for the energy loss

$$-\frac{\mathrm{d}E}{\mathrm{d}x} = \frac{2Z_1^2}{v^2} \rho \int \frac{\mathrm{d}^2\mathbf{r}_\perp}{r_\perp^2} G(\rho, v, r_\perp), \tag{50}$$

where ρ is the unperturbed density of the electron gas, the factor $G(\rho, v, r_\perp)$ is defined as

$$G(\rho, v, r_\perp) = -\frac{r_\perp^2}{2\pi^2\rho} \Im \int_0^\infty \frac{\mathrm{d}k}{k} \int_0^{kv} \mathrm{d}\omega\omega k_\parallel [k_\parallel J_0(k_\perp r_\perp) K_0(k_\parallel r_\perp) + k_\perp J_1(k_\perp r_\perp) K_1(k_\parallel r_\perp)] \left(\frac{1}{\varepsilon(\mathbf{k}, \omega)} - 1 \right). \tag{51}$$

Here $\mathbf{k} = (k_\parallel, \mathbf{k}_\perp)$, $k_\parallel = \omega/v$, $k_\perp = \sqrt{k^2 - k_\parallel^2}$, J_n and K_n are the common notations for the Bessel functions. Apart from the new correction factor $G(\rho, v, r_\perp)$, expression (50) coincides with the expression for free electrons (equation (29)). It can be anticipated that, in the present linear response approach, the factor G will take into account the quantum effects

(at small $r_\perp$) and also the screening of the projectile field due to the electron gas polarization.

The RPA dielectric function is determined by the expression [5]

$$\varepsilon(\mathbf{k},\omega) = 1 + \frac{\omega_p^2}{k^2}\sum_{\mathbf{k}_0} g(\mathbf{k}_0)\left(\frac{1}{\dfrac{(\mathbf{k}_0+\mathbf{k})^2}{2} - \dfrac{k_0^2}{2} + \omega + \mathrm{i}\delta} + \frac{1}{\dfrac{(\mathbf{k}_0+\mathbf{k})^2}{2} - \dfrac{k_0^2}{2} - \omega - \mathrm{i}\delta}\right), \tag{52}$$

where $\omega_p = \sqrt{4\pi\rho}$ is the plasma frequency of the electron gas. For a degenerate electron gas, the summation over the initial electron momenta $\mathbf{k}_0$ is restricted by the Fermi sphere, $k_0 < k_\mathrm{F} = (3\pi^2\rho)^{1/3}$, the weight factor $g(\mathbf{k}_0)$ has a constant value normalized to unity.

One may disregard the initial velocities of electrons if the projectile moves much faster. Such an approximation is obtained by putting $\mathbf{k}_0 = 0$ in all terms of the sum (52). As a result, the dielectric function obtains a simpler form:

$$\varepsilon(\mathbf{k},\omega) = 1 + \frac{\omega_p^2}{(k^2/2)^2 - (\omega + \mathrm{i}\delta)^2}. \tag{53}$$

If we will also ignore the interaction between electrons, the dielectric approach should be converted to the free electron model considered in Section 3.1.1. The simplest way to check this consists in the replacement of the factor $1/\varepsilon - 1$ (equations (49) and (51)) by $\varepsilon - 1$. As follows from the meaning of the dielectric function, such a replacement is equivalent to switching off the inter-electron interaction.

To characterize the properties of the electron gas, it is convenient to use the variable $\chi^2 = 1/\pi k_\mathrm{F}$. The value of this variable presents the ratio between the mean potential energy of nearby electrons and their kinetic energy. Also, the role of quantum effects can be characterized by the value of the parameter $y = 2v^2/\omega_p$ which is the screening distance $a_\mathrm{s} = v/\omega_p$ in units of the deBroglie wave length $\lambda = 1/v$. Instead of $r_\perp$ we again use the reduced variable $\xi = 2s/\lambda = 2vs$.

The behavior of $G(\chi, y, \xi)$ as a function of ξ is illustrated in Fig. 2. The set of curves for $v/v_\mathrm{F} = 5$ ($v_\mathrm{F} = k_\mathrm{F}$ is the Fermi velocity) and $\chi^2 = 1, 0.1, 0.01$ demonstrates the general features of the model. The exponential decrease of G at large ξ is due to the screening of the projectile Coulomb field. The value of $\xi_\mathrm{ad} = y = \sqrt{3}(v/v_\mathrm{F})^2/\chi$ is a good estimate of the distance ξ where the screening becomes effective. At small ξ, $G(\chi, y, \xi)$ behaves analogously to the case of free electrons that demonstrates the minor role of the screening in

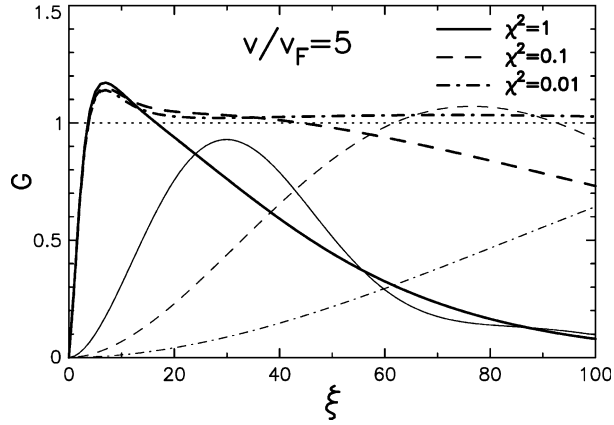

Fig. 2. The correction factor $G(\eta, \xi)$, equation (51), for the indicated values of χ. Thin curves show the contribution of plasma excitations.

close collisions. The contribution of the plasmon excitations is shown separately. As is ordinarily assumed, the generation of plasmons occurs at large distances $r_\perp \sim a_s$. At these distances the effect of inter-electron interaction becomes comparable with that produced by the projectile field. In contrast, the contribution of single electron excitations is mainly restricted to relatively small values of ξ. From Fig. 1 it is also seen that the contribution of single-electron excitations oscillates at large ξ. Such behavior is a consequence of the wave-like structure of the potential (48).

As an illustration, we present in Fig. 3 an example of the current density distribution $\mathbf{j}(\mathbf{r}, 0)$. For comparison, we also present the distribution for equivalent gas of non-interacting electrons. As it should be, the plasma oscillations behind the projectile (left-hand side of Fig. 2) are not present in this case.

3.2.2. The Barkas correction

Assuming that the screening of the projectile field takes place at large distances ($v/\omega_p \gg a$) where the picture of linear response is realized, we can combine the results of the dielectric approach with that obtained with the free electron model (Section 3.1.1). In this way, both the higher order effects and the screening can be taken into account in a general scheme. The combined model can be constructed if the dielectric approach is used to describe the current density $\mathbf{j}(\mathbf{r}, t)$ at large distances while in close surrounding of the projectile the free-electron model is applied. The similarity of the final expressions of two approaches, equations (29) and (50), provides a possibility to do this in a simple way: to present simultaneously

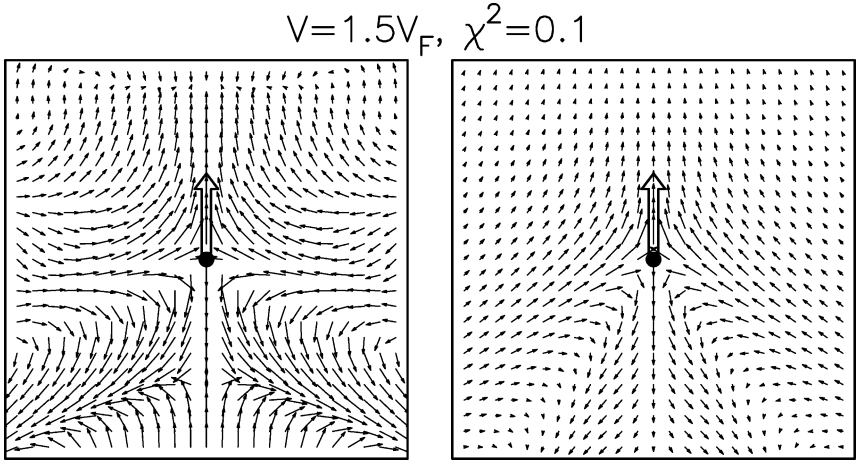

Fig. 3. The pattern of current induced in a uniform electron gas for the shown values of v and χ. The direction of projectile motion is shown by the arrow. The left-hand side of the figure presents the results of calculation using equation (4). For comparison, the same pattern for a static electron gas ($\varepsilon(\mathbf{k}, \omega)$ is defined by equation (53)) is shown on the right-hand side.

the main features of both models we can use and the common correction factor defined as

$$C(\eta, \chi, y; \xi) = Q(\eta, \xi)G(\chi, y, \xi)/Q(0, \xi), \tag{54}$$

where the factors $Q(\eta, \xi)$ and $G(\chi, y, \xi)$ are defined by equations (30) and (51).

In contrast to the free-electron model where the higher order effect, the Bloch correction, is even over the projectile charge, the combined model also yields the odd-order effect. This can be seen by comparing the behavior of the factor $Q(\eta, \xi)$ for different signs of η (Fig. 1). The factor $Q(\eta, \xi)$ demonstrates the value of higher order correction at a specific distance from the projectile trajectory ξ, the Bloch correction is obtained as the integral over all ξ. The screening results in vanishing of the contribution from large ξ. It is seen in Fig. 1 that this contribution can either be positive or negative depending on the sign of η. If the screening distance $\xi_{\text{scr}} = y = 2v^2/\omega_p$ is large, the odd-order correction can be easily estimated. With the known behavior of the factor Q at large ξ, $Q \approx 1 + 2\pi\eta/\xi$, we can determine the contribution to integral (29) from the region $\xi > \xi_{\text{scr}}$. As a result, the odd-order correction is presented by the expression

$$\Delta L_{\text{odd}} \approx -\int_{2v^2/\omega_p}^{\infty} \frac{\mathrm{d}\xi}{\xi}(Q - Q_{\text{pert}}) \approx \frac{\pi Z_1 \omega_p}{v^3}. \tag{55}$$

In its main details, this consideration is consistent with the Lindhard's interpretation of Barkas correction [14]. In this treatment, the Barkas correction (55) has a simple classical origin. As discussed in Section 3.1.1, the violation of the perturbation approach at large ξ reflects the classical effect of displacement of electrons from the initial positions. For one free electron, the total effect of displacement does not depend on the sign of Z_1 (see equation (41)). However, the transverse displacement results in a concentration of electron trajectories closer to the projectile (for a positively charged projectile, the inverse situation is realized if $Z_1 < 0$). As a result, the restriction of the interaction region due to the adiabatic effect results in asymmetry over the projectile charge. An alternative reason for the adiabatic effect is the binding of atomic electrons [15–17]. It can be recognized that, in this model, the odd-order correction reflects, in fact, the same effect of electron displacement.

4. LOCAL RESPONSE APPROACH, ENERGY LOSS TO ATOMIC ELECTRONS

According to the general expression (1), the energy loss in ion–atom collision can be found if the density of current induced in atomic shell, $\mathbf{j}(\mathbf{r}, t)$, is known. In general case, this problem can be solved only using some approximate model. In this section, we present the local response approach where the description of current density is based on the results for a uniform electron gas.

4.1. General concepts

In the local response approach, the response of each element of the atomic shell is considered to be independent of what happens at the other points. As an efficient approximation, the local response at a given point $\mathbf{r}$ (the induced current density $\mathbf{j}(\mathbf{r}, t)$) can be presented as being analogous to the response of an electron gas. The density of electron gas ρ is taken as equal to the atomic electron density $\rho_{\mathrm{at}}(\mathbf{r})$.

Having in mind this idea and assuming a straight-line trajectory of the projectile, the energy loss in ion–atom collision as a function of the impact parameter $\mathbf{b}$ can be written as

$$\Delta E(\mathbf{b}) = \frac{2Z_1^2}{v^2} \int \mathrm{d}^3\mathbf{r} \frac{\rho_{\mathrm{at}}(\mathbf{r})}{r_\perp^2} C(\eta, \chi, y; \xi), \tag{56}$$

where the distance from the projectile trajectory $r_\perp$ is determined as $r_\perp = |\mathbf{r} - (\mathbf{rv})\mathbf{v}/v^2 - \mathbf{b}|$ and the parameters χ and y are defined through the local

electron density $\rho_{at}(\mathbf{r})$. The picture presented in this approach is rather peculiar: it displays, just in terms of position, how the energy loss is distributed within the atomic shell.

Knowing the impact-parameter dependence of energy loss $\Delta E(\mathbf{b})$, we can determine the stopping cross-section:

$$S = \int \mathrm{d}^2\mathbf{b}\Delta E(\mathbf{b}) = \frac{4\pi Z_1^2 Z_2}{v^2} L(Z_1, Z_2, v), \tag{57}$$

where

$$L(Z_1, Z_2, v) = \frac{1}{Z_2} \int \mathrm{d}^3\mathbf{r}\rho_{at}(\mathbf{r})\mathscr{L}(\rho_{at}, v), \tag{58}$$

$$\mathscr{L}(\rho_{at}, v) = \int_0^\infty \frac{\mathrm{d}\xi}{\xi} C(\eta, \chi, y; \xi). \tag{59}$$

Formally, expression (58) reproduces that obtained in the Lindhard–Sharff model [18]: the stopping number for uniform electron gas is averaged over the density distribution in atomic shell. Moreover, if the linear response model is considered ($C = G$, the factor G is defined by equation (51)) the basic expression of LS model is reproduced exactly:

$$\mathscr{L}(\rho_{at}, v) = -\frac{1}{2\pi^2\rho} \Im \int_0^\infty \frac{\mathrm{d}k}{k} \int_0^{kv} \mathrm{d}\omega\omega \left(\frac{1}{\varepsilon(\mathbf{k}, \omega)} - 1 \right). \tag{60}$$

It should be noted that in the LS model intended to describe only stopping cross-section, the concept of local response is not ascertained. The only necessary information here is the local response averaged over the uniform flux of projectiles. In this respect, the present approach provides a physical basis to the LS model. Also, this model is supplied by a possibility to describe the higher order corrections over the projectile charge Z_1.

4.2. Numerical results

As an illustration of the quality of the description provided by the current density approach, we present in Fig. 4 the calculated specific energy loss of protons and antiprotons in Si and Au. The results of calculations using equations (57–59) are compared with the experimental results [19]. It is seen from the figure that at $E > 200$ keV the current density approach reproduces well the data for energy loss, particularly the higher order correction. For lower energies, we find a significant disagreement between the calculation and experimental results. It can be supposed that this insufficiency of the description is mainly due to two reasons. First, the phenomenological procedure applied when the free electron and dielectric models are combined, can fail in accuracy. At low energies, the screening radius a_s is

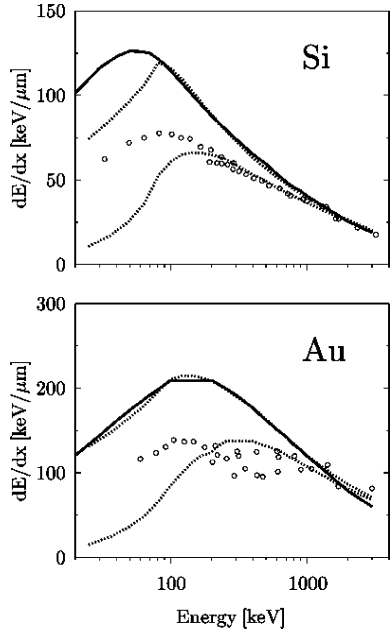

Fig. 4. Stopping power of Si and Au for protons and antiprotons. The solid curve and the points show the experimental data [19], respectively, for protons and antiprotons. Our calculations are shown by dotted curves.

small and, thus, the screening effects take place at distances where the higher order effects are also significant. It is more probable, however, that the disagreement for Si is mainly due to neglecting the solid-state effects in the electron density distribution. In the calculation, an isolated silicon atom was considered. It can be concluded, at least, that our calculations reproduce the magnitude of non-linear effect and its dependence on the projectile energy.

In Fig. 5 we show the results of calculation of the impact-parameter dependence of energy loss in collision of 100 keV protons with Ar atom. The calculations were made in the linear response approach (equations (50) and (51)). To demonstrate the effect of additional approximations, we compare this result with the calculation where the dielectric function is described by equation (53) (the static electron gas) and with calculation made in the local density approach (LDA) [20]. In the latter approach the energy loss is determined according to electron density on the ion trajectory. It is seen from the figure that both these approximations can result in significant defects of description. Particularly, the fact that the energy loss is distributed within the atomic shell (in contrast with LDA) turns out to be important.

The results of $\Delta E(b)$ calculations with the higher order effects taken into account are shown in Fig. 6. We show cases where 0.5 MeV/a.u. protons and

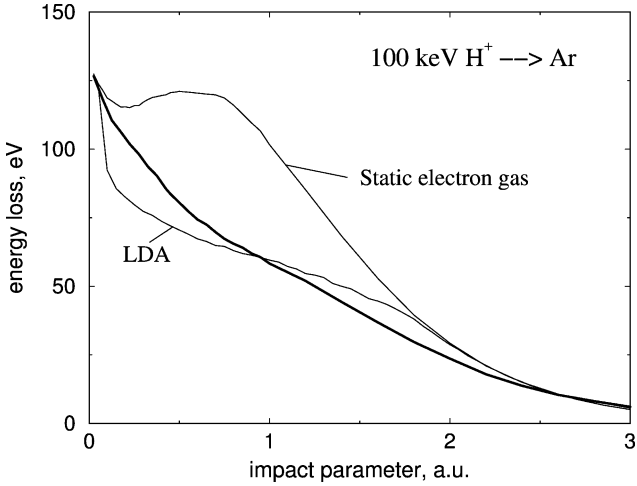

Fig. 5. Impact parameter dependence of energy loss in collisions of 100 keV protons with argon atoms determined using equation (50) with $G(\eta, \xi)$ given by equation (52) (thick curve). The results obtained in the LDA approach and that for the static electron gas ($\varepsilon(\mathbf{k}, \omega)$ is from equation (53)) are also presented in the figure.

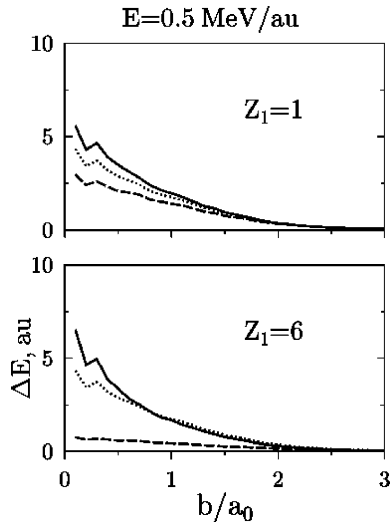

Fig. 6. The impact-parameter dependence of energy loss in collision of hydrogen and carbon ions with gold atom at a projectile energy $E = 0.5$ MeV/a.u. For comparison the first-order perturbation results (the doted curves) and that for equivalent negative projectiles (the dashed curves) are also shown.

bare carbon ions collide with a gold atom. The data obtained in the linear response approach are shown for comparison. Also, to demonstrate separately the role of Barkas correction, we present in the figure results for the equivalent negatively charged projectiles. For positively charged projectiles, the Barkas and Bloch corrections are of opposite signs and they are both negative in case of a negatively charged projectile. The consequence is seen in the figure showing that the total correction for protons and carbon ions is significantly smaller than in the case of negatively charged projectiles. The data for carbon ions show how strong the effect of charge-sign asymmetry would be if measurements with highly charged negative particles could be performed. The wiggle-like structure of the curves at small b reflects the competition between the increase of electron density and the consequent decrease of interaction efficiency, the more effective screening, when the projectile penetrates into the central part of the atomic shell.

5. ENERGY LOSS-DEFLECTION ANGLE CORRELATION

Ordinarily, the energy loss and projectile deflection in ion–atom collisions are considered as independent. Both the mean energy loss ΔE and the deflection angle $\Delta\varphi$ are assumed to be unambiguous functions of the impact parameter $\mathbf{b}$. The angle of deflection $\Delta\varphi(\mathbf{b})$ is determined by the potential of interaction of the projectile with the screened atomic nucleus. It seems that this assumption is reliable, at least for close collisions where the deflection of projectile is mainly due to the interaction with the atomic nucleus. In the case of small scattering angles $\Delta\varphi$, however, the disturbance of the projectile motion due to the interaction with atomic electrons can be significant. One cannot exclude that the angle of deflection $\Delta\varphi(\mathbf{b})$ depends significantly on the energy loss realized in the collision.

Such a correlation has been recognized in the detailed experimental results obtained using the COLTRIMS technique [22]. The same problem, referred to as three-body effect, is discussed in Ref. [23] where the experimental results for energy loss in single ion–atom collisions are presented. These results are shown in Fig. 7 together with our calculations made in the current density approach. In the experiment, the energy loss was measured as a function of scattering angle; the transformation to the impact-parameter scale was performed as in the case of potential scattering. We emphasize, however, that in this specific case such a procedure is hardly approvable. In fact, the fluctuations of the angle of deflection $\Delta\varphi$, estimated as the angle of multiple scattering on electrons $(\Delta E/M_1E)^{1/2}$, turn out to be comparable with the angles for which the energy loss has been measured.

An indication that a strong correlation exists between energy loss and projectile deflection is found when we try to describe our measurements of

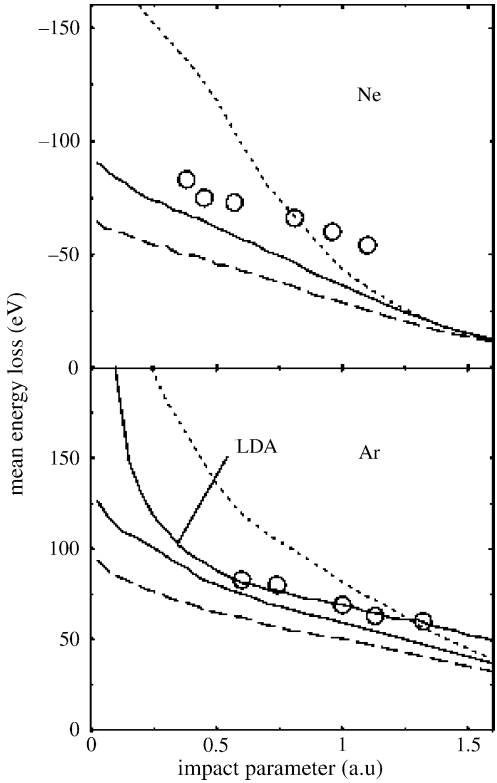

Fig. 7. Calculated $\Delta E(b)$ compared with the experimental data [23] for scattering of 100 keV proton from Ne and Ar atoms (circles). The dashed curves present the results obtained in the linear response approach. The calculations with higher order effects taken into account are shown by the solid curves. Also shown are the results of calculation in the LDA approach and that obtained in the harmonic oscillator model [21] (dotted curves).

energy loss in ion transmission through a thin gold foil [3]. The energy losses of protons, deuterons, He, Li and C ions have been measured as a function of exit angle. Figure 8 shows the experimental results for ion energies $E = 1.0$ MeV/a.u. compared with our calculations. The dependence $\Delta E(\Theta)$ is obtained by simulation of the sequence of collisions during the passage of an ion through the foil. The calculations for protons and deuterons, where the energy loss and deflection are described independently, show significant disagreement with the experimental results. It is hardly believable that the reason for this disagreement is insufficiency of the theoretical description: to improve the agreement the values of $\Delta E(b)$ at small b should be increased by an order of magnitude.

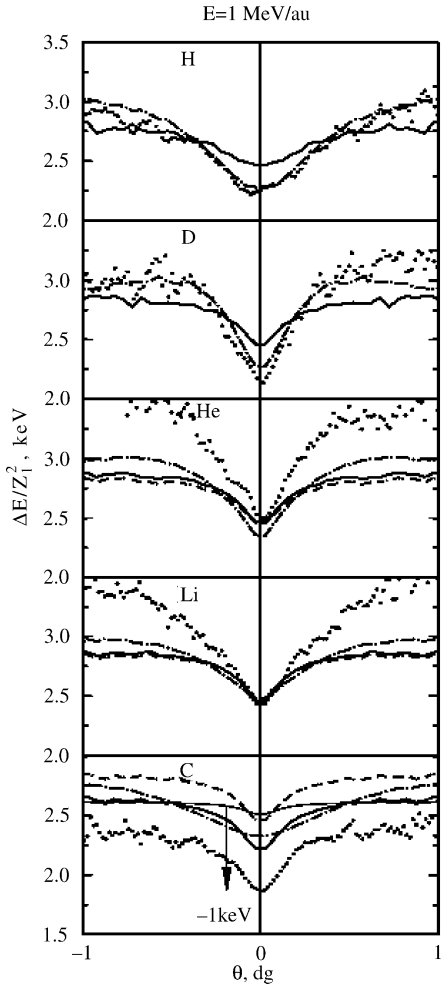

Fig. 8. Dependence of mean energy loss of ions transmitted through a 20 nm gold foil on the exit angle, $\Delta E(\Theta)$. The experimental results are shown by points. Solid curves represent the results of calculation where the energy loss and deflection are not correlated. The dashed lines present the results of linear response approach. The dot-dashed lines show the results of calculation where the correlation between energy loss and deflection is taken into account (see text). The plot for carbon ions includes the result of calculation for $Z_1 = -6$ (thin solid line).

In the calculations made, the correlation between energy loss and deflection angle is assumed to be only due to the fact that they both correspond to the same value of impact parameter **b**. However, the real dynamics of electrons is not considered in such interpretation. In this section

we present the analysis of two (seeming main) features of electron dynamics which could result in significant correlation between ΔE and $\Delta\varphi$.

5.1. Independent-electron model, the three-body effect

The fact that electron excitations influence the projectile motion is taken into account when the full quantum description of scattering is made in the Born approach. The interaction with electrons and with the atomic nucleus can be considered simultaneously if the unperturbed states of the projectile are taken as states of scattering on the atomic core (the DWBA). Assuming a large energy of the projectile, we will treat the interaction with the 'active' electron in first-order perturbation approach.

Due to the short-wave character of projectile states, the straightforward use of DWBA approach needs enormous calculation efforts. Even with an additional, eikonal, approximation [24,25], the complexity of calculations restricts significantly the possibilities of application of this approach. One can notice, however, that the promising feature of the considered problem is that the projectile motion could be described in the quasiclassical approach. This goal can be achieved in the following way [26].

In the DWBA approach, the amplitude of inelastic scattering is determined by the expression

$$A_{if,\mathbf{k}_i,\mathbf{k}_f} = 2\pi\langle \Psi^-_{\mathbf{k}_f}|U_{if}(\mathbf{R})|\Psi^+_{\mathbf{k}_i}\rangle, \tag{61}$$

where $\mathbf{R}$ is the radius-vector of the projectile, $\mathbf{k}_i$ and $\mathbf{k}_f$ its initial and final momenta, $\Psi^{+(-)}_{\mathbf{k}}(\mathbf{R})$ the distorted waves which describe the projectile scattering on the atomic core. The matrix element of electron transition $U_{if}(\mathbf{R})$ is determined by the expression

$$U_{if}(\mathbf{R}) = \int \mathrm{d}\mathbf{r}\ \psi^*_f V(\mathbf{r}-\mathbf{R})\psi_i, \tag{62}$$

where $\psi_{i(f)}$ is the wave function of initial (final) state of 'active' electron, V the potential energy of projectile–electron interaction.

To separate effectively the inter-nuclear and the projectile–electron interactions we use the closure relation to represent the amplitude (61) in the form

$$A_{if,\mathbf{k}_i\mathbf{k}_f} = 2\pi \sum_{\mathbf{k}'} \langle \Psi^-_{\mathbf{k}_f}|\Psi^+_{\mathbf{k}'}\rangle\langle \Psi^+_{\mathbf{k}'}|U_{if}(\mathbf{R})|\Psi^+_{\mathbf{k}_i}\rangle. \tag{63}$$

In such a form, the amplitude presents the scattering as a sequence of two transitions in the projectile state. The second factor in the terms of the sum (63) depends explicitly on the projectile–electron interaction. On the other

hand, the first factor, which differs from zero only at $k' = k_f$, describes the elastic scattering on the target nucleus. It is reasonable to assume that this factor presents the main effect of inter-nuclear interaction. In this case, the distorted waves in the second factor can be replaced by plane waves.

The main advantage of representation (63) is that it provides a possibility to combine the plane-wave Born approach for scattering on electrons and the well-developed approaches for elastic scattering on atomic nucleus. The correlated variations of the two factors in equation (63) for different intermediate momenta $\mathbf{k}'$ simulate the three-body effects.

The first factor in equation (63) can be expressed through the amplitude of elastic scattering on the atomic core $A_{\mathbf{k}'\mathbf{k}_f}$:

$$\langle \Psi^-_{\mathbf{k}_f} | \Psi^+_{\mathbf{k}'} \rangle = \delta(\mathbf{k}' - \mathbf{k}_f) + A_{\mathbf{k}'\mathbf{k}_f}\, \delta(|\mathbf{k}'| - |\mathbf{k}_f|). \tag{64}$$

As a result, the amplitude of inelastic collision (63) is transformed to the form

$$A_{if,\mathbf{k}_i\mathbf{k}_f} = A_e + A_{ne}, \tag{65}$$

where

$$A_e = 2\pi \langle \Psi^+_{\mathbf{k}_f} | U_{if}(\mathbf{R}) | \Psi^+_{\mathbf{k}_i} \rangle \tag{66}$$

is the amplitude of scattering on the electron and

$$A_{ne} = 2\pi \sum_{\mathbf{k}'} A_{\mathbf{k}'\mathbf{k}_f} \langle \Psi^+_{\mathbf{k}'} | U_{if}(\mathbf{R}) | \Psi^+_{\mathbf{k}_i} \rangle \tag{67}$$

is the amplitude of double scattering, on the electron and on the nucleus of the target atom. As intended, the distorted waves $\Psi^+_{\mathbf{k}}(\mathbf{R})$ in equation (67) will be replaced by the plane waves $\exp(\mathrm{i}\mathbf{k}\mathbf{R})$.

In the quasiclassical approach, the amplitude of elastic scattering is given by the expression [27]

$$A_{\mathbf{k}'\mathbf{k}_f} = \mathrm{e}^{\mathrm{i}(\mathbf{k}'-\mathbf{k}_f)\mathbf{b}+\mathrm{i}\alpha(\mathbf{b})} |A_{\mathbf{k}'\mathbf{k}_f}|, \tag{68}$$

where $\mathbf{b}$ is the classical impact parameter corresponding to the momentum transfer $\Delta\mathbf{k} = \mathbf{k}_f - \mathbf{k}'$ and the modulus of the amplitude $|A_{\mathbf{k}'\mathbf{k}_f}|$ is determined in the classical terms:

$$|A_{\mathbf{k}'\mathbf{k}_f}| = \left(\frac{b}{\sin \Delta\varphi \, \mathrm{d}\Delta\varphi / \mathrm{d}b} \right)^{1/2}. \tag{69}$$

The term $\alpha(\mathbf{b})$ in the phase of the amplitude (69) is slowly varying with $\mathbf{b}$.

The quasiclassical approach can be used to clarify the conditions for applicability of the SCA approach. To find how the corresponding expression for the differential cross-section emerges from the full quantum description, we insert the amplitude (68) in equation (67). Taking into

account that both the factor $e^{i\mathbf{k}'\mathbf{b}}$ in equation (68) and the plane-wave factor $e^{i\mathbf{k}'\mathbf{R}}$ in $\Psi^{+}_{\mathbf{k}'}(\mathbf{R})$ are rapidly oscillating with $\mathbf{k}'_{\perp}$, the transverse component of $\mathbf{k}'$, we can conclude that the summation over $\mathbf{k}'$ in equation (67) will result in a factor like $\delta(\mathbf{R}_{\perp} - \mathbf{b})$. Thus, the straight-line classical trajectory $\mathbf{R}_{\perp} = \mathbf{b}$ is selected in the integration over $\mathbf{R}$ in equation (67). It can be expected that, taking into account all features of $\Psi^{+}_{\mathbf{k}'}(\mathbf{R})$, we will receive analogous selection of the real (curved) trajectory of the projectile. Finally, according to the recipe for calculation of quasiclassical matrix elements ([28], §48), the remaining one-dimensional integral is expressed as

$$2\pi \int d\mathbf{R}\, \delta(\mathbf{R}_{\perp} - \mathbf{R}_{\perp}(t))\Psi^{+*}_{\mathbf{k}'} U_{if}(\mathbf{R})\Psi^{+}_{\mathbf{k}_i} = \int dt\, e^{i\Delta\varepsilon_{if}t} U_{if}(\mathbf{R}(t)), \quad (70)$$

where $\mathbf{R}(t)$ is the projectile classical trajectory, $\Delta\varepsilon_{if} = (k_i^2 - k_f^2)/2M_1 = \varepsilon_f - \varepsilon_i$. With this expression we receive the familiar SCA result

$$|A_{ne}|^2 = |A(\mathbf{k}_i \rightarrow \mathbf{k}_f)|^2 P_{if}(\mathbf{b}), \quad (71)$$

where $A(\mathbf{k}_i \rightarrow \mathbf{k}_f)$ is the amplitude of the elastic collision with the atomic nucleus and

$$P_{if}(\mathbf{b}) = \left| \int dt\, e^{i\Delta\varepsilon_{if}t} U_{if}(\mathbf{R}(t)) \right|^2 \quad (72)$$

the probability of electron transition.

This derivation recovers significant insufficiencies of the SCA approach, not recognized previously. First, the contribution of the Born term A_e is totally absent in the SCA cross-section. This is contrary to the common view that, for a heavy projectile, the SCA and Born approaches are equivalent in the description of the total cross-section of excitation. The second (natural) conclusion is that SCA can be used only if $\Delta E = \varepsilon_{if} \ll E = k_i^2/2M_1$. This condition follows from the condition of applicability of the quasiclassical approach [28]. The condition is rather critical, its violation results in an exponential decrease of the amplitude A_{ne}.

To take into account the three-body effect we should calculate accurately the sum over $\mathbf{k}'$ in equation (67). Figure 9 presents the energy spectra of ejected electrons for fixed angles of the projectile deflection. The contributions of two terms in the scattering amplitude (65) are shown separately by the thin (A_{ne}) and dashed (A_e) lines. The interference of these terms has been neglected in the calculations, the quasiclassical phase $\alpha(\mathbf{b})$ in equation (68) has significant uncertainties. It is seen from the figure that, at large $\Delta\varphi$, the spectra of electrons are mainly concentrated at small energies. In general, the spectra resemble those realizing in collisions with free electrons, the large angle deviations of the projectile occur mainly due to the

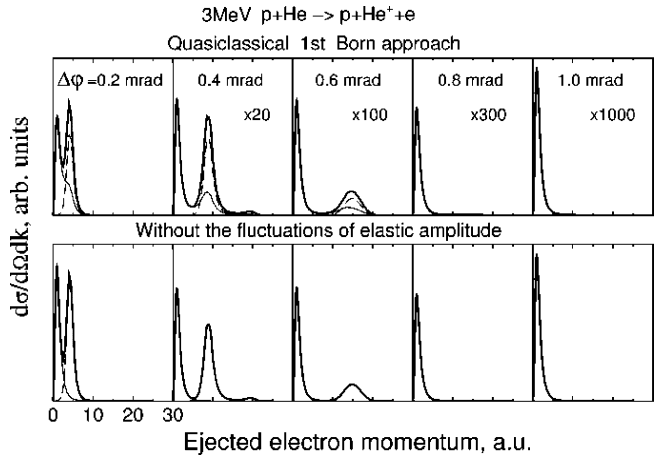

Fig. 9. The momentum distribution of ejected electrons in collisions of 3 MeV protons with He atom for different angles of deflection of the projectile $\Delta\varphi$.

inter-nuclear interaction. On the other hand, the small-angle deflection can be either due to the scattering on atomic nucleus or be the result of a close collision with electron. The competition of these two possibilities is well seen at small $\Delta\varphi$. The contribution of the Born amplitude A_e results in the formation of separate peaks (the Bethe ridge). Interestingly, at $\Delta\varphi = 0.4$ mrad, a third peak at higher energies is recognized. This peak can be interpreted as a result of two successive collisions: a violent collision with the electron resulting in a large deflection angle of the projectile and a collision with the atomic nucleus which results in opposite deflection. At the lower part of Fig. 9 we present the results of calculations where, in the amplitude A_{ne} (equation (68)), the dependence on $\mathbf{k}'$ is left only in the exponential factor. These results show that the variation of module of the scattering amplitude does not play an important role.

Figure 10 demonstrates the consequences of the three-body effect in energy loss. In these calculations only the contribution of ionization was considered. The marked difference with the results of the first-order Born approach is seen at all $\Delta\varphi$. This is just a consequence of the difference in the energy spectra shown in Fig. 9. The boundary angle for Born approach (≈ 0.5 mrad) is marked by a noticeable change in behavior of $\langle \Delta E \rangle(\Delta\varphi)$. As is seen in Fig. 10, the SCA approach strongly fails in description of energy loss at small scattering angles. The corresponding impact parameters are too large for electrons to be excited.

The three-body effect modifies mainly the scatterings on small angles. This can be significant for data presented in Fig. 7. On the other hand, the exit angular dependence of energy loss in thin foil (Fig. 8) reflects mainly the

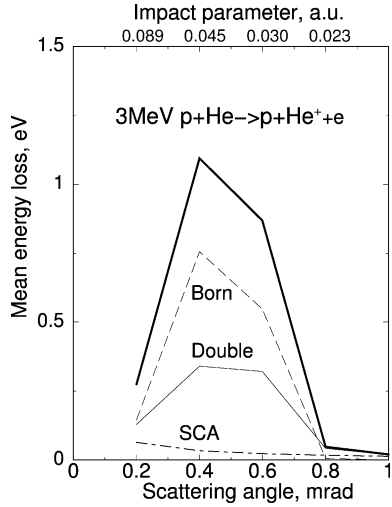

Fig. 10. The mean energy loss of 3 MeV protons as a function of the angle of scattering from He atom. The contributions of the Born, A_e, and the double-scattering, A_{ne}, amplitudes are shown separately. The results of the SCA approach, where the energy loss and deflection angle are considered to be independent, are also shown.

energy losses in close ion–atom collisions which is hardly influenced by the three-body effect.

5.2. Effect of entanglement of atomic electron states

The one-electron model considered in Section 5.1 does not take into account the entanglement of states of atomic electrons. The possible consequence of the entanglement is recognized in the first-order plane-wave Born approach. Considering elastic scattering, we receive in this approach the familiar picture: the scattering in the screened potential of atomic nucleus. However, the picture looks different in the case of inelastic collision, the interaction with atomic nucleus becomes ineffective and, in the independent-electron model, the interaction with all electrons except the one that is excited is also non-effective. As a result, the scattering looks like the scattering on a one-electron wave packet.

When the inter-nuclear interaction is strong (large Z_1Z_2/v) the problem cannot be treated in the first-order perturbation approach. At least, this is not allowed for large-angle scattering. Instead, we can apply the distorted wave approach. In this approach the unperturbed states of the projectile are described by Coulomb scattering waves: $\psi^+_{\mathbf{p}}(\mathbf{R})$ and $\psi^-_{\mathbf{p}'}(\mathbf{R})$, respectively, for the initial and final states. Here, $\mathbf{p}$ and $\mathbf{p}'$ are the initial and final momenta of

the projectile. In the general form the state of the whole system can be written as

$$\Psi^{\pm}(\mathbf{R};\mathbf{r}_1,\mathbf{r}_2,\ldots)=(\mathbf{I}+\mathscr{G}^{\pm}V+(\mathscr{G}^{\pm}V)^2+\cdots)\Psi_0^{\pm}(\mathbf{R};\mathbf{r}_1,\mathbf{r}_2,\ldots), \quad (73)$$

where $\mathscr{G}^{\pm}=(E-H\pm \mathrm{i}\varepsilon)^{-1}$ is the Green function of the unperturbed Hamiltonian H and $\Psi_0^{\pm}$ is the unperturbed state of the system.

The sum in the right-hand side of equation (73) describes the perturbation of the scattering at atomic nucleus due to the multiple scattering on electrons. In the first approximation, the scattering matrix is determined as

$$T_{i\mathbf{p},f\mathbf{p}'}=\delta_{if}(\psi_{\mathbf{p}'}^{-},\psi_{\mathbf{p}}^{+})+\langle f\mathbf{p}'|V|i\mathbf{p}\rangle, \quad (74)$$

where i and f designate the initial and final states of electrons.

An important conclusion can be obtained when the unperturbed states of atomic electrons are described by the Hartree model

$$\phi_{i(f)}(\mathbf{r}_1,\mathbf{r}_2,\ldots)=\varphi_{i_1(f_1)}(\mathbf{r}_1)\varphi_{i_2(f_2)}(\mathbf{r}_2)\cdots, \quad (75)$$

where φ_k are the states of electrons in the self-consistent potential of the atom. For elastic collisions ($i=f$, $p=p'$), the second term in equation (74) describes the effect of screening of the atomic nucleus by the electrons. Due to the additive character of the perturbation $V=\sum V_i$, the screening potential is presented as a sum of contributions of all electrons.

This conclusion breaks down in the case of inelastic collisions. Here, the only contribution to the scattering amplitude is from the second term in equation (74). After the integration over the electron coordinates it can be written as

$$T_{i\mathbf{p},\,f\mathbf{p}'}=(\psi_{\mathbf{p}'}^{-},V_{i_n,f_n}\psi_{\mathbf{p}}^{+}), \quad (76)$$

where

$$V_{i_n,f_n}(\mathbf{R})=(\varphi_{f_n}(\mathbf{r}_\mathbf{n}),-\frac{Z_1}{|\mathbf{R}-\mathbf{r}_\mathbf{n}|}\varphi_{i_n}(\mathbf{r}_\mathbf{n})). \quad (77)$$

Here, the excitation of the atomic electron shell is considered as an excitation of one, nth, electron. Due to the orthogonality of φ_{f_n} and φ_{i_n}, the interaction with all other electrons in equation (76) does not contribute to the transition amplitude. The rapidly oscillating character of the wave functions $\psi_{\mathbf{p}'}^{-}$ and $\psi_{\mathbf{p}}^{+}$ makes the matrix element (76) difficult to estimate. However, based on the quasi-classical interpretation of the scattering states (73), we may arrive at the following. Equation (76) describes the Rutherford scattering of the projectile on the atomic nucleus, disturbed by the

interaction with only one (excited) electron according to the effective perturbation (77). The main conclusion is that the screening by the remaining electrons turns out to be ineffective.

It could be expected that the promotion to larger deflection angles when the target atom is excited will result in a sharpening of the calculated curves $\Delta E(\Theta)$ shown in Fig. 8. To follow these conclusions in the simulation of ion transmission through the foil, we need to know the full probability of atom excitation. To estimate this probability, we can associate it with the probability to find an electron close to the projectile trajectory. It has been found that the final results are weakly dependent on how we define the maximum distance for excitation. The corresponding simulation of ion transmission through the foil was made. The results shown in Fig. 8 were obtained assuming the boundary energy for excitation to be equal to the mean ionization potential $I = 10Z_2$ eV [10]. The improved agreement with the experiment seems to indicate that the effect of entanglement is really visible in the hydrogen ion–atom collisions.

For heavier ions, the remaining disagreement seems indicative that the local response approach for description of the induced current is not accurate enough to reproduce the higher order effects in energy loss (the main attention should be given to the shape of the curves in Fig. 8, some uncertainty in vertical position of experimental results can be due to the uncertainty of the foil thickness in different measurements). The quality of description of stopping cross-section (Fig. 4) suggests that, mostly, the approach reproduces the current density distribution well. It is not guaranteed, however, that this approach is applicable to describe the currents induced in the region close to the atomic nucleus.

6. FINAL REMARKS AND CONCLUSION

The current density approach is shown to be effective in the analysis of the stopping phenomenon and also presents itself as a method for realistic description of experimental results. In the case of a uniform electron gas, the combination of free-electron and dielectric models provides a possibility to take into account both the higher order effects and the screening of the projectile field. In addition, the free-electron model provides a possibility to analyze, in detail, the role of quantum effects. It has been shown that origin of the Bloch correction is closely related to this problem. The results for uniform electron gas can be used to describe the energy loss in atomic substances if, additionally, the local response approach is applied. The Lindhard–Sharff model can be considered as a particular case where electron dynamics is treated in the linear response approach.

It has been found that, being well appropriate to describe the total stopping cross-section, the current density approach shows a dramatic

disagreement with data on the impact-parameter of energy loss. In order to find a reason for this disagreement, we analyze effects which could result in violation of the unique relation between energy loss and angle of deflection. Specifically, the three-body effect and the fact that the states of atomic electrons are entangled can result in significant correlation between energy loss and deflection. With these effects taken into account, a better agreement with the experimental results is achieved.

The remaining disagreement for ions with $Z_1 > 1$ can be attributed to insufficiencies of description of the current density in the internal region of atomic shell. The local response approximation, the most critical in the density functional theory, could fail in this region due to the fast variation of electron density. However, to make this conclusion certain and to improve the description, additional efforts are necessary in both the experimental and theoretical study. As a further development of the theoretical approach, we can consider the possibility to use TDDFT to treat the current density distribution more properly. Particularly, this is the way to estimate the role of exchange and correlation effects.

ACKNOWLEDGEMENTS

The author gratefully acknowledges the hospitality extended to him during his stay at the Centro de Micro-Análisis de Materiales, Universidad Autónoma de Madrid. I thank D. O. Boerma for his valuable discussions and reading of the manuscript.

REFERENCES

[1] V. A. Khodyrev, *J. Phys. B*, 2000, **33**, 5045.
[2] V. A. Khodyrev, *Phys. Scr.*, 2001, **64**, 53.
[3] V. A. Khodyrev, W. M. Arnoldbik, G. A. Iferov and D. O. Boerma, *Nucl. Instrum. Methods B*, 2000, **164/165**, 191.
[4] S. K. Ghosh and A. K. Dhara, *Rev. Rev. A*, 1988, **38**, 1149.
[5] J. Lindhard and K. Dan, *Vidensk. Selsk. Mat.-Fys. Medd.*, 1954, **28** (8).
[6] M. Abramowitz and I. A. Stegun, *Handbook of Mathematical Functions*, Dover, New York, 1972.
[7] V. A. Khodyrev and E. I. Sirotinin, *Phys. Status Solidi B*, 1983, **116**, 659.
[8] N. Bohr and K. Dan, *Vidensk. Selsk. Mat.-Fys. Medd.*, 1948, **24** (19).
[9] A. Nordsieck, *Phys. Rev.*, 1954, **93**, 785.
[10] F. Bloch, *Ann. Phys. (Leipzig)*, 1933, **16**, 285.
[11] J. Lindhard and A. H. Sørensen, *Phys. Rev. A*, 1996, **53**, 2443.
[12] A. H. Sørensen, *Phys. Rev. A*, 1997, **55**, 2896.
[13] J. Lindhardi, A. Winther and K. Dan, *Vidensk. Selsk. Mat.-Fys. Medd.*, 1964, **34** (4).
[14] J. Lindhard, *Nucl. Instrum. Methods*, 1976, **132**, 1.

[15] J. C. Ashley, R. H. Ritchie and W. Brandt, *Phys. Rev. B*, 1972, **5**, 2393.
[16] J. C. Ashley, R. H. Ritchie and W. Brandt, *Phys. Rev. A*, 1973, **8**, 2402.
[17] J. D. Jackson and R. L. McCarthy, *Phys. Rev. B*, 1972, **6**, 4131.
[18] J. Lindhard, M. Sharff and K. Dan, *Vidensk. Selsk. Mat.-Fys. Medd.*, 1953, **27** (15).
[19] S. P. Moller, E. Uggerhoj, H. Bluhme, H. Knudsen, U. Mikkelsen, K. Paludan and E. Morenzoni, *Phys. Rev. A*, 1997, **56**, 2930.
[20] H. Ascolani and N. R. Arista, *Phys. Rev. A*, 1986, **33**, 2352.
[21] E. H. Mortinsen, H. H. Mikkelsen and P. Sigmund, *Nucl. Instrum. Methods B*, 1991, **61**, 139.
[22] J. Ullrich, R. Moshammer, R. Dörner, O. Jagutzki, V. Mergel, H. Schmidt-Böcking and L. Spielberger, *J. Phys. B*, 1997, **30**, 2917.
[23] C. Auth and H. Winter, *Nucl. Instrum. Methods B*, 1994, **93**, 123.
[24] A. Salin, *J. Phys. B*, 1989, **22**, 3901.
[25] H. Fukuda, I. Shimamura, L. Végh and T. Watanabe, *Phys. Rev. A*, 1991, **44**, 1565.
[26] V.A. Khodyrev, *International Conference on the Physics of Highly Charged Ions and Atomic Collisions*, Book of Abstract, University de Caen, 2002, p. 102.
[27] R. G. Newton, *Scattering Theory of Waves and Particles*, McGraw-Hill, New York, 1968.
[28] L. D. Landau and E. M. Lifshitz, *Quantum Mechanics*, Pergamon Press, Oxford, 1977.

The Use of Green's Functions in the Calculation of Proton Stopping Power

E. J. McGuire

Ejmcguire Physics Research, 3567 Sequoia Pl NW, Albuquerque, NM 87120, USA

Abstract

The generalized oscillator strength formulation of the plane wave Born approximation to the calculation of stopping power is modified by introducing radial Green's functions in place of the infinite sums over bound excited states and integrations over the continuum. Some properties of the resulting expressions are examined.

Contents

1. INTRODUCTION

The Bethe theory [1] of stopping power is the asymptotic limit of the plane wave Born approximation (pwBa). The pwBa should then provide accurate stopping powers at intermediate and high-projectile energies, reproduce the Bethe theory results asymptotically, provide results that can be compared with experiments without semi-empirical parameterizations, and incorporate stopping power into the general body of ion–atom interaction physics. Over many years I have calculated stopping power [2,3] using the pwBa in the generalized oscillator strength (GOS) formalism, i.e., the matrix element of $\exp[i\mathbf{k}\cdot\mathbf{r}]$ between all occupied and unoccupied orbitals. The GOS can be used to calculate cross-sections for subshell inelastic processes with electrons, protons, and structured [4] projectiles. The individual cross-sections can be tested against experiment, e.g., using subshell fluorescence yields. There are a number of problems with the pwBa applied to heavy particle interactions [3] and in stopping power. It is well established at

ADVANCES IN QUANTUM CHEMISTRY, VOLUME 45
ISSN: 0065-3276 DOI 10.1016/S0065-3276(04)45007-2

intermediate energies for bare projectiles of charge Z incident on hydrogen that the ionization cross-section divided by Z^2 is not independent of Z, as it must be in the pwBa, but decreases monotonically with Z [5]. This, and other effects discussed in Ref. [3], suggests that the theory must go beyond the pwBa. In the jargon of stopping power theory this dependence on Z beyond Z^2 is known as the Barkas (Z^3) and Bloch (Z^4) effects. This is an intermediate energy effect. Measurements of these effects in energy loss require greater precision than in ionization cross-section measurements because energy-loss measurements sum over atomic subshells. At high energies in stopping power, the discrepancy [6] between calculated (for atoms) and measured (on solids) Bethe mean excitation energies, I, remains an open question. The discrepancy does not appear to have an obvious analog in ion–atom cross-section physics which leads this author to suspect that the discrepancy is an artifact of the corrections used in analyzing the data. Alternatively, it has been suggested [7] that the discrepancy arises from the neglect of correlations in the ground state wavefunction of the atom, i.e., the atomic calculations are incorrect if correlations are neglected. Calculations with this hypothesis have been performed for Be [7] where the discrepancy is particularly strong, but with additional hypotheses. It has been suggested that the discrepancy represents a real difference between stopping power in atoms and solids [8], but no calculations have been carried out with this hypothesis. Finally the Bethe–Born theory appears not to apply to plasmas without additional corrections [9,10].

In the GOS calculations themselves there are numerical problems [11] with continuum orbitals of high angular momentum, l, and high scaled energy, $\varepsilon/E_{nl} > 25$, where E_{nl} is a bound subshell ionization energy. At high ε/E_{nl} and k^2/E_{nl} the GOS is dominated by the Bethe ridge, i.e., sharply peaked at $\varepsilon = k^2$. Approximations to the Bethe ridge, e.g., delta functions or hydrogenic values must be sutured to numerical calculations in a manner that preserves sum rules. This adds unphysical structure to the GOS [11].

Here, I present an alternative computational scheme that replaces the sum over all unoccupied states in the GOS approach with a characteristic Green's function. That is, the sum over discrete and continuum excited states is eliminated, reducing the numerical complexity, i.e., the detailed GOS approach is sufficient to calculate stopping power but is not necessary. Further, the approach allows the separation of the calculation into radial integrals involving products of ground state orbitals, Green's functions evaluated at ground state orbital energies and a pwBa operator. This should allow relatively straightforward calculations with different ground state orbitals, e.g., using the Wigner–Seitz model to study the difference between atomic and solid state stopping power, and using an ion sphere model to make a similar comparison for plasmas.

2. INTRODUCTION OF THE GREEN'S FUNCTION

The contribution of electrons in the nl subshell to proton stopping power can be written in terms of the GOS [2] as

$$-\frac{1}{n}\frac{\mathrm{d}E}{\mathrm{d}x}\bigg|_{nl} = 4\pi a_0^2\left(\frac{M_\mathrm{p}}{m_\mathrm{e}}\right)\frac{1}{E_\mathrm{p}}B_{nl} \tag{1a}$$

where

$$B_{nl} = \sum_{n'l'}\int_{K^2_{\min}}^{K^2_{\max}} \mathrm{d}q^2 \frac{f_{nl,n'l'}(q^2)}{q^2} + \int_0^{E_\mathrm{p}-E_{nl}} \mathrm{d}\varepsilon \int_{K^2_{\min}}^{K^2_{\max}} \mathrm{d}q^2 \frac{1}{q^2}\frac{\mathrm{d}f_{nl}(\varepsilon l', q^2)}{\mathrm{d}\varepsilon} \tag{1b}$$

where E_p and M_p are the proton energy and mass, E_{nl} is the subshell ionization energy, $f_{nl,n'l'}(q^2)$ is the calculated GOS from occupied or partially occupied subshell (with n_{nl} of a maximum N_{nl} electrons) to partially occupied or unoccupied level, $n'l'$, and

$$K^2|_{\max,\min} = \frac{M_\mathrm{p}}{m_\mathrm{e}}\left\{\sqrt{E_\mathrm{p}} \pm \sqrt{E_\mathrm{p} - \Delta E_{nl}}\right\}^2 \tag{1c}$$

with $\Delta E_{nl} = E_{n'l'} - E_{nl}$ for excitation and $\Delta E_{nl} = |E_{nl}| + \varepsilon$ for ionization. All energies and squared momentum transfers are in Rydbergs. Suppose we define a least momentum transfer squared, L^2, by

$$L^2|_{\max,\min} = \frac{M_\mathrm{p}}{m_\mathrm{e}}\left\{\sqrt{E_\mathrm{p}} \pm \sqrt{E_\mathrm{p} - (\Delta E_{nl})_{\min}}\right\}^2 \tag{2a}$$

then we may rewrite equation (1b) as

$$\begin{aligned} B_{nl} = &\sum_{n'l'}\int_{L^2_{\min}}^{L^2_{\max}} \mathrm{d}q^2 \frac{f_{nl,n'l'}(q^2)}{q^2} \\ &+ \sum_{l'}\int_0^{E_\mathrm{p}-E_{nl}} \mathrm{d}\varepsilon \int_{L^2_{\min}}^{L^2_{\max}} \mathrm{d}q^2 \frac{1}{q^2}\frac{\mathrm{d}f_{nl}(\varepsilon l', q^2)}{\mathrm{d}\varepsilon} + C^1_{nl} + C^2_{nl} \end{aligned} \tag{2b}$$

where

$$\begin{aligned} C^1_{nl} = &\sum_{n'l'}\int_{L^2_{\min}}^{K^2_{\min}} \mathrm{d}q^2 \frac{f_{nl,n'l'}(q^2)}{q^2} \\ &+ \sum_{l'}\int_0^{E_\mathrm{p}-E_{nl}} \mathrm{d}\varepsilon \int_{L^2_{\min}}^{K^2_{\min}} \mathrm{d}q^2 \frac{1}{q^2}\frac{\mathrm{d}f_{nl}(\varepsilon l', q^2)}{\mathrm{d}\varepsilon} \end{aligned} \tag{2c}$$

and

$$C_{nl}^2 = \sum_{n'l'} \int_{L_{\max}^2}^{K_{\max}^2} \mathrm{d}q^2 \frac{f_{nl,n'l'}(q^2)}{q^2} + \sum_{l'} \int_0^{E_p - E_{nl}} \mathrm{d}\varepsilon \int_{L_{\max}^2}^{K_{\max}^2} \mathrm{d}q^2 \frac{1}{q^2} \frac{\mathrm{d}f_{nl}(\varepsilon l', q^2)}{\mathrm{d}\varepsilon} \tag{2d}$$

Next, if we take the upper limit to infinity in the integral over ε in equation (2b), we have

$$B_{nl} = \sum_{n'l'} \int_{L_{\min}^2}^{L_{\max}^2} \mathrm{d}q^2 \frac{f_{nl,n'l'}(q^2)}{q^2} + \sum_{l'} \int_0^{\infty} \mathrm{d}\varepsilon \int_{L_{\min}^2}^{L_{\max}^2} \mathrm{d}q^2 \frac{1}{q^2} \frac{\mathrm{d}f_{nl}(\varepsilon l', q^2)}{\mathrm{d}\varepsilon} + C_{nl}^1 + C_{nl}^2 - C_{nl}^3 \tag{3a}$$

where

$$C_{nl}^3 = \sum_{l'} \int_{E_p - E_{nl}}^{\infty} \mathrm{d}\varepsilon \int_{L_{\min}^2}^{L_{\max}^2} \mathrm{d}q^2 \frac{1}{q^2} \frac{\mathrm{d}f_{nl}(\varepsilon l', q^2)}{\mathrm{d}\varepsilon} \tag{3b}$$

The one electron GOS for transitions to the continuum is given by

$$\frac{\mathrm{d}f_{nl}(\varepsilon l', k^2)}{\mathrm{d}\varepsilon} = |\langle nl|\mathrm{e}^{\mathrm{i}\mathbf{k}\cdot\mathbf{r}}|\varepsilon l'\rangle|^2 \frac{(|E_{nl}| + \varepsilon)}{k^2} \tag{4a}$$

where $|E_{nl}| + \varepsilon = \varepsilon - E_{nl}$, since E_{nl} is negative. With the expansion of the exponential term in terms of Legendre polynomials and spherical Bessel functions, the matrix element can be reduced to

$$\langle nl|\mathrm{e}^{\mathrm{i}\mathbf{k}\cdot\mathbf{r}}|\varepsilon l'\rangle = \sum_{t=0}^{L(l,l')} C(l, l', t) \int_0^{\infty} j_{|l'-l|+2t}(kr)\phi_{nl}(r)\phi_{\varepsilon l'}(r)\mathrm{d}r \tag{4b}$$

where $j_s(x)$ is a spherical Bessel function, $L(x, y)$ is the lesser of x or y, and the coefficients, $C(l, l', t)$ are given in Refs. [12,13]. When $l = l'$, $t = 0$, and $k \rightarrow 0$, the Bessel function in equation (4b) $\rightarrow 1$, and the integral should vanish by orthogonality. To insure that this occurs numerically I have used the device

$$j_0(kr) \rightarrow j_0(kr) - 1 \tag{4c}$$

in equation (4b). At small argument $j_0(kr) - 1 \approx -(kr)^2/6$. This will be important later in the analysis.

The one electron orbitals in equation (4b) satisfy the differential equations

$$\left\{\frac{\mathrm{d}^2}{\mathrm{d}r^2} + \frac{2Z(r)}{r} - \frac{l(l+1)}{r^2} - |E_{nl}|\right\}\phi_{nl}(r) = 0 \tag{5a}$$

and

$$\left\{\frac{\mathrm{d}^2}{\mathrm{d}r^2} + \frac{2Z(r)}{r} - \frac{l'(l'+1)}{r^2} + \varepsilon\right\}\phi_{\varepsilon l'}(r) = 0 \tag{5b}$$

Multiply equation (5a) by $j_s(x)\phi_{\varepsilon l'}$, and equation (5b) by $j_s(x)\phi_{nl}$ and subtracting leads to

$$\begin{aligned} & j_s(kr)\left[\phi_{nl}(r)\frac{\mathrm{d}^2\phi_{\varepsilon l'}(r)}{\mathrm{d}r^2} - \phi_{\varepsilon l'}(r)\frac{\mathrm{d}^2\phi_{nl}(r)}{\mathrm{d}r^2}\right] \\ & \quad - \frac{[l'(l'+1) - l(l+1)]}{r^2} j_s(kr)\phi_{nl}(r)\phi_{\varepsilon l'}(r) \\ & \quad = -(\varepsilon + |E_{nl}|) j_s(kr)\phi_{nl}(r)\phi_{\varepsilon l'}(r) \end{aligned} \tag{6a}$$

But

$$\begin{aligned} & j_s(kr)\left[\phi_{nl}(r)\frac{\mathrm{d}^2\phi_{\varepsilon l'}(r)}{\mathrm{d}r^2} - \phi_{\varepsilon l'}(r)\frac{\mathrm{d}^2\phi_{nl}(r)}{\mathrm{d}r^2}\right] \\ & \quad = \frac{\mathrm{d}}{\mathrm{d}r}\left\{j_s(kr)\left[\phi_{nl}(r)\frac{\mathrm{d}\phi_{\varepsilon l'}(r)}{\mathrm{d}r} - \phi_{\varepsilon l'}(r)\frac{\mathrm{d}\phi_{nl}(r)}{\mathrm{d}r}\right]\right\} \\ & \quad\quad - \frac{\mathrm{d}j_s(kr)}{\mathrm{d}r}\left[\phi_{nl}(r)\frac{\mathrm{d}\phi_{\varepsilon l'}(r)}{\mathrm{d}r} - \phi_{\varepsilon l'}(r)\frac{\mathrm{d}\phi_{nl}(r)}{\mathrm{d}r}\right] \end{aligned} \tag{6b}$$

Inserting equation (6b) into equation (6a) and integrating over r leads to

$$\begin{aligned} & -(\varepsilon + |E_{nl}|)\int_0^\infty \mathrm{d}r\, j_s(kr)\phi_{nl}(r)\phi_{\varepsilon l'}(r) \\ & \quad = j_s(kr)\left[\phi_{nl}(r)\frac{\mathrm{d}\phi_{\varepsilon l'}(r)}{\mathrm{d}r} - \phi_{\varepsilon l'}(r)\frac{\mathrm{d}\phi_{nl}(r)}{\mathrm{d}r}\right]\Bigg|_0^\infty \\ & \quad\quad - \int_0^\infty \mathrm{d}r\left\{\frac{\mathrm{d}j_s(kr)}{\mathrm{d}r}\left[\phi_{nl}(r)\frac{\mathrm{d}\phi_{\varepsilon l'}(r)}{\mathrm{d}r} - \phi_{\varepsilon l'}(r)\frac{\mathrm{d}\phi_{nl}(r)}{\mathrm{d}r}\right]\right. \\ & \quad\quad\quad \left. + \frac{[l'(l'+1) - l(l+1)]}{r^2} j_s(kr)\phi_{nl}(r)\phi_{\varepsilon l'}(r)\right\} \end{aligned} \tag{7a}$$

The first term on the right hand side (RHS) of equation (7a) vanishes at infinity since ϕ_{nl} is a bound orbital. It vanishes at $r = 0$ since the minimum s is $l' - l$ and at small r, $j_{l'-l}(kr)$ is proportional to $r^{l'-l}$ if $l' \geq l$, and proportional to $r^{l-l'-1}$ if $l' < l$, while $\phi_{nl}\phi_{l'}$ is proportional to $r^{l+l'+2}$, and

$\phi\,\mathrm{d}\phi/\mathrm{d}r$ is proportional to $r^{l+l'+1}$. Then at small r the first term is proportional to $r^{2l'+1}$ if $l' \geq l$, and r^{2l} if $l' < l$. But if $l' < l$, then $l \geq 1$. Thus the first term on the RHS of equation (7a) vanishes at $r = 0$. Further, integrating by parts leads to

$$-\int_0^\infty \mathrm{d}r \frac{\mathrm{d}j_s(kr)}{\mathrm{d}r}\phi_{nl}(r)\frac{\mathrm{d}\phi_{\varepsilon l'}(r)}{\mathrm{d}r}$$

$$= -\phi_{nl'}(r)\phi_{\varepsilon l'}(r)\frac{\mathrm{d}j_s(kr)}{\mathrm{d}r}\bigg|_0^\infty + \int_0^\infty \mathrm{d}r\ \phi_{\varepsilon l'}(r)\frac{\mathrm{d}}{\mathrm{d}r}\left[\phi_{nl}(r)\frac{\mathrm{d}j_s(kr)}{\mathrm{d}r}\right] \quad (7b)$$

By the arguments given above the first term on the RHS of equation (7b) vanishes at the upper and lower limits, so that

$$\int_0^\infty \mathrm{d}r \frac{\mathrm{d}j_s(kr)}{\mathrm{d}r}\phi_{nl}(r)\frac{\mathrm{d}\phi_{\varepsilon l'}(r)}{\mathrm{d}r}$$

$$= \int_0^\infty \mathrm{d}r\ \phi_{\varepsilon l'}(r)\left[\frac{\mathrm{d}\phi_{nl}(r)}{\mathrm{d}r}\frac{\mathrm{d}j_s(kr)}{\mathrm{d}r} + \phi_{nl}(r)\frac{\mathrm{d}^2 j_s(kr)}{\mathrm{d}\,r^2}\right]$$

$$= \int_0^\infty \mathrm{d}r\ \phi_{\varepsilon l'}(r)\left\{\frac{\mathrm{d}\phi_{nl}(r)}{\mathrm{d}r}\frac{\mathrm{d}j_s(kr)}{\mathrm{d}r} + \phi_{nl}(r)\left[\frac{-2}{r}\frac{\mathrm{d}j_s(kr)}{\mathrm{d}r} - k^2 j_s(kr) + \frac{s(s+1)}{r^2}j_s(kr)\right]\right\} \quad (7c)$$

Then

$$-(\varepsilon + |E_{nl}|)\int_0^\infty \mathrm{d}r j_s(kr)\phi_{nl}(r)\phi_{\varepsilon l'}(r)$$

$$= -\int_0^\infty \mathrm{d}r\left[-2\frac{\mathrm{d}\phi_{nl'}(r)}{\mathrm{d}r}\frac{\mathrm{d}j_s(kr)}{\mathrm{d}r} + \phi_{nl}(r)\left(\frac{2}{r}\frac{\mathrm{d}j_s(kr)}{\mathrm{d}r} + \left\{k^2 - \frac{[s(s+1)+l(l+1)-l'(l'+1)]}{r^2}\right\}j_s(kr)\right)\right]\phi_{\varepsilon l'}(r) \quad (8a)$$

or

$$\int_0^\infty \mathrm{d}r j_s(kr)\phi_{nl}(r)\phi_{\varepsilon l'}(r) = \frac{1}{(\varepsilon + |E_{nl}|)}\int_0^\infty \mathrm{d}r\, T(k,nl,l',t,r)\phi_{\varepsilon l'}(r) \quad (8b)$$

where

$$T(k,nl,l',t,r)$$

$$= -2\frac{\mathrm{d}\phi_{nl}(r)}{\mathrm{d}r}\frac{\mathrm{d}j_s(kr)}{\mathrm{d}r} + \phi_{nl}(r)\left(\frac{2}{r}\frac{\mathrm{d}j_s(kr)}{\mathrm{d}r} + \left\{k^2 - \frac{[s(s+1)+l(l+1)-l'(l'+1)]}{r^2}\right\}j_s(kr)\right) \quad (8c)$$

Note that

$$T(-k,nl,l',t,r)=(-1)^s T(k,nl,l',t,r) \tag{8d}$$

where $s=l'-l+2t$.

Then equation (4b) becomes

$$\begin{aligned}\langle nl|\mathrm{e}^{\mathrm{i}\mathbf{k}\cdot\mathbf{r}}|\varepsilon l'\rangle &= \sum_{t=0}^{l} C(l,l',t)\int_0^\infty j_{l'-l+2t}(kr)\phi_{nl}(r)\phi_{\varepsilon l'}(r)\mathrm{d}r \\ &= \sum_{t=0}^{l}\frac{C(l,l',t)}{(\varepsilon+|E_{nl}|)}\int_0^\infty T(k,nl,l',t,r)\phi_{\varepsilon l'}(r)\mathrm{d}r \\ &= \sum_{t=0}^{l}\frac{C(l,l',t)}{(\varepsilon-E_{nl})}\int_0^\infty T(k,nl,l',t,r)\phi_{\varepsilon l'}(r)\mathrm{d}r \end{aligned} \tag{9}$$

As a result the first two terms on the RHS of equation (3a) can be written as

$$\begin{aligned} B_{\mathrm{M}}(nl) &= \sum_{n'l'}\int_{L_{\min}^2}^{L_{\max}^2}\frac{\mathrm{d}q^2}{q^2}f_{nl,n'l'}(q^2)+\sum_{l'}\int_0^\infty \mathrm{d}\varepsilon\int_{L_{\min}^2}^{L_{\max}^2}\frac{\mathrm{d}q^2}{q^2}\frac{\mathrm{d}}{\mathrm{d}\varepsilon}f_{nl}(\varepsilon l',q^2) \\ &= \sum_{l'}\int_{L_{\min}^2}^{L_{\max}^2}\frac{\mathrm{d}q^2}{q^4}\sum_{t=0}^{l}C(l,l',t)\sum_{t'=0}^{l}C(l,l',t') \\ &\quad\times\int_0^\infty \mathrm{d}r\int_0^\infty \mathrm{d}r'\,T(q,nl,l',t,r)T(q,nl,l',t',r') \\ &\quad\times\left[\sum_{n'}\frac{\phi_{n'l'}(r)\phi_{n'l'}(r')}{(E_{n'l'}-E_{nl})}+\int_0^\infty \mathrm{d}\varepsilon\frac{\phi_{\varepsilon l'}(r)\phi_{\varepsilon l'}(r')}{(\varepsilon-E_{nl})}\right] \end{aligned} \tag{10}$$

But the last term in equation (10) is the modified Green's function, i.e., 'modified' since it is a sum over excited one electron orbitals and does not include occupied orbitals. To proceed further I replace E_{nl} in equation (10) with F_{nl}, where $F_{nl}=E_{nl}+\delta$ and the limit $\delta\to 0$ is taken at the end of the calculation. That is, the solution to the equation

$$\frac{1}{r}\frac{\mathrm{d}^2}{\mathrm{d}r^2}[rg_l(r,r',E)]+\left[\frac{2Z(r)}{r}-\frac{l(l+1)}{r^2}+E\right]g_l(r,r',E)=\frac{\delta(r-r')}{r^2} \tag{11a}$$

is

$$g_l(r,r',E)=-\left[\sum_{\text{all }m}\frac{\phi_{ml}(r)\phi_{ml}(r')}{(E_{ml}-E)}+\int_0^\infty \mathrm{d}\varepsilon\frac{\phi_{\varepsilon l}(r)\phi_{\varepsilon l}(r')}{(\varepsilon-E)}\right] \tag{11b}$$

where $\phi_{ml}(r)$ satisfies

$$\frac{1}{r}\frac{\mathrm{d}^2}{\mathrm{d}r^2}[r\phi_{ml}(r)]+\left[\frac{2Z(r)}{r}-\frac{l(l+1)}{r^2}+E_{ml}\right]\phi_{ml}(r)=0 \tag{11c}$$

Then

$$\sum_{n'}\frac{\phi_{n'l'}(r)\phi_{n'l'}(r)}{(E_{n'l'}-F_{nl})}+\int_0^\infty\frac{\phi_{\varepsilon l'}(r)\phi_{\varepsilon l'}(r')}{(\varepsilon-F_{nl})}$$
$$=-g_{l'}(r,r',F_{nl})+\sum_{\text{occupied }m}\frac{\phi_{ml'}(r)\phi_{ml'}(r')}{(E_{ml'}-F_{nl})} \tag{12a}$$

so that equation (10) becomes

$$B_{\mathrm{M}}(nl)=B_{\mathrm{G}}(nl)+B_{\mathrm{IS}}(nl) \tag{12b}$$

where

$$B_{\mathrm{G}}(nl)=-\sum_{l'}\int_{L^2_{\min}}^{L^2_{\max}}\frac{\mathrm{d}q^2}{q^4}\sum_{t,t'=0}C(l,l',t)C(l,l',t')$$
$$\times\int_0^\infty\mathrm{d}r\int_0^\infty\mathrm{d}r'\,T(q,nl,l',t,r)T(q,nl,l',t',r')$$
$$\times\left[g_{l'}(r,r',F_{nl})-\delta_{l,l'}\frac{\phi_{nl}(r)\phi_{nl}(r')}{(E_{nl}-F_{nl})}\right] \tag{12c}$$

and

$$B_{\mathrm{IS}}(nl)=\sum_{l'}\int_{L^2_{\min}}^{L^2_{\max}}\frac{\mathrm{d}q^2}{q^4}\sum_{t,t'=0}^{l}C(l,l',t)C(l,l',t')$$
$$\times\int_0^\infty\mathrm{d}r\int_0^\infty\mathrm{d}r'\,T(q,nl,l',t,r)T(q,nl,l',t',r')$$
$$\times\sum_{\text{occupied }m,ml'\neq nl}\frac{\phi_{ml'}(r)\phi_{ml'}(r')}{(E_{ml'}-F_{nl})} \tag{12d}$$

Equation (11b) is merely notational; one still has an infinite sum and an infinite integral. The advantage in using a Green's function is that one can replace the eigenfunction expansion for the Green's function with the characteristic Green's function, i.e., $g_{l'}(r,r',E_{nl})=\phi_{l'}(r_<,E_{nl})\psi_{l'}(r_>,E_{nl})$ where $\phi_{l'}(r,E_{nl})$ and $\psi_{l'}(r_>,E_{nl})$ are the regular and irregular solutions to equation (11c), and the arguments contain the smaller and larger of r, r',

respectively. The infinite sum and infinite integral are no longer required in the Green's function. The Green's functions are readily calculated [14].

3. THE 'CORRECTION' TERMS TO ORDER $1/E_{\mathrm{p}}$

Consider first C_{nl}^{1} in equation (2c). For sufficiently large E_{p} both $K^2|_{\min}$ and $L^2|_{\min}$ are small for $\varepsilon < 10E_{nl}$. For $\varepsilon > 10E_{nl}$, the GOS decreases as $1/\varepsilon^{3+\alpha}$ for q^2/E_{nl} small, where $\alpha \geq 0$. Then for the contribution of the low energy GOS we can use

$$K^2|_{\min} = \left(\frac{M_{\mathrm{p}}}{m_{\mathrm{e}}}\right)\left\{\sqrt{E_{\mathrm{p}}} - \sqrt{E_{\mathrm{p}} - \Delta E_{nl}}\right\}^2 = \left(\frac{M_{\mathrm{p}}}{m_{\mathrm{e}}}\right)\frac{(\Delta E_{nl})^2}{E_{\mathrm{p}}}\left(1 + \frac{\Delta E_{nl}}{2E_{\mathrm{p}}}\right) \tag{13a}$$

$$\begin{aligned} L^2|_{\min} &= \left(\frac{M_{\mathrm{p}}}{m_{\mathrm{e}}}\right)\left\{\sqrt{E_{\mathrm{p}}} - \sqrt{E_{\mathrm{p}} - (\Delta E_{nl})_{\min}}\right\}^2 \\ &= \left(\frac{M_{\mathrm{p}}}{m_{\mathrm{e}}}\right)\frac{[(\Delta E_{nl})_{\min}]^2}{E_{\mathrm{p}}}\left(1 + \frac{(\Delta E_{nl})_{\min}}{2E_{\mathrm{p}}}\right) \end{aligned} \tag{13b}$$

and

$$\frac{\mathrm{d}}{\mathrm{d}\varepsilon} f_{nl}(\varepsilon l', q^2) = \frac{\mathrm{d}}{\mathrm{d}\varepsilon} f_{nl}(\varepsilon l', 0) + q^2 \frac{\mathrm{d}}{\mathrm{d}q^2}\frac{\mathrm{d}}{\mathrm{d}\varepsilon} f_{nl}(\varepsilon l', q^2)\bigg|_{q^2=0} \tag{13c}$$

Thus, to order $1/E_{\mathrm{p}}$, the contribution of the low energy GOS to C_{nl}^{1} is

$$\begin{aligned} C_{nl}^{1} = &\sum_{n'l'} f_{nl,n'l'}(0)\ln\left(\frac{K_{\min}^2}{L_{\min}^2}\right) + \sum_{l'}\int_0^{E_{\mathrm{p}}-E_{nl}} \mathrm{d}\varepsilon \frac{\mathrm{d}}{\mathrm{d}\varepsilon} f_{nl}(\varepsilon l', 0)\ln\left(\frac{K_{\min}^2}{L_{\min}^2}\right) \\ &+ \sum_{n'l'} \frac{\mathrm{d}}{\mathrm{d}q^2} f_{nl,n'l'}(q^2)\bigg|_{q^2=0} (K_{\min}^2 - L_{\min}^2) \\ &+ \sum_{l'}\int_0^{E_{\mathrm{p}}-E_{nl}} \mathrm{d}\varepsilon \frac{\mathrm{d}}{\mathrm{d}q^2}\frac{\mathrm{d}}{\mathrm{d}\varepsilon} f_{nl}(\varepsilon l', q^2)\bigg|_{q^2=0} (K_{\min}^2 - L_{\min}^2) \end{aligned} \tag{14}$$

The first two terms in equation (14) are

$$C_{nl}^{1} = 2Z_{nl}[\ln(I_{nl}) - \ln|(\Delta E_{nl})_{\min}|] + \frac{Z_{nl}}{2E_{\mathrm{p}}}[J_{nl} - (\Delta E_{nl})_{\min}] \tag{15a}$$

where

$$Z_{nl} = \sum_{n'l'} f_{nl,n'l'}(0) + \sum_{l'} \int_0^\infty \mathrm{d}\varepsilon \frac{\mathrm{d}}{\mathrm{d}\varepsilon} f_{nl}(\varepsilon l', 0) \tag{15b}$$

$$Z_{nl} \ln(I_{nl}) = \sum_{n'l'} f_{nl,n'l'}(0) \ln|E_{n'l'} - E_{nl}| + \sum_{l'} \int_0^\infty \mathrm{d}\varepsilon \frac{\mathrm{d}}{\mathrm{d}\varepsilon} f_{nl}(\varepsilon l', 0) \ln(\varepsilon + E_{nl}) \tag{15c}$$

and

$$Z_{nl} J_{nl} = \sum_{n'l'} f_{nl,n'l'}(0) |E_{n'l'} - E_{nl}| + \sum_{l'} \int_0^\infty \mathrm{d}\varepsilon \frac{\mathrm{d}}{\mathrm{d}\varepsilon} f_{nl}(\varepsilon l', 0)(\varepsilon + E_{nl}) \tag{15d}$$

Taking the upper limit as ∞ in equations (15a–d) rather than $E_\mathrm{p} - E_{nl}$ introduces a $1/(E_\mathrm{p})^2$ term. The last two terms in equation (14) are

$$\frac{M_\mathrm{p}}{m_\mathrm{e}} \frac{\mathrm{D}_{nl}}{E_\mathrm{p}} \{\Delta^2 - [(\Delta E_{nl})_{\min}]^2\} \tag{16a}$$

where

$$\mathrm{D}_{nl} = \sum_{n'l'} \frac{\mathrm{d}}{\mathrm{d}q^2} f_{nl,n'l'}(q^2)\bigg|_{q^2=0} + \sum_{l'} \int_0^\infty \mathrm{d}\varepsilon \frac{\mathrm{d}}{\mathrm{d}q^2} \frac{\mathrm{d}}{\mathrm{d}\varepsilon} f_{nl}(\varepsilon l', q^2)\bigg|_{q^2=0} \tag{16b}$$

and

$$D_{nl}\Delta^2 = \sum_{n'l'} \frac{\mathrm{d}}{\mathrm{d}q^2} f_{nl,n'l'}(q^2)\bigg|_{q^2=0} |E_{n'l'} - E_{nl}| + \sum_{l'} \int_0^\infty \mathrm{d}\varepsilon \frac{\mathrm{d}}{\mathrm{d}q^2} \frac{\mathrm{d}}{\mathrm{d}\varepsilon} f_{nl}(\varepsilon l', q^2)\bigg|_{q^2=0} (\varepsilon + E_{nl})^2 \tag{16c}$$

At large ε the generalized oscillator is sharply peaked at $\varepsilon = q^2$, the Bethe ridge. To simplify the analysis I choose it to be a delta function normalized to n_{nl}, and assume that this approximation introduces terms that drop off faster than $1/E_\mathrm{p}$: I discuss this elsewhere [15]. Then the high

energy contribution to C_{nl}^1 is

$$n_{nl}\int_0^{E_p-E_{nl}}\frac{d\varepsilon}{\varepsilon}\theta(K^2|_{\min}-\varepsilon)=n_{nl}\int_{4E_pM_p/m_e}^{E_p-E_{nl}}\frac{d\varepsilon}{\varepsilon}=n_{nl}\ln\left[\frac{m_e}{4M_p}\frac{(E_p-E_{nl})}{E_p}\right]$$
$$\approx -n_{nl}\ln\left(\frac{4M_p}{m_e}\right)-n_{nl}\frac{E_{nl}}{E_p} \tag{17}$$

Similarly, $L^2|_{\max}$ is so large that only the Bethe ridge contributes to C_{nl}^2.

$$C_{nl}^2=n_{nl}\int_0^{E_p-E_{nl}}\frac{d\varepsilon}{\varepsilon}\theta(\varepsilon-L^2|_{\max}) \tag{18}$$

But the condition in the step function of equation (18) is $\varepsilon\geq 4(M_p/m_e)E_p$ which is impossible since $\varepsilon\leq E_p-|E_{nl}|$. Thus, C_{nl}^2 can be neglected to order $1/E_p$.

Lastly for C_{nl}^3, by the same reasoning

$$C_{nl}^3=n_{nl}\int_{E_p-E_{nl}}^{\infty}\frac{d\varepsilon}{\varepsilon}\theta(L^2|_{\max}-\varepsilon)=n_{nl}\int_{E_p-E_{nl}}^{4E_pM_p/m_e}\frac{d\varepsilon}{\varepsilon}$$
$$=n_{nl}\ln\left[\frac{4M_p}{m_e}\frac{E_p}{(E_p-E_{nl})}\right] \tag{19}$$

But this is minus the high-energy contribution to C_{nl}^1. Then the sum of the correction terms is

$$C_{nl}^1+C_{nl}^2-C_{nl}^3=2Z_{nl}[\ln(I_{nl})-\ln|(\Delta E_{nl})_{\min}|]$$
$$-2n_{nl}\ln\left(\frac{4M_p}{m_e}\right)-2n_{nl}\frac{E_{nl}}{E_p}+\frac{Z_{nl}}{2E_p}[J_{nl}-(\Delta E_{nl})_{\min}]$$
$$+\frac{M_p}{m_e}\frac{D_{nl}}{E_p}\left\{\Delta^2-[(\Delta E_{nl})_{\min}]^2\right\} \tag{20}$$

4. THE STRUCTURE OF THE GREEN'S FUNCTION TERM

Some of the structure of the integral over q in equation (12c) can be found analytically. In general, we want to isolate the terms that contribute to order $1/E_p$ or lower. In addition we want to show that there are no divergences. Using the differential expression

$$\frac{d}{dr}j_s(qr)=\frac{s}{r}j_s(qr)-qj_{s+1}(qr) \tag{21a}$$

one can write

$$T(q, nl, l', t, r) = a_1(r) j_s(qr) + q a_2(r) j_{s+1}(qr) + q^2 \phi_{nl}(r) j_s(qr) \tag{21b}$$

where

$$a_1(r) = -\frac{2s}{r}\frac{\mathrm{d}}{\mathrm{d}r}\phi_{nl}(r) + \frac{2s}{r^2}\phi_{nl}(r) - \frac{[s(s+1) + l(l+1) - l'(l'+1)]}{r^2}\phi_{nl}(r) \tag{21c}$$

and

$$a_2(r) = 2\frac{\mathrm{d}}{\mathrm{d}r}\phi_{nl}(r) - \frac{2}{r}\phi_{nl}(r) \tag{21d}$$

Then in the integral over q in equation (12c) the integrand is

$$\begin{aligned}
&\frac{T(q, nl, l', t, r) T(q, nl, l', t', r')}{q^3} \\
&= \frac{a_1(r) a_1(r') j_s(qr) j_{s'}(qr')}{q^3} \\
&\quad + \frac{1}{q^2}[a_1(r) a_2(r') j_s(qr) j_{s'+1}(qr') + a_2(r) a_1(r') j_{s+1}(qr) j_{s'}(qr')] \\
&\quad + \frac{1}{q}[a_1(r)\phi_{nl}(r') + \phi_{nl}(r) a_1(r')] j_s(qr) j_{s'}(qr') \\
&\quad + \frac{1}{q} a_2(r) a_2(r') j_{s+1}(qr) j_{s'+1}(qr') + a_2(r)\phi_{nl}(r') j_{s+1}(qr) j_{s'}(qr') \\
&\quad + \phi_{nl}(r) a_2(r') j_s(qr) j_{s'+1}(qr') + q\phi_{nl}(r)\phi_{nl}(r') j_s(qr) j_{s'}(qr')
\end{aligned} \tag{22}$$

Because of their possible divergence at large q, we are initially interested in the final three terms, i.e., those proportional to $1/q$, q^0 and q. First, I define a cut-off $Q(s, s')$, e.g., the second zero of $j_S(z)$ where S is the larger of s or s'. For $q > Q(s, s')$, the first two terms of the asymptotic expansion are

$$j_s(qr) = \frac{1}{qr}\left\{\left[1 + \frac{b(s)}{(qr)^2}\right]\sin(qr - \pi s/2) + \frac{a(s)}{qr}\cos(qr - \pi s/2)\right\} \tag{23a}$$

where

$$a(s) = s(s+1)/2 \tag{23b}$$

and

$$b(s) = -(s-1)s(s+1)(s+2)/8 \tag{23c}$$

Then the terms proportional to $1/q$ in equation (22) have a leading term of the form

$$\frac{j_s(qr)j_{s'}(qr')}{q} \approx \frac{1}{rr'}\frac{1}{q^3}\sin(qr-\pi s/2)\sin(qr'-\pi s'/2)$$

$$\approx \frac{1}{2rr'}\frac{(-1)^{t-t'}}{q^3}\cos[q(r-r')] \tag{24a}$$

which when integrated by parts over q in equation (12c) is

$$\frac{(-1)^{t-t'}}{2rr'}\int_{Q(s,s')}^{L_{\max}^2}\frac{\mathrm{d}q}{q^3}\cos[q(r-r')]$$

$$= \frac{(-1)^{t-t'}}{2rr'}\left[\frac{\sin[q(r-r')]}{q^3(r-r')}\right]\Bigg|_{Q(s,s')}^{L_{\max}^2}$$

$$+ \frac{3(-1)^{t-t'}}{2rr'(r-r')}\int_{Q(s,s')}^{L_{\max}^2}\frac{\mathrm{d}q}{q^4}\sin[q(r-r')] \tag{24b}$$

which, ostensibly, goes as $1/q^3$ at large q, i.e., drops off faster than $1/E_{\mathrm{p}}$. However, at $r = r'$, equation (24b) becomes

$$-\frac{(-1)^{t-t'}}{2rr'}\frac{1}{2q^2}\Bigg|_{Q(s,s')}^{L_{\max}^2} = \frac{(-1)^{t-t'}}{2rr'}\frac{1}{q^2}\Bigg|_{Q(s,s')}^{L_{\max}^2} - \frac{3}{4}\frac{(-1)^{t-t'}}{2rr'}\frac{1}{q^2}\Bigg|_{Q(s,s')}^{L_{\max}^2}$$

$$= -\frac{(-1)^{t-t'}}{2rr'}\frac{1}{2q^2}\Bigg|_{Q(s,s')}^{L_{\max}^2} \tag{24c}$$

That is, one must keep this $1/q$ term if one wants to isolate explicitly terms which drop off as $1/E_{\mathrm{p}}$; i.e., one uses

$$\int_{Q(s,s')}^{L_{\max}^2}\mathrm{d}q\frac{j_s(qr)j_{s'}(qr')}{q}$$

$$= \frac{(-1)^{t-t'}}{2rr'}\left[\frac{\sin[q(r-r')]}{q^3(r-r')}\right]\Bigg|_{Q(s,s')}^{L_{\max}^2} + \frac{3(-1)^{t-t'}}{2rr'(r-r')}\int_{Q(s,s')}^{L_{\max}^2}\frac{\mathrm{d}q}{q^4}\sin[q(r-r')]$$

$$+ \int_{Q(s,s')}^{L_{\max}^2}\mathrm{d}q\left[\frac{j_s(qr)j_{s'}(qr')}{q} - \frac{(-1)^{t-t'}}{2rr'}\frac{\cos[q(r-r')]}{q^3}\right] \tag{24d}$$

The terms proportional to q^0 in equation (22) are of the form

$$\begin{aligned} & j_s(qr)j_{s'+1}(qr') \\ & \quad \approx \frac{1}{rr'}\frac{1}{q^2}\sin(qr-\pi s/2)\sin(qr'-\pi(s'+1)/2) \\ & \quad = \frac{1}{rr'}\frac{1}{q^2}\cos\left[q(r-r')-(s-s')\frac{\pi}{2}+\frac{\pi}{2}\right] \\ & \quad = \frac{1}{2rr'}\frac{(-1)^{t-t'}}{q^2}\cos\left[q(r-r')+\frac{\pi}{2}\right] = -\frac{(-1)^{t-t'}}{2rr'q^2}\sin[q(r-r')] \end{aligned} \tag{25a}$$

and

$$\begin{aligned} & \frac{(-1)^{t-t'}}{2rr'}\int_{Q(s,s')}^{L_{\max}^2}\frac{\mathrm{d}q}{q^2}\sin[q(r-r')] \\ & \quad = \frac{(-1)^{t-t'}}{2rr'}\left[\frac{\cos[q(r-r')]}{q^2(r-r')}\right]\Bigg|_{Q(s,s')}^{L_{\max}^2} \\ & \qquad + \frac{2(-1)^{t-t'}}{2rr'(r-r')}\int_{Q(s,s')}^{L_{\max}^2}\frac{\mathrm{d}q}{q^3}\cos[q(r-r')] \end{aligned} \tag{25b}$$

In this case, at $r = r'$, equation (25b) remains proportional to $1/E_{\mathrm{p}}$. Then here we use

$$\begin{aligned} & \int_{Q(s,s')}^{L_{\max}^2}\mathrm{d}q\, j_s(qr)j_{s'+1}(qr') \\ & \quad = \frac{(-1)^{t-t'}}{2rr'}\left[\frac{\cos[q(r-r')]}{q^2(r-r')}\right]\Bigg|_{Q(s,s')}^{L_{\max}^2} + \frac{(-1)^{t-t'}}{rr'(r-r')}\int_{Q(s,s')}^{L_{max}^2}\frac{\mathrm{d}q}{q^3}\cos[q(r-r')] \\ & \qquad + \int_{Q(s,s')}^{L_{\max}^2}\mathrm{d}q\left[j_s(qr)j_{s'}(qr') + \frac{(-1)^{t-t'}}{2rr'q^2}\sin[q(r-r')]\right] \end{aligned} \tag{25c}$$

The terms proportional to q in equation (22) are of the form

$$\begin{aligned} qj_s(qr)j_{s'}(qr) \approx \frac{(-1)^{t-t'}}{2rr'q}\Bigg\{ & \sin[q(r-r')] + \frac{1}{q}\left[\frac{a(s')}{r'} - \frac{a(s)}{r}\right]\sin[q(r-r')] \\ & + \frac{1}{q^2}\left[\frac{a(s)a(s')}{rr'} + \frac{b(s)}{r^2} + \frac{b(s')}{(r')^2}\right]\cos[q(r-r')]\Bigg\} \end{aligned} \tag{26a}$$

and the integral by parts of the RHS of equation (26a) is

$$R(t,t',r,r') = \frac{(-1)^{t-t'}}{2rr'}\left(\left[\frac{\sin[q(r-r')]}{q(r-r')}\right]\Bigg|_{Q(s,s')}^{L^2_{\max}} + \frac{1}{(r-r')}\int_{Q(s,s')}^{L^2_{\max}}\frac{\mathrm{d}q}{q^2}\sin[q(r-r')] - \left[\frac{a(s')}{r'} - \frac{a(s)}{r}\right] \times\left\{\left[\frac{\cos[q(r-r')]}{q^2(r-r')}\right]\Bigg|_{Q(s,s')}^{L^2_{\max}} + \frac{2}{(r-r')}\int_{Q(s,s')}^{L^2_{\max}}\frac{\mathrm{d}q}{q^3}\cos[q(r-r')]\right\} + \left[\frac{a(s)a(s')}{rr'} + \frac{b(s)}{r^2} + \frac{b(s')}{(r')^2}\right]\left\{\left[\frac{\sin[q(r-r')]}{q^3(r-r')}\right]\Bigg|_{Q(s,s')}^{L^2_{\max}} + \frac{3}{(r-r')}\int_{Q(s,s')}^{L^2_{\max}}\frac{\mathrm{d}q}{q^4}\sin[q(r-r')]\right\}\right) \tag{26b}$$

Note that at $r = r'$ the first term in equation (26b) vanishes, i.e., $1|_a^b = 0$ while the second term is $\ln(q)|_{Q(s,s')}^{L^2_{\max}}$, i.e., a term diverging as $\ln(E_\mathrm{p})$. Thus we have

$$\int_{Q(s,s')}^{L^2_{\max}}\mathrm{d}q\, qj_s(qr)j_{s'}(qr) = R(t,t',r,r') + \int_{Q(s,s')}^{L^2_{\max}}\mathrm{d}q\Bigg(qj_s(qr)j_{s'}(qr) - \frac{(-1)^{t-t'}}{2rr'}\frac{1}{q}\Bigg\{\cos[q(r-r')] + \frac{1}{q}\left[\frac{a(s')}{r'} - \frac{a(s)}{r}\right] \times\sin[q(r-r')] + \frac{1}{q^2}\left[\frac{a(s)a(s')}{rr'} + \frac{b(s)}{r^2} + \frac{b(s')}{(r')^2}\right] \times\cos[q(r-r')]\Bigg\}\Bigg) \tag{26c}$$

Finally at small q, the first term in equation (22), $a_1(r)a_1(r')j_s(qr)j_{s'}(qr')/q^3$, nominally leads to a $1/q^3$ dependence for $s = s' = 0$, but $1/q$, i.e., logarithmic if $s \neq s'$. But as discussed near equation (4c) for $s = 0$ we replace $j_0(qr)$ with $j_0(qr) - 1$ (to enforce orthogonality), which goes as $-(qr)^2/6$, reducing the integrand to $1/q$. Thus at small q there is no worse than a $1/q$ dependence in the integrand.

5. SUMMARY

There are several positive features of the Green's function approach to pwBa stopping power. (1) We have eliminated the sums over bound states and the integrals over the continuum, i.e., we can calculate stopping power in

the pwBa without using the GOS. (2) The evaluations at high energy using a delta function approximation are with upper and lower limits, $K^2_{\max}$ and $L^2_{\max}$, which both go to ∞ with E_p, unlike formulations [16] that use an intermediate cut-off fixed in q^2. Similarly, the optical limit approximation is used with upper and lower limits, $K^2_{\min}$ and $L^2_{\min}$, which are small. (3) Models other than the free electron atom can be evaluated with an order of magnitude less calculation than in the full GOS formulation of pwBa stopping power.

The negative feature is that we are still left with I_{nl} values from integrals over optical oscillator strengths. The structure of the Green's function result in equation (12c) suggest that the stopping power of a ground state atom should be a function of ground state orbitals and Green's functions only. The I_{nl} value is a ground state property and one would hope that it could be calculated with ground state orbitals and Green's functions, i.e., the optical oscillator strength is sufficient to calculate I_{nl} but not necessary. However, the proof of this conjecture remains elusive.

Numerical results will be presented elsewhere.

REFERENCES

[1] H. A. Bethe, *Ann. Phys. (Leipzig)*, 1930, **5**, 325. H. A. Bethe, *Z. Phys.*, 1932, **76**, 293.
[2] E. J. McGuire, *Phys. Rev. A*, 1971, **3**, 267.
[3] E. J. McGuire, *Phys. Rev. A*, 1997, **56**, 488.
[4] D. R. Bates, in *Atomic and Molecular Processes* (ed. D. R. Bates), Academic Press, New York, 1962.
[5] M. B. Shah and H. B. Gilbody, *J. Phys. B*, 1982, **15**, 413.
[6] J. L. Dehmer, M. Inokuti and R. P. Saxon, *Phys. Rev. A*, 1975, **12**, 102.
[7] J. Oddershede and J. R. Sabin, *Phys. Rev. A*, 1989, **39**, 5565.
[8] M. Inokuti, *Radiat. Effects Defects Solids*, 1991, **117**, 143.
[9] F. C. Young, D. Mosher, S. J. Stephanakis, S. A. Goldstein and T. A. Mehlhorn, *Phys. Rev. Lett.*, 1982, **49**, 549.
[10] J. N. Olsen, T. A. Mehlhorn, J. Maenchen and D. J. Johnson, *J. Appl. Phys.*, 1985, **58**, 2958.
[11] E. J. McGuire, to be published.
[12] E. J. McGuire, *Phys. Rev. A*, 1977, **16**, 62.
[13] E. J. McGuire, *Phys. Rev. A*, 1979, **20**, 445.
[14] E. J. McGuire, *Phys. Rev. A*, 1981, **23**, 4186.
[15] E. J. McGuire, to be published.
[16] A. Dalgarno, in *Atomic and Molecular Processes* (ed. D. R. Bates), Academic Press, New York, 1962.

Charge Exchange Processes in Low Energy Ion–Metal Collisions

R. C. Monreal and F. Flores

Departamento de Física Teórica de la Materia Condensada C-V, Universidad Autónoma de Madrid, E-28049 Madrid, Spain

Abstract

Charge exchange processes in low energy ion scattering are analyzed and some case study systems (H and He scattered off metals) are discussed in detail. For the He^+/Al system, we show that Hagstrum's neutralization model holds if the ion perpendicular energy is smaller than 100 eV. For larger energies, He^+ penetrates the metal surface layer and resonant processes become operative; then charge exchange processes have to be analyzed combining the Auger and resonant mechanisms. For the H/Al system, charge exchange can be understood considering only the resonant mechanism. The ion levels and the ion–metal interactions necessary for calculating the charge exchange processes in the He/Al and H/Al systems, are also presented in this chapter.

Contents

1. INTRODUCTION

The pioneering work of Bohr [1] on the slowing down of swift alpha particles in matter defines one of the main events opening the way to modern physics. The ion–matter interaction depends crucially on the ion velocity; in the high

ADVANCES IN QUANTUM CHEMISTRY, VOLUME 45
ISSN: 0065-3276 DOI 10.1016/S0065-3276(04)45008-4

speed limit, $v \gg v_0 Z_1^{2/3}$ (v_0 is the Bohr velocity and Z_1 the ion atomic number), the ion is stripped of its electron charge and the ion stopping power can be described using linear response theory for the target electrons [2–4]; this approach enabled a unified description of single-particle and collective excitations of the electron gas. At projectile speeds such that $v_0 < v < v_0 Z_1^{2/3}$, an ion can lose electrons to, or capture electrons from, the medium. Bohr proposed a useful criterion for estimating the number of electrons bound to the projectile [5]. Brandt generalized this approach [6] and proposed the following equation:

$$Z_1^* = Z_1\left[1 - \exp\left(-\frac{v}{v_0} Z_1^{2/3}\right)\right], \tag{1}$$

for the effective charge Z_1^* of the ion.

An *ab initio* theory of the stopping power of ions at intermediate and low velocities, $v < Z_1^{2/3} v_0$, needs a complete description of the ion charge states as a function of v. For an ion moving in a metal, Fig. 1 shows the different capture and loss processes associated with these ion charge states [7]. In the Auger process illustrated in Fig. 1(a), an electron is captured (or lost) by the ion to (or from) a bound state; this is assisted by the excitation of an electron–hole pair or a plasmon in the solid. The coherent resonant mechanism is illustrated in Fig. 1(b): electron exchange processes are induced by the time-dependent crystal potential as seen from the fixed ion. A third mechanism is the shell process shown in Fig. 1(c); in this case an inner electron of the target can be captured by the moving ion. These three mechanisms have been analyzed for calculating the charge states of different ions [8–10]. For H and He, these charge states have been used for

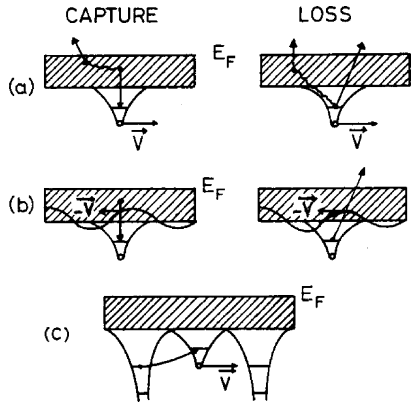

Fig. 1. (a) Capture and loss Auger processes for an ion moving in an electron gas; (b) coherent resonant processes; (c) capture shell process.

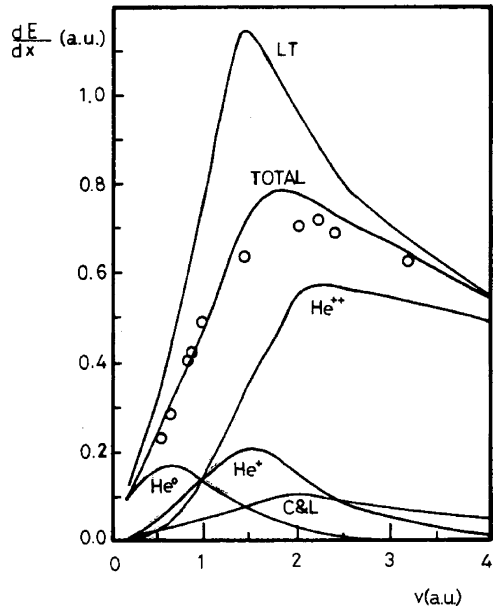

Fig. 2. Stopping powers for He moving in Al (LT, linear theory). The total stopping power is separated into the ion charge states contribution and the capture and loss contribution.

determining their stopping powers in the range of low and intermediate velocities [9,10]. Figure 2 shows the case of He on Al: the total stopping power is calculated as the sum of several contributions, three associated with the charge states He^{++}, He^{+} and He^{0}, the fourth one being due to the capture and loss processes.

Similar arguments can be applied to ions interacting with surfaces. In this chapter, we concentrate our discussion on low energy ion scattering (LEIS) [11], when ions of low velocity $v \ll v_0$ are reflected off the first metal layer. Then, the different charge exchange mechanisms defining the ion charge are shown in Fig. 3. Figure 3(a) shows the Auger process [14], similar to the one shown in Fig. 1(a) for atoms moving inside matter. Figure 3(b) shows a resonant process [12,13] whereby electrons are transferred between the metal and the atom. Notice that, for this process to be operative, the atomic level should resonate with the metal band, a condition that depends on the atom–metal distance as the atomic levels change with the atom–metal interaction. Notice that for LEIS, the equivalent of the shell process of Fig. 1(c) can be neglected [7].

Calculating the stopping powers of ions near surfaces needs a full calculation of their charge states [15]. In this chapter we review the work

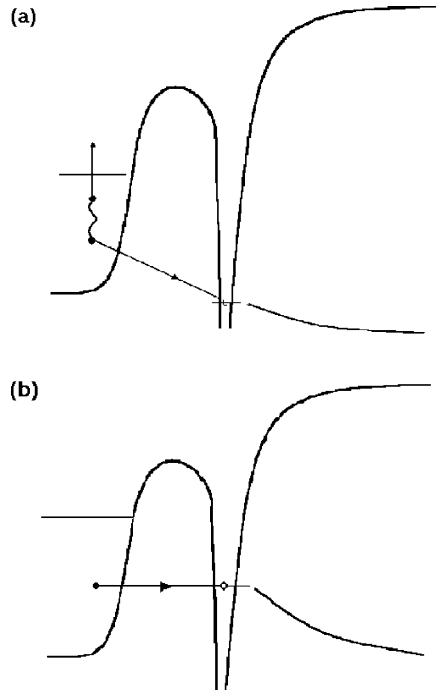

Fig. 3. Charge exchange mechanisms near a metal surface: (a) Auger process, (b) resonant process. The atomic energy level is shown as a function of the distance to the surface.

done in our group for analyzing the resonant and Auger processes associated with different ion states of H and He. As in bulk, *ab initio* description of the stopping power of ions near surfaces should combine the description of their charge states with a calculation of the stopping power of different species, say He^{++}, He^{+}, He^{0} and H^{+} or H but this is a subject beyond the scope of this chapter.

In Section 2 we analyze the ion–metal interaction and show how to calculate the atomic levels and their linewidths as a function of the atom–metal distance. An important message of our work is that the energy position of these levels play a crucial role in understanding how the resonant and Auger charge exchange mechanisms operate. In Section 3, we discuss how to obtain a full quantum mechanical solution for resonant processes and in Section 4 we consider Auger processes. Section 5 is devoted to discussing how to combine in a full solution both the resonant and Auger mechanisms and analyzing some specific results for H and He interacting with metal surfaces. Finally our conclusions are presented in Section 6.

2. ION–METAL INTERACTION: ION LEVELS AND LINEWIDTHS

For calculating the probability for resonant processes between a metal and the ion states of H or He it is important to determine carefully the position of the ion levels as a function of the ion–metal distance. In the following discussion, for the sake of clarity, we will refer to the case of He^+, unless specified otherwise, and consider the charge exchange between He^+ and He^0 associated with the interaction of the He-1s level with the metal.

In a first approach to this problem one can consider using a conventional density functional (DF) method and calculate, for each He–metal distance, the He-1s level and its linewidth. The difficulty with this approach is that DF calculations do not necessarily yield a good description of the energy levels; in particular, image potential effects are not easily included in these calculations. A way of obtaining an accurate description of the ion levels is to calculate their energies as the differences of the ground states energies of two systems defined by their charges, say, He^+ and He^0. This implies calculating the He-1s level by the following equation:

$$E_{1s} - E_F = E[He^0] - E[He^+], \tag{2}$$

where $E[He^+]$ ($E[He^0]$) represents the energy of a system for which the ion charge is He^+ (He^0). In equation (2) the He-1s level is measured with respect to the metal Fermi level E_F.

Applying equation (2) to a conventional plane wave-DF calculation is not simple, the reason being that, if the He-1s level is resonating with the metal band, one cannot fix an ion charge state due to the ion–metal charge transfer included in the calculation. We can use, however, equation (2) changing this point of view and using a local orbital-DF approach [16] instead of the more conventional plane wave-DF methods. In a local orbital-DF approach we use an orthogonal local basis, $\phi_{i\alpha}$, and introduce the total electron energy of the system in the following way:

$$E[n_{i\alpha\sigma}] = T[n_{i\alpha\sigma}] + E^H[n_{i\alpha\sigma}] + E^{xc}[n_{i\alpha\sigma}], \tag{3}$$

where the total energy E is written as a function of $n_{i\alpha\sigma}$, the $i\alpha\sigma$ electron occupancy which, in this approach, plays the role of $\rho(\mathbf{r})$ in the conventional DF method [17]. In equation (3), T, E^H and E^{xc} are the kinetic, Hartree and exchange-correlation energies of the electron gas, respectively. In this approach, the occupancies $n_{i\alpha\sigma}$ are obtained minimizing the energy $E[n_{i\alpha\sigma}]$,

$$\frac{\partial E[n_{i\alpha\sigma}]}{\partial n_{i\alpha\sigma}} = \mu. \tag{4}$$

Using Kohn–Sham theorem one can solve equation (4) by obtaining the self-consistent solution of the following Hamiltonian:

$$\hat{H} = \sum_{i\alpha\sigma} \varepsilon_{i\alpha\sigma} \hat{n}_{i\alpha\sigma} + \sum_{i\alpha,j\beta\sigma} T_{i\alpha,j\beta} \hat{c}^{\dagger}_{i\alpha\sigma} \hat{c}_{j\beta\sigma} + \sum_{i\alpha\sigma} \left[\frac{\partial E^{\mathrm{H}}[n_{i\alpha\sigma}]}{\partial n_{i\alpha\sigma}} + \frac{\partial E^{\mathrm{xc}}[n_{i\alpha\sigma}]}{\partial n_{i\alpha\sigma}} \right] \hat{n}_{i\alpha\sigma}, \tag{5}$$

where the energy levels, $\varepsilon_{i\alpha\sigma}$, and the hopping integrals, $T_{i\alpha,j\beta}$, define the one-electron part of the total Hamiltonian.

Using this local orbital DF approach, we define the different ion charge states by the orbital occupancy, $n_{i\alpha\sigma}$ (for example, for He^0 we take $n_{i\alpha\sigma} = 1$). Moreover, to be consistent, at the same time we have to take zero the hopping parameters between the atomic orbitals and the metal [19]. With these assumptions, we have to solve Hamiltonian (5) and calculate, say, $E[He^+]$ and $E[He^0]$.

In the next step, to analyze the resonant processes associated with charge exchange between He^+ and He^0, we consider a spin-less Newns–Anderson Hamiltonian [18] where the level E_{1s} and the hopping terms $T_{1s,i\alpha}$ that have been neglected to calculate $E[He^+]$ and $E[He^0]$, are introduced. This Hamiltonian reads

$$\hat{H}_{\mathrm{N-A}} = E_{1s} \hat{n}_{1s} + \sum_i \varepsilon_i \hat{n}_i + \sum_i [T_{1s,i} \hat{c}^{\dagger}_i \hat{c}_{1s} + \mathrm{h.c.}] + \sum_{i \neq j} T_{i,j} \hat{c}^{\dagger}_i \hat{c}_j, \tag{6}$$

where ε_i and $T_{i,j}$ are parameters associated with the electronic band structure of the metal.

Similar arguments can be applied to resonant charge exchange processes between H^+ and H^0 or H^0 and H^-. In the last case, we define the H-affinity level, A, by means of the equation

$$A - E_{\mathrm{F}} = E[H^-] - E[H^0], \tag{7}$$

while the ionization level, I, is defined by

$$I - E_{\mathrm{F}} = E[H^0] - E[H^+]. \tag{8}$$

Using equations (7) and (8) we can introduce the following many-body Hamiltonian

$$\hat{H}^{\mathrm{m.b.}} = \sum_{\sigma} I \hat{n}_{1s,\sigma} + (A - I) \hat{n}_{1s\uparrow} \hat{n}_{1s\downarrow} + \sum_{i\sigma} T_{1s,i} [\hat{c}^{\dagger}_{i\sigma} \hat{c}_{1s\sigma} + \mathrm{h.c.}] + \sum_{i} \varepsilon_{i\sigma} \hat{n}_{i\sigma} + \sum_{i \neq j} T_{i,j} \hat{c}^{\dagger}_{i\sigma} \hat{c}_{j\sigma} \tag{9}$$

where we have defined the effective electron–electron interaction within the H-atom by $(A - I)\hat{n}_{1s\uparrow}\hat{n}_{1s\downarrow}$. One can treat approximately the affinity and the ionization levels independently by considering a spin-less Hamiltonian,

similar to the one given by equation (6), where the 1s-atomic level is replaced by either the ionization or the affinity levels of H.

2.1. He–metal interaction

Calculations for the case of a He–Al interaction are shown in Figs. 4 and 5 [18]. Figure 4 shows $T_{1s,i}$ for different Al-orbitals as a function of the He–Al distance, where i stands for the 2s, 2p, 3s and 3p orbitals of Al. Notice that the He-interaction with the Al-2s or 2p orbitals is practically zero for d larger than 2.5 a.u.; however, at small distances (say, less than 1 a.u.) their values are very large, reflecting the strong interaction between the He-1s level and the Al-core orbitals.

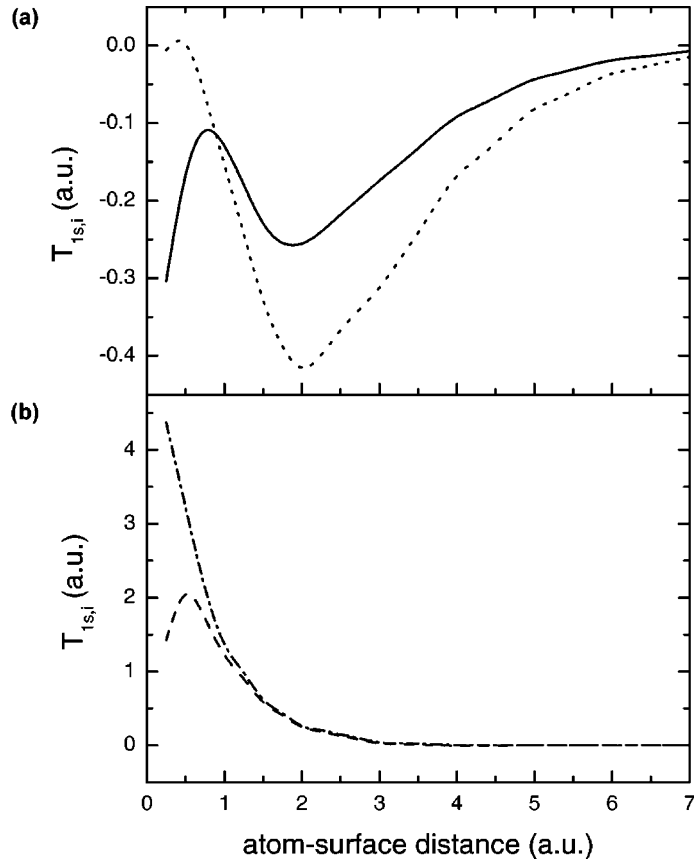

Fig. 4. The hopping parameters $T_{1s,i}$ for the He-1s level and different atomic orbitals of Al as a function of the He–metal distance; (a) continuous line: 3s, dotted line: $3p_z$; (b) dot-dashed line: 2s, dashed line: $2p_z$.

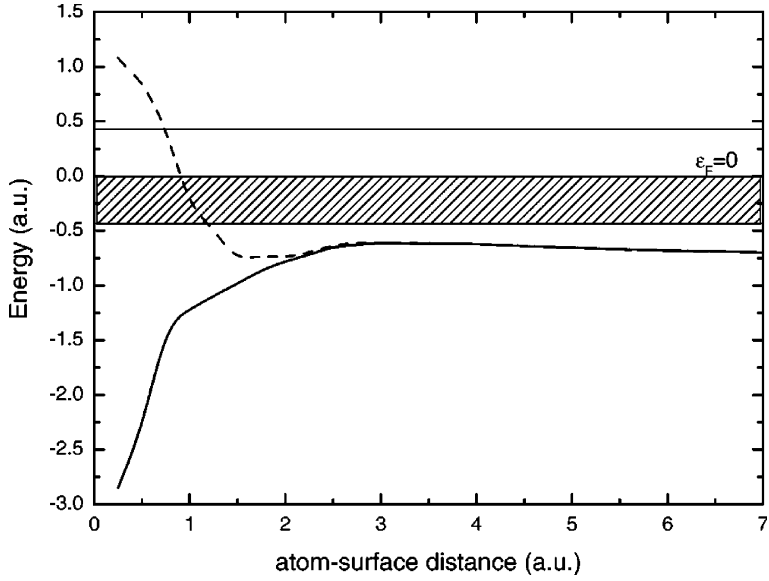

Fig. 5. He-1s energy level, E_{1s}, as a function of the atom–surface distance (continuous line). The $\tilde{E}_{1s}$-level resulting from the interaction with the Al-core orbitals is also shown (dashed line). The top and the bottom of the Al-conduction band are drawn as two horizontal straight lines.

Figure 5 shows E_{1s} as a function the atom–surface distance [18]. As the metal band is described using only 3s and 3p-orbitals, its density of states is limited to a finite range of energy. At large distances, the E_{1s}-level follows the image potential limit (the ionization level of He is located 20.5 eV below E_F), while at small distances it bends down, basically due to the electrostatic interaction between the He-1s level and the Al-atomic charge. At short distances (d smaller than $\sim$ 1 a.u.), as mentioned above, the hopping interaction between the He-1s level and the Al-core levels is very large; this is reflected in the very strong repulsion of the He-1s level to high energies as shown by the $\tilde{E}_{1s}$-level of Fig. 5 that is calculated modifying the E_{1s}-level by its interaction with the Al-core orbitals. The $\tilde{E}_{1s}$-level can be considered as the effective level for calculating the interaction between He and the conduction band of Al, embodying all the Al-core level effects in $\tilde{E}_{1s}$. Notice the general behavior of $\tilde{E}_{1s}$: at long distances follows the image potential interaction; at $d \sim 3$ a.u., it bends down due to the electrostatic interaction between the 1s-level and the Al-atomic charge; at $d \sim 2$ a.u., the $\tilde{E}_{1s}$-level is promoted to high energies due to the repulsion between the He-1s level and the Al-core orbitals. Due to this repulsion, the He-1s level enters the metal band for distances smaller than $\sim$ 1.1 a.u., making the resonant processes operative.

2.2. H–metal interaction

The case of H interacting with an Al-surface is shown in Fig. 6 and Table 1 [19]. Figure 6(a) and (b) shows the 1s-affinity and ionization levels for H approaching the Al(100)-top and center positions. For the affinity level, we see how it follows the image potential at large distances, bends slightly down between 5 and 7 a.u. due to the attraction of the Al-charge and, eventually, it is shifted to high energies due to the Pauli repulsion between the 1s-level and the metal charge. The ionization level also follows the image potential at long distances and it is shifted to high energies for distances smaller than 5 a.u. due to the Pauli repulsion with the metal charge [20]. In these calculations we have only included the 3s and 3p-orbitals of Al. As seen in the He-case, the effect of the Al-core orbitals starts to be important for $d \sim 2.0$ a.u.; for smaller distances, the effect of the core-levels can be expected to be a strong repulsion on both the ionization and affinity levels.

Finally, in Table 1 we show the hopping interactions between H-1s level and the Al-3s and 3p orbitals, as a function of the H-metal distance [19].

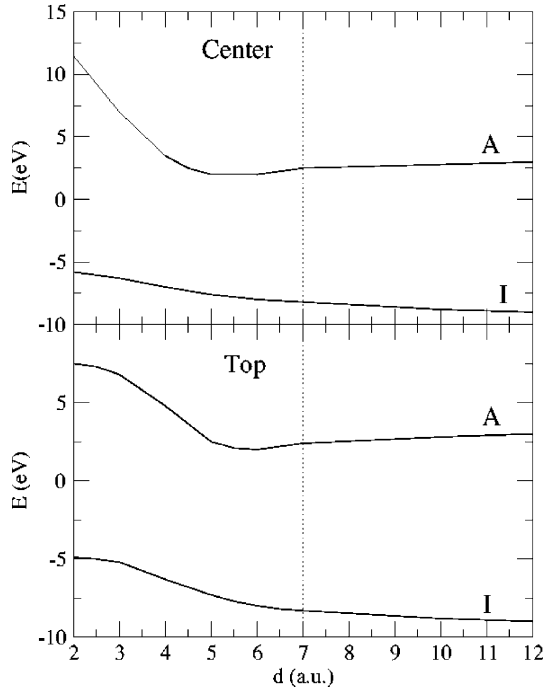

Fig. 6. Affinity (A) and ionization (I) levels of H as a function of the ion–metal distance, for center and top sites of Al(100).

Table 1. Absolute value of the hopping integrals for the H-1s state with the Al-3s and Al-3p states

	Top		Center	
d (a.u.)	t_{s-s} (eV)	t_{s-p} (eV)	t_{s-s} (eV)	t_{s-p} (eV)
2.0	7.54	9.55	2.79	4.05
3.0	3.98	6.36	2.12	3.01
4.0	2.19	3.72	1.51	2.03
5.0	1.18	2.21	0.78	1.04
6.0	0.59	1.11	0.41	0.52
7.0	0.27	0.44	0.21	0.25

In the center case, the hopping has been projected onto the line joining one Al atom with the H.

Figure 6 and Table 1 provide the necessary information for calculating the H–Al resonant processes that we discuss in Section 5.

3. RESONANT PROCESSES: DYNAMIC SOLUTION OF THE NEWNS–ANDERSON HAMILTONIAN

One can use different methods for calculating the population of the ionic species from equation (6) or (9), as the particles evolve towards and from the surfaces. A common method is to derive semiclassical master equations [21, 22]; these equations are a set of coupled equations in which the populations of the different species depend on time *via* the rates of the available channels for charge transfer. For instance, for charge transfer between H^- and H^0, these master equations involve the time derivative of the occupation numbers $n(H^-)$ and $n(H^0)$. A semiclassical approach such as this can only be valid if the ion level is far from the edge of the metal band; this is the case of H^-, where one can safely use these rate equations [19,22]. In other cases, one should analyze the ion occupation number using full quantum mechanical techniques for obtaining the dynamic solution of the Newns–Anderson Hamiltonian. We have followed this approach by using Keldysh–Green function techniques [23]. In this method we calculate the Green-function $G^r_{1s,1s}(t, t')$ associated with the 1s-ion level [22,24,25]. This Green-function satisfies the following integro-differential equation

$$\mathrm{i}\mathrm{d}G^r_{1s,1s}(t,t')/\mathrm{d}t - \tilde{E}_{1s}(\mathbf{R}(t))G^r_{1s,1s}(t,t') = \delta(t-t') + \int_{t'}^{t} \mathrm{d}t_1\, \Sigma^r_{1s,1s}[\mathbf{R}(t), \mathbf{R}(t_1); t, t_1]G^r_{1s,1s}(t_1, t'), \qquad (10)$$

where the self-energy $\Sigma^r_{1s,1s}$ is given by

$$\Sigma^r_{1s,1s}[\mathbf{R}(t), \mathbf{R}(t_1); t, t_1]$$

$$= \int_{-\infty}^{+\infty} \frac{d\omega}{2\pi} \Theta(t - t_1) e^{-i\omega(t-t_1)} \sum_{i,j} T_{1s,i}(\mathbf{R}(t)) g^r_{i,j}(\omega) T_{j,1s}(\mathbf{R}(t_1)), \quad (11)$$

$g^r_{i,j}(\omega)$ being the retarded Green-function of the unperturbed metal surface. In equations (10) and (11) $\tilde{E}_{1s}$, and $T_{1s,i}$ depend on the time-dependent ion position $\mathbf{R}(t)$. Notice that for $\mathbf{R}$ independent of time, equations (10) and (11) reduce to

$$\left[\omega - \tilde{E}_{1s} - \Sigma^r_{1s,1s}(\omega)\right] G^r_{1s,1s} = \delta(t - t') \quad (12)$$

and

$$\Sigma^r_{1s,1s}(\omega) = \sum_{i,j} |T_{1s,i}|^2 g^r_{i,j}(\omega) \quad (13)$$

which have often been used to analyze the chemisorption of a level on a surface characterized by $g^r_{i,j}(\omega)$.

Once we calculate $G^r_{1s,1s}(t, t')$, the occupancy $n_{1s}(t)$ is given by

$$n_{1s}(t) = n_{1s}(t_0)|G^r_{1s,1s}(t, t_0)|^2 + \sum_{i,j} \int_{-\infty}^{+\infty} d\omega n_F(\omega) \rho_{i,j}(\omega)$$

$$\times \int_{t_0}^{t} dt_1 G^r_{1s,1s}(t, t_1) T_{1s,i}(\mathbf{R}(t_1)) \int_{t_0}^{t} dt_2 G^{r*}_{1s,1s}(t, t_2) T_{1s,j}(\mathbf{R}(t_2)) e^{-i\omega(t_1 - t_2)}, \quad (14)$$

where $n_F(\omega)$ is the Fermi–Dirac distribution function of the metal electrons and $\rho_{i,j}(\omega)$ the density matrix for the metal surface

$$\rho_{i,j}(\omega) = -\frac{1}{\pi} \mathrm{Im}\, g^r_{i,j}(\omega). \quad (15)$$

In equation (14), t_0 is the initial time and the first term of this equation represents the 'memory' contribution associated with the initial condition, $n_{1s}(t_0)$, for the occupancy $n_{1s}(t)$. The second term of this equation takes into account all the back and forth electron resonant jumps between the ion and the metal. For an incident ion, say He^+, $n_{1s}(t_0) = 0$, while for an incident neutral atom, like He^0, $n_{1s}(t_0) = 1$. The initial time is defined by the initial

ion–metal distance d_0 large enough to have the atom decoupled from the metal.

Notice that in the static limit only the second term of equation (14) contributes to n_{1s} (there is no 'memory' contribution) and equation (14) reads

$$n_{1s} = \sum_{i,j} \int_{-\infty}^{+\infty} d\omega n_F(\omega) T_{1s,i} \rho_{i,j}(\omega) T_{j,1s} |G^r_{1s,1s}(\omega)|^2, \tag{16}$$

or

$$n_{1s} = -\frac{1}{\pi} \mathrm{Im} \int_{-\infty}^{E_F} \frac{d\omega}{\omega - \tilde{E}_{1s} - \Sigma^r_{1s,1s}(\omega)} \tag{17}$$

as it should be.

4. AUGER PROCESSES

This section is devoted to the analysis of Auger processes, treated independently of resonant processes. Such an analysis is relevant in the case of low-lying atomic energy levels that cannot be resonantly neutralized, like He on Al at distances larger than ~ 1 a.u.

Auger processes have been poorly described in the theoretical literature mainly because they involve at least two metal electrons, the one that neutralizes the ion and the one that is excited. Actually, the process involves *many* electrons because the Coulomb repulsion between the two electrons giving rise to the Auger process will be screened by the rest of the system. The most striking effect of the screening properties of a many-electron system is the existence of collective excitations known as plasmons. One possible channel for ion neutralization at metals consists of the capture of a metal electron by the ion with the released energy and momentum being taken by a plasmon. This channel, termed in the literature as plasmon-assisted neutralization, has been assumed to be important in theoretical calculations [26,27] but has not been properly taken into account [27]. Recently, the excitation of surface and bulk plasmons during ion neutralization at surfaces have been reported experimentally [28,29].

The model presented here is the generalization of the theory of ion neutralization in bulk [7,9] to a surface system [30]. The key quantity is the Auger transition rate given by Fermi's golden rule

$$\frac{1}{\tau} = 2\pi \sum_{i,f} |\langle f|\hat{V}|i\rangle|^2 \delta(E_f - E_i). \tag{18}$$

We consider the interaction of the neutralizing electron with $N-1$ metal electrons and write for the initial, $|i\rangle$ and the final, $|f\rangle$, states appearing in equation (18)

$$|i\rangle = |0\rangle\otimes|\mathbf{k}_{\mathrm{or}}\rangle, \qquad |f\rangle = |n\rangle\otimes|a\rangle, \tag{19}$$

where $|0\rangle$ and $|n\rangle$ are the ground and an excited state of the many-body electron gas with energies E_0 and E_n, respectively, $|a\rangle$ is the final state of one electron in the atomic ion core with energy E_{a} and $|\mathbf{k}_{\mathrm{or}}\rangle$ is a one-electron state representing the initial state of the electron that neutralizes the ion core. Since $|\mathbf{k}_{\mathrm{or}}\rangle$ and $|a\rangle$ should be solutions of the same Hamiltonian, we take for $|\mathbf{k}_{\mathrm{or}}\rangle$ a one-electron metallic state, $|\mathbf{k}\rangle$, orthogonalized to $|a\rangle$ [7,8]. The interaction potential $\hat{V}$ is the Coulomb interaction between the charge densities induced in the metal, δn and in the atom, $\delta\rho$, associated to the $|\mathbf{k}_{\mathrm{or}}\rangle \rightarrow |a\rangle$ transition

$$\hat{V} = \int \mathrm{d}\mathbf{r}_1 \int \mathrm{d}\mathbf{r}_2 \, \frac{\delta n(\mathbf{r}_1)\rho(\mathbf{r}_2)}{|\mathbf{r}_1 - \mathbf{r}_2|}. \tag{20}$$

Then, upon Fourier transforming in the coordinates $\mathbf{x}$ parallel to the surface, the matrix elements of equation (18) read

$$\langle f|\hat{V}|i\rangle = \int \frac{\mathrm{d}\mathbf{q}}{(2\pi)^2} \int \mathrm{d}z_1 \langle n|\delta n(\mathbf{q}, z_1)|0\rangle \Phi(\mathbf{k}; \mathbf{q}, z_1), \tag{21}$$

where we have defined

$$\Phi(\mathbf{k}; \mathbf{q}, z_1) = \frac{2\pi}{q} \langle a|\mathrm{e}^{\mathrm{i}\mathbf{q}\cdot\mathbf{x}_2} \, \mathrm{e}^{-q|z_1 - z_2|}|\mathbf{k}_{\mathrm{or}}\rangle. \tag{22}$$

Finally, by substituting equation (21) into equation (18) and making use of the standard expression relating the imaginary part of the susceptibility $\chi(\omega, q; z, z')$ for interacting electrons (screened susceptibility) to the density operators $\delta n(\mathbf{q}, z)$ and $\delta n(\mathbf{q}, z')$, the final expression for the Auger capture rate is obtained as

$$\frac{1}{\tau}(z_{\mathrm{a}}) = 2 \sum_{\mathbf{k}<k_{\mathrm{F}}} \int_0^\infty \mathrm{d}\omega \int \frac{\mathrm{d}\mathbf{q}}{(2\pi)^2} \int \mathrm{d}z \int \mathrm{d}z' [-\mathrm{Im}\ \chi(\omega, q; z, z')] \times \Phi(\mathbf{k}; \mathbf{q}, z) \Phi^*(\mathbf{k}; \mathbf{q}, z') \delta(\omega + E_{\mathrm{a}} - E_{\mathrm{k}}). \tag{23}$$

In equation (23) k_{F} is the Fermi wave vector and the transition rate depends on the distance z_{a} between ion and surface through the wave function of the state $|a\rangle$ in equation (22).

The physics behind equation (23) is clear. $\Phi(\mathbf{k}; \mathbf{q}, z)\exp[\mathrm{i}(E_{\mathrm{a}} - E_{\mathrm{k}})t]$, where Φ is given by equation (22), is the effective potential associated with the transition from a metal-electron state $|k\rangle\exp(-\mathrm{i}E_{\mathrm{k}}t)$ to the core-ion state $|a\rangle\exp(-\mathrm{i}E_{\mathrm{a}}t)$. This potential, which oscillates in time with frequency

$\omega = E_a - E_k$, produces fluctuations of charge density in the many-electron system and the imaginary part of the induced charge density $\delta n(\mathbf{k}; \mathbf{q}, \omega, z)$ given by

$$\delta n(\mathbf{k}; \mathbf{q}, \omega, z) = \int dz' \chi(q, \omega; z, z') \Phi(\mathbf{k}; \mathbf{q}, z') \tag{24}$$

is related to energy losses. In fact the quantity,

$$-\mathrm{Im} \int dz\, \delta n(\mathbf{k}; \mathbf{q}, \omega, z) \Phi^*(\mathbf{k}; \mathbf{q}, z) \tag{25}$$

gives the rate at which the oscillating potential produces metal excitations of energy ω and momentum $\mathbf{q}$. Then, when adding the contributions of all possible electrons that can neutralize the ion, the Auger rate of equation (23) gives the total rate at which metal excitations are produced in the Auger neutralization process.

The screened susceptibility $\chi(q, \omega; z, z')$ appearing in equation (23) is a smooth function of the spatial coordinates that interpolates from zero very far from the surface to the bulk value. It contains the spectrum of the single-particle and collective modes and their coupling. This coupling, known as Landau-damping, depends on distance and it is the only channel that allows decaying of a collective mode in the jellium theory. Surface plasmons of parallel momentum q different from zero are Landau-damped but bulk plasmons cannot decay into electron–hole pairs below a critical frequency in this linear theory. Collective modes can show up in electron emission spectra [28,29] because they are coupled to electron–hole pairs.

The theory in which the susceptibility is formally defined for jellium surfaces is the time-dependent density functional theory (TDDFT). In this theory, the susceptibility for interacting electrons (also called screened susceptibility) $\chi(q, \omega; z, z')$ is related to the susceptibility for non-interacting (independent) electrons $\chi_0(q, \omega, q; z, z')$ *via* the integral equation

$$\chi(q, \omega; z, z') = \chi_0(q, \omega; z, z') + \int dz_1 \int dz_2 \chi_0(q, \omega; z, z_1) R(q, \omega; z_1, z_2) \chi(q, \omega; z_2, z'), \tag{26}$$

with

$$R(q, \omega; z_1, z_2) = \frac{2\pi}{q} e^{-q|z_1 - z_2|} + \mu'_{xc}(z_1) \delta(z_1 - z_2) \tag{27}$$

with μ'_{xc} being the derivative of the exchange-correlation potential. When the effective interaction is simply the Coulomb potential ($\mu'_{xc} = 0$), χ is said to be evaluated in the random phase approximation (RPA). Excellent agreement between theory and experiments of electron energy loss [31] and

photoyield [32] has been achieved if χ_0 is calculated for a Lang–Kohn jellium surface [33] and then χ is evaluated either in the TDDFT or the RPA approximations. However, the computation of the Auger rate of equation (23) is very involved because it is necessary to evaluate χ for as many values as required to perform the eight-dimensional integral. This is one of the reasons why the problem of calculating a realistic Auger transition rate at surfaces has been a long-standing one and many approximations to the matrix elements and/or interaction potentials can be found in the literature. One common approximation is the calculation of the matrix elements using the bare (unscreened) Coulomb potential [34] (or, equivalently, the use of χ_0 instead of χ in equation (23)). This approximation is a good one when the energy transfer ω is much larger than the plasma frequency ω_P; only in this case do electrons behave like independent particles. If the energy ω is of the order of ω_P, the independent-particle calculation ignores the existence of collective excitations while if ω is much smaller than ω_P the independent-particle calculation does not take into account the strong screening of a nearly static Coulomb potential. This is clearly seen in Fig. 7 (taken from Ref. [35]), where we have plotted the Auger rate per unit frequency $\frac{1}{\tau}(\omega)$, which is defined from equation (23) as

$$\frac{1}{\tau}(z_a) = \int_0^\infty d\omega \frac{1}{\tau}(\omega, z_a) \tag{28}$$

for neutralization of He^+ at a distance of $z_a = 5$ a.u. from a Lang–Kohn jellium surface of $r_s = 2.0$ a.u. representing Al [33].

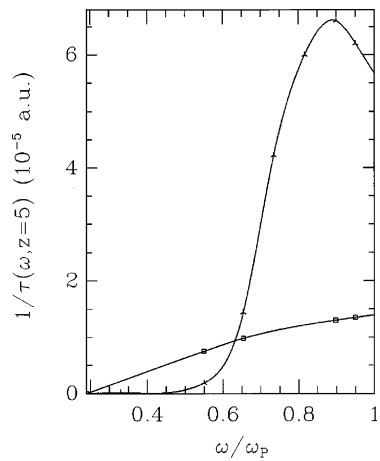

Fig. 7. Neutralization rate of He^+ on Al per unit of transferred energy at 5 a.u. from the jellium edge. Squares: independent-particle calculation. Crosses: interacting-particle calculation.

The independent-particle calculation, represented by the line with squares in Fig. 7, yields a smooth function of ω, while the interacting-particle calculation, in which χ is evaluated in the TDDFT, raises sharply above $\omega \sim 0.65\omega_P$. This is the range of frequencies of the collective surface modes of Al [31] which are obviously absent in the independent-particle calculation. Then the comparison between both calculations shows that the plasmon-assisted neutralization channel is indeed the dominant one at these energies. The opposite happens in the limit of small ω. In this case the independent-particle calculation overestimates the electron–hole pair channel because it does not take into account the screening of the Coulomb potential at very low frequencies. The overall effect on the total rate of Auger neutralization of He^+ on Al is not so dramatic, however, as is shown in Fig. 8. This is due to the compensation of the electron–hole channel with the plasmon-assisted channel when integrating in ω (equation (24)), but one must remember that such a compensation does not appear in other systems. For Ar^+ scattered off Mg, the energy transfer ω is in the range between $0.46\omega_P$ and $1.1\omega_P$ and the plasmon-assisted channel dominates [28]. H^+ scattered off Al belongs to the opposite case because the energy transfer is below $0.6\omega_P$.

Another possible simplification to the full calculation of the Auger capture rate consist of the use of the asymptotic long-distance limit of

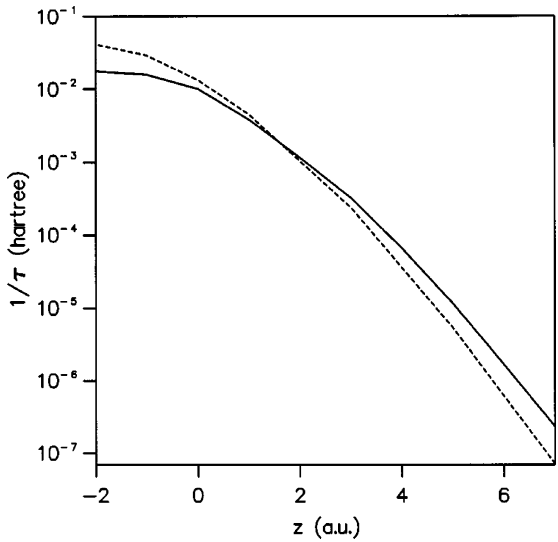

Fig. 8. Neutralization rate of He^+ on Al as a function of the distance to the jellium edge. Continuous line: interacting-particle calculation. Dashed line: independent-particle calculation.

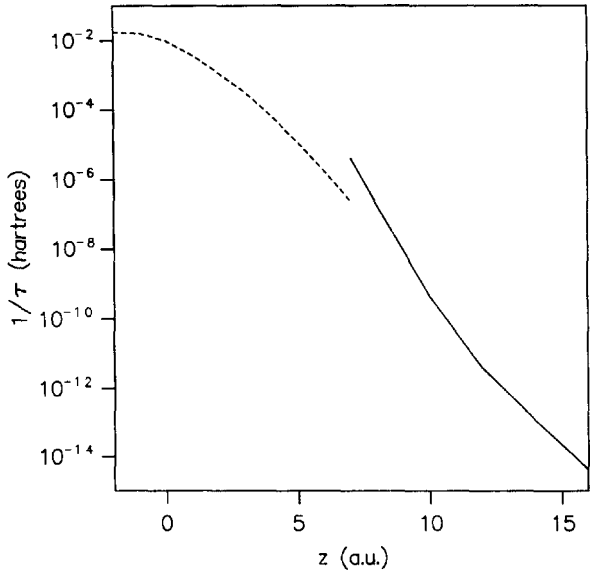

Fig. 9. The long-distance limit for neutralization of He on Al (continuous line) is compared with the interacting particle calculation of Fig. 8 (here shown by a dashed line).

equation (22) [35]. In Fig. 9 we present the results of this long-distance calculation together with the exact results of equation (23). We can appreciate that the long-distance approximation overestimates the Auger rate for distances larger than 10 a.u.

5. RESULTS

This section is devoted to discussing results for some specific cases where we can illustrate the analysis presented above. Three different examples will be analyzed: (a) H^- scattering off an Al-surface; here, the resonant processes analyzed using master equations yield a good description of the charge exchange mechanism. (b) He^+ scattering off metal surfaces at glancing incidence; in this case, the ion perpendicular energy is so small that the incoming ion does not penetrate too much the surface electron charge; then, the He-1s level does not overlap with the metal band states and the only operative charge exchange process is the Auger one. (c) He^+ scattering off metal surfaces at large incidence angles. Contrary to case (b), He^+ does penetrate the surface electron charge and, for small ion–metal distances, the He-1s level overlap with the metal conduction band. We find that, in this case,

both resonant and Auger mechanisms play a crucial role in determining the He-charge states.

5.1. H^- on Al

This case is analyzed using the H^--levels and the H–Al interactions given in Fig. 6 and Table 1, respectively. As the H^--level is always above the metal Fermi level, we can use semiclassical master equations for solving the Newns–Anderson Hamiltonian of this problem [21,22].

Figure 10 shows our results for the total fraction of H^- as a function of the detection angle for incident protons of either 4 or 1 keV [36]. In our calculations we assumed that the ion penetrates the surface up to 3 a.u. away from the first atomic layer. This assumption is not, however, crucial because the population of H^- is determined by the charge exchange processes occurring around the freezing distance characterizing the process; for instance, for exit angles smaller than 20°, that freezing distance is larger than 6 a.u. We should mention that for freezing distances larger than 6 a.u. the 2sp levels also play an important role in the resonant process and, in our calculations, we have included them following Ref. [37].

We conclude this section by mentioning that the results shown in Fig. 10 only depend on the H-1s level for exit angles larger than 20°; then the freezing distance is smaller than 6 a.u. and the effect of the 2sp-levels can be

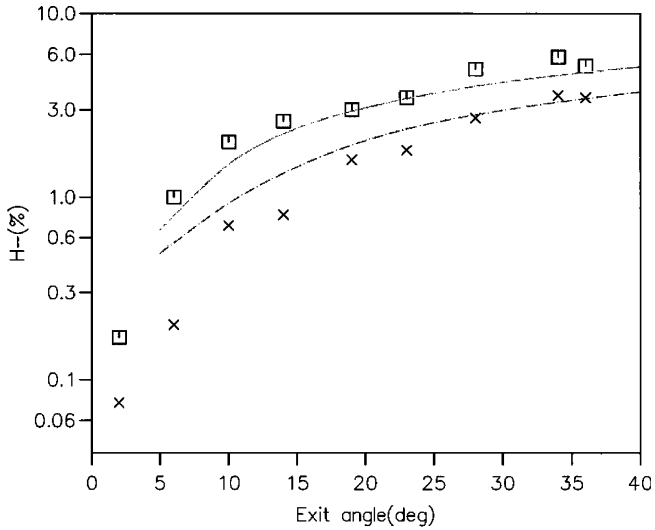

Fig. 10. Total fraction of H^- scattered off Al(100). Squares: incident protons of 4 keV; crosses: incident protons of 1 keV. Experiments from Ref. [36].

neglected. It is remarkable the good agreement found between theory and experiments in this limit, when we consider the large angles of Fig. 10.

5.2. He^+ on metal surfaces: glancing incidence

When a beam of He^+ ions with total energy of 1–20 keV is incident on metal surfaces at glancing angles (here the angle of the beam with the surface is typically smaller than 10°) the component of the ion velocity perpendicular to the surface is so small that the ions never get closer than ~ 1.5 a.u. from the first atomic layer. For Al, as we showed in Section 2.2, the He-1s level never resonates with the conduction band of the metal, this fact making Auger processes the only ones responsible for neutralization of the incoming He^+ ion.

The pioneering work by Hagstrum [14] settled down both experiments and theory in this range of small perpendicular energies and his ideas have formed a kind of established understanding until very recently. Hagstrum's measurements of electron spectra revealed that the 1s-level of He was shifted up in energies by about 2 eV when He^+ was neutralized. Equating 2 eV to the classical image potential, he obtained a distance of neutralization of about 4 a.u. from the image plane (7 a.u. from the first atomic layer). Then assuming that the Auger rate decreases exponentially with the distance to the surface, z_a, as $\frac{1}{\tau}(z_a) = A \exp(-az_a)$, one can fix A and a to get He^+ neutralized at 4 a.u. from the image plane. More recent experiments of mean energy gain of He^+ incident on Al(111) [38] were analyzed in the same way and from that kind of analysis an Auger rate was retrieved that was larger by several orders of magnitude than the ones obtained by the best and more sophisticated theoretical calculations of Refs. [35,39]. However, the origin of the discrepancy between calculated and retrieved Auger rates can be traced back to the incorrect assumption of the image shift of the He-1s level at the distances where neutralization occurs. It was pointed out in Ref. [40] that calculated Auger rates and measured energy gains are not in discrepancy when one uses a He-1s level that is accurately calculated as a function of the distance to the surface. Using the results of Fig. 5, one can see that the mean energy gain of 1.8 eV measured for He^+ on Al in Ref. [38] is compatible with neutralization distances of about 3 and 7 a.u. from the first atomic layer. The latter is located in the asymptotic image potential region and corresponds to the general belief. The former is, however, also consistent with the calculated Auger rates, as it was shown in Ref. [40]. Identical conclusion was reached in Ref. [41] when analyzing electron emission spectra.

Very recently it has been possible to measure the very small fraction of ions that survive Auger neutralization in collisions of He^+ with Ag surfaces at grazing incidence [42–44]. These experiments reveal a number of survivals of 10^{-3}–10^{-4}, which are many orders of magnitude larger than the

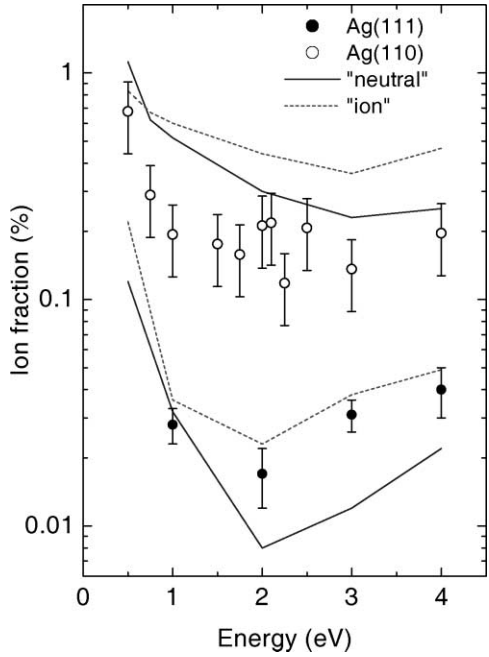

Fig. 11. Experimental ion fractions for random scattering direction for the Ag(110) (open dots) and Ag(111) (full dots) surfaces. The lines labelled 'ion' and 'neutral' correspond to calculated Auger survival probabilities for two types of trajectories.

number it would be obtained under the assumption that neutralization takes place at distances of ~ 7 a.u. from the metal surface. However, the correct number of survivals is obtained by using the theoretical Auger rates, as shown in Fig. 11 [44]. Therefore, we conclude that the theories presented in Sections 2 and 4 for calculating energy level variation of ions in front of surfaces and Auger neutralization rates are able to account for current experimental findings in the range of very low incident kinetic energies.

5.3. He^+ on metals: normal incidence

In this section we consider the case of He^+ scattering off metal surfaces with incident and scattering angles close to the surface perpendicular direction. He^+, having a kinetic energy of around 1 keV, penetrates the electron surface charge and collides with the metal atoms; typically, the ion suffers a binary collision and recedes back to vacuum. We analyze the charge exchange processes assuming the ion to move along two straight trajectories, before and after the binary collision.

In order to understand the charge exchange processes of this He^+–metal collision, we take into account the different mechanisms discussed in this paper, resonant and Auger processes. In our approach to this problem, one has to distinguish two clearly separated regimes: in one of them only Auger neutralization is operative, this mechanism being active for He^+–metal distances larger than ~ 1 a.u. As shown in Fig. 5, the He-1s level overlaps the metal band states for He^+–metal distances smaller than ~ 1 a.u.; this is the range of distances for which the second regime appears. In this regime, Auger processes are negligible and resonant processes are fully operative up to the turning point of the trajectory, which we find to be ~ 0.3 a.u. As Auger and resonant processes are spatially separated, we can calculate independently their contributions [18,45]. Then, we calculate the fraction of positive ions, P^+, by introducing the Auger survival probabilities for the incoming and outgoing paths, $P^+_{A,\text{in}}$ and $P^+_{A,\text{out}}$, respectively, as well as the probabilities for He^+ to survive and He^0 to be reionized in the close collision P^+_{surv} and P_{reion}, respectively. From these quantities we obtain the total ion fraction after the whole ion–surface interaction, P^+, by means of the following equation:

$$P^+ = P^+_{A,\text{in}} P^+_{\text{surv}} P^+_{A,\text{out}} + (1 - P^+_{A,\text{in}}) P_{\text{reion}} P^+_{A,\text{out}}, \tag{29}$$

where the first and second parts of equation (29) represent the survival channel and the reionization channel, respectively [18,45]. In equation (29), the Auger probabilities $P^+_{A,\text{in}}$ and $P^+_{A,\text{out}}$ are calculated by means of a classical master equation while the resonant probabilities P^+_{surv} and P_{reion} are obtained from the dynamic solution of the Newns–Anderson model presented in Section 3. It was shown in [46] that the semiclassical master equations provide an excellent approximation to the full dynamic solution when only Auger processes are operative. Also, the use of equation (29) was justified in Ref. [47].

Figure 12 shows the fraction of He^+ backscattered from Al, P^+, as a function of the incident kinetic energy. Survival and reionization ion fractions are also shown in this figure. Notice that for ion energies smaller than 100 eV (distances of closest approach larger than 1 a.u.) the resonant channel is practically closed and the ion fraction is determined by Auger processes. For larger energies, the ion approaches the metal surface and the resonant mechanism starts to be operative. In the calculations of Fig. 12, P^+ shows an unusual behavior with two minima around 150 and 400 eV. Although the appearance of the one at the lowest energy might depend on a more accurate calculation of the Auger and resonant processes for these energies [47], these results doubtlessly show that the energy regime 120–260 eV represents a transition regime where resonant processes become important, leading to an increase of P^+ once that the resonant channel is fully open.

The case of He^+ backscattered from Pd has also been analyzed in Ref. [18]. Important differences have been found with respect to the case of Al; while for Al the He-1s level resonates with the metal conduction band at

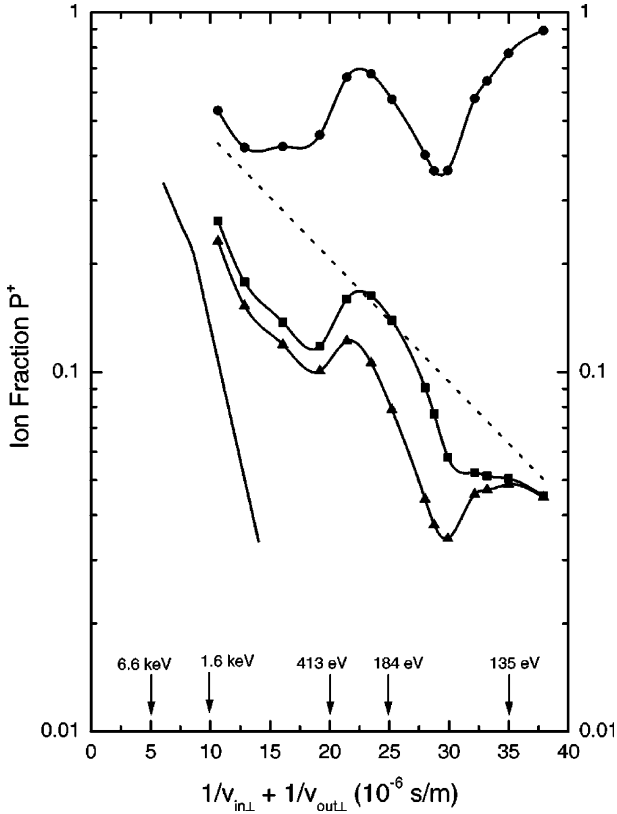

Fig. 12. Ion fraction, P^+, of He^+ backscattered off Al. Dashed line: Auger survival probability. Full circles: survival probability including resonant processes only. Full triangles: survival channel. Full squares: our full calculation (equation (29)). The experimental data of Ref. [48] are shown by a continuous line.

distances smaller than ~ 1 a.u., this resonance appears for Pd at distances of 2 a.u., making the resonant charge transfer between He^+ and Pd less effective. This explains why the ion fraction for the He^+/Pd collision is basically determined by Auger neutralization processes.

6. CONCLUSIONS

Charge exchange processes in LEIS have been analyzed and some case study systems, like H and He scattered off metals, have been discussed in detail.

It has been commonly accepted that, for He^+, Hagstrum's Auger neutralization model holds in the LEIS regime, namely for ion kinetic energies of the order of 1 keV. Our analysis for the He/Al system

confirms this point of view if the ion perpendicular energy is smaller than 100 eV. For larger perpendicular energies, however, our discussion shows that He penetrates the metal surface layer and that the He-1s energy level resonates with the metal conduction band, making resonant processes fully operative. We conclude that, for He, Auger processes are the only ones responsible for charge transfer at low perpendicular energies, while the resonant mechanism becomes also operative at high energies (>100 eV). In the low energy regime, He^+ is neutralized very efficiently at the image plane, which is located about 3 a.u. in front of the first metallic layer. We have also shown how the high energy limit can be analyzed combining the Auger and resonant mechanisms; the Auger process is dominant at long ion–metal distances (>1.2 a.u.), while the resonant one also contributes at closer distances.

In the case of H, the 1s-energy level is always resonating with the Al-conduction band and resonant charge transfer occurs for large ion–metal distances. In particular, we have seen how charge exchange processes for the H^-/Al system can be understood considering only the resonant mechanism.

We also conclude that a detailed calculation of the different mechanisms operating in the ion–metal charge exchange processes depends on a careful description of the ion levels as a function of the ion–metal distance. In this paper, these levels as well as the ion–metal hopping interactions and the Auger capture rates, have been presented for the H/Al and He/Al systems.

ACKNOWLEDGEMENTS

We gratefully acknowledge financial support by the Spanish Comisión Interministerial de Ciencia y Tecnología under projects MAT-2001-0665 and BFM 2001-0150. We also acknowledge many fruitful discussions with P. Bauer, H. H. Brongersma, R. A. Baragiola, V. A. Esaulov, Evelina A. García, E. C. Goldberg, N. Lorente, J. Merino, W. More, P. Pou and N. P. Wang.

REFERENCES

[1] N. Bohr, *Phil. Mag.*, 1913, **25**, 16.
[2] E. Fermi, *E. Phys.*, 1927, **29**, 135.
[3] E. J. Williams, *Rev. Mod. Phys.*, 1945, **17**, 217.
[4] J. Lindhard, *K. Dan. Vindensk. Selsk. Mat.-Fys. Med.*, 1954, **28** (8).
[5] N. Bohr, *K. Dan. Vindensk. Selsk.*, 1948, **18** (8).
[6] W. Brandt, in *Atomic Collisions in Solids* (eds S. Datz, B. R. Appleton and C. D. Moak), Plenum Press, New York, 1975.
[7] P. M. Echenique, F. Flores and R. H. Ritchie, in *Solid State Physics: Advances in Research and Applications*, (eds H. Ehrenreich and D. Turnbull), Academic Press, New York, 1990, Vol. 43, p. 229.

[8] F. Sols and F. Flores, *Phys. Rev. B*, 1984, **30**, 4878.
[9] A. Arnau, M. Peñalva, P. M. Echenique, F. Flores and R. H. Ritchie, *Phys. Rev. Lett.*, 1990, **65**, 1024.
[10] M. Peñalva, A. Arnau, P. M. Echenique, F. Flores and R. H. Ritchie, *Europhys. Lett.*, 1992, **19**, 45.
[11] H. H. Brongersma, P. A. C. Groenen and J.-P. Jacobs, Application of low-energy ion scattering to oxidic surfaces in *Science of Ceramic Interfaces II* (ed. J. Nowotny), Materials Science Monographs, Elsevier, London, 1994, Vol. 81, p. 113.
[12] A. Blandin, A. Nourtier and D. W. Hone, *J. Phys. (Paris)*, 1976, **37**, 369.
[13] J. J. C. Geerlings and J. Los, *Phys. Rep.*, 1990, **190**, 133.
[14] H. D. Hagstrum, *Phys. Rev.*, 1954, **96**, 336.
[15] A. Närmann, R. Monreal, P. M. Echenique, F. Flores, W. Heiland and S. Schubert, *Phys. Rev. Lett.*, 1990, **64**, 1601.
[16] P. Pou, R. Pérez, F. Flores, A. Levy Yeyati, A. Martín-Rodero, F. J. García-Vidal and J. Ortega, *Phys. Rev. B*, 2000, **62**, 4309.
[17] F. J. García-Vidal, J. Merino, R. Pérez, R. Rincón, J. Ortega and F. Flores, *Phys. Rev. B*, 1994, **50**, 10537; F. J. García-Vidal, A. Martín-Rodero, F. Flores, J. Ortega and R. Pérez, *Phys. Rev. B*, 1991, **47**, 11712.
[18] N. P. Wang, E. A. García, R. Monreal, F. Flores, E. C. Goldberg, H. H. Brongersma and P. Bauer, *Phys. Rev. A*, 2001, **64**, 12901.
[19] J. Merino, N. Lorente, P. Pou and F. Flores, *Phys. Rev. B*, 1996, **54**, 10959.
[20] In Fig. 6 we have corrected the results of Ref. [19] that have a small error in the calculations.
[21] J. J. C. Geerlings, J. Los, J. P. Gauyacq and N. M. Temme, *Surf. Sci.*, 1986, **172**, 257.
[22] D. C. Langreth and P. Nordlander, *Phys. Rev. B*, 1991, **43**, 2541.
[23] L. V. Keldysh, *Zh. Eksp. Teor. Fz.*, 1964, **47**, 1515, *Sov. Phys. JETP*, 1965, **20**, 1018.
[24] J. Merino, N. Lorente, W. More, F. Flores and M. Yu. Gusev, *Nucl. Instrum. Methods Phys. Res. B*, 1997, **125**, 250.
[25] A. T. Dorsey, K. W. Jacobsen, Z. H. Levine and J. W. Wilkins, *Phys. Rev. B*, 1989, **40**, 3417.
[26] P. Apell, *J. Phys. B*, 1988, **21**, 2665.
[27] A. A. Almulhem and M. D. Girardeau, *Surf. Sci.*, 1989, **210**, 138.
[28] R. A. Baragiola and C. A. Dukes, *Phys. Rev. Lett.*, 1996, **76**, 2547.
[29] P. Riccardi, P. Barone, A. Bonanno, A. Oliva and R. A. Baragiola, *Phys. Rev. Lett.*, 2000, **84**, 378.
[30] R. Monreal and N. Lorente, *Phys. Rev. B*, 1995, **52**, 4760.
[31] K. D. Tsuei, E. W. Plummer, A. Liebsch, K. Kempa and P. Baksi, *Phys. Rev. Lett.*, 1990, **64**, 44.
[32] H. J. Levinson, E. W. Plummer and P. J. Feibelman, *Phys. Rev. Lett.*, 1979, **43**, 952.
[33] N. D. Lang and W. Kohn, *Phys. Rev. B*, 1970, **1**, 4555.
[34] T. Fonden and A. Zwartkruis, *Surf. Sci.*, 1992, **269/270**, 601.
[35] N. Lorente and R. Monreal, *Phys. Rev. B*, 1996, **53**, 9622; N. Lorente and R. Monreal, *Surf. Sci.*, 1997, **370**, 324.
[36] M. Maazouz, R. Baragiola, A. Borisov, V. A. Esaulov, S. Lacombe, J.-P. Gauyacq, L. Guillemot and D. Teillet-Billy, *Surf. Sci.*, 1996, **364**, L568.
[37] A. G. Borisov, D. Teillet-Billy and J. P. Gauyacq, *Phys. Rev. Lett.*, 1992, **68**, 2842.
[38] T. Hecht, H. Winter and A. G. Borisov, *Surf. Sci.*, 1998, **406**, L607.
[39] M. A. Cazalilla, N. Lorente, R. Diez Muiño, J.-P. Gauyacq, D. Teillet-Billy and P. M. Echenique, *Phys. Rev. B*, 1998, **58**, 13991.
[40] W. More, J. Merino, R. Monreal, P. Pou and F. Flores, *Phys. Rev. B*, 1998, **58**, 7385.

[41] B. van Someren, P. A. Zeijlmans van Emmichoven and A. Niehaus, *Phys. Rev. A*, 2000, **61**, 022902.
[42] S. Wethekam, A. Mertens and H. Winter, *Phys. Rev. Lett.*, 2003, **90**, 037602.
[43] R. C. Monreal, L. Guillemot and V. A. Esaulov, *J. Phys.: Condens. Matter*, 2003, **15**, 1165.
[44] Yu. Bandurin, V. A. Esaulov, L. Guillemot and R. C. Monreal, *Phys. Rev. Lett.*, 2004, **92**, 017601-1.
[45] E. C. Goldberg, R. Monreal, F. Flores, H. H. Brongersma and P. Bauer, *Surf. Sci.*, 1999, **440**, L875.
[46] E. A. García and R. Monreal, *Phys. Rev. B*, 2000, **61**, 13565.
[47] E. A. García, N. P. Wang, R. C. Monreal and E. C. Goldberg, *Phys. Rev. B*, 2003, **67**, 2054261.
[48] G. C. van Leerdam and H. H. Brongersma, *Surf. Sci.*, 1991, **254**, 152; L. C. A. van den Otelaar, S. N. Mikhailov and H. H. Brongersma, *Nucl. Instrum. Methods Phys. Res. B*, 1994, **45**, 420.

This Page Intentionally Left Blank

Nonlinear Screening and Electron Capture Processes of Ions in Metals

R. Díez Muiño[1,2] and A. Arnau[1,2,3]

[1] *Unidad de Física de Materiales, Centro Mixto CSIC-UPV/EHU, Paseo Manuel de Lardizabal 3, 20018 San Sebastián, Spain*
[2] *Donostia International Physics Center DIPC, Paseo Manuel de Lardizabal 4, 20018 San Sebastián, Spain*
[3] *Departamento de Física de Materiales, Facultad de Químicas UPV/EHU, Apartado 1072, 20080 San Sebastián, Spain*

Abstract

Slow ions interacting with metals introduce a strong rearrangement of electronic charge in their vicinity. We show the way in which density functional theory can be used to describe such displacement of charge and the subsequent modification of the screening properties of the medium. We also discuss some of the electron capture processes that lead to the eventual neutralization of the ions. We particularly focus into the Auger and radiative processes and review some theoretical calculations of the rates for these processes.

Contents

ADVANCES IN QUANTUM CHEMISTRY, VOLUME 45
ISSN: 0065-3276 DOI 10.1016/S0065-3276(04)45009-6

1. INTRODUCTION

Slow single- or multiple-charged ions interacting with bulk metals are rapidly screened by the medium electrons. The valence-band electronic density is locally modified by the ion perturbation and accommodates to screen the long-range Coulomb potential of the ion, ensuring charge neutrality at large distances. The induced polarization strongly depends on the particle charge state that varies along the ion trajectory. Several electron capture processes can reduce the ion charge state. Among them, we quote (i) Auger processes, in which one electron is captured from the valence band of the metal with a simultaneous electronic excitation, (ii) quasiresonant charge transfer, in which the one-electron levels of ion and target are very close in energy, and (iii) radiative capture, in which the energy released in the electron capture is emitted in the form of photons. Electron loss from a bound state of the projectile to unoccupied states of the metal can happen as well. For slow ions, the competition between the capture and loss processes can eventually lead to the complete neutralization of the projectile. The time scale at which the neutralization process takes place is crucial to understand the experimental outputs provided by different spectroscopies.

An accurate theoretical study of the charge exchange processes between the ion and the metal target requires to account for the large rearrangement of charge induced by the ion. This is even more important in the case of multicharged ions [1], for which the ion screening is made by a very localized electronic cloud. The screening cloud concentrates as many electrons as the value of the ion charge in the range of a few atomic units of space. Our goal in this paper is twofold: to show the local effects that the presence of an ion has in the valence-band electronic density of a metal, and to account for these effects in the calculation of the rates of some electron capture processes that determine the neutralization and relaxation times of ions in metals. We review some of the models that were used in the past to calculate these rates and discuss the accuracy of the results.

Atomic units are used throughout unless otherwise stated.

2. NONLINEAR SCREENING OF IONS IN METALS

A slow ion interacting with a metal induces a strong perturbation in the electronic density of the metal. There is a large rearrangement of electronic density due to the Coulomb potential of the projectile. The metal electrons are piled up in a spatial region within a few atomic units around the charge and screen the long-range Coulomb interaction. In the limit of ion velocities much smaller than the Fermi velocity of the medium electrons, the screening process can be described in a static picture, i.e., as if the ion were not moving. In this section, we use density functional theory (DFT) to study the

nonlinear screening of a static ion in a metal. The screening is primarily made by the metal valence electrons, that we describe using the free electron gas (FEG) model. First, we describe the actual way in which DFT can be applied to this problem and, second, we discuss some general ideas about the screening process, using some specific examples.

2.1. Density functional theory of ion screening

We use DFT and the Kohn–Sham (KS) equations [2]

$$\left\{-\frac{1}{2}\nabla^2 + V_{\text{eff}}(\mathbf{r})\right\}\varphi_i(\mathbf{r}) = \varepsilon_i\varphi_i(\mathbf{r}), \tag{1}$$

to calculate self-consistently the effective potential $V_{\text{eff}}(\mathbf{r})$ and the electronic density $\Delta n(\mathbf{r}) = n(\mathbf{r}) - n_0$ induced by a charge Z embedded in a FEG [3,4]. The electronic density of the FEG without impurity is constant and its value is n_0. It is customary to define the parameter r_s to describe the FEG from $1/n_0 = 4\pi r_s^3/3$. The Fermi level of the FEG is obtained as a function of r_s as $\varepsilon_f = (9\pi)^{2/3}/2^{7/3}/r_s^2$. In equation (1), $\varphi_i(\mathbf{r})$ and ε_i are the KS eigenfunctions and eigenvalues, respectively. The effective potential $V_{\text{eff}}(\mathbf{r})$ is composed of three terms, namely:

$$\begin{aligned} V_{\text{eff}}(\mathbf{r}) &= V_{\text{ext}}(\mathbf{r}) + V_{\text{es}}(\mathbf{r}) + V_{\text{xc}}(\mathbf{r}) \\ &= -\frac{Z}{r} + \int \mathrm{d}\mathbf{r}' \frac{\Delta n(\mathbf{r}')}{|\mathbf{r} - \mathbf{r}'|} + \{v_{\text{xc}}[n(\mathbf{r})] - v_{\text{xc}}[n_0]\}, \end{aligned} \tag{2}$$

where $V_{\text{ext}}(\mathbf{r})$ is the external potential created by the ion, $V_{\text{es}}(\mathbf{r})$ is the electrostatic potential due to the change in electronic density $\Delta n(\mathbf{r})$ induced by the charge Z, and $V_{\text{xc}}(\mathbf{r}) = v_{\text{xc}}[n(\mathbf{r})] - v_{\text{xc}}[n_0]$ is the change in the exchange-correlation potential, that we calculate in the local density approximation (LDA) using the parametrization of Ref. [5]. The electronic density is obtained as a sum over occupied KS states

$$n(\mathbf{r}) = \sum_{i \in \text{occ.}} |\varphi_i(\mathbf{r})|^2 = 2\sum_{\varepsilon_i < 0} |\varphi_i(\mathbf{r})|^2 + 2\int_0^{\varepsilon_f} \mathrm{d}\varepsilon_i |\varphi_i(\mathbf{r})|^2. \tag{3}$$

The occupied KS states can be either those bound to the external charge (i.e., those KS states with negative eigenvalue $\varepsilon_i < 0$) or the scattering KS states with eigenvalues lower than the Fermi level $\varepsilon_i = k_i^2/2 < \varepsilon_f$. Hence, the induced electronic density $\Delta n(\mathbf{r})$ can be split into two terms

$$\Delta n(\mathbf{r}) = \Delta n^{\text{b}}(\mathbf{r}) + \Delta n^{\text{c}}(\mathbf{r}), \tag{4}$$

one accounting for the contribution of the KS bound states $\Delta n^{\text{b}}(\mathbf{r})$, and a second one accounting for the contribution of the scattering states $\Delta n^{\text{c}}(\mathbf{r})$ [6].

From the practical point of view, the results that we show in this section are obtained using a numerical procedure similar to some classical references in the field [4]. As the system has spherical symmetry, we expand $\varphi_i(\mathbf{r})$ in the spherical harmonic basis set and solve self-consistently the set of KS equations (Equation (1)).

Although DFT is only rigorously founded for the calculation of ground state properties, it has been shown to be very useful in the description of ion/metal interactions [6–9], even if this situation corresponds to an excited state of the system. In practice, the study of ions can be accomplished by filling just some of the bound KS states, those that correspond to the electronic configuration of choice, and allowing some 'holes' in the configuration. The self-consistent iterative procedure is then performed in the usual way. Several authors have discussed the validity of this approximation [10,11]. From a more practical point of view, the presence of holes in these excited configurations may be seen as if one were using a sort of 'pseudopotential' for the external potential $V_{\text{ext}}(\mathbf{r})$, to represent the incident ion core region. This approximation should remain valid as long as the lifetime of the holes τ_{h} is longer than the typical response time of the system $\tau_{\text{h}} \gg 1/\omega_{\text{p}}$ (with ω_{p} being the plasmon energy: $\omega_{\text{p}}^2 = 4\pi n_0$). If this is the case, the perturbation induced by the ion in the valence band of the metal, which is the one of interest, is calculated with as much precision as LDA allows. The screening of the n_{h} holes is provided by the electronic charge induced in the continuum $\Delta n^{\text{c}}(\mathbf{r})$, and integrates to the net charge of the ion. This leads to a generalization of Friedel sum rule [12] for the charge neutrality of the system:

$$Z + n_{\text{h}} = \frac{2}{\pi} \sum_l (2l+1)\delta_l(\varepsilon_{\text{f}}), \tag{5}$$

where $\delta_l(\varepsilon_{\text{f}})$ are the scattering phase shifts at the Fermi level, and l is the angular momentum index in the partial wave expansion of the KS wavefunctions. The addition of n_{h} to Z in equation (5) accounts for the lack of n_{h} electrons in the empty bound states. The number of holes n_{h} also determines how many of the electronic states are bound. As n_{h} decreases, the outer bound orbitals merge into the continuum, without an appreciable variation of the spatial shape of the induced electronic density. This means that the screening by a low-lying orbital in the continuum is very similar to that of a weakly bound state [13].

A useful quantity to understand the ion screening process and the spatial distribution of the electronic screening cloud is the induced density of levels in the continuum $\delta\rho(k)$, with $\varepsilon = k^2/2$. Formally, $\delta\rho(k)$ is defined as

$$\delta\rho(k) = 2k^2 \int \mathrm{d}\Omega_{\mathbf{k}} \int \mathrm{d}^3\mathbf{r}[|\varphi_k(\mathbf{r})|^2 - |\varphi_k^0(\mathbf{r})|^2], \tag{6}$$

where $\varphi_i^0(\mathbf{r})$ are the wavefunctions in the absence of external charge (plane waves in our case), and spin degeneracy is taken into account. With this

definition, $\delta\rho(k)$ is a density in k-space and the total number of electrons induced in the continuum N_e is

$$N_e = \int dk\, \delta\rho(k). \tag{7}$$

In practice, $\delta\rho(k)$ can be calculated in an easier way, using the phase shifts of the KS radial wavefunctions:

$$\delta\rho(k) = \frac{2}{\pi} \sum_l (2l+1) \frac{d}{dk} \delta_l(k). \tag{8}$$

2.2. Piling up of charge in the vicinity of the ion

As an illustration of the strong perturbation introduced by an ion in a metal and of the theoretical description of it in nonlinear theory of screening, we show some results obtained for the interaction of Ne ions with metals. Multicharged Ne ions have been widely used in the experimental study of ion neutralization and electron emission processes at metal surfaces [14–16]. We plot in Fig. 1 the electronic density induced by a Ne ion in a FEG of

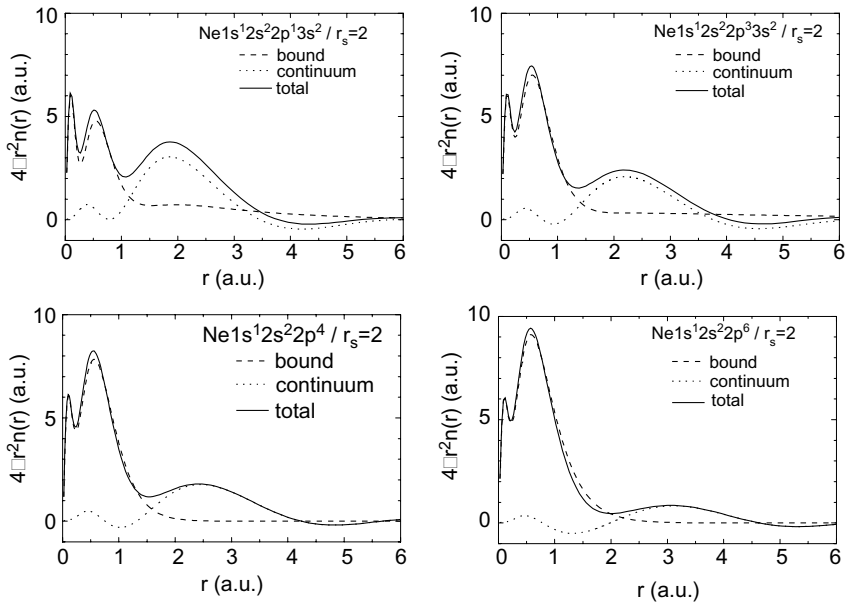

Fig. 1. Radial dependence of the induced electronic density around a Ne ion in a free electron gas ($r_s = 2$) for different electronic configurations, as shown in the plots. The solid line is the total induced density, the dashed line is the contribution from the bound states, and the dotted line is that from the continuum states.

$r_s = 2.0$, as well as the bound and continuum contributions to it [8]. Figure 1 shows several electronic configurations, that can be found in the neutralization sequence of a Ne^{+9} ion inside a metal [15]. There is one K-shell hole in all the configurations shown, but the number of L-shell holes is different in each of the plots. An electronic screening cloud surrounds the ion as well. The screening cloud is made by the continuum electrons and occasionally by an additional contribution that originates from M-shell states, if bound. This negatively charged cloud completely screens the ion at large distances. The quantities that determine whether the M shell is bound or not are n_0 and the number of electrons in the inner shells. In the case of a Ne ion with one K-shell hole inside a FEG with $r_s = 2.0$, the 3s orbital is bound only if the number of L-shell electrons n_L is ≤ 5 [8].

For $r_s = 2$ and when $n_L > 5$, the 3s orbital merges into the continuum. This modification does not affect much the shape of the electronic cloud, as shown in Fig. 1. This may be better understood with the help of Fig. 2, in which we present the induced density of states in the continuum and its angular momentum components, as defined in equation (8), for several L-shell configurations. The contribution of each continuum l-component

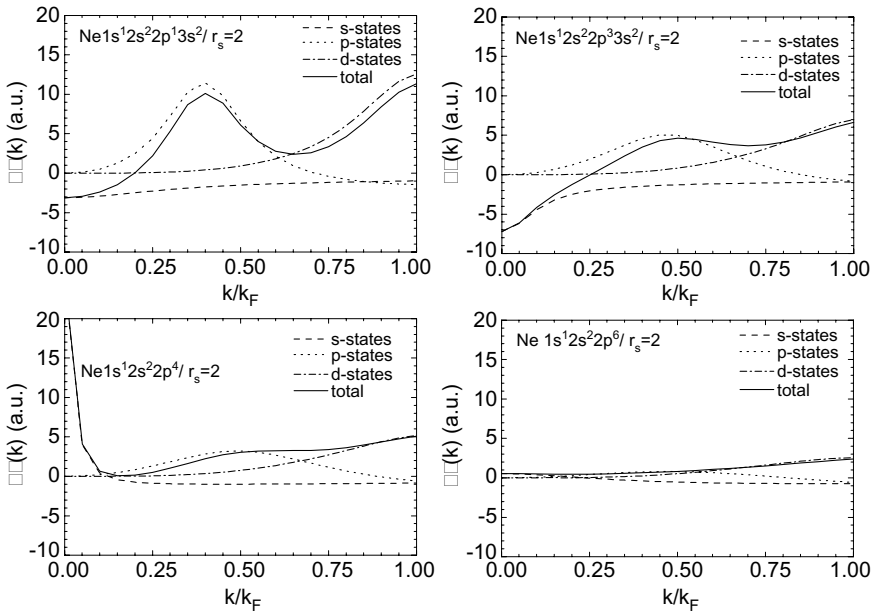

Fig. 2. Induced density of levels in the continuum for a Ne ion in a free electron gas ($r_s = 2$) Different electronic configurations are shown. The solid line is the total induced density of levels. Dashed lines, dotted lines and dash-dotted lines are the partial contributions of s, p, and d states, respectively.

strongly depends on the existence of weakly bound states with the same l symmetry. For instance, there is a low-energy peak in the s-wave line that appears when the sixth electron is deposited into the L shell. This peak corresponds to the mentioned merging of the 3s orbital into the continuum. Otherwise, the main components of the screening density are the p-wave and the d-wave. The first one is favored only when few electrons populate the bound 2p orbital and the second one when the core shells are nearly filled and the screening cloud radius extends up to 3–4 a.u. Actually, the behavior of the p-wave for the highest charge state may be understood as a 3p resonance of the Ne ion in the continuum. This is a general picture that helps to understand the way in which the screening is built up for multicharged ions interacting with metals.

One of the most interesting features in the highly charged Ne-ion screening process is that the electronic screening cloud has an M-shell character, that does not depend very much on the electronic density of the medium in which it is embedded. The induced electronic density looks like that of a neutral Ne atom in the gas phase with the same number of inner-shell holes. We show an example of that in Fig. 3, in which we plot the electronic density induced in the continuum by a $Ne1s^13s^2$ ion for two different values of the FEG electronic density, namely $r_s = 1.5$ and 2. We compare these results to the electronic density of the p and d electrons of a neutral Ne atom in the gas phase in the excited electronic configuration $1s^13s^23p^63d^1$. The gas-phase calculation is made in the Hartree–Fock–Slater approximation. Figure 3 shows that the electronic density induced in the continuum by the embedded Ne ion is very similar for the two values of r_s, and resembles that of the atomic calculation. In a general way, we can

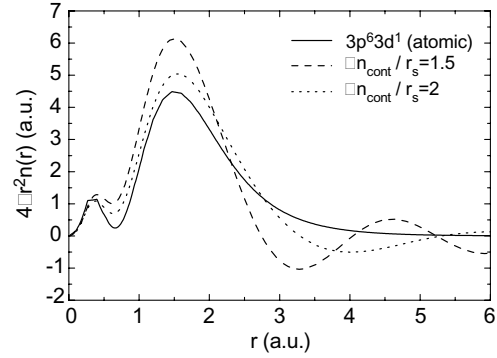

Fig. 3. Radial dependence of the electronic density induced in the continuum by a Ne $1s^13s^2$ ion in a free electron gas of $r_s = 1.5$ (dashed line) and $r_s = 2$ (dotted line). The solid line is the p and d electronic density for a neutral Ne atom in the gas phase in the electronic configuration Ne $1s^13s^23p^63d^1$, as calculated in the Hartree–Fock–Slater model.

state that the induced screening cloud around the ion mimics the charge-distribution of the outer-shells in gas-phase neutral atoms with inner-shell holes [17,18].

3. ELECTRON CAPTURE PROCESS

The time scale at which slow multicharged ions are neutralized and relaxed in solids determines the depth at which the potential energy of the incoming ion is deposited. Several processes are responsible for the neutralization of slow multicharged ions traveling through metals [1]. Quasiresonant capture from metal core levels and Auger transitions are the most effective ones in filling the ion inner shells, except for very heavy ions. Quasiresonant capture plays a role only if the electronic levels of projectile and target are close in energy [17,18]. In the following, we focus our attention on Auger processes. We also discuss radiative recombination processes, that become competitive for increasing transition energies (i.e., increasing ion charges).

3.1. Theoretical description of Auger capture processes

Let us start by describing the Auger capture process in a simple one-electron picture: an electron decays from a metal valence band state $|\varphi_1\rangle$ of energy $\varepsilon_1 = k_1^2/2$ to a bound state of the ion $|\varphi_\alpha\rangle$ of energy ε_α. The energy balance is compensated by an excitation of energy $\omega = \varepsilon_1 - \varepsilon_\alpha$ in the metal. The charge state of the ion is thus modified by the Auger process. The process is schematically shown in Fig. 4.

In the self-energy formalism, the probability of Auger capture per unit time Γ can be calculated in terms of the screened Coulomb interaction $W(\mathbf{r}, \mathbf{r}', \omega)$ [19]

$$\Gamma = -2 \sum_{\varphi_1 \in \text{occ.}} \text{Im}\left\{ \int d\mathbf{r}\, d\mathbf{r}' \varphi_\alpha^*(\mathbf{r}) \varphi_1^*(\mathbf{r}') W(\mathbf{r}, \mathbf{r}', \omega) \varphi_\alpha(\mathbf{r}') \varphi_1(\mathbf{r}) \right\}, \quad (9)$$

where $\text{Im}\{x\}$ denotes imaginary part of the complex number x, and the sum over occupied states φ_1 includes all scattering states with energies from the bottom of the band $\varepsilon_1 = 0$ to the Fermi level $\varepsilon_1 = \varepsilon_f$. The probability Γ is the rate per spin state. The screened interaction $W(\mathbf{r}, \mathbf{r}', \omega)$ has to be evaluated at the energy ω, which corresponds to the energy difference between the initial and final states. $W(\mathbf{r}, \mathbf{r}', \omega)$ can be calculated in terms of the many-body response function of the system $\chi(\mathbf{r}, \mathbf{r}', \omega)$ and the bare Coulomb potential $V_C(\mathbf{r}, \mathbf{r}') = 1/|\mathbf{r} - \mathbf{r}'|$:

$$W(\mathbf{r}, \mathbf{r}', \omega) = V_C(\mathbf{r}, \mathbf{r}') + \int d\mathbf{r}_1\, d\mathbf{r}_2\, V_C(\mathbf{r}, \mathbf{r}_1) \chi(\mathbf{r}_1, \mathbf{r}_2, \omega) V_C(\mathbf{r}_2, \mathbf{r}'). \quad (10)$$

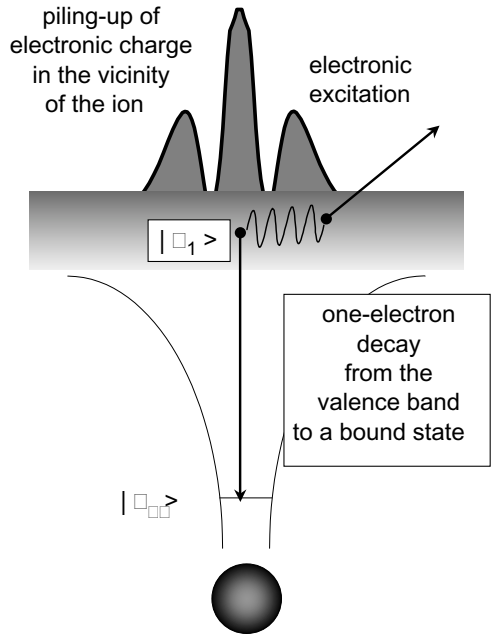

Fig. 4. Schematic picture of the Auger capture process. An electron is captured from a valence band state $|\varphi_1\rangle$ to a state bound to the ion $|\varphi_\alpha\rangle$. An electronic excitation (either an electron–hole pair or a collective excitation) is created at the same time in the medium.

Using equations (9) and (10), the rate Γ can be written as well in terms of the response function $\chi(\mathbf{r}, \mathbf{r}', \omega)$:

$$\Gamma = -2 \sum_{\varphi_1 \in \text{occ.}} \text{Im}\left\{ \int d\mathbf{r}\, d\mathbf{r}' [v^{\text{ext}}_{\alpha,1}(\mathbf{r})]^* \chi(\mathbf{r}, \mathbf{r}', \omega) v^{\text{ext}}_{\alpha,1}(\mathbf{r}') \right\}, \tag{11}$$

where the external potential $v^{\text{ext}}_{\alpha,1}(\mathbf{r})$ has been defined as:

$$v^{\text{ext}}_{\alpha,1}(\mathbf{r}) = \int d\mathbf{r}_1 \frac{\varphi_\alpha(\mathbf{r}_1)\varphi_1^*(\mathbf{r}_1)}{|\mathbf{r} - \mathbf{r}_1|}. \tag{12}$$

Equation (11) allows to interpret the electronic excitation in the Auger process as the medium response to a dynamic fluctuation of charge between the states $\varphi_1(\mathbf{r})$ and $\varphi_\alpha(\mathbf{r})$. From this point of view, we apply linear response theory to an external perturbation which is the electrostatic potential $v^{\text{ext}}_{\alpha,1}(\mathbf{r})$ created by such charge fluctuation. In general terms, the response function $\chi(\mathbf{r}, \mathbf{r}', \omega)$ completely determines the behavior of the system in response to an external perturbation, provided that the latter is sufficiently small and thus linear theory is applicable. The imaginary part of $\chi(\mathbf{r}, \mathbf{r}', \omega)$ contains

information on the system excitation spectrum. The simplest approximation to calculate $\chi(\mathbf{r}, \mathbf{r}', \omega)$ is the so-called Hartree level, in which the electronic excitations are described as one-electron processes. The response function in this approximation $\chi_0(\mathbf{r}, \mathbf{r}', \omega)$ is a sum over single-particle electronic wavefunctions $\varphi_2(\mathbf{r})$ and $\varphi_3(\mathbf{r})$ (with energies ε_2 and ε_3) [20]:

$$\chi_0(\mathbf{r}, \mathbf{r}', \omega) = \sum_{\varphi_2 \in \text{occ.}} \sum_{\varphi_3 \notin \text{occ.}} \left[\frac{\varphi_2^*(\mathbf{r})\varphi_2(\mathbf{r}')\varphi_3^*(\mathbf{r}')\varphi_3(\mathbf{r})}{\omega + \varepsilon_2 - \varepsilon_3 + \mathrm{i}\delta} - \frac{\varphi_2(\mathbf{r})\varphi_2^*(\mathbf{r}')\varphi_3(\mathbf{r}')\varphi_3^*(\mathbf{r})}{\omega - \varepsilon_2 + \varepsilon_3 + \mathrm{i}\delta} \right], \tag{13}$$

where the sum over $\varphi_2(\varphi_3)$ runs over occupied (unoccupied) scattering states, and δ is a positive infinitesimal. In practice, the sum over final states can be simplified with the help of one-electron Green functions $G(\mathbf{r}, \mathbf{r}', \omega)$ [21]:

$$\chi_0(\mathbf{r}, \mathbf{r}', \omega) = \sum_{\varphi_2 \in \text{occ.}} [\varphi_2^*(\mathbf{r})\varphi_2(\mathbf{r}')G(\mathbf{r}, \mathbf{r}', \varepsilon_2 + \omega) + \varphi_2(\mathbf{r})\varphi_2^*(\mathbf{r}')G^*(\mathbf{r}, \mathbf{r}', \varepsilon_2 - \omega)], \tag{14}$$

It can be shown that the calculation of $\mathrm{Im}[\chi_0]$ in real space and its subsequent substitution in the expressions for the Auger rate, equations (9) and (10), leads to the standard Fermi's golden rule for the calculation of the Auger rate when the excitations in the medium are obtained in the single-particle approximation [22]:

$$\Gamma = 2\pi \sum_{\varphi_1 \in \text{occ.}} \sum_{\varphi_2 \in \text{occ.}} \sum_{\varphi_3 \notin \text{occ.}} \left| \int \mathrm{d}\mathbf{r}\, \mathrm{d}\mathbf{r}' \varphi_\alpha^*(\mathbf{r})\varphi_3^*(\mathbf{r}')V_C(\mathbf{r}, \mathbf{r}')\varphi_2(\mathbf{r}')\varphi_1(\mathbf{r}) \right|^2 \delta(\varepsilon_1 + \varepsilon_2 - \varepsilon_\alpha - \varepsilon_3). \tag{15}$$

A more sophisticated approximation to calculate the Auger rate involves the inclusion of many-body effects in the medium excitations. This can be achieved by using the many-body response function of the interacting-electron system $\chi(\mathbf{r}, \mathbf{r}', \omega)$ [19]. In the random-phase approximation (RPA), χ is obtained in a self-consistent way:

$$\chi(\mathbf{r}, \mathbf{r}', \omega) = \chi^0(\mathbf{r}, \mathbf{r}', \omega) + \int \mathrm{d}\mathbf{r}_1\, \mathrm{d}\mathbf{r}_2\, \chi^0(\mathbf{r}, \mathbf{r}_1, \omega)V_C(\mathbf{r}_1, \mathbf{r}_2)\chi(\mathbf{r}_2, \mathbf{r}', \omega). \tag{16}$$

Collective excitations, that may be of importance for a certain range of energies, are included in χ.

For the unperturbed FEG, the calculation of χ in the RPA leads to the Lindhard function [23] or some variations of it, such as the Mermin function [24]. The Lindhard function is equivalent to the use of plane waves as one-electron wavefunctions in Eq. (13), before the self-consistent calculation of χ

is made. For the unperturbed FEG, the calculation of χ and consequently that of the Auger rate Γ is simplified by working in Fourier space [25]. The equivalent of equation (11) is then

$$\Gamma = \frac{4}{\pi} \sum_{\varphi_1 \in \text{occ.}} \int \frac{\mathrm{d}^3\mathbf{q}}{q^4} \left| \int \mathrm{d}\mathbf{r}\ \varphi_\alpha(\mathbf{r}) \mathrm{e}^{\mathrm{i}\mathbf{q}\mathbf{r}} \varphi_1(\mathbf{r}) \right|^2 \mathrm{Im}[\chi(\mathbf{q}, \omega)] \qquad (17)$$

3.2. Auger capture rates for ions in metals

Let us start by reviewing some calculations of the Auger capture rates for highly charged Ne ions in metals [7,8]. The calculations were performed by using equation (17), with the initial $\varphi_1(\mathbf{r})$ and final $\varphi_\alpha(\mathbf{r})$ wavefunctions approximated by KS orbitals, as calculated in the embedding of a Ne ion with a given electronic configuration in a FEG. The response function χ is the Mermin response function, that facilitates the discussion on the relative importance of collective excitations in the Auger capture process. These approximations imply that we are taking into account the strong rearrangement of electronic charge induced by the Ne ion in the calculation of the decay process, but not in the medium response.

To make a connection with experimental measurements [15] we consider that the Ne ion has only one K-shell electron. We also assume that, once the ion has entered the solid, its M shell (if bound) is rapidly filled. The electronic configuration of the Ne ion then has the mentioned K-shell hole and a given number of L-shell holes. We plot in Fig. 5 the L-shell Auger capture rate Γ_L for Ne ions in a FEG of $r_\mathrm{s} = 1.5$ and 2.0, as a function of the

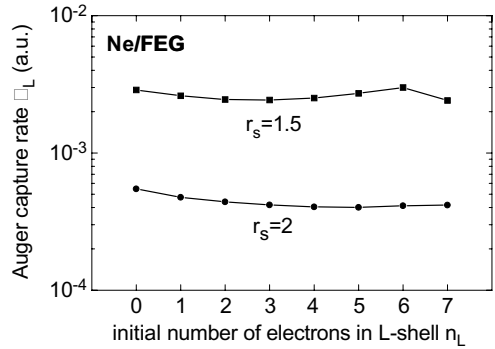

Fig. 5. Probability (per unit time) of Auger capture to the L shell of a Ne ion embedded in a FEG Γ_L as a function of the number of L-shell electrons bound to the ion before the capture. Γ_L is in atomic units. Two different values of the electronic density $r_\mathrm{s} = 1.5$ and 2 are shown.

initial number of electrons in the L shell n_L. n_L is the sum of the initial number of electrons in the 2s orbital n_{2s} plus the initial number of electrons in the 2p orbital n_{2p} ($n_L = n_{2s} + n_{2p}$). The total L-shell rate Γ_L is obtained from the rates per spin state (as calculated in equation (17)) to the 2s (Γ_{2s}) and 2p (Γ_{2p}) states, and taking into account the spin degeneracy:

$$\Gamma_L = (6 - n_{2p})\Gamma_{2p} + (2 - n_{2s})\Gamma_{2s}. \tag{18}$$

In the case of $r_s = 2.0$, there is an additional channel (not shown in the plot) that contributes to the Auger L-shell filling for $n_L \leq 5$: the decay of the M shell bound electrons to the L shell [8]. This channel is absent in the $r_s = 1.5$ case because the M shell is never bound, no matter which the number of electrons in the L shell is.

The L-shell filling rates of Ne atoms are weakly dependent on the number of electrons in the L shell. This is due to the compensation of two effects: the number of available final states enhances the total rate when n_L is small (see equation (18)), but the rate per spin state increases with n_L as the overlap between the initial and final orbitals is larger and the transition energy ΔE is lower. This behavior is not general. If the transition energy ω becomes smaller than the plasmon energy of the metal, excitation of plasmons in the medium is inhibited and the transition rates appreciably decrease. This is the case for the L-shell filling rates of N ions in metals, that are shown in Fig. 6. In the case of Ne, as can be seen in Fig. 7 for a FEG with $r_s = 2$, the transition energies in the Auger capture are always above the plasmon peak,

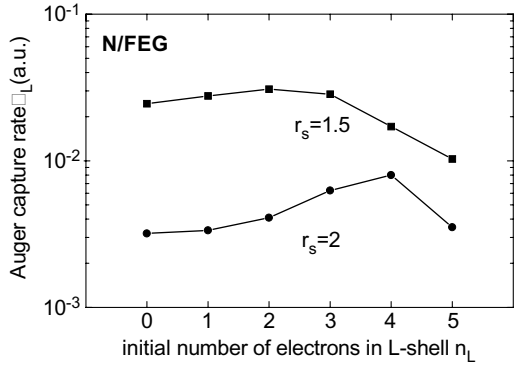

Fig. 6. Probability (per unit time) of Auger capture to the L shell of a N ion embedded in a FEG Γ_L as a function of the number of L-shell electrons bound to the ion before the capture. Γ_L is in atomic units. Two different values of the electronic density $r_s = 1.5$ and 2 are shown. For $n_L > 5$ the 2p KS orbital merges into the continuum and is no longer bound.

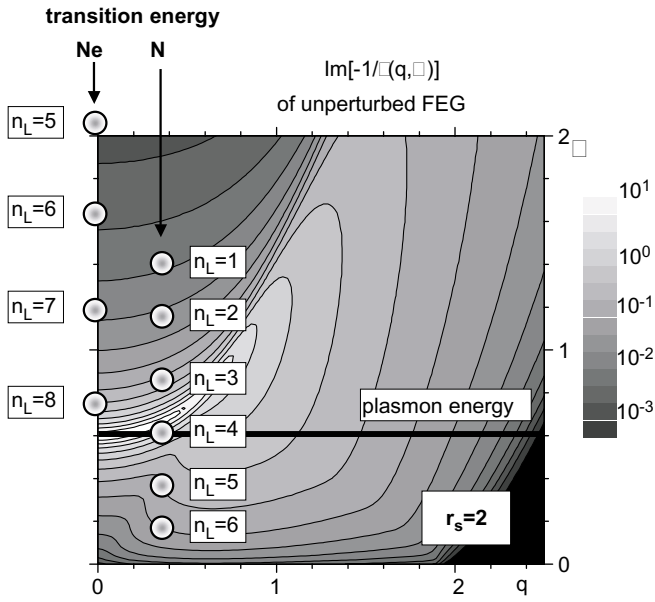

Fig. 7. Contour plot of the inverse of the dielectric function imaginary part $\mathrm{Im}[-1/\epsilon(q,\omega)]$ for an unperturbed electron gas of $r_s = 2$, as a function of the momentum transfer q and the transition energy ω. All quantities in atomic units. The dielectric function is calculated using the Mermin model. The contour plot is in logarithmic scale. The KS eigenenergies of the 2p orbital for Ne and N ions embedded in the electron gas are shown with circles for different electronic configurations (all of them with a K-shell hole and a given number of electrons n_L in the L shell). The value of the plasmon energy is also shown with a thick solid line.

even for the largest values of n_L. However, in the case of N ions with similar electronic configurations, the transition energies can be smaller than the plasmon energy when a large number of electrons are bound to the L shell. The disappearance of the plasmon-excitation channel in the Auger process is reflected in the nonmonotonic behavior of Γ as a function of n_L.

We recall that the results shown above have been obtained using the unperturbed electron gas response function, i.e., without taking into account the ion perturbation in the electronic response of the system. However, this might be seen as a rough approximation, considering the strong rearrangement of charge in the vicinity of the ion. For the localized excitations created in the Auger capture process, it is reasonable to assume that at least the excitation of electron–hole pairs should be affected by the presence of the ion. We will come back to this point in Section 4.

3.3. Radiative capture processes for ions in metals

In the same way that the rearrangement of charge is crucial to determine the Auger capture rates from the valence band of a metal, it is reasonable to assume that it should also be of great importance to calculate radiative rates from the metal valence band. Nevertheless, the theoretical approach is simpler because the energy associated to the decay is released in the form of photons, and no electronic excitations are created in the medium. The radiative capture process is shown schematically in Fig. 8. We call radiative capture to the process in which the initial state of the electron is a valence-band state, the final state is a bound state of the ion, and the energy balance is compensated by the emission of light.

We focus here into the radiative processes that modify the ion charge state, i.e., those that involve the capture of an electron from the target valence band. We do not include radiative relaxation processes in which one electron decays between two bound states of the ion, although they can be of the same importance in the description of a realistic neutralization and relaxation

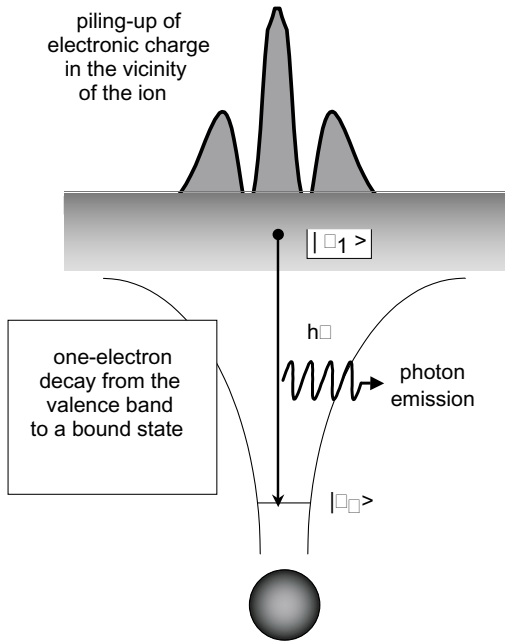

Fig. 8. Schematic picture of the radiative capture process. An electron is captured from a valence band state $|\varphi_1\rangle$ to a state bound to the ion $|\varphi_\alpha\rangle$. The transition energy is compensated by the emission of a photon.

process. The probability per unit time and per spin state Γ for the radiative capture process to a bound state φ_α in the dipole approximation is given by

$$\Gamma = \sum_{\varphi_1 \in \text{occ.}} \frac{4\alpha}{3c^2}\omega^3 |\langle \varphi_1 | \mathbf{r} | \varphi_\alpha \rangle|^2, \tag{19}$$

where the probability is averaged over all possible orientations of the light polarization, α is the fine structure constant, and c the speed of light.

To account for the target modification, we show results for which the initial $\varphi_1(\mathbf{r})$ and final $\varphi_\alpha(\mathbf{r})$ one-electron wavefunctions have been approximated by the KS orbitals of the ion embedded in a FEG. This is specially important in the description of the initial wavefunctions in the capture process $\varphi_1(\mathbf{r})$, but not in the case of the bound wavefunctions $\varphi_\alpha(\mathbf{r})$: the range of energies for which radiative processes are important usually corresponds to very deeply bound levels, for which the effects of embedding the ion in the electron gas are often negligible, and a simple atomic description of the deeply bound wavefunctions would be sufficiently accurate for the processes we are interested in. Although the cubic factor in the transition energy is not responsible for the whole dependence on the transition energy (the dipolar matrix elements are usually larger for decreasing transition energies), it is already an indication that radiative transitions play a prominent role for heavy ions.

We show in Fig. 9 the radiative capture rates to the K and L shells for an Ar ion embedded in a FEG of $r_s = 1.97$, that may represent Si, for instance [26].

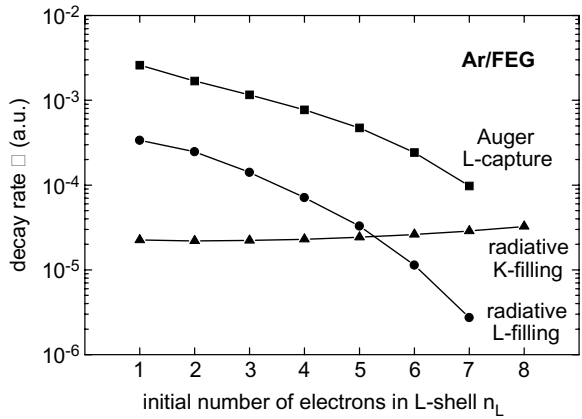

Fig. 9. Probability (per unit time) of radiative capture to the K and L shells of an Ar ion embedded in a FEG of $r_s = 1.97$, as a function of the number of L-shell electrons bound to the ion before the capture. The Ar ion has one K-shell hole. The Auger capture rate to the L shell is shown as well.

The rates are shown as a function of the number of L-shell electrons bound to the ion before the capture. The Ar ion has one K-shell hole as well. The M-shell orbitals are filled, if bound. For the sake of comparison, the Auger capture rates to the L shell are shown as well. We see that the latter are roughly one order of magnitude larger than those of the radiative capture, showing that the Auger mechanism is still the dominant one for the L shell of Ar.

4. DYNAMIC RESPONSE OF A STRONGLY PERTURBED ELECTRON GAS

We have shown in previous sections that the presence of ions induces a strong modification of the electronic density of metals. This is due to the high mobility of the valence-band electrons in this kind of systems. Let us show how this rearrangement of electronic charge determines the local dynamic response of the valence electrons to external perturbations. The piling up of charge introduced by the ion in the target can be included in the calculation of the response function in the following way: First, one calculates the embedding of the ion in the FEG using DFT. Afterwards, the KS states can be used to calculate the Hartree response function χ_0 (Equation (13)). Finally, the self-consistent response function χ can be obtained by matrix inversion in a real-space finite grid by means of equation (16) [27].

The response function χ so obtained includes new effects introduced in the electron excitation spectrum by the ion-induced rearrangement of charge.

4.1. Screened Coulomb interaction

One of the key magnitudes that characterize electron dynamics in the vicinity of the ion is the screened interaction $W(\mathbf{r}, \mathbf{r}', \omega)$ (Equation (10)). The probability of inelastic processes is determined by the imaginary part of the screened interaction $\mathrm{Im}[-W(\mathbf{r}, \mathbf{r}', \omega)]$. We show in Fig. 10 the value of $\mathrm{Im}[-W(x, x', \omega)]$ for the case of a neutral Ar atom embedded in a FEG of $r_s = 2$ along a line that joins the position of the Ar (the origin of coordinates) and the position of the Coulomb source x. $\mathrm{Im}[-W(x, x', \omega)]$ is calculated in the low-energy range $\omega \approx 0.17\omega_p$. The calculation includes the effect introduced by the Ar atom in the response function, and it is compared to the results obtained by using a Lindhard response function (unperturbed FEG). In both cases the absolute value of $\mathrm{Im}[-W(x, x', \omega)]$ is maximum at approximately $x = x'$. However, $\mathrm{Im}[-W(x, x', \omega)]$ is substantially affected by the rearrangement of electronic charge induced by the Ar atom in the valence band that reduces the interaction strength and introduces some structure in the shape of $\mathrm{Im}[-W(x, x', \omega)]$. Therefore, electron-excitation processes taking place in the neighborhood of the Ar ion are influenced by

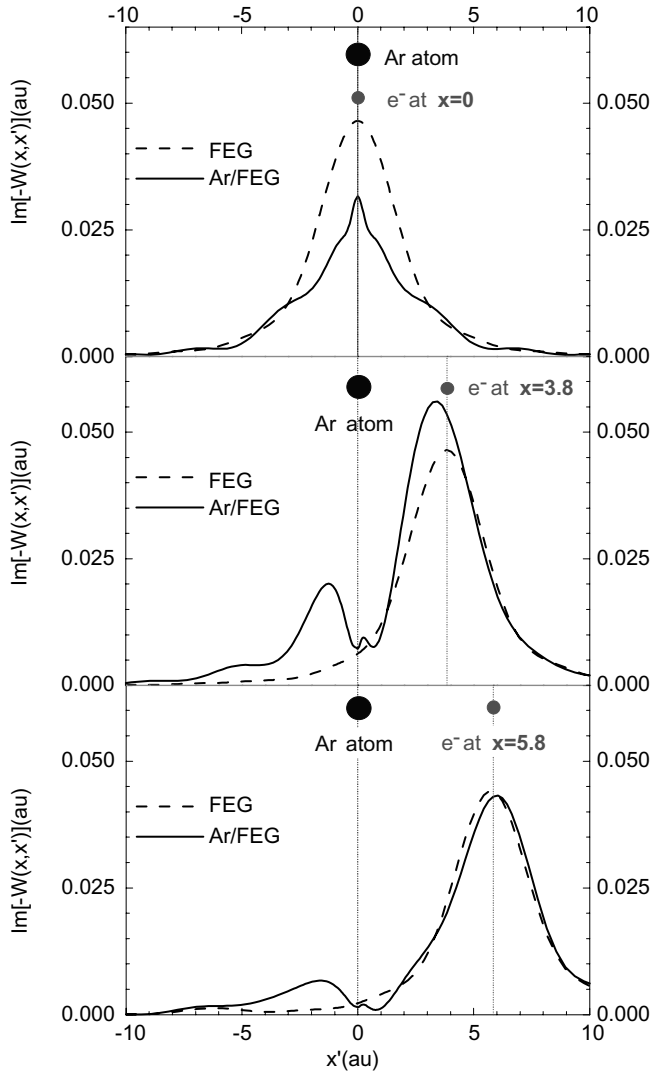

Fig. 10. From top to bottom, magnitudes in atomic units: imaginary part of the screened interaction $\mathrm{Im}[-W(x, x', \omega)]$ as a function of x', for different values of x ($x = 0$, 3.8 and 5.8), when an Ar atom is embedded in a free electron gas of $r_s = 2$. The Ar atom is located at the origin of coordinates. The solid line is the result including the Ar ion in the calculation, and the dashed line is the unperturbed electron gas result. The energy is $\omega = 0.17\omega_p$. All other magnitudes in atomic units.

this effect. For larger values of x, corresponding to a Coulomb source farther from the Ar atom (bottom panel), total screening of the ion is already achieved, and the unperturbed FEG result is practically recovered. The breakdown of symmetry introduced by the Ar atom is essentially different from that introduced by a surface: in the latter, the electronic excitations are always created *inside* the surface, and the maximum value of $\mathrm{Im}[-W(x, x', \omega)]$ does not necessarily correspond to the position $x = x'$ [19].

4.2. Auger rates using a self-consistent response function

As an example of the influence that this modification has in the probability of inelastic excitations, we show in Figs 11 and 12 the Auger capture rate to the 3p state of an Ar ion, for two different electronic configurations (corresponding to two different energy regimes). The rates are plotted as a function of k_1 (where $\varepsilon_1 = k_1^2/2$). Figure 11 shows the results for an Ar^+ ion with a 3p hole that gets neutralized by the electron capture. The maximum transition energy for this configuration is that corresponding to one electron decaying from the Fermi level of the FEG to the 3p bound state ($\omega \approx 0.9\omega_p$). We are thus in the relatively low energy regime, in which the self-consistent effects in the calculation of the response function are crucial. Figure 12

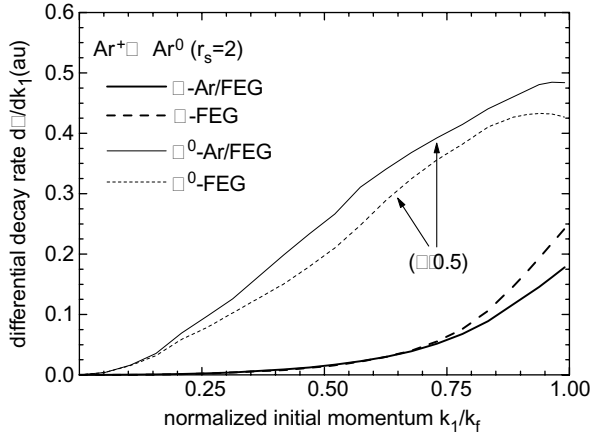

Fig. 11. Differential transition rate $\mathrm{d}\Gamma/\mathrm{d}k_1$ (in atomic units) as a function of the initial momentum of the electron (normalized to the Fermi momentum) k_1/k_f for an Auger capture process from a free electron gas of $r_\mathrm{s} = 2$ to the 3p state of an Ar^+ ion. Solid lines include the Ar in the calculation of the response function. Dashed lines are the unperturbed free electron gas results. Thick lines are calculated with the self-consistent response function χ, while thin lines show the results using the Hartree response χ_0 (the latter are multiplied by 0.5 before being plotted).

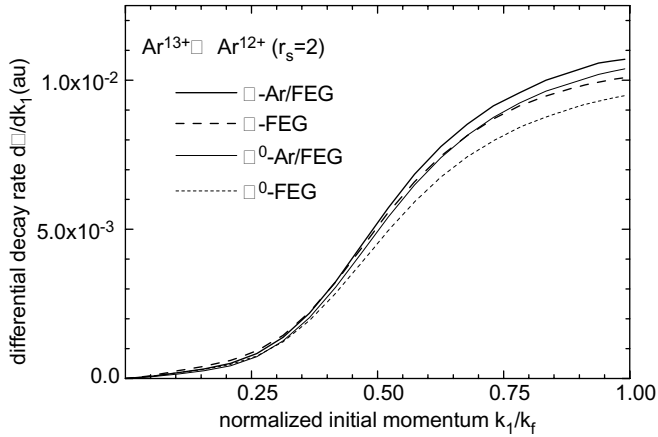

Fig. 12. The same as Fig. 11, but for an Auger capture process from a free electron gas of $r_s = 2$ to the 3p state of an Ar^{13+} ion.

shows the case of an Ar^{13+} ion that captures an electron to the 3p orbital. The electronic configuration of the Ar^{13+} ion is $1s^1 3s^2 3p^2$. The transition energy is in the high-energy regime (the maximum transition energy is $\omega \approx 2.8\omega_p$). The electronic density of the FEG is $r_s = 2$ in both cases.

Different levels of approximation in the calculation of the response function are plotted in Figs 11 and 12: thick (thin) lines show the results of using a self-consistent (single-particle) response function χ (χ_0). Solid lines include the Ar in the calculation, whereas dashed lines show the unperturbed FEG results. The free-electron-gas χ (thick dashed line) is the Lindhard response function.

Figure 11 shows significant electron-correlation effects in the low excitation-energy range. An accurate description of the medium response to the external fluctuation of charge requires a many-body description of the system. The screening of the external perturbation by medium electrons is highly underestimated in the independent-particle approximation. Perturbation of the medium by the ion introduces a reduction of roughly 20% in the value of the total rate Γ, obtained after integrating the differential rate from the bottom of the band $k_1 = 0$ to the Fermi level $k_1 = k_f$ in the low energy range (Fig. 11).

For higher excitation energies (Fig. 12), an independent-particle response function χ_0 gives reasonable results. The differences between the calculation with and without including the Ar ion are also smaller, of the order of 5–10%. It is worth to mention that, for this high-energy regime, the rate is increased when Ar is taken into account in the calculation. The behavior is thus opposite to what happens at low energies. Actually, this is due to two competing effects brought about by the localization of screening charge

induced by the ion: there is a change in the electron–electron interaction strength due to the stronger screening, but there is also an enhancement in the probability of electron excitation, due to the local increase of available electrons near the ion. The relative weight of these two effects depends on the particular value of the excitation energy ω. In simple terms, one could say that, as far as determining the imaginary part of the screened Coulomb interaction is concerned, the electron–electron screening effect is more important for low ω, while the increase in the available number of excitations (modification of phase space) is more important at high ω. The nontrivial balance between these two effects makes difficult to predict *a priori* the influence of the ion on the time-scales of inelastic transitions that depend on the electron–electron interaction in its vicinity.

5. FINAL REMARKS AND CONCLUSIONS

In summary, we have shown that an ion entering a metallic medium induces a large localization of screening charge, that strongly modifies electron dynamics through a change in the electron–electron interaction strength and in the probability of electron excitation. We have discussed the effects derived from this rearrangement of electronic charge in different inelastic processes that modify the charge state of the ion, such as Auger and radiative capture processes. Actually, our conclusions are not specific of these particular transitions, but could be generalized to any other inelastic process that depends on electron–electron interactions and is highly localized in space. We conclude that an accurate calculation of the rates for these processes requires a refined description of the ion/gas system, at least in the region within a few atomic units of the ion.

ACKNOWLEDGEMENTS

This work was supported in part by the Basque Departamento de Educación, Universidades e Investigación, the University of the Basque Country UPV/EHU (Grant No. 9/UPV 00206.215-13639/2001), and the Spanish Ministerio de Ciencia y Tecnología (Grant No. MAT2001-0946).

REFERENCES

[1] A. Arnau, F. Aumayr, P. M. Echenique, M. Grether, W. Heiland, J. Limburg, R. Morgenstern, P. Roncin, S. Schippers, R. Schuch, N. Stolterfoht, P. Varga, T. J. M. Zouros and H. P. Winter, *Surf. Sci. Rep.*, 1997, **27**, 117.
[2] W. Kohn and L. J. Sham, *Phys. Rev.*, 1965, **140**, A1133.

[3] C. O. Almbladh, U. von Barth, Z. D. Popovic and M. J. Stott, *Phys. Rev. B*, 1976, **14**, 2250.
[4] E. Zaremba, L. M. Sander, H. B. Shore and J. H. Rose, *J. Phys. F*, 1977, **7**, 1763.
[5] O. Gunnarson and B. I. Lundqvist, *Phys. Rev. B*, 1976, **13**, 4274.
[6] A. Arnau, P. A. Zeijlmans van Emmichoven, J. I. Juaristi and E. Zaremba, *Nucl. Instrum. Methods B*, 1995, **100**, 279.
[7] R. Díez Muiño, N. Stolterfoht, A. Arnau, A. Salin and P. M. Echenique, *Phys. Rev. Lett.*, 1996, **76**, 4636.
[8] R. Díez Muiño, A. Salin, N. Stolterfoht, A. Arnau and P. M. Echenique, *Phys. Rev. A*, 1998, **57**, 1126.
[9] J. I. Juaristi, A. Arnau, P. M. Echenique, C. Auth and H. Winter, *Phys. Rev. Lett.*, 1999, **82**, 1048.
[10] A. R. Williams and U. von Barth, in *Theory of the Inhomogeneous Electron Gas* (eds S. Lundqvist and N. H. March), Plenum Press, New York, 1983, Chapter 4.
[11] R. M. Dreizler and E. K. Gross, *Density Functional Theory*, Springer, Berlin-Heidelberg, 1990.
[12] J. Friedel, *Phil. Mag.*, 1953, **43**, 153.
[13] W. Kohn and C. Majumdar, *Phys. Rev.*, 1965, **138**, A1617.
[14] H. Kurz, K. Töglhofer, H. P. Winter, F. Aumayr and R. Mann, *Phys. Rev. Lett.*, 1992, **69**, 1140.
[15] M. Grether, A. Spieler, R. Köhrbrück and N. Stolterfoht, *Phys. Rev. A*, 1995, **52**, 426.
[16] M. Grether, D. Niemann, A. Spieler and N. Stolterfoht, *Phys. Rev. A*, 1997, **56**, 3794.
[17] A. Arnau, R. Köhrbrück, M. Grether, A. Spieler and N. Stolterfoht, *Phys. Rev. A*, 1995, **51**, R3399.
[18] N. Stolterfoht, A. Arnau, M. Grether, R. Köhrbrück, A. Spieler, R. Page, A. Saal, J. Thomaschewski and J. Bleck-Neuhaus, *Phys. Rev. A*, 1995, **52**, 445.
[19] P. M. Echenique, J. M. Pitarke, E. V. Chulkov and A. Rubio, *Chem. Phys.*, 2000, **251**, 1.
[20] A. Zangwill and P. Soven, *Phys. Rev. A*, 1980, **21**, 1561.
[21] M. J. Stott and E. Zaremba, *Phys. Rev. A*, 1980, **21**, 12.
[22] S. A. Deutscher, R. Díez Muiño, A. Arnau, A. Salin and E. Zaremba, *Nucl. Instrum. Methods B*, 2001, **182**, 8.
[23] J. Lindhard and K. Dans, *Vidensk. Selsk. Mat. Fys. Medd.*, 1954, **28** (8), 1.
[24] N. D. Mermin, *Phys. Rev. B*, 1970, **1**, 2362.
[25] P. M. Echenique, F. Flores and R. H. Ritchie (eds H. Ehrenreich and D. Turnbull), *Solid State Physics Series*, Academic Press, New York, 1990, Vol. 43, p. 229.
[26] D. Isaacson, *Compilation of r_s Values, Radiation and Solid State Laboratory*, New York University, New York, 1975.
[27] R. Díez Muiño, A. Arnau, A. Salin and P. M. Echenique, *Phys. Rev. B*, 2003, **68**, 041102(R).

This Page Intentionally Left Blank

Energy Loss in the Interaction of Atomic Particles with Solid Surfaces

M. Alducin[1] and J. I. Juaristi[2]

[1] *Donostia International Physics Center (DIPC), P. Manuel de Lardizabal 4, 20018 San Sebastián, Spain*

[2] *Depto. de Física de Materiales and Centro Mixto CSIC-UPV/EHU, Facultad de Química, UPV/EHU, Apartado 1072, 20080 San Sebastián, Spain*

Abstract

Recent studies on the energy loss of atomic particles interacting with solid surfaces are reviewed. Different approximations for the treatment of the screening and scattering are presented and their validity in the different coupling regimes is discussed. Illustrative comparisons with available experiments are provided.

Contents

1. INTRODUCTION

The study of the interaction of atomic particles with solid surfaces constitutes an active field of research. The use of different kind of projectiles

ADVANCES IN QUANTUM CHEMISTRY, VOLUME 45
ISSN: 0065-3276 DOI 10.1016/S0065-3276(04)45010-2

(neutral atoms, highly charged ions, spin-polarized projectiles, etc.) and targets (metals, insulators, ferromagnetic materials, etc.) enables to observe a variety of different phenomena. In this way, one can gain information on the structural and electronic properties of surfaces, as well as characterize the interaction process itself.

A large amount of the studies on this field are devoted to the analysis of the energy loss of atomic particles scattered off surfaces under grazing angle of incidence. The aim of this work is to review some recent developments on this problem. We focus on the theoretical approaches that have been used to characterize and understand the energy loss mechanisms under these conditions.

The work is divided in two parts. In Section 2 we use linear response theory to describe the dynamic screening and the energy loss of the projectile. This approach is justified in the weak coupling limit $Z_1/v \ll 1$, where Z_1 is the projectile charge and v its velocity. In Section 3 we treat the strong coupling limit ($Z_1/v \gg 1$). In this case, linear approaches are not justified due to the strong perturbation that the ion represents to the target. In these conditions one needs to use nonlinear screening approaches, like density functional theory (DFT) and scattering theory with full phase-shift calculation of the cross-sections, to arrive at a quantitative agreement with the measured data. We present examples in which these different approaches have been used and provide comparison with experiments where available.

The common feature of most of the theoretical approaches presented here is the use of the free electron gas model. In this model the only parameter used is the mean electronic density of the system n_0. In this respect, it is customary to use the one-electron radius r_s, defined as $1/n_0 = 4/3\pi r_s^3$. Finally, in different parts of this work atomic units (a.u.) are used, in which $\hbar = e^2 = m_e = 1$ where m_e and e are the electron mass and charge, respectively. In these units, the unit of length is the Bohr radius ($a_0 = 0.529$ Å), the unit of velocity is the Bohr velocity ($v_0 = 2.19 \times 10^8$ cm/s) and the unit of energy is the Hartree (1 Hartree = 27.2107 eV).

2. LINEAR THEORY OF ION–SURFACE INTERACTIONS

2.1. General

When an ion approaches a metal surface, the energy associated to its motion perpendicular to the surface determines whether it will penetrate the solid or it will be reflected at the top-most atomic layer. If one wants to obtain information about the structure of the surface, the trajectories of interest are those for which the particle interacts for a long duration with the metal surface before it is reflected. This situation is achieved by using projectiles

with small energy in the normal motion, as it is the case in grazing ion–surface collisions [1].

In the analysis of these experiments a central quantity is the so-called distance-dependent stopping power, i.e., the energy lost per unit path length traveled by the ion parallel to the metal surface, as a function of the ion–surface separation. Echenique and Pendry [2] used a local response function to calculate this quantity and applied it to obtain the energy loss of fast electrons traveling parallel to a surface. In later works, wave-vector dependent surface dielectric functions were used [3–8]. These calculations were based on the specular reflection model (SRM) [9,10]. This model permits to obtain the surface response function in terms of the bulk response function. The approximation consists in assuming that the conduction electrons are confined by an infinite potential barrier at the surface, and in neglecting the quantum interference between the outgoing and incoming components of the electrons reflected at this barrier. In a different approach Gravielle and collaborators [11,12] studied the interaction of a charged particle with the conduction electrons bounded by a finite step potential at the surface. This model described single particle excitations (electron–hole creation) but did not include collective excitations (plasmons). Finally, in the most advanced calculations of the distance-dependent stopping power known to date [13–15], the Kohn–Sham formulation [16] of the DFT [17] was used to calculate self-consistently a finite and smooth surface potential barrier. In these works, the jellium model was used to describe the conduction band of the metal: The ionic background made up of nuclei and core electrons was replaced by a uniform positive charge distribution. In Refs. [13,14] the Kohn–Sham orbitals were used to construct the response function of the system in the random phase approximation (RPA) [18,19]. In Ref. [15] exchange and correlation effects were also included in the calculation of the response within the so-called adiabatic local density approximation (ALDA) [20]. Nevertheless, it was observed that the stopping power for a particle traveling parallel to a metal surface was almost insensitive to this correction. On the contrary, the use of a self-consistently calculated finite surface barrier improved significantly the results obtained within the SRM up to velocities of the order of $v = 2 - 3v_0$, for both the stopping power and the total energy loss [13,14]. At higher velocities the SRM showed to be a reliable approximation.

A general description of the problem can be made as follows: a point charge Z_1 is moving parallel to the surface with velocity $\mathbf{v}$ along the x-direction at a distance $z_0 > 0$. Henceforth, z is the coordinate of the position vector normal to the surface. The top-most atomic layer is at $z = 0$ and the solid in the $z < 0$ side. We use capital letters for the coordinates parallel to the surface [$\mathbf{r} = (\mathbf{R}, z)$]. When a swift charged particle interacts

with a metal surface it loses energy creating excitations in the valence band of the target. In linear response theory, the contribution of valence band excitations to the stopping power is given by [13]:

$$\frac{\mathrm{d}E_{\mathrm{val}}}{\mathrm{d}x}(z_0) = \frac{-Z_1^2}{v}\int \frac{\mathrm{d}^2\mathbf{Q}}{2\pi^2}\mathbf{Q}\cdot\mathbf{v}\ \mathrm{Im}\{W^{\mathrm{ind}}(Q, z_0, z_0, \mathbf{Q}\cdot\mathbf{v})\}\,\Theta(\mathbf{Q}\cdot\mathbf{v}). \quad (1)$$

In this expression, $\mathbf{Q}$ is the component parallel to the surface of the momentum transferred to the medium (v and Q are the modulus of their corresponding magnitudes) and $W^{\mathrm{ind}}(Q, z, z', \omega)$ is the induced interaction, which is defined in terms of $\chi(Q, z_1, z_2, \omega)$, the two-dimensional Fourier transform of the density–density correlation function:

$$W^{\mathrm{ind}}(Q, z, z', \omega) = \left(\frac{2\pi}{Q}\right)^2 \int \mathrm{d}z_1 \int \mathrm{d}z_2\ \exp[-Q(|z_1 - z| + |z_2 - z'|)] \times \chi(Q, z_1, z_2, \omega). \quad (2)$$

In the RPA, $\chi(Q, z, z', \omega)$ satisfies the following integral equation [18,19]:

$$\chi(Q, z, z', \omega) = \chi_0(Q, z, z', \omega) + \frac{2\pi}{Q}\int \mathrm{d}z_1 \int \mathrm{d}z_2 \times \chi_0(Q, z, z_1, \omega)\ \mathrm{e}^{-Q|z_1 - z_2|}\chi(Q, z_2, z', \omega) \quad (3)$$

where $\chi_0(Q, z, z', \omega)$ is the density–response function for noninteracting electrons, that can be written in terms of the one-electron wavefunctions and eigenvalues of the one-electron Hamiltonian.

We note that far away from the surface ($z \gg z_1$ and $z' \gg z_2$) a useful approximation consists in writing the induced interaction in terms of the so-called surface response function $g(Q, \omega)$:

$$W^{\mathrm{ind}}(Q, z, z', \omega) = -\frac{2\pi}{Q} g(Q, \omega)\mathrm{e}^{-Q(z+z')} \quad (4)$$

and

$$g(Q, \omega) = -\frac{2\pi}{Q}\int \mathrm{d}z_1 \int \mathrm{d}z_2\ \mathrm{e}^{Q(z_1+z_2)}\chi(Q, z_1, z_2, \omega). \quad (5)$$

For well-behaved free electron metals these quantities can be calculated using the SRM which, as explained above, has shown to constitute a valid approximation to obtain the energy loss of fast protons. Expressions for the screened interaction within the SRM can be found in Ref. [21]. In the subsequent construction, the electronic surface is located using the standard prescription that consists of placing it at a distance $d/2$ in front

of the top-most atomic layer, where d is the interplanar separation. Thus, the stopping power for positions outside ($z_0 > d/2$) and inside ($z_0 < d/2$) the solid is given by [3,4]

$$\frac{\mathrm{d}E_{\mathrm{val}}}{\mathrm{d}x}(z_0) = \frac{2Z_1^2}{\pi v^2}\int_0^\infty \mathrm{d}\omega\,\omega \int_0^\infty \frac{\mathrm{d}q}{Q}\mathrm{e}^{-2Q(z_0-d/2)} \times \mathrm{Im}\left\{\frac{\varepsilon_{\mathrm{s}}(Q,\omega)-1}{\varepsilon_{\mathrm{s}}(Q,\omega)+1}\right\}, \qquad z_0 > d/2, \tag{6}$$

$$\frac{\mathrm{d}E_{\mathrm{val}}}{\mathrm{d}t}(z_0) = \frac{2Z_1^2}{\pi v^2}\int_0^\infty \mathrm{d}\omega\,\omega \int_0^\infty \frac{\mathrm{d}q}{Q} \times \mathrm{Im}\left\{\varepsilon_{\mathrm{s}}(Q,\omega)+\varepsilon_{\mathrm{s}}(Q,2z_0,\omega)-\frac{2(\varepsilon_{\mathrm{s}}(Q,z_0,\omega))^2}{\varepsilon_{\mathrm{s}}(Q,\omega)+1}\right\}, \quad z_0 < d/2, \tag{7}$$

where $Q = \sqrt{q^2+\omega^2/v^2}$, $\varepsilon_{\mathrm{s}}(Q,\omega) = \varepsilon_{\mathrm{s}}(Q,d/2,\omega)$, and $\varepsilon_{\mathrm{s}}(Q,z_0,\omega)$ is calculated according to the following expression [22]:

$$\varepsilon_{\mathrm{s}}(Q,z_0,\omega) = \frac{Q}{\pi}\int_{-\infty}^{\infty}\frac{\mathrm{d}k_z}{k^2}\frac{\mathrm{e}^{\mathrm{i}k_z(z_0-d/2)}}{\varepsilon(k,\omega)}. \tag{8}$$

In this equation $k^2 = k_z^2 + Q^2$ and $\varepsilon(k,\omega)$ is the bulk dielectric response function. Note that in the SRM, the surface response function $g(Q,\omega)$, defined in equation (5), takes the following form:

$$g(Q,\omega) = \frac{1-\varepsilon_{\mathrm{s}}(Q,\omega)}{1+\varepsilon_{\mathrm{s}}(Q,\omega)}. \tag{9}$$

In the examples presented here, the extension to the Lindhard RPA [23] suggested by Mermin [24] is used for the bulk dielectric function. This allows one to use non-zero values of the electron gas damping, keeping the number of electrons in the system constant. We want to emphasize that this description incorporates both single-particle excitations (creation of electron–hole pairs) and collective excitations (bulk and surface plasmons).

2.2. Energy loss of fast protons scattered off metal surfaces under grazing incidence

As an application of the approach presented above we present some studies performed to calculate the energy lost by fast protons reflected by metal surfaces. We note that for the high velocities under consideration in addition to the valence band excitations, one has to consider that the projectile can also excite electrons in the inner-shells of the target atoms. This contribution to the energy loss can be obtained in terms of the impact-parameter dependent

energy loss in single encounters of the external charge with the target atoms, which is calculated within first-order Born approximation [25]. In order to obtain the contribution of this channel to the stopping power

$$\frac{\mathrm{d}E_{\mathrm{s}}}{\mathrm{d}x}(z_0),$$

an average over the trajectory is performed. We refer the reader to Ref. [6] for details.

As an example, we show in Fig. 1 the results obtained for $\mathrm{d}E/\mathrm{d}x$ in the case of 700 keV protons ($v = 5.29$ a.u.) as a function of the distance from an Al (111) surface. We plot the different contributions to the energy loss rate (valence band and inner-shell excitations) and the total sum. In the inner-shell contribution only the L-shell of Al has been considered since the K-shell is too strongly bound to be efficiently excited by protons of this energy. It is important to stress the different behavior with the distance of $\mathrm{d}E_{\mathrm{val}}/\mathrm{d}x$ as compared to $\mathrm{d}E_{\mathrm{s}}/\mathrm{d}x$. On the one hand, the latter takes significant values at distances of the order of the target atoms size, where it dominates over the valence band contribution in the range of energies under consideration. On the other hand, $\mathrm{d}E_{\mathrm{val}}/\mathrm{d}x$ is important up to distances of the order of the jellium edge position [$z_0 \approx 2.2$ a.u., for Al (111)]. Consequently, the valence band contribution dominates over the inner-shell contribution except very close to the atomic surface ($z_0 = 0$).

In order to compare the theoretical predictions with experimentally measured energy losses it is necessary to perform the calculation of the trajectory of the ion under the combined influence of the repulsive surface

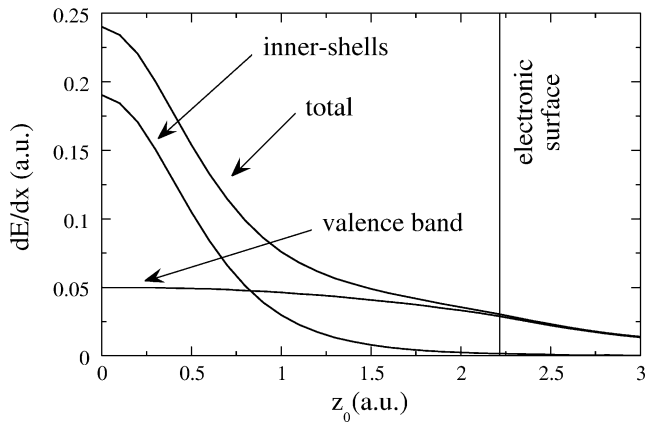

Fig. 1. Stopping power of a 700 keV proton traveling parallel to an Al (111) surface as a function of its distance to the top-most layer z_0. The contributions of the valence band excitations and inner-shells excitations are distinguished.

atomic planar potential and the attractive image potential. For specularly reflected ions the incoming and outgoing trajectories are identical, and one can calculate the total energy loss ΔE in the following way:

$$\Delta E = 2v \int_{z_{tp}}^{\infty} \frac{dE}{dx}(z) \frac{1}{v_z(z)} dz, \tag{10}$$

where z_{tp} and $v_z(z)$ are the turning point and the value of the component of the velocity normal to the surface, respectively. Both quantities are obtained from the trajectory calculation for any given angle of incidence.

In Fig. 2 we show different contributions to the total energy loss ΔE as a function of the grazing angle of incidence for 700 keV protons. We observe that, at the same time as the contribution of valence band excitations decreases, the contribution due to inner-shell excitations increases when increasing the angle of incidence. The reason for this can be easily understood from the dependence of both dE_{val}/dx and dE_s/dx on the distance to the surface. Increasing the angle of incidence results in the reduction of the time that the proton spends close to the surface, where dE_{val}/dx varies slowly with the distance z_0, and therefore, the energy loss due to this contribution is reduced. On the contrary, the inner-shell contribution becomes relevant only when the turning point is very close to the atomic surface, where dE_s/dx takes appreciable values. The turning point is closer to the atomic surface for larger angles of incidence, and therefore, this contribution increases with the angle of incidence. The sum of both contributions, i.e., the total energy

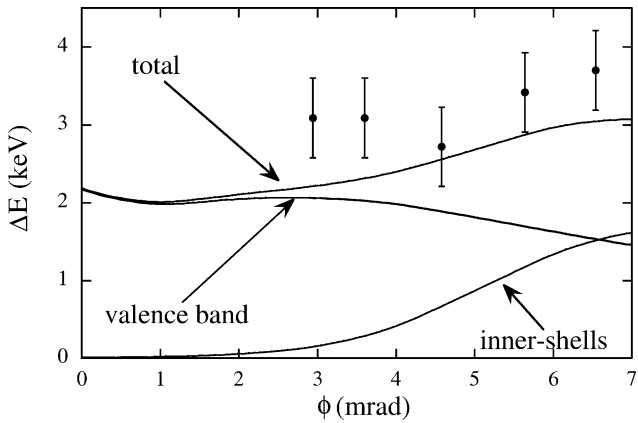

Fig. 2. Energy loss of 700 keV protons specularly reflected at an Al (111) surface as a function of the angle of incidence ϕ. The contributions of the valence band excitations and inner-shells excitation are shown, separately. The results are compared to the experimental data of Ref. [26].

loss ΔE, varies smoothly in the range 2–3 keV as a function of the angle of incidence. In this figure we also show the experimental results obtained by Winter *et al.* for 710 keV protons [26]. Even if the initial energy is not exactly the same, a significant difference in the total energy loss is not expected. The agreement obtained between the theoretical and experimental results is remarkable. Moreover, this theoretical approach is able to reproduce the main features found in the fast proton–surface scattering experiments: the smooth dependence of the total energy loss with the initial energy and angle of the projectile [26,27].

2.3. Band structure effects

It has to be stated that the above mentioned works, that invoke the jellium model, are expected to be valid for simple metals such as Al, for which the conduction band can be approximated by an electron gas. In the following we show recent calculations of the position dependent stopping power in which information about the real band structure of the target is included. The Cu (111) surface is a good candidate to analyze the band structure effects in the stopping due to the presence of a surface band gap and a surface state.

We compute the one-electron eigenfunctions involved in the evaluation of the independent particle density response function $\chi_0(q, z, z', \omega)$ (equation (3)) by solving the Schrödinger equation with the one-dimensional model potential of Ref. [28]. This potential reproduces the main peculiarities of the Cu (111) surface: (i) the bulk band structure exhibits a gap for the electron motion along the surface normal between -5.83 and -0.69 eV; (ii) there is an occupied surface state located at -5.33 eV. All these energies are measured from the vacuum level.

In Fig. 3 the stopping power is presented for a proton traveling parallel to the Cu (111) surface, with velocity $v = 1$ a.u., as a function of the distance from the proton to this surface. The results obtained with the model, which includes the band structure of the target are represented by a solid line. In the inner part of the solid the stopping power shows oscillations reflecting the layer structure of the target. In the outer part, the stopping power decreases as the distance to the top-most layer increases.

In order to understand the relevance of the surface state in the stopping power, we also present results in which the contribution of the surface state in the calculation of $\chi_0(Q, z, z', \omega)$ is neglected (short-dashed line). In the inner part of the solid, both calculations give roughly the same values of the stopping. However, in the outer part the stopping is clearly underestimated when the effect of the surface state is not considered. Moreover, comparison between the two curves (solid and short-dashed) shows that the last maximum of the stopping obtained within the complete calculation, that appears outside the top-most layer, is due to the presence of the surface state.

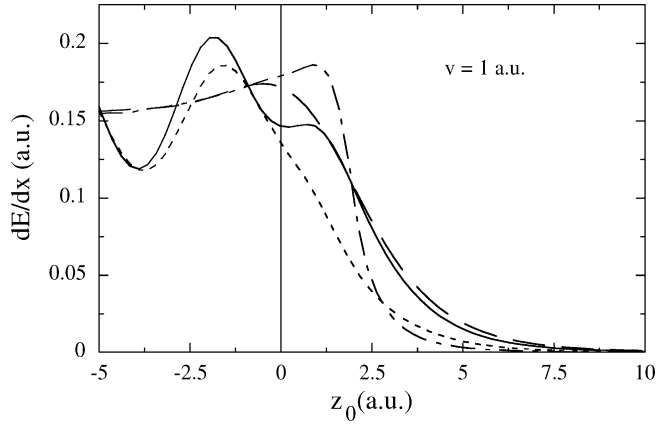

Fig. 3. Stopping power as a function of the distance to the top-most layer for $v = 1$ a.u. protons traveling parallel to the Cu (111) surface. The solid line is the result of the model in which the surface band structure of the target is considered, the short-dashed line is obtained neglecting the surface state in the calculation, the long-dashed line is the result of using the jellium model and constructing $\chi_0(Q, z, z', \omega)$ within the RPA using the self-consistent solutions for a finite step potential (see text), and the dot-dashed line is obtained in the jellium model within the SRM.

In this figure we also show the results of two different calculations performed within the jellium model, i.e., neglecting all band structure effects. In one case (long-dashed line) the wave functions and energies entering the calculation of $\chi_0(Q, z, z', \omega)$ (equation (3)) are calculated solving the self-consistent Kohn–Sham equations of the DFT for a smooth and finite potential barrier. In the other case (dot-dashed line) the SRM is used. In this case, we use the Lindhard RPA as the bulk dielectric function from which the surface response function is obtained *via* equations (8) and (9). In these two calculations, the jellium edge, located half-interlayer distance outside the top-most layer, is at ≈ 1.97 a.u. Inside the bulk, the stopping calculated with these models tends to a constant value, which is the average of the oscillations obtained with the complete calculation. The important observation is that the jellium model (without the oversimplification of the SRM) and the complete band structure calculation (long-dashed and solid lines, respectively) give very similar results outside the surface. Note that this is the important region for specularly reflected projectiles. In some respect, one may conclude that in the band structure-based calculation the surface state compensates the existence of the band gap, and one nearly recovers the jellium results. This effect was verified for a relatively wide range of velocities ($0.25 \leq v \leq 2$ a.u.) [29]. Note that in the case of the jellium model it is important to perform the self-consistent calculation for

the finite potential barrier. For instance, the SRM (dot-dashed line) underestimates the value of the stopping at large distances because in this model the induced charge is confined to the surface by the infinite potential barrier. Nevertheless, we want to remark that for high enough velocities ($v \geq 1$ a.u.) and not too small angles of incidence the SRM is a reliable approximation to obtain the total energy loss overcome by protons reflected at the surface [30].

3. SLOW PROJECTILES: NONLINEAR THEORY

3.1. Theory

3.1.1. Nonlinear screening

In the strong coupling limit ($Z_1/v \gg 1$) the projectile represents a strong perturbation for the system and linear response theory is no longer valid. The piling-up of charge in the vicinity of the ion, particularly in the spatial region within a few atomic units around the nucleus, requires a nonlinear description of the electronic density modification. In this respect, DFT has been successfully used in the description of the nonlinear screening effects associated with the interaction of slow ions with metals [31]. The starting point is the DFT formalism as applied to a static impurity of charge Z_1 embedded in a free electron gas of mean density n_0 [32–34]. The static approximation is appropriate for ion velocities well below the Bohr velocity.

In practice, one uses the Kohn–Sham scheme that consists in solving self-consistently the following one-electron equations [16]:

$$\left\{-\frac{1}{2}\nabla^2 + v_{\text{eff}}[n]\right\}\phi_i = \varepsilon_i \phi_i, \tag{11}$$

where $v_{\text{eff}} = v_{\text{ext}} + v_{\text{es}} + v_{\text{xc}}$ is the effective potential, with

$$v_{\text{ext}} = -\frac{Z_1}{r}, \tag{12}$$

$$v_{\text{es}} = \int \mathrm{d}\mathbf{r}' \frac{\Delta n(r')}{|\mathbf{r} - \mathbf{r}'|}, \tag{13}$$

$\Delta n(r) = n(r) - n_0$ is the induced density and v_{xc} is the exchange and correlation potential, that can be obtained in the LDA [35].

The electronic density $n(r)$ is obtained from the sum over occupied states:

$$n(r) = \sum_{i \in \text{occ.}} |\phi_i|^2. \tag{14}$$

This sum includes a contribution originating from the occupied bound states and another one coming from the integration over the continuum up to

the Fermi level. In this way, Kohn–Sham equations allow us to determine the perturbed potential created by the ion and the electronic density around it.

One can also extract from this calculation the scattering phase shifts δ_l for the conduction band. In this respect, a number of physical quantities can be expressed in terms of the phase shifts at the Fermi level $\delta_l(k_F)$, which obey, due to the complete screening of the nuclear charge Z_1, the Friedel sum rule [36]

$$Z_1 = \frac{2}{\pi} \sum_l (2l+1)\delta_l(k_F). \tag{15}$$

3.1.2. Stopping power

The energy loss of slow charges in an electron gas has been widely studied from the theoretical point of view [37–40]. It has been shown that the description of the scattering process by the first Born approximation is not fully satisfactory for slow ions at metallic densities. This is true even for a proton. The use of scattering theory to calculate the cross-sections from the phase shifts allows, in principle, to obtain a result, which is valid to all orders in the projectile charge. Therefore, this approach requires a nonlinear calculation of the self-consistent scattering potential for arbitrary charge Z_1. As explained above, this can be done within the framework of DFT as applied to the problem of a static impurity in an electron gas [34,41–43]. In this respect, a static calculation for the screening is justified up to the Fermi velocity [44,45].

At low velocities the stopping power can be written in terms of the transport cross-section at the Fermi level $\sigma_T(k_F)$ as [34]:

$$\frac{dE}{dx} = n_0 v k_F \sigma_T(k_F) = Qv, \tag{16}$$

where $Q = n_0 k_F \sigma_T(k_F)$ is the so-called friction coefficient, k_F is the Fermi momentum, the transport cross-section $\sigma_T(k_F)$ is calculated from

$$\sigma_T(k_F) = \frac{4\pi}{k_F^2} \sum_l (l+1)\sin^2[\delta_l(k_F) - \delta_{l+1}(k_F)], \tag{17}$$

and $\delta_l(k_F)$ are the scattering phase shifts at the Fermi level for electron scattering off the self-consistent screened potential. In equation (16) the product $k_F\sigma_T(k_F)$ is the integrated scattering rate for momentum transfer, which governs the dissipative process. Therefore, one can interpret the stopping power described by this formula as the result of the momentum transfer per unit time to a uniform current of independent electrons ($n_0 v$) scattered by a fixed screened potential.

3.2. Z_1 oscillations in the energy loss of slow ions interacting with metal surfaces

One of the advantages of this approach is that it allows to understand in a straightforward manner the so-called Z_1 oscillations, an experimentally observed oscillatory behavior of the stopping power with increasing projectile atomic number Z_1 for ions traveling through metals [46–51]. In this respect, recently, quantitative agreement between theory and experiment has been obtained by measuring the energy loss of ions with atomic number $1 \leq Z_1 \leq 20$ and velocity $v = 0.5$ a.u. scattered off an Al (111) surface under grazing angle of incidence [52]. Performing a detailed analysis of the trajectory it is possible to obtain from these experiments the distance-dependent stopping power

$$\frac{\mathrm{d}E}{\mathrm{d}x}(z_0).$$

Equation (16) is derived for an ion traveling through a jellium, and it is expected to be valid for ions traveling through uniform electronic density regions. In case of a surface experiment the ions travel through a region of varying electron density. In order to obtain a position dependent stopping power the natural way to proceed is the following. First, one calculates the electronic density profile at the Al (111) surface $n_0(z_0)$. Then, at each distance z_0, one defines a local Fermi momentum $k_{\mathrm{F}}(z_0) = \sqrt[3]{3\pi^2 n_0(z_0)}$ and introduces it in equation (16) to obtain

$$\frac{\mathrm{d}E}{\mathrm{d}x}(z_0).$$

In Fig. 4 we show the experimental stopping power at $z_0 = 1.2$ a.u. compared to the theoretical value of the stopping power. At this distance the corresponding density parameter is $r_{\mathrm{s}} = 2.2$ a.u. The figure shows an excellent quantitative agreement between theory and experiment. Note that at $z_0 = 1.2$ a.u. the electronic density is very close to the bulk value. In this case, effects due to the nonuniformity of the electronic density seem to be negligible, and equation (16), valid for uniform systems, is applicable.

In Fig. 5 we show the experimental and theoretical results for a larger distance $z_0 = 3.7$ a.u. Now the value of the electronic density is much smaller than the bulk value and corresponds to $r_{\mathrm{s}} = 5$. Nevertheless, it has to be stated that a conservative estimate on the uncertainty in the determination of z_0 of the order of 0.5 a.u. leads us to deduce that for this distance one should use a value of r_{s} of the order of $4 \leq r_{\mathrm{s}} \leq 6$. In this case the agreement between experiments and theory is not good. Furthermore, one cannot invoke the uncertainty in the determination of $r_{\mathrm{s}}(z_0)$ mentioned above, since there is not any r_{s} value that reproduces the amplitude and phase of the data. This indicates that for large atom–surface separations the nonuniformity of

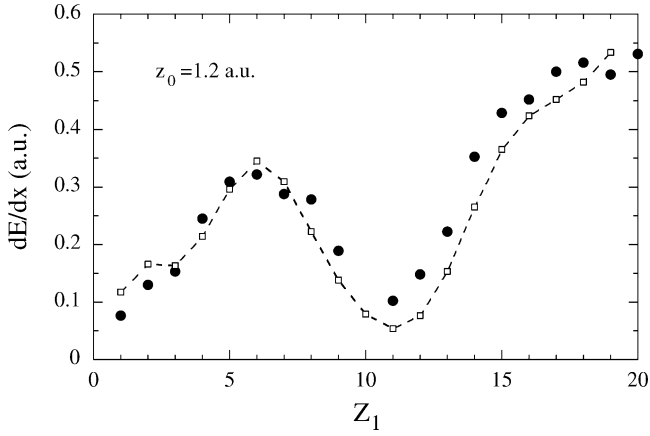

Fig. 4. Stopping power of ions with $v = 0.5$ a.u. as a function of the atomic number Z_1 at a distance $z_0 = 1.2$ a.u. from an Al (111) surface. Full circles denote the experimental data and open squares the results obtained for $r_s = 2.2$ a.u. with equation (16).

the electronic density profile plays an important role. At these distances, at which the value of the electronic density is low, the value of the stopping power is small, and therefore, one may expect that nonuniformity corrections are relatively more important than at high densities (small distance).

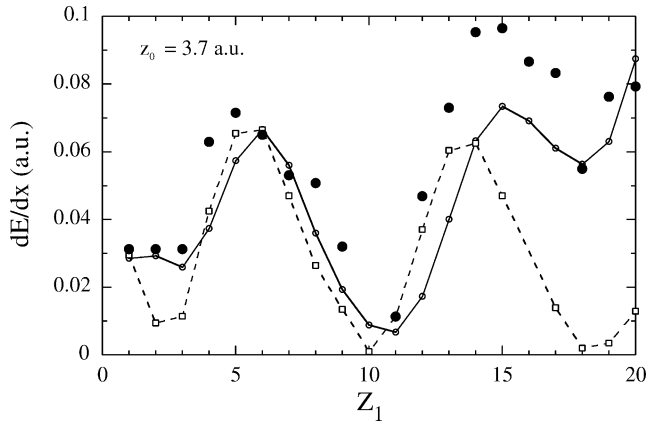

Fig. 5. Stopping power of ions with $v = 0.5$ a.u. as a function of the atomic number Z_1 at $z_0 = 3.7$ a.u. Full circles are experimental data, dashed lines connect results obtained with equation (16) for $r_s = 5$ a.u. (open squares), and solid lines and open circles are results obtained using equation (19) with $r_{s1} = 4$ a.u. and $r_{s2} = 2.7$ a.u.

Therefore, we conclude that for large atom–surface separations equation (16) is inappropriate.

The simplest way to take into account the nonuniformity of the electronic density profile in an approximate manner is to modify equation (16) according to the physical interpretation of the stopping power as a uniform current of electrons scattered off by a fix potential. One defines two density parameters: r_{s1} to characterize the current density $n_{01}v = 3v/(4\pi r_{s1}^3)$ and r_{s2} to describe the effective scattering impulse $v_{F2} = 1.92/r_{s2}$. Whereas r_{s1} is obtained from the density profile as before, r_{s2} is defined in order to approximately include the modification of the kinetic energy density for nonuniform systems, i.e., the so-called von Weizsäcker term. This term accounts for the increase in kinetic energy due to gradients of the electronic density. For an exponential decay $\exp(-\beta z_0)$ of the density leads to an increase from $v_{F1}^2/2$ to [53]

$$\frac{v_{F2}^2}{2} \cong \frac{v_{F1}^2}{2} + \frac{\beta^2}{8}, \tag{18}$$

with $v_{F1} = 1.92/r_{s1}$. Therefore, a proper modification of equation (16) for the case of nonuniform density is given by

$$\frac{dE}{dx} = (n_{01}v)[k_{F2}\sigma_T(k_{F2})], \tag{19}$$

where $[k_{F2}\sigma_T(k_{F2})]$ is the scattering rate and $(n_{01}v)$ has already been defined as current density. Figure 5 also shows the results obtained by using equation (19) with $r_{s1} = 4$ and $r_{s2} = 2.7$. The value of r_{s1} is within the range of acceptable r_s values given above. The value of r_{s2} is obtained from equation (18) with $\beta = 2\sqrt{2\Phi}$, where Φ is the work function of the Al (111) surface. As shown in Fig. 5, at these large distances, a significant improvement in the overall quantitative description of the experimental data using equation (19) instead of equation (16) is found.

In summary, the description of the stopping power of slow ions in front of a metal surface using the model presented above (DFT and scattering theory with full phase-shift calculation of the cross-sections) gives a remarkable quantitative agreement with experiments in the small distance (high density) region, where the projectile interacts in good approximation with a uniform electron gas. At larger distances from the surface, the nonuniformity of the electron density plays an important role.

3.3. Charge state dependence of the energy loss of slow ion interacting with metal surfaces

Another problem of interest that has been successfully treated using the above-described formalism is the study of the energy loss of slow

multicharged ions in metals as a function of their initial charge state [54, 55]. The interesting question that one has to answer is how preequilibrium of charge states does affect the energy loss of multicharged projectiles.

In an experiment performed by Winter *et al.* in the Humboldt University in Berlin, the mean energy loss of N ions after scattering from an Al (111) surface under a grazing angle of incidence $\phi = 0.7°$ was measured [54,55]. In Fig. 6 we plot the mean energy loss as a function of the charge state q of the incident ions. Since, for a N^{q+} ion, the energy loss is constant for a variation of the angle of incidence [56], the analysis of the data is simplified. More precisely, the observed constancy of ΔE with variations of ϕ allows one to neglect effects on the energy loss by changing the trajectory [27]. In other words, the observed increase of the energy loss with the incident charge state can only be due to a corresponding enhancement of the stopping power with the charge state.

Nevertheless, the screening effects by conduction band electrons make the electronic stopping of atomic projectiles a complex problem. In this respect, one needs to incorporate the effect produced in the electronic stopping by the presence of inner-shell vacancies [57]. With this aim we generalize the formalism developed in Section 3.1.1 in order to study projectiles with vacancies in their bound states. This is done by using the Kohn–Sham orbitals in an approximate way as monoelectronic wavefunctions. Accordingly, we can fix the number n_h of empty orbitals when solving iteratively the set of equations (11)–(14). This leads to a generalization of Friedel sum rule for the charge neutrality of the system [31]:

$$Z_1 + n_h = \frac{2}{\pi} \sum_l (2l+1)\delta_l(k_F). \tag{20}$$

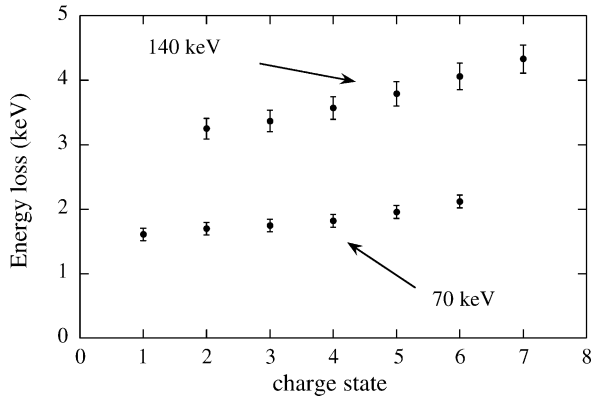

Fig. 6. Measured energy loss for 70 and 140 keV N^{q+} ions as a function of q the incident charge state of the projectiles after scattering from an Al (111) surface under a grazing angle of incidence $\phi = 0.7°$.

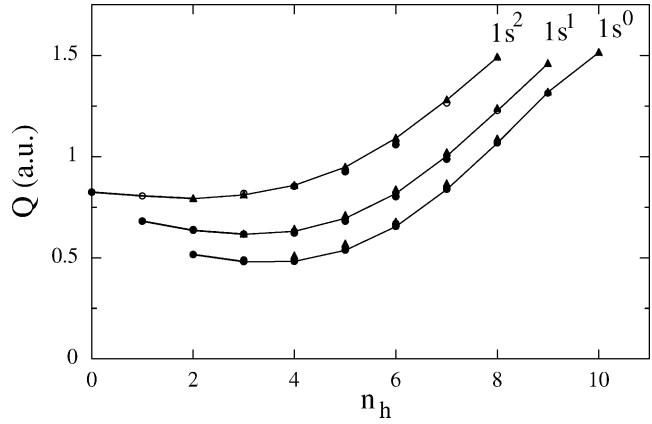

Fig. 7. Friction coefficient Q as a function of the total number of inner-shell holes n_h for $Z_1 = 7$ in an electron gas with $r_s = 2$ a.u. The curve $1s^2$ is obtained for a filled K shell, $1s^1$ for one electron in the K shell, and $1s^0$ for an empty K shell. The solid circles represent the $2s^2$, the open circles represent $2s^1$, and the solid triangles represent $2s^0$ configurations of the L shell. The solid lines are drawn to guide the eye.

The addition of n_h to Z_1 in equation (20) accounts for the lack of n_h electrons in the empty bound states. The number of holes n_h not only determines the total number of electronic states, but also how many of them are bound. As n_h decreases, the outer bound orbitals merge into the continuum, without appreciably varying their spatial shape. This means that the screening by a low-lying orbital in the continuum is very similar to that of a weakly bound state.

Using this model one can calculate the stopping power (or accordingly the friction coefficient Q) as given by equation (16) for different configurations of inner-shell vacancies. In Fig. 7 we present the results obtained for the friction coefficient Q of N ions traveling through an Al metal as a function of n_h. As explained, Q is calculated in terms of the transport cross-section at the Fermi level, obtained for electron scattering at the potential induced by the projectile. This potential, is calculated within DFT, for different inner-shell configurations. It is observed that for a given K-shell occupancy the stopping is affected in an appreciable manner by the number of L-shell electrons: Q increases as the number of L-shell holes increases for $n_h > 3$, whereas it is essentially constant for $n_h \leq 3$. The L-subshell distribution of electrons has practically no influence on Q. However, Q decreases as the number of holes in the K shell increases when n_h is low, and is almost constant when n_h is high. This opposite behavior of Q with the number of holes in the K and L-shells is related to the degree of spatial localization of the different orbitals (see Ref. [54] for details).

The three different sets of data in Fig. 7 can be used to understand the neutralization/relaxation sequences for incident N^{5+}, N^{6+} and N^{7+} ions. In case of ions without K-shell vacancies one should use the curve labeled $1s^2$. For instance, for N^{5+} one should start from the point that corresponds to the fully unoccupied L-shell ($n_h = 8$), with the highest value of the stopping power. Along its incoming trajectory the number of electrons in the L-shell will increase due to LVV Auger processes, and the value of the stopping will be reduced. Comparing to N^{5+}, the main difference for N^{6+} and N^{7+} ions is a longer neutralization sequence due to the presence of inner-shell vacancies. The filling of the K-shell vacancy is interpreted as a transition to the adjacent curve in the figure towards smaller n_h value for a KVV process and towards a larger value of n_h for a KLL process.

Therefore, the enhanced energy loss for higher charge states of incident ions observed in Fig. 6, is attributed to the enhanced friction coefficients Q obtained in the calculation for ions with several L-shell vacancies. Whereas the calculation shows an enhancement of electronic stopping for projectiles with empty L-shells (N^{5+}, N^{6+}, and N^{7+} ions) over ground state ions by a factor of 2, the experimental energy loss increases with charge only by up to 35%. This finding can be considered as an indication of the fact that the lifetime of L-shell vacancies is shorter than the interaction time of the ions with the surface. From these observations one can infer a lifetime of the L-shell vacancies of the order of 2 fs, which is consistent with theoretical calculations [58–60].

This study shows that the charge state dependence of the energy loss of slow multicharged ions traveling through the electron gas of a metal is the outcome of a complex situation, where both the different screening (and the resulting different stopping powers) and the lifetimes of the excitation states of the ions play a role. As an example, for N^{q+} ions it is found (i) an opposite behavior of the dependence of the stopping power on the number of vacancies in K and L-shells, and (ii) that the experimentally observed increase of the energy loss with the charge state of the ion can be explained by a larger stopping power of ions with vacancies in the L-shell and by a longer lifetime of the configurations with K-shell holes.

3.4. Energy loss of slow ions in insulators

In recent years, a number of experimental and theoretical works have been devoted to the study of the energy loss of low velocity ions interacting with wide band gap insulators [61–66]. For metals, a linear velocity dependence of the stopping power is found. The predominant role played by excitations of conduction band electrons close to the Fermi level is the reason for this behavior. However, for insulators, as in gaseous targets [67], these low energy excitations are expected to be suppressed due to the energy gap. This would imply a threshold effect for projectile stopping with respect to ion

velocity [68,69], and therefore, a deviation from the linear velocity dependence of the stopping power. In transmission experiments with a LiF target no threshold effect was observed down to 2.5 keV proton energies [62], that corresponds to a velocity $v = 0.32$ a.u. This finding was interpreted as a local reduction of the electronic band gap in close collisions of the projectiles with the target atoms, enabling low energy electronic excitations.

In surface scattering experiments a threshold effect was observed below 2 keV [63], energies not accessible so far in transmission experiments. From an analysis of the energy loss spectra, electronic charge exchange processes were identified as the dominant mechanism of electronic stopping of protons in LiF. In this regime, combining in coincidence energy loss and electron emission, Roncin *et al.* [64] identified surface exciton population as an energy loss channel.

Nevertheless, except in these extreme cases (very slow ions and grazing incidence geometry) in which the ion does not get close enough to the surface, it can be considered a weak perturbation, no effect related to the insulator character of the target could be observed. In other words, the same free electron gas model that is used to obtain the stopping power of slow ions in metals showed to be applicable in the case of insulators [65,66].

In Figs 8 and 9 we compare experimental results obtained in LiF to the predictions of the free electron gas model. Figure 8 shows the measured energy loss as a function of atomic number Z_1 of the projectile, for specularly reflected ions at the same velocity $v = 0.5$ a.u. under $\phi = 1^\circ$ angle of incidence. Z_1 oscillations similar to those in metals are observed, reflecting the shell structure of the projectile levels: a minimum appears at $Z_1 = 12$

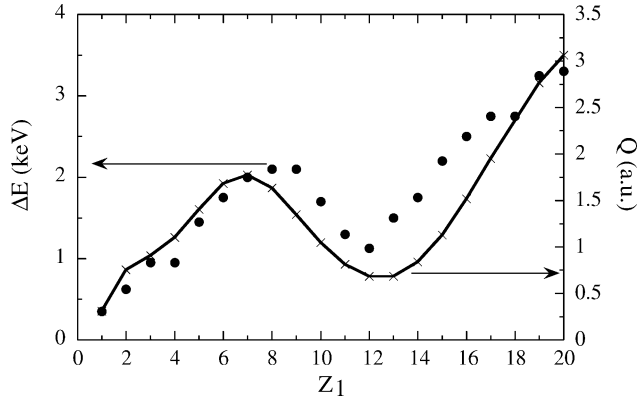

Fig. 8. Energy loss (in keV) of $v = 0.5$ a.u. projectiles scattered off a LiF (100) surface under grazing angle of incidence $\phi = 1^\circ$ as a function of the projectile atomic number Z_1 solid circles). The solid line joins the theoretical results obtained for the friction coefficient Q (in a.u.) with $r_s = 1.5$.

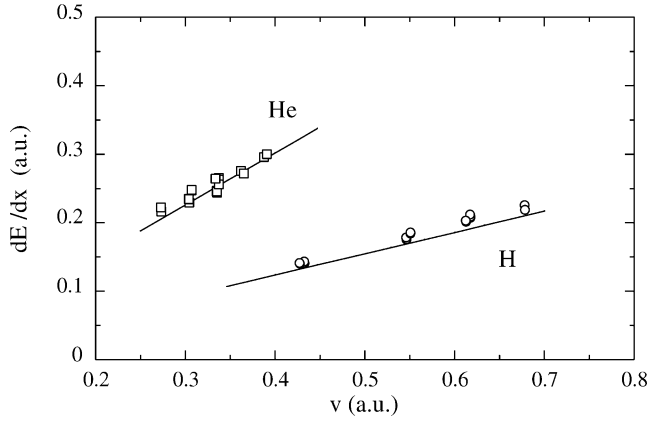

Fig. 9. Stopping power (in a.u.) of H and He ions traveling through a LiF target as a function of the projectile velocity. The circles correspond to the experimental data obtained in transmission for H projectiles and the squares to He projectiles. The theoretical results (solid lines) are calculated using $r_s = 1.5$.

shifted from the noble gas value ($Z_1 = 10$) due to screening, and a maximum around $Z_1 = 8-9$ *via* a 2p resonance. Figure 9 shows the experimental data for H and He projectiles traveling through LiF as a function of the projectile velocity. A linear velocity dependence of the stopping power is clearly observable, which reflects the lack of a noticeable influence of the band gap. In both figures the results are compared to theoretical stopping power values obtained within the nonlinear screening and scattering approach, previously described. It has to be stated that, in order to perform the comparison between the energy loss data and the theoretical stopping power values of Fig. 8, one has to use the fact that the trajectories do not strongly depend on Z_1. Note also, that the theoretical quantity that is plotted in Fig. 8 is the friction coefficient Q, i.e., the stopping power divided by the projectile velocity.

In the theoretical approach used, there is only one free parameter r_s. In both cases, transmission and reflection, the experimental data are reproduced using $r_s = 1.5$. So, it is tempting to assume that in both cases comparable mechanisms are responsible for projectile energy loss. Moreover, $r_s = 1.5$ is the value that one obtains considering the 2p and 2s electrons of F^- as free electrons. This value is also consistent with the measured bulk plasmon energy $\hbar\omega_p \approx 25$ eV [70]. We note that the value $r_s = 1.5$ corresponds to a rather high electronic density: for instance, it is larger than the electronic density of Al ($r_s = 2.07$).

Nevertheless, since the valence band of LiF does not constitute a free electron gas, the theoretical model that has been used to describe the problem

is clearly out of its range of applicability. However, we claim that the outstanding agreement obtained with this model, that uses a single parameter (r_s, that can be in some way justified by the above reasoning), with two completely different experiments (reflection and transmission), that cover a wide range of projectile atomic numbers ($1 \leq Z_1 \leq 20$) in one case, and a wide range of velocities ($0.25 \leq v \leq 0.7$ a.u.) in the other case, cannot be fortuitous.

Though the reason behind this finding is not completely clear at present, we will try to propose a possible explanation. We start by pointing out that the model used in Ref. [63] to interpret the energy loss of slow protons invoked charge transfer processes between (almost) undisturbed target and projectile electronic levels. The large target–projectile distance resulting from the low value of the component of the proton energy normal to the surface in those experiments justifies the assumption of undisturbed levels. However, in the case of the surface scattering experiment of Fig. 8 the distances of closest approach are around 1.3 a.u. from the top-most atomic layer. The slow projectile gets so close to the target that it represents a strong-coupling problem. This suggests that molecular orbitals are formed and that one can no longer assume that the target and projectile levels remain undisturbed. Obviously, the same argument is valid for the transmission experiments in which a large overlap of the target and projectile electron clouds takes place. Under these conditions, it is not possible to distinguish between electron–hole pairs or excitons (target excitations) and charge exchange processes (projectile and target excitations) since one deals with a complex target–projectile unified system. The employed theoretical model seems to describe the average excitations of the complex system in a proper way. In this case, the Fermi velocity has the same meaning as when this model is applied for transition metals; it corresponds to the effective number of electrons participating in the stopping. In conclusion, for positive slow ions at energies above 2 keV/amu the energy loss mechanisms in insulators seem to be similar to those in metals due to the strong local perturbation that the projectile represents, and can be described within the same self-consistent model.

4. FINAL REMARKS AND CONCLUSIONS

In this work we have reviewed some recent developments in the energy loss of ions scattered off solid surfaces. In the weak-coupling regime ($Z_1/v \ll 1$) linear response theory allows one to calculate the distance-dependent stopping power. In this respect, we have shown that a linear approach with the SRM is capable to reproduce the measured energy losses of fast protons reflected at metal surfaces. Additionally, in this weak-coupling limit we have seen that in the case of metal targets details of the surface band structure do

not seem to affect the energy loss. More precisely, for Cu (111) the effect of the surface band gap is compensated by the presence of the surface state, which makes the jellium model a reliable approximation.

In the strong-coupling limit ($Z_1/v \gg 1$), in which linear approaches are not valid, an approach developed for slow ions traveling through jellium based on DFT and a full phase-shift calculation of the cross-sections is successful in accounting for the value of the stopping power at short distances from the surface, where density nonuniformities are small. We remark the excellent agreement obtained by this model for the measured Z_1 oscillations of the stopping power close to an Al surface. Clearly, at large distances from the surface the nonuniformity of the density profile gains importance and the model is not able to reproduce the measured data. Nevertheless, since most of the energy loss of the slow ions takes place in the region close to the surface this model allows one to understand, for instance, the measured charge state dependence of the energy loss. Finally, we want to finish noting the surprising outstanding agreement obtained by this model for insulator targets. This suggests the appearance of non-trivial effects related to the strong-coupling regime that are well described by the model even if the solid is not a metal. The reason for this fact remains an open question that deserves further investigation on the governing microscopic mechanisms.

ACKNOWLEDGEMENTS

The authors are indebted to P.M. Echenique, H. Winter, A. Arnau, I. Nagy, R. Díez Muiño, F.J. García de Abajo, V.M. Silkin, P. Bauer, and E.V. Chulkov for many discussions and for crucial contributions in some of the presented works. We acknowledge partial support by the Eusko Jaurlaritza, Gipuzkoako Foru Aldundia, Euskal Herriko Unibertsitatea (project number: 9/UPV00206.215-13639/2001) and by the Spanish MCyT (project number: BFM-2001-0076).

REFERENCES

[1] H. Winter, *Phys. Rep.*, 2002, **367**, 387.
[2] P. M. Echenique and J. B. Pendry, *J. Phys. C*, 1975, **8**, 2936.
[3] R. Nuñez, P. M. Echenique and R. H. Ritchie, *J. Phys. C*, 1980, **13**, 4229.
[4] N. Zabala and P. M. Echenique, *Ultramicroscopy*, 1990, **32**, 327.
[5] J. I. Juaristi and F. J. García de Abajo, *Nucl. Instrum. Methods B*, 1994, **90**, 252.
[6] J. I. Juaristi, F. J. García de Abajo and P. M. Echenique, *Phys. Rev. B*, 1996, **53**, 13839.
[7] Y. H. Song and Y. N. Wang, *Nucl. Instrum. Methods B*, 1999, **153**, 186.
[8] Y. H. Song, Y. N. Wang and Z. L. Miskovic, *Phys. Rev. A*, 2001, **63**, 052902.
[9] R. H. Ritchie and A. L. Marusak, *Surf. Sci.*, 1966, **4**, 234.
[10] D. Wagner, *Z. Naturforsch. A*, 1966, **21**, 634.

[11] M. S. Gravielle, *Phys. Rev. A*, 1998, **58**, 4622.
[12] M. S. Gravielle and J. E. Miraglia, *Phys. Rev. A*, 2002, **65**, 022901.
[13] M. A. Cazalilla and F. J. García de Abajo, *Nucl. Instrum. Methods B*, 1997, **125**, 106.
[14] M. A. Cazalilla and J. I. Juaristi, *Nucl. Instrum. Methods B*, 1999, **157**, 104.
[15] A. García-Lekue and J. M. Pitarke, *Phys. Rev. B*, 2001, **64**, 035423.
[16] W. Kohn and L. J. Sham, *Phys. Rev.*, 1965, **140**, A1133.
[17] P. Hohenberg and W. Kohn, *Phys. Rev.*, 1964, **136**, B864.
[18] A. G. Eguiluz, *Phys. Rev. Lett.*, 1983, **51**, 1907.
[19] A. G. Eguiluz, *Phys. Rev. B*, 1985, **31**, 3303.
[20] A. Zangwill and P. Soven, *Phys. Rev. A*, 1980, **21**, 1561.
[21] P. M. Echenique, F. J. García de Abajo, V. H. Ponce and M. E. Uranga, *Nucl. Instrum. Methods B*, 1995, **96**, 583.
[22] D. M. Newns, *Phys. Rev. B*, 1970, **1**, 3304.
[23] J. Lindhard, *K. Dan. Vidensk. Selsk. Mat. Fys. edd.*, 1954, **28** (8), 1.
[24] N. D. Mermin, *Phys. Rev. B*, 1970, **1**, 2362.
[25] R. McCarroll and A. Salin, *C. R. Sci. Paris, 263B*, 1966, 329.
[26] H. Winter, M. Wilke and M. Bergomaz, *Nucl. Instrum. Methods B*, 1997, **125**, 124.
[27] K. Kimura, M. Hasegawa and M. Mannami, *Phys. Rev. B*, 1987, **36**, 7.
[28] E. V. Chulkov, V. M. Silkin and P. M. Echenique, *Surf. Sci.*, 1997, **391**, L1217.
[29] M. Alducin, V. M. Silkin, J. I. Juaristi and E. V. Chulkov, *Phys. Rev. A*, 2003, **67**, 032903.
[30] M. Alducin, V. M. Silkin, J. I. Juaristi and E. V. Chulkov, *Nucl. Instrum. Methods B*, 2002, **193**, 585.
[31] A. Arnau, P. A. Zeijlmans van Emmichoven, J. I. Juaristi and E. Zaremba, *Nucl. Instrum. Methods B*, 1995, **100**, 279.
[32] E. Zaremba, L. M. Sander, H. B. Shore and J. H. Rose, *J. Phys. F*, 1977, **7**, 1763.
[33] C. O. Almbladh, U. von Barth, Z. D. Popovic and J. Stott, *Phys. Rev. B*, 1976, **14**, 2250.
[34] P. M. Echenique, R. M. Nieminen and R. H. Ritchie, *Solid State Commun.*, 1981, **37**, 779.
[35] O. Gunnarson and B. I. Lundqvist, *Phys. Rev. B*, 1976, **13**, 4274.
[36] J. Friedel, *Phil. Mag.*, 1953, **43**, 153.
[37] P. M. Echenique, F. Flores and R. H. Ritchie in *Solid State Physics: Advances in Research and Applications* (eds H. Ehrenreich and D. Turnbull), Academic, New York, 1990, Vol. 43, p. 229.
[38] P. M. Echenique, I. Nagy and A. Arnau, *Int. J. Quantum Chem.*, 1989, **23**, 521.
[39] I. Nagy, B. Apagyi and K. Ladányi, *Phys. Rev. A*, 1990, **42**, 1806.
[40] K. Ladányi, I. Nagy and B. Apagyi, *Phys. Rev. A*, 1992, **45**, 2989.
[41] P. M. Echenique, R. M. Nieminen, J. C. Ashley and R. H. Ritchie, *Phys. Rev. A*, 1986, **33**, 897.
[42] I. Nagy, A. Arnau and P. M. Echenique, *Phys. Rev. B*, 1989, **40**, 11983.
[43] I. Nagy, A. Arnau and P. M. Echenique, *Phys. Rev. A*, 1989, **40**, 987.
[44] E. Zaremba, A. Arnau and P. M. Echenique, *Nucl. Instrum. Methods B*, 1995, **96**, 619.
[45] A. Salin, A. Arnau, P. M. Echenique and E. Zaremba, *Phys. Rev. B*, 1999, **59**, 2537.
[46] J. H. Omrod and H. E. Duckworth, *Can. J. Phys. C*, 1963, **41**, 1424.
[47] J. H. Omrod, J. R. Macdonald and H. E. Duckword, *Can. J. Phys. C*, 1965, **43**, 275.
[48] F. H. Eisen, *Can. J. Phys. C*, 1968, **46**, 561.
[49] J. Böttiger and F. Bason, *Radiat. Effects*, 1969, **2**, 105.
[50] G. Högberg, *Phys. Status Solidi B*, 1971, **46**, 829.
[51] D. Ward, H. R. Andrews, I. V. Mitchell, W. N. Lennard, R. E. Walker and N. Rud, *Can. J. Phys. C*, 1979, **57**, 645.
[52] H. Winter, J. I. Juaristi, I. Nagy, A. Arnau and P. M. Echenique, *Phys. Rev. B*, 2003, **67**, 245401.

[53] A. Arnau and E. Zaremba, *Nucl. Instrum. Methods B*, 1994, **90**, 32.
[54] J. I. Juaristi, A. Arnau, P. M. Echenique, C. Auth and H. Winter, *Phys. Rev. Lett.*, 1999, **82**, 1048.
[55] J. I. Juaristi, A. Arnau, P. M. Echenique, C. Auth and H. Winter, *Nucl. Instrum. Methods B*, 1999, **157**, 87.
[56] H. Winter, C. Auth, A. Mertens, A. Kirste and M. J. Steiner, *Europhys. Lett.*, 1998, **41**, 437.
[57] J. I. Juaristi and A. Arnau, *Nucl. Instrum. Methods B*, 1996, **115**, 173.
[58] R. Díez Muiño, A. Salin, N. Stolterfoht, A. Arnau and P. M. Echenique, *Phys. Rev. A*, 1998, **57**, 1126.
[59] R. Díez Muiño, N. Stolterfoht, A. Arnau, A. Salin and P. M. Echenique, *Phys. Rev. Lett.*, 1996, **76**, 4636.
[60] N. Vaeck and J. E. Hansen, *J. Phys. B*, 1992, **25**, 883.
[61] P. Bauer, M. Rösler and P. Mertens, *Nucl. Instrum. Methods B*, 1992, **69**, 46.
[62] K. Eder, D. Semrad, P. Bauer, R. Golser, P. Maier-Komor, F. Aumayr, M. Peñalba, A. Arnau, J. M. Ugalde and P. M. Echenique, *Phys. Rev. Lett.*, 1997, **79**, 4112.
[63] C. Auth, A. Mertens, H. Winter and A. Borisov, *Phys. Rev. Lett.*, 1998, **81**, 4831.
[64] P. Roncin, J. Villette, J. P. Atanas and H. Khemliche, *Phys. Rev. Lett.*, 1999, **83**, 864.
[65] J. I. Juaristi, C. Auth, H. Winter, A. Arnau, K. Eder, D. Semrad, F. Aumayr, P. Bauer and P. M. Echenique, *Phys. Rev. Lett.*, 2000, **84**, 2124.
[66] M. Peñalba, J. I. Juaristi, E. Zarate, A. Arnau and P. Bauer, *Phys. Rev. A*, 2001, **64**, 012902.
[67] R. Golser and D. Semrad, *Phys. Rev. Lett.*, 1991, **66**, 1831.
[68] A. Arnau, P. M. Echenique and R. H. Ritchie, *Nucl. Instrum. Methods B*, 1988, **33**, 138.
[69] D. Semrad, *Phys. Rev. A*, 1986, **33**, 1646.
[70] J. R. Fields, P. C. Gibbons and S. E. Schnatterly, *Phys. Rev. Lett.*, 1977, **38**, 430.

This Page Intentionally Left Blank

Nonlinear, Band-Structure, and Surface Effects in the Interaction of Charged Particles with Solids

J. M. Pitarke,[1,2] I. G. Gurtubay,[1] and V. U. Nazarov[3]

[1] *Materia Kondentsatuaren Fisika Saila, Zientzi Fakultatea, UPV/EHU, 644 Posta Kutxatila, E-48080 Bilbo, Basque Country, Spain*
[2] *Donostia International Physics Center (DIPC) and Centro Mixto CSIC-UPV/EHU, E-20018 Donostia, Basque Country, Spain*
[3] *Department of Physics and Institute of Condensed Matter Physics, Chonnam National University, Kwangju 500-757, South Korea*

Abstract

A survey is presented of various aspects of the interaction of charged particles with solids. In the framework of many-body perturbation theory, we study the nonlinear interaction of charged particles with a free gas of interacting electrons; in particular, nonlinear corrections to the stopping power are analyzed, and special emphasis is made on the separate contributions that are originated in the excitation of either electron–hole pairs, single plasmons, or double plasmons. *Ab initio* calculations of the electronic energy loss of ions moving in real solids are also presented, and the energy loss of charged particles interacting with simple metal surfaces is addressed.

Contents

ADVANCES IN QUANTUM CHEMISTRY, VOLUME 45
ISSN: 0065-3276 DOI 10.1016/S0065-3276(04)45011-4

1. INTRODUCTION

A quantitative description of the interaction of charged particles with solids is of basic importance in many different theoretical and applied areas [1]. When a moving charged particle penetrates a solid material, it may lose energy to the medium through various elastic and inelastic collision processes that are based on electron excitation and nuclear recoil motion in the solid. While energy losses due to nuclear recoil may become dominant at very low energies of the projectile [2], in the case of electrons or ions moving with nonrelativistic velocities that are comparable to the mean speed of electrons in the solid, the most significant energy losses are due to the generation of electronic excitations such as electron–hole (e–h) pairs, collective excitations, i.e., plasmons, and inner-shell excitations and ionizations.

In 1913 Niels Bohr published a seminal paper on the energy loss of charged particles interacting with electrons bound to atoms [3], which laid the ground for Bethe's quantum theory of stopping power [4]. The many-body problem of interacting conduction electrons in metals was investigated by Bohm and Pines [5] in the so-called *jellium* model, by simply replacing the ionic lattice of the solid by a homogeneous background which serves to provide neutrality to the system. Within linear-response theory, the electronic response of conduction electrons to external charged particles is determined by a wavevector- and frequency-dependent longitudinal dielectric function. In the self-consistent-field, or random-phase, approximation (RPA), the dielectric function of interacting free electrons was derived by Lindhard [6], and, subsequently, a number of workers have derived alternative dielectric functions that incorporate various many-body higher-order local-field corrections [7,8] and band-structure effects [9]. The effect of dissipative processes occurring in a real metal and conversion of plasmons into multiple e–h pairs has been allowed phenomenologically by including a damping coefficient in the dielectric function [10].

The validity of linear-response theory, which treats the perturbing potential to the lowest order, is not obvious *a priori*. While lowest-order perturbation theory leads to energy losses that are proportional to the square of the projectile charge $Z_1 e$, the energy loss of either positive and negative pions [11] or protons and antiprotons [12,13] is known to exhibit a measurable dependence on the sign of the charge [14–16]. Experimentally observed nonlinear double-plasmon excitations [17,18] are also beyond the realm of standard linear-response theory [19–21]; nonlinearities may play an important role in the electronic wake generated by moving ions in solids [22, 23], and lowest-order perturbation theory breaks down when the projectile is capable of carrying bound electrons with it [24].

The first full nonlinear calculation of the electronic stopping power of an electron gas was performed by Echenique *et al*. [25] in the low-velocity limit.

They used a scattering approach to the stopping power, and the scattering cross-sections were calculated for a statically screened potential which was determined self-consistently by using density-functional theory (DFT) [26]. These static-screening calculations were then extended to projectile velocities approaching the Fermi velocity of the target [27]. Alternatively, an effective charge can be assigned to the projectile [28] and nonlinearities can then be investigated within quadratic-response theory, thereby providing results for arbitrary projectile velocities [29].

To calculate the electronic stopping power of real solids from the knowledge of the full-band structure of the solid and the corresponding Bloch eigenfunctions and eigenvalues is a laborious problem. Hence, early theoretical investigations were based on semiempirical treatments of the electronic excitations in the solid [30–34]. Attempts to introduce the full electronic band structure in the evaluation of the electronic stopping power of alkaline metals for low-projectile velocities include a one-band calculation [35] as well as a calculation based on a linear combination of atomic orbitals [36]. The low-velocity limit was also investigated, in the case of silicon, on the basis of a static treatment of the density response of the solid [37]. *Ab initio* band-structure calculations that are based on a full evaluation of the dynamical density-response of the solid have been carried out only very recently [38–40].

In this chapter, we summarize recent investigations on the impact of nonlinear, band-structure, and surface effects in the interaction of charged particles with solids. We present general procedures to calculate, within many-body perturbation theory, the nonlinear potential induced by moving ions in an interacting free-electron gas (FEG), Z_1^3 contributions to the stopping power of a FEG, and double-plasmon excitation probabilities. Self-consistent calculations of the energy-loss spectra of charged particles moving near a metal surface are also presented. Finally, we consider the electronic stopping power of valence electrons in real solids, which we evaluate within random conditions.

Unless otherwise stated, atomic units are used throughout this chapter, i.e., $e^2 = \hbar = m_e = 1$. The atomic unit of length is the Bohr radius, $a_0 = \hbar^2/m_e^2 = 0.529$ Å, the atomic unit of energy is the Hartree (1 Hartree $= e^2/a_0 = 27.2$ eV), and the atomic unit of velocity is the Bohr velocity, $v_0 = \alpha c = 2.19 \times 10^8$ cm s^{-1}, α and c being the fine structure constant and the velocity of light, respectively.

2. THEORY

We consider a recoiless particle of charge Z_1 [41] moving in an arbitrary inhomogeneous electron system with nonrelativistic velocity, for which retardation effects and radiation losses can be neglected. The energy that

the probe particle loses per unit time due to electronic excitations in the medium can be written as [42]

$$-\frac{\mathrm{d}E}{\mathrm{d}t} = -\int \mathrm{d}\mathbf{r}\, \rho^{\mathrm{ext}}(\mathbf{r},t)\frac{\partial V^{\mathrm{ind}}(\mathbf{r},t)}{\partial t}, \tag{1}$$

where $\rho^{\mathrm{ext}}(\mathbf{r},t)$ represents the probe-particle charge density

$$\rho^{\mathrm{ext}}(\mathbf{r},t) = Z_1\,\delta(\mathbf{r}-\mathbf{r}_0-\mathbf{v}t), \tag{2}$$

and $V^{\mathrm{ind}}(\mathbf{r},t)$ is the induced potential. Keeping terms of first and second order in the external perturbation, time-dependent perturbation theory yields

$$\begin{aligned} V^{\mathrm{ind}}(\mathbf{r},t) = & \int \mathrm{d}\mathbf{r}' \int_{-\infty}^{+\infty} \mathrm{d}t' \int_{-\infty}^{+\infty} \frac{\mathrm{d}\omega}{2\pi} \mathrm{e}^{-\mathrm{i}\omega(t-t')} \int \mathrm{d}\mathbf{r}_1 \\ & \times \int \mathrm{d}\mathbf{r}_3\, v(\mathbf{r},\mathbf{r}_1) \Bigg[\chi(\mathbf{r}_1,\mathbf{r}_3;\omega) \\ & + \int \mathrm{d}\mathbf{r}'' \int_{-\infty}^{+\infty} \mathrm{d}t'' \int_{-\infty}^{+\infty} \frac{\mathrm{d}\omega'}{2\pi} \mathrm{e}^{-\mathrm{i}(\omega+\omega')(t'-t'')} \\ & \times \int \mathrm{d}\mathbf{r}_2 Y(\mathbf{r}_1,\mathbf{r}_2,\mathbf{r}_3;\omega,\omega') v(\mathbf{r}_2,\mathbf{r}'') \rho^{\mathrm{ext}}(\mathbf{r}'',t'') \Bigg] \\ & \times v(\mathbf{r}_3,\mathbf{r}')\rho^{\mathrm{ext}}(\mathbf{r}',t'), \end{aligned} \tag{3}$$

where $v(\mathbf{r},\mathbf{r}') = 1/|\mathbf{r}-\mathbf{r}'|$ is the bare Coulomb interaction, and $\chi(\mathbf{r}_1,\mathbf{r}_2;\omega)$ and $Y(\mathbf{r}_1,\mathbf{r}_2,\mathbf{r}_3;\omega,\omega')$ are the so-called linear and quadratic density-response functions of the electron system:

$$\chi(\mathbf{r}_1,\mathbf{r}_2;\omega) = \frac{1}{\Omega}\sum_n \left[\frac{[\hat{\rho}(\mathbf{r}_1)]_{0n}[\hat{\rho}(\mathbf{r}_2)]_{n0}}{\omega-\omega_{n0}+\mathrm{i}\eta} - \frac{[\hat{\rho}(\mathbf{r}_2)]_{0n}[\hat{\rho}(\mathbf{r}_1)]_{n0}}{\omega+\omega_{n0}+\mathrm{i}\eta} \right] \tag{4}$$

and

$$\begin{aligned} Y(\mathbf{r}_1,\mathbf{r}_2,\mathbf{r}_3;\omega,\omega') = & -\frac{1}{2\Omega}\sum_{n,l} \Bigg[\frac{[\hat{\rho}(\mathbf{r}_1)]_{0n}[\hat{\rho}(\mathbf{r}_3)]_{nl}[\hat{\rho}(\mathbf{r}_2)]_{l0}}{[\omega-\omega_{n0}+\mathrm{i}\eta][\omega'+\omega_{l0}-\mathrm{i}\eta]} \\ & + \frac{[\hat{\rho}(\mathbf{r}_2)]_{0n}[\hat{\rho}(\mathbf{r}_1)]_{nl}[\hat{\rho}(\mathbf{r}_3)]_{l0}}{[\omega'-\omega_{n0}-\mathrm{i}\eta][\omega''+\omega_{l0}-\mathrm{i}\eta]} \\ & + \frac{[\hat{\rho}(\mathbf{r}_3)]_{0n}[\hat{\rho}(\mathbf{r}_2)]_{nl}[\hat{\rho}(\mathbf{r}_1)]_{l0}}{[\omega''-\omega_{n0}-\mathrm{i}\eta][\omega+\omega_{l0}+\mathrm{i}\eta]} \\ & + \frac{[\hat{\rho}(\mathbf{r}_1)]_{0n}[\hat{\rho}(\mathbf{r}_2)]_{nl}[\hat{\rho}(\mathbf{r}_3)]_{l0}}{[\omega-\omega_{n0}+\mathrm{i}\eta][\omega''+\omega_{l0}-\mathrm{i}\eta]} \end{aligned}$$

$$+\frac{[\hat{\rho}(\mathbf{r}_3)]_{0n}[\hat{\rho}(\mathbf{r}_1)]_{nl}[\hat{\rho}(\mathbf{r}_2)]_{l0}}{[\omega'' - \omega_{n0} - \mathrm{i}\eta][\omega' + \omega_{l0} - \mathrm{i}\eta]}$$
$$+\frac{[\hat{\rho}(\mathbf{r}_2)]_{0n}[\hat{\rho}(\mathbf{r}_3)]_{nl}[\hat{\rho}(\mathbf{r}_1)]_{l0}}{[\omega' - \omega_{n0} - \mathrm{i}\eta][\omega + \omega_{l0} + \mathrm{i}\eta]}\Bigg]. \tag{5}$$

Here, Ω is the normalization volume, $\hat{\rho}(\mathbf{r})$ is the particle-density operator, and $[\hat{\rho}(\mathbf{r})]_{nl}$ are matrix elements taken between the exact many-electron states Ψ_n and Ψ_l of energy E_n and E_l.Φ_0 and E_0 represent the exact many-electron ground state and energy, respectively, $\omega_{nl} = E_n - E_l$, $\omega'' = -(\omega + \omega')$, and η is a positive infinitesimal.

The total energy lost by the probe particle is simply

$$-\Delta E = \int_{-\infty}^{+\infty} \mathrm{d}t\left(-\frac{\mathrm{d}E}{\mathrm{d}t}\right), \tag{6}$$

which can also be obtained by first considering the probability $P_{\mathbf{q},\omega}$ for the probe particle to transfer momentum $\mathbf{q}$ and energy ω to the many-electron system and then multiplying $P_{\mathbf{q},\omega}$ by the energy transfer ω and summing over all $\mathbf{q}$ and ω [29,43–45].

The many-body ground and excited states of a many-electron system are *unknown*; hence, the exact linear and quadratic density-response functions are difficult to calculate. In the framework of time-dependent density functional theory (TDDFT) [46], the exact density-response functions are obtained from the knowledge of their noninteracting counterparts and the exchange-correlation (xc) kernel $f_{\mathrm{xc}}(\mathbf{r}, \mathbf{r}', \omega)$ which equals the second functional derivative of the *unknown* xc energy functional $E_{\mathrm{xc}}[n]$. In the so-called time-dependent Hartree approximation or RPA, the xc kernel is simply taken to be zero.

In the case of a noninteracting Fermi gas, the ground state is obtained by simply filling all the single-particle states of noninteracting electrons below the Fermi level. When acting on the ground state, the particle-density operator $\hat{\rho}(\mathbf{r})$ produces single-particle transitions in which a given particle is scattered from some state inside the Fermi sea to a state outside. Hence, the linear and quadratic density-response functions of equations (4) and (5) reduce to their noninteracting counterparts

$$\chi^0(\mathbf{r}_1, \mathbf{r}_2; \omega) = \frac{2}{\Omega}\sum_{i,j} f_i\Bigg[\frac{\phi_i(\mathbf{r}_1)\phi_j^*(\mathbf{r}_1)\phi_j(\mathbf{r}_2)\phi_i^*(\mathbf{r}_2)}{\omega - \omega_{ji} + \mathrm{i}\eta}$$
$$-\frac{\phi_i(\mathbf{r}_2)\phi_j^*(\mathbf{r}_2)\phi_j(\mathbf{r}_1)\phi_i^*(\mathbf{r}_1)}{\omega + \omega_{ji} + \mathrm{i}\eta}\Bigg] \tag{7}$$

and

$$
\begin{aligned}
Y^0(\mathbf{r}_1,\mathbf{r}_2,\mathbf{r}_3;\omega,\omega') = -\frac{1}{\Omega}\sum_{i,j,k} f_i \Bigg[& \frac{\phi_i(\mathbf{r}_1)\phi_j^*(\mathbf{r}_1)\phi_j(\mathbf{r}_3)\phi_k^*(\mathbf{r}_3)\phi_k(\mathbf{r}_2)\phi_i^*(\mathbf{r}_2)}{[\omega-\omega_{ji}+\mathrm{i}\eta][\omega'+\omega_{ki}-\mathrm{i}\eta]} \\
& + \frac{\phi_i(\mathbf{r}_2)\phi_j^*(\mathbf{r}_2)\phi_j(\mathbf{r}_1)\phi_k^*(\mathbf{r}_1)\phi_k(\mathbf{r}_3)\phi_i^*(\mathbf{r}_3)}{[\omega'-\omega_{ji}-\mathrm{i}\eta][\omega''+\omega_{ki}-\mathrm{i}\eta]} \\
& + \frac{\phi_i(\mathbf{r}_3)\phi_j^*(\mathbf{r}_3)\phi_j(\mathbf{r}_2)\phi_k^*(\mathbf{r}_2)\phi_k(\mathbf{r}_1)\phi_i^*(\mathbf{r}_1)}{[\omega''-\omega_{ji}-\mathrm{i}\eta][\omega+\omega_{ki}+\mathrm{i}\eta]} \\
& + \frac{\phi_i(\mathbf{r}_1)\phi_j^*(\mathbf{r}_1)\phi_j(\mathbf{r}_2)\phi_k^*(\mathbf{r}_2)\phi_k(\mathbf{r}_3)\phi_i^*(\mathbf{r}_3)}{[\omega-\omega_{ji}+\mathrm{i}\eta][\omega''+\omega_{ki}-\mathrm{i}\eta]} \\
& + \frac{\phi_i(\mathbf{r}_3)\phi_j^*(\mathbf{r}_3)\phi_j(\mathbf{r}_1)\phi_k^*(\mathbf{r}_1)\phi_k(\mathbf{r}_2)\phi_i^*(\mathbf{r}_2)}{[\omega''-\omega_{ji}-\mathrm{i}\eta][\omega'+\omega_{ji}-\mathrm{i}\eta]} \\
& + \frac{\phi_i(\mathbf{r}_2)\phi_j^*(\mathbf{r}_2)\phi_j(\mathbf{r}_3)\phi_k^*(\mathbf{r}_3)\phi_k(\mathbf{r}_1)\phi_i^*(\mathbf{r}_1)}{[\omega'-\omega_{ji}-\mathrm{i}\eta][\omega+\omega_{ki}+\mathrm{i}\eta]} \Bigg],
\end{aligned}
\tag{8}
$$

where $\omega_{ji} = \varepsilon_j - \varepsilon_i$, and f_i are Fermi–Dirac occupation factors. At zero temperature $f_i = \Theta(\varepsilon_\mathrm{F} - \varepsilon_i)$, ε_F being the Fermi energy, and $\Theta(x)$, the Heaviside step function. The single-particle states $\phi_i(\mathbf{r})$ and energies ε_i entering equations (7) and (8) are usually chosen to be the eigenfunctions and eigenvalues of an effective Hartree [47], Kohn–Sham [48], or quasiparticle [49,50] Hamiltonian [51].

In the RPA, the induced potential $V^{\mathrm{ind}}(\mathbf{r},t)$ is simply obtained as the potential induced in a noninteracting Fermi system by both the probe-particle charge density $\rho^{\mathrm{ext}}(\mathbf{r},t)$ and the induced electron density $\rho^{\mathrm{ind}}(\mathbf{r},t)$, i.e.,

$$
\begin{aligned}
V^{\mathrm{ind}}(\mathbf{r},t) = & \int \mathrm{d}\mathbf{r}' \int_{-\infty}^{+\infty} \mathrm{d}t' \int_{-\infty}^{+\infty} \frac{\mathrm{d}\omega}{2\pi} \mathrm{e}^{-\mathrm{i}\omega(t-t')} \int \mathrm{d}\mathbf{r}_1 \int \mathrm{d}\mathbf{r}_3 \; v(\mathbf{r},\mathbf{r}_1) \\
& \times \Bigg\{ \chi^0(\mathbf{r}_1,\mathbf{r}_3;\omega) + \int \mathrm{d}\mathbf{r}'' \int_{-\infty}^{+\infty} \mathrm{d}t'' \int_{-\infty}^{+\infty} \frac{\mathrm{d}\omega'}{2\pi} \mathrm{e}^{-\mathrm{i}(\omega+\omega')(t'-t'')} \\
& \times \int \mathrm{d}\mathbf{r}_2 Y^0(\mathbf{r}_1,\mathbf{r}_2,\mathbf{r}_3;\omega,\omega') v(\mathbf{r}_2,\mathbf{r}'') [\rho^{\mathrm{ext}}(\mathbf{r}'',t'') + \rho^{\mathrm{ind}}(\mathbf{r}'',t'')] \Bigg\} \\
& \times v(\mathbf{r}_3,\mathbf{r}') [\rho^{\mathrm{ext}}(\mathbf{r}',t') + \rho^{\mathrm{ind}}(\mathbf{r}',t')].
\end{aligned}
\tag{9}
$$

Assuming that

$$
V^{\mathrm{ind}}(\mathbf{r},t) = \int \mathrm{d}\mathbf{r}' v(\mathbf{r},\mathbf{r}') \rho^{\mathrm{ind}}(\mathbf{r}',t),
\tag{10}
$$

one easily finds that the induced potential $V^{\mathrm{ind}}(\mathbf{r},t)$ of equation (9) is of the form of equation (3) with the exact interacting linear and quadratic

density-response functions being replaced by the following integral equations

$$\chi(\mathbf{r},\mathbf{r}';\omega)=\chi^0(\mathbf{r},\mathbf{r}';\omega)+\int d\mathbf{r}_1\int d\mathbf{r}_2\,\chi^0(\mathbf{r},\mathbf{r}_1;\omega)v(\mathbf{r}_1,\mathbf{r}_2)\chi(\mathbf{r}_2,\mathbf{r}';\omega) \quad (11)$$

and

$$Y(\mathbf{r},\mathbf{r}',\mathbf{r}'';\omega,\omega')=\int d\mathbf{r}_1\int d\mathbf{r}_2\int d\mathbf{r}_3\,K(\mathbf{r},\mathbf{r}_1;\omega)Y^0(\mathbf{r}_1,\mathbf{r}_2,\mathbf{r}_3;\omega,\omega') \times K(\mathbf{r}_2,\mathbf{r}';-\omega')K(\mathbf{r}_3,\mathbf{r}'';\omega+\omega'), \quad (12)$$

where $K(\mathbf{r},\mathbf{r}';\omega)$ is the so-called inverse dielectric function

$$K(\mathbf{r},\mathbf{r}';\omega)=\delta(\mathbf{r}-\mathbf{r}')+\int d\mathbf{r}_1\,\chi(\mathbf{r},\mathbf{r}_1;\omega)v(\mathbf{r}_1,\mathbf{r}'). \quad (13)$$

2.1. Uniform electron gas

In the case of a uniform FEG, there is translational invariance in all directions. Hence, equation (6) yields

$$-\Delta E=L\left(-\frac{dE}{dx}\right), \quad (14)$$

where L is the normalization length, and $(-dE/dx)$ is the energy loss per unit path length of the projectile, i.e., the so-called stopping power of the electron system

$$-\frac{dE}{dx}=4\pi Z_1^2\int\frac{d\mathbf{q}}{(2\pi)^3}\int_0^\infty\frac{d\omega}{2\pi}\,\omega v_{\mathbf{q}}\delta(\omega-\mathbf{q}\cdot\mathbf{v}) \times\left[-\operatorname{Im}K_{\mathbf{q},\omega}+2\pi Z_1\int\frac{d\mathbf{q}_1}{(2\pi)^4}\int_{-\infty}^\infty\frac{d\omega_1}{2\pi} \operatorname{Im}Y_{\mathbf{q},\omega;-\mathbf{q}_1,-\omega_1}v_{\mathbf{q}_1}v_{\mathbf{q}-\mathbf{q}_1}\delta(\omega_1-\mathbf{q}_1\cdot\mathbf{v})\right], \quad (15)$$

$v_{\mathbf{q}}=4\pi/q^2$, $K_{\mathbf{q},\omega}$, and $Y_{\mathbf{q}_1,\omega_1;\mathbf{q}_2,\omega_2}$ being Fourier transforms of the bare Coulomb interaction $v(\mathbf{r},\mathbf{r}')$, the inverse dielectric function $K(\mathbf{r},\mathbf{r}',\omega)$, and the quadratic density-response function $Y(\mathbf{r},\mathbf{r}',\mathbf{r}'';\omega,\omega')$, respectively.

In the RPA,

$$K_{\mathbf{q},\omega}=1+\chi_{\mathbf{q},\omega}v_{\mathbf{q}}, \quad (16)$$

$$\chi_{\mathbf{q},\omega}=\chi^0_{\mathbf{q},\omega}+\chi^0_{\mathbf{q},\omega}v_{\mathbf{q}}\chi_{\mathbf{q},\omega}, \quad (17)$$

and

$$Y_{\mathbf{q}_1,\mathbf{q}_2;\omega_1,\omega_2}=K_{\mathbf{q}_1,\omega_1}Y^0_{\mathbf{q}_1,\mathbf{q}_2;\omega_1,\omega_2}K_{-\mathbf{q}_1,-\omega_1}K_{\mathbf{q}_1+\mathbf{q}_2,\omega_1+\omega_2}, \quad (18)$$

$\chi^0_{\mathbf{q},\omega}$ and $Y^0_{\mathbf{q}_1,\mathbf{q}_2;\omega_1,\omega_2}$ being Fourier transforms of the noninteracting linear and quadratic density-response functions $\chi^0(\mathbf{r}_1,\mathbf{r}_2;\omega)$ and $Y^0(\mathbf{r}_1,\mathbf{r}_2,\mathbf{r}_3;\omega,\omega')$ (see equations (7) and (8)). Noting that for a uniform electron gas the single-particle states $\phi_i(\mathbf{r})$ entering equations (7) and (8) are simply plane waves of the form

$$\phi_{\mathbf{k}}(\mathbf{r}) = \frac{1}{\sqrt{\Omega}} e^{i\mathbf{k}\cdot\mathbf{r}}, \tag{19}$$

analytic expressions for both $\chi^0_{\mathbf{q},\omega}$ and $Y^0_{\mathbf{q}_1,\mathbf{q}_2;\omega_1,\omega_2}$ can be obtained. $\chi^0_{\mathbf{q},\omega}$ is the Lindhard function [6,47]. Explicit expressions for the real and imaginary parts of the noninteracting quadratic density-response function $Y^0_{\mathbf{q}_1,\mathbf{q}_2;\omega_1,\omega_2}$ were reported in Refs. [52] and [16,29], respectively, and an extension to imaginary frequencies was later reported in Ref. [53].

2.1.1. High-velocity limit

For high projectile velocities, the zero-point motion of the electron gas can be neglected and it can be considered, therefore, as if it were at rest. Thus, in this approximation all energies ε_i entering equations (7) and (8) can be set equal to zero. If one further assumes that $v^2 \gg \omega_p$, ω_p being the plasmon frequency for which $K_{0,\omega}$ diverges, equation (15) is found to yield [29]

$$-\frac{dE}{dx} \approx \frac{4\pi n Z_1^2}{v^2}(L_0 + Z_1 L_1), \tag{20}$$

where

$$L_0 = \ln\frac{2v^2}{\omega_p} \tag{21}$$

and

$$L_1 = 1.42\frac{\pi\omega_p}{v^3}\ln\frac{2v^2}{2.13\omega_p}, \tag{22}$$

n being the density of free electrons in the target. The first term, which for a relatively low projectile charge Z_1 gives the main contribution to the stopping power, is proportional to Z_1^2 and has the same form as the Bethe formula for the inelastic stopping power of atoms [4] as long as the plasma frequency ω_p is replaced by the mean excitation energy of electrons in the atom. The second term, which originates the so-called Barkas effect, i.e., the dependence of the stopping power on the sign of the projectile charge, has been found to yield excellent agreement with stopping-power measurements at high velocities [16,54].

2.1.2. *Double-plasmon excitation*

In the RPA, the linear-response contribution to the stopping power of equation (15), which is proportional to Z_1^2, is fully originated in the creation of single e–h pairs and plasmons. Furthermore, the contribution to the actual (beyond RPA) Z_1^2 stopping power due to coherent multiple excitations such as double plasmons is expected to be relatively small. Nevertheless, accurate measurements of electron energy-loss spectra showed evidence for the existence of coherent double-plasmon excitations [17,18].

In the framework of many-body perturbation theory, one first defines the scattering matrix S as a time-ordered exponential in terms of the perturbing Hamiltonian and field operators [47]. Then, one considers the matrix elements corresponding to the process in which the recoiless probe particle carries the system either from an initial state $a_{\mathrm{i}}^{+}\Phi_0$ to a final state $a_{\mathrm{f}}^{+}\Phi_0$ (single excitation) or from an initial state $a_{\mathrm{i}_1}^{+}a_{\mathrm{i}_2}^{+}\Phi_0$ to a final state $a_{\mathrm{f}_1}^{+}a_{\mathrm{f}_2}^{+}\Phi_0$ (double excitation)

$$S_{\mathrm{f,i}} = \frac{\langle \Phi_0 | a_{\mathrm{f}} S a_{\mathrm{i}}^{+} | \Phi_0 \rangle}{\langle \Phi_0 | S | \Phi_0 \rangle} \tag{23}$$

and

$$S_{\mathrm{f}_1,\mathrm{f}_2;\mathrm{i}_1,\mathrm{i}_2} = \frac{\langle \Phi_0 | a_{\mathrm{f}_1} a_{\mathrm{f}_2} S a_{\mathrm{i}_1}^{+} a_{\mathrm{i}_2}^{+} | \Phi_0 \rangle}{\langle \Phi_0 | S | \Phi_0 \rangle}, \tag{24}$$

where a_{i} and a_{i}^{+} are annihilation and creation operators, respectively, and Φ_0 represents the vacuum state. Finally, one calculates the probability for the probe particle to transfer momentum $\mathbf{q}$ and energy ω to the many-electron system by moving either one, two, or more particles from inside the Fermi sea to outside

$$\begin{aligned} P_{\mathbf{q},\omega} = {} & 2\sum_{\mathbf{s}} f_{\mathbf{s}} \sum_{\mathbf{p}} (1 - f_{\mathbf{p}}) |S_{\mathrm{f,i}}|^2 \delta^4_{q,p-s} + 4 \sum_{\mathbf{q}_1} \sum_{\omega_1} \sum_{\mathbf{s}_1} f_{\mathbf{s}_1} \sum_{\mathbf{s}_2} f_{\mathbf{s}_2} \sum_{\mathbf{p}_1} (1 - f_{\mathbf{p}_1}) \\ & \times \sum_{\mathbf{p}_2} (1 - f_{\mathbf{p}_2}) |S_{\mathrm{f}_1,\mathrm{f}_2;\mathrm{i}_1,\mathrm{i}_2}|^2 \delta^4_{q_1,p_1-s_1} \delta^4_{q-q_1,p_2-s_2} + \cdots, \end{aligned} \tag{25}$$

$\delta^4_{q,q'} = \delta^3_{\mathbf{q},\mathbf{q}'}\delta_{\omega,\omega'}$ being the symmetric Kronecker δ symbol. If the probe-particle is not a heavy particle, energy conservation should be ensured by introducing recoil into the argument of the delta functions. If the probe is an electron, a step function should also be introduced to ensure that the probe electron does not lose enough energy to fall below the Fermi level.

The stopping power of the electron system is obtained by first multiplying the probability $P_{\mathbf{q},\omega}$ of equation (25) by the energy transfer ω and then

summing over all $\mathbf{q}$ and ω:

$$-\frac{\mathrm{d}E}{\mathrm{d}x} = \frac{1}{L}\sum_{\mathbf{q}}\sum_{\omega}\omega P_{\mathbf{q},\omega}. \tag{26}$$

A careful analysis of the various contributions to the probability $P_{\mathbf{q},\omega}$ that are proportional to Z_1^2 and Z_1^3 yields, to third order in the RPA screened interaction $v_{\mathbf{q}}K_{\mathbf{q},\omega}$, an expression for the stopping power that exactly coincides with equation (15) [44]. Alternatively, the inverse mean free path is obtained as follows:

$$\lambda^{-1} = \frac{1}{L}\sum_{\mathbf{q}}\sum_{\omega}P_{\mathbf{q},\omega}. \tag{27}$$

The lowest-order Z_1^2 contribution to the probability $P^{2p}_{\mathbf{q},\omega}$ for a probe-electron ($Z_1 = -1$) to excite a double plasmon, which is of fourth order in the RPA screened interaction $v_{\mathbf{q}}K_{\mathbf{q},\omega}$, is found to be given by the following expression

$$\begin{aligned} P^{2p}_{\mathbf{q},\omega} = 16\pi Z_1^2 v_{\mathbf{q}}^{-2}K^{-2}_{\mathbf{q},\omega}\sum_{\mathbf{q}_1} v_{\mathbf{q}_1}v_{\mathbf{q}-\mathbf{q}_1}\int_0^{\omega}\frac{\mathrm{d}\omega_1}{2\pi}\,\mathrm{Im}\,K_{\mathbf{q}_1,\omega_1} \\ \times \mathrm{Im}\,K_{\mathbf{q}-\mathbf{q}_1,\omega-\omega_1}|Y_{\mathbf{q},\mathbf{q}_1;\omega,\omega_1}|^2\delta(\omega-\omega_{\mathbf{v}}+\omega_{\mathbf{v}-\mathbf{q}}) \\ \times \Theta(\omega_{\mathbf{v}-\mathbf{q}}-\varepsilon_{\mathrm{F}}), \end{aligned} \tag{28}$$

where $\omega_{\mathbf{k}} = k^2/2$. If one approximates both the linear and quadratic density-response functions entering equation (28) by their low-$\mathbf{q}$ limits, one only keeps the high-velocity limit of this probability in an expansion in terms of the inverse velocity, and one introduces this limit into equation (27), one obtains the following result for the Z_1^2 contribution to the inverse mean free path that is due to the excitation of a double plasmon [20,55]

$$\lambda_{2p}^{-1} \approx 0.164\, Z_1^2\,\frac{\sqrt{r_s}}{36\pi v^2}, \tag{29}$$

r_s being the so-called electron-density parameter defined by the relation $1/n = (4\pi/3)(r_s a_0)^3$. Numerical study shows [21] that introduction of the full RPA linear and quadratic density-response functions into equation (28) yields a result for λ_{2p}^{-1} which has, in the high-velocity limit, the same velocity dependence as the approximation of equation (29), though for $r_s = 2.07$ the full RPA λ_{2p}^{-1} is found to be larger than this approximation by a factor of 2.16.

2.2. Bounded electron gas

In the case of charged particles moving inside a solid, nonlinear effects are known to be crucial in the interpretation of energy-loss measurements.

However, these corrections have been shown to be less important when the charged particle moves outside the solid [56]. Hence, in the case of a bounded three-dimensional electron gas we restrict the calculations to linear-response theory. Assuming translational invariance in two directions, which we take to be normal to the z-axis, to first order in the external perturbation (linear-response theory) the energy loss of equation (6) may be expressed as follows [57]

$$-\Delta E = -\frac{Z_1^2}{\pi}\int \frac{\mathrm{d}\mathbf{q}_\parallel}{(2\pi)^2}\int_{-\infty}^{+\infty}\mathrm{d}t\int_{-\infty}^{+\infty}\mathrm{d}t'\int_0^{\infty}\mathrm{d}\omega\;\omega \mathrm{e}^{-\mathrm{i}(\omega-\mathbf{q}_\parallel\cdot\mathbf{v}_\parallel)(t-t')} \times \mathrm{Im}\; W[z(t), z(t'); \mathbf{q}_\parallel, \omega], \tag{30}$$

where $\mathbf{q}_\parallel$ and $\mathbf{v}_\parallel$ are components of the momentum transfer and the velocity in the plane of the surface, $z(t)$ represents the position of the projectile relative to the surface, and

$$W(z, z'; \mathbf{q}_\parallel, \omega) = v(z, z', \mathbf{q}_\parallel) + \int \mathrm{d}z_1 \int \mathrm{d}z_2\; v(z, z_1; \mathbf{q}_\parallel) \times \chi(z_1, z_2; \mathbf{q}_\parallel, \omega) v(z_2, z'; \mathbf{q}_\parallel), \tag{31}$$

$v(z, z'; \mathbf{q}_\parallel) = (2\pi/q_\parallel)\mathrm{e}^{-q_\parallel|z-z'|}$ and $\chi(z, z'; \mathbf{q}_\parallel, \omega)$ being two-dimensional Fourier transforms of the bare Coulomb interaction and the density-response function, respectively.

In the RPA,

$$\chi(z, z'; \mathbf{q}_\parallel, \omega) = \chi^0(z, z'; \mathbf{q}_\parallel, \omega) + \int \mathrm{d}z_1 \int \mathrm{d}z_2\; \chi^0(z, z_1; \mathbf{q}_\parallel, \omega) \times v(z_1, z_2; \mathbf{q}_\parallel)\chi(z_2, z'; \mathbf{q}_\parallel, \omega), \tag{32}$$

where

$$\chi^0(z, z'; \mathbf{q}_\parallel, \omega) = 2\sum_{i,j}\phi_i(z)\phi_j^*(z)\phi_j(z')\phi_i^*(z') \times \int \frac{\mathrm{d}\mathbf{k}_\parallel}{(2\pi)^2}\,\frac{f_i - f_j}{E_i - E_j + (\omega + \mathrm{i}\eta)}. \tag{33}$$

Here,

$$E_i = \varepsilon_i + \frac{\mathbf{k}_\parallel^2}{2} \tag{34}$$

and

$$E_j = \varepsilon_j + \frac{(\mathbf{k}_\parallel + \mathbf{q}_\parallel)^2}{2}, \tag{35}$$

the wave functions $\phi_i(z)$ and energies ε_i, which describe motion normal to the surface, being the eigenfunctions and eigenvalues of a one-dimensional Hartree, Kohn–Sham, or quasiparticle Hamiltonian.

Equation (30) gives the energy that a charged particle moving with constant velocity along an arbitrary trajectory loses due to electronic excitations in an electron system that is translationally invariant in two directions, as occurs in the case of a simple metal surface modeled by jellium.

2.2.1. *Parallel trajectory*

In the glancing incidence geometry ions penetrate into the material, they skim the outermost layer of the solid, and are then repelled by a repulsive, screened Coulomb potential, as discussed by Gemmell [58]. Through use of the appropriate effective potentials the ion trajectory $z(t)$ can be calculated and the energy loss is then obtained from equation (30). Under extreme grazing-incidence conditions, incident charged particles can be assumed to move with constant velocity $\mathbf{v}$ along a definite trajectory at a fixed distance z from a jellium surface. Equation (30) then yields equation (14), as in the case of charged particles moving in a uniform electron gas, but with the energy loss per unit path length now being given by the following expression [57]:

$$-\frac{\mathrm{d}E}{\mathrm{d}x} = -\frac{2}{v}Z_1^2 \int \frac{\mathrm{d}\mathbf{q}_\parallel}{(2\pi)^2} \int_0^\infty \mathrm{d}\omega\, \omega\, \mathrm{Im}\, W(z,z;\mathbf{q}_\parallel,\omega)\delta(\omega - \mathbf{q}_\parallel\cdot\mathbf{v}). \quad (36)$$

2.2.2. *High-velocity limit*

At high velocities, the energy-loss spectrum for charged particles moving outside a solid is known to be dominated by long-wavelength ($q_\parallel \to 0$) surface-plasmon excitations [59]. In this long-wavelength limit, the imaginary part of equation (31) yields [60]

$$\mathrm{Im}\, W(z,z';q_\parallel,\omega) = -\frac{\pi^2}{q_\parallel} \mathrm{e}^{-q_\parallel(z+z')} \omega_s\, \delta(\omega - \omega_s), \quad (37)$$

where $\omega_s = \omega_\mathrm{p}/\sqrt{2}$, $\omega_\mathrm{p} = (4\pi n)^{1/2}$ being the classical plasma frequency of a uniform electron gas of density n.

Introducing equation (37) into equation (36), one easily reproduces the classical expression of Echenique and Pendry [61]:

$$-\frac{\mathrm{d}E}{\mathrm{d}x} = Z_1^2 \frac{\omega_s^2}{v^2} \mathrm{K}_0(2\omega_s z/v), \quad (38)$$

where K_0 is the zero-order modified Bessel function. For large values of z ($z \gg v/\omega_s$), equation (38) reduces to

$$-\frac{dE}{dx} = Z_1^2 \frac{\omega_s}{2v}\sqrt{\pi\omega_s/zv}\, e^{-2\omega_s z/v}. \tag{39}$$

2.3. Periodic crystals

For a periodic crystal, we introduce the following Fourier expansion of the linear density-response function

$$\chi(\mathbf{r}, \mathbf{r}'; \omega) = \frac{1}{\Omega}\sum_{\mathbf{q}}^{BZ}\sum_{\mathbf{G},\mathbf{G}'} e^{i(\mathbf{q}+\mathbf{G})\cdot\mathbf{r}} e^{-i(\mathbf{q}+\mathbf{G}')\cdot\mathbf{r}'}\chi_{\mathbf{G},\mathbf{G}'}(\mathbf{q}, \omega), \tag{40}$$

where the first sum runs over $\mathbf{q}$ vectors within the first Brillouin zone (BZ), and $\mathbf{G}$ and $\mathbf{G}'$ are reciprocal lattice vectors.

In the RPA,

$$\chi_{\mathbf{G},\mathbf{G}'}(\mathbf{q}, \omega) = \chi^0_{\mathbf{G},\mathbf{G}'}(\mathbf{q}, \omega) + \sum_{\mathbf{G}''}\chi^0_{\mathbf{G},\mathbf{G}''}(\mathbf{q}, \omega)v_{\mathbf{q}+\mathbf{G}''}\chi_{\mathbf{G}'',\mathbf{G}'}(\mathbf{q}, \omega), \tag{41}$$

where $v_{\mathbf{q}+\mathbf{G}}$ and $\chi^0_{\mathbf{G},\mathbf{G}'}(\mathbf{q}, \omega)$ represent the Fourier coefficients of the bare Coulomb interaction $v(\mathbf{r}, \mathbf{r}')$ and the noninteracting density-response function $\chi^0(\mathbf{r}, \mathbf{r}'; \omega)$, respectively:

$$v_{\mathbf{q}+\mathbf{G}} = \frac{4\pi}{|\mathbf{q}+\mathbf{G}|^2} \tag{42}$$

and

$$\chi^0_{\mathbf{G},\mathbf{G}'}(\mathbf{q}, \omega) = \frac{1}{\Omega}\sum_{\mathbf{k}}^{BZ}\sum_{n,n'}(f_{\mathbf{k},n} - f_{\mathbf{k}+\mathbf{q},n'}) \times \frac{\langle\phi_{\mathbf{k},n}|e^{-i(\mathbf{q}+\mathbf{G})\cdot\mathbf{r}}|\phi_{\mathbf{k}+\mathbf{q},n'}\rangle\langle\phi_{\mathbf{k}+\mathbf{q},n'}|e^{i(\mathbf{q}+\mathbf{G}')\cdot\mathbf{r}}|\phi_{\mathbf{k},n}\rangle}{E_{\mathbf{k},n} - E_{\mathbf{k}+\mathbf{q},n'} + \hbar(\omega + i\eta)}, \tag{43}$$

$\phi_{\mathbf{k},n}$ and $E_{\mathbf{k},n}$ being Bloch eigenfunctions and eigenvalues of a three-dimensional Hartree, Kohn–Sham, or quasiparticle Hamiltonian.

The stopping power of a periodic crystal is obtained by first introducing equations (2) and (3) into equation (1), and then introducing equation (1) into equation (6). Within linear-response theory, i.e., to first order in the external perturbation, the result is of the form of equation (14) with the energy loss per unit path length being given by the following expression

$$\left[-\frac{dE}{dx}\right]_{\mathbf{b}} = -\frac{2Z_1^2}{v\Omega}\sum_{\mathbf{q}}^{BZ}\sum_{\mathbf{G}}\sum_{\mathbf{G}'_\perp}\omega\, e^{i\mathbf{G}'_\perp\cdot\mathbf{b}}v_{\mathbf{q}+\mathbf{G}+\mathbf{G}'_\perp}\,\mathrm{Im}\,K_{\mathbf{G},\mathbf{G}+\mathbf{G}'_\perp}(\mathbf{q}, \omega), \tag{44}$$

where $\mathbf{b}$ is the impact vector of the projectile, the sum $\sum_{\mathbf{G}'_\perp}$ is restricted to those reciprocal-lattice vectors that are perpendicular to the projectile velocity ($\mathbf{G}'_\perp \cdot \mathbf{v} = 0$), $\omega = (\mathbf{q} + \mathbf{G}) \cdot \mathbf{v}$, and $K_{\mathbf{G},\mathbf{G}'}(\mathbf{q}, \omega)$ represent the Fourier coefficients of the inverse dielectric function $K(\mathbf{r}, \mathbf{r}'; \omega)$:

$$K_{\mathbf{G},\mathbf{G}'}(\mathbf{q}, \omega) = \delta_{\mathbf{G},\mathbf{G}'} + v_{\mathbf{q}+\mathbf{G}} \chi_{\mathbf{G},\mathbf{G}'}(\mathbf{q}, \omega). \tag{45}$$

The stopping power of equation (44) is the so-called position-dependent stopping power. The most important contribution to this quantity is provided by the term $\mathbf{G}'_\perp = 0$, the magnitude of the other terms depending on the direction of the velocity. For a few highly symmetric or *channeling* directions nonnegligible corrections to the $\mathbf{G}'_\perp = 0$ contribution are found, thus exhibiting the characteristic anisotropy of the position-dependent stopping power. However, for those directions for which the condition $\mathbf{G}'_\perp \cdot \mathbf{v} = 0$ is never satisfied, only the $\mathbf{G}'_\perp = 0$ term contributes and one finds

$$\left[-\frac{\mathrm{d}E}{\mathrm{d}x} \right]_{\text{random}} = -\frac{2Z_1^2}{v\Omega} \sum_{\mathbf{q}}^{\text{BZ}} \sum_{\mathbf{G}} \omega v_{\mathbf{q}+\mathbf{G}} \, \text{Im} \, K_{\mathbf{G},\mathbf{G}}(\mathbf{q}, \omega). \tag{46}$$

This is the so-called random stopping power, which is also obtained as the average over impact parameters of the position-dependent stopping power of equation (44). For simple metals like Al the diagonal elements of the inverse dielectric matrix $K_{\mathbf{G},\mathbf{G}}(\mathbf{q}, \omega)$ are rather isotropic, in which case there is little dependence of the random stopping power on the direction of the projectile velocity.

3. RESULTS

In this section, we review existing calculations of the stopping power of both an infinite (uniform) and a semi-infinite (bounded) free gas of interacting electrons, double-plasmon inverse mean free paths, and the linear (lowest-order) first-principles stopping power of real Al and Si. New calculations of the various contributions to the stopping power due to the excitation of e–h pairs and plasmons are also reported, existing double-plasmon calculations are extended to low velocities where both recoil and the probe-particle statistics play a role, and existing first-principles calculations of the stopping power of Al and Si are extended by allowing transitions with large values of the momentum transfer.

3.1. Uniform electron gas

Here we consider a uniform gas of interacting electrons, the electron density n being equal to the average density of valence electrons in aluminum metal ($r_s = 2.07$), for which the Fermi momentum [$q_{\text{F}} = (3\pi^2 n)^{1/3}$] and

bulk plasma frequency $[\omega_p = (4\pi n)^{1/2}]$ are $q_F = 0.927 a_0^{-1}$ and $\omega_p = 15.8$ eV, respectively. We set $Z_1 = 1$ (probe bare protons) for the stopping-power calculations and $Z_1 = -1$ (probe electrons) for the calculations of the double-plasmon inverse mean free path. Our results can then be easily extended to arbitrary values of Z_1, as linear and quadratic contributions to the stopping power and the inverse mean free path are proportional to Z_1^2 and Z_1^3, respectively.

3.1.1. Stopping power

The second-order stopping power of a homogeneous FEG is given by equation (15). In Fig. 1 we show, as a function of the projectile velocity, our full RPA calculations for the separate Z_1^2 and Z_1^3 contributions to the stopping power of equation (15). We note that both Z_1^2 and Z_1^3 contributions to the stopping power exhibit a linear dependence on the projectile velocity up to velocities approaching the stopping maximum. This linear dependence is also exhibited by full nonlinear DFT calculations of the stopping power of a FEG [25] and by recent measurements of the electronic energy loss of protons and antiprotons [13].

The linear dependence of the Z_1^3 contribution to the stopping power is a consequence of two competing effects. On the one hand, there is the effect of one-step single excitations, like those entering the Z_1^2 contribution to the stopping power, but now generated by the quadratically screened potential of

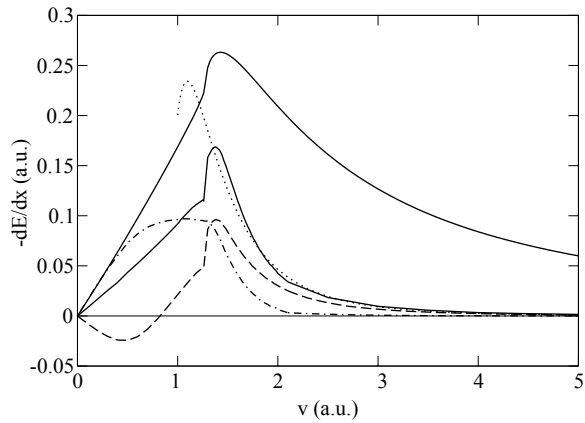

Fig. 1. Solid lines represent RPA Z_1^2 and Z_1^3 contributions to the stopping power of equation (15), for $Z_1 = 1$ and $r_s = 2.07$, as a function of the velocity of the projectile. Dashed and dashed-dotted lines represent the RPA $[-\mathrm{d}E/\mathrm{d}x]^1$ and $[-\mathrm{d}E/\mathrm{d}x]^2$ contributions to the Z_1^3 stopping power, respectively. The dotted line is the high-velocity limit dictated by the second term of equation (20).

the probe particle. On the other hand, there is the effect of second-order two-step single excitations generated by the linearly screened probe potential. In the RPA, these contributions to the Z_1^3 effect are given by the following expressions [29]

$$\left[-\frac{\mathrm{d}E}{\mathrm{d}x}\right]^1 = -\frac{4}{v}Z_1^3\int\frac{\mathrm{d}\mathbf{q}}{(2\pi)^3}\int_0^\infty\frac{\mathrm{d}\omega}{2\pi}\omega v_{\mathbf{q}}\,\mathrm{Im}\,K_{\mathbf{q},\omega}\,\delta(\omega-\mathbf{q}\cdot\mathbf{v})$$
$$\times\int\frac{\mathrm{d}\mathbf{q}_1}{(2\pi)^4}\int_{-\infty}^\infty\frac{\mathrm{d}\omega_1}{2\pi}\mathrm{Re}\,Y^{\mathrm{TO}}_{\mathbf{q},\omega;-\mathbf{q}_1,-\omega_1}v_{\mathbf{q}_1}\,\mathrm{Re}\,K_{\mathbf{q}_1,\omega_1}v_{\mathbf{q}-\mathbf{q}_1}$$
$$\times\,\mathrm{Re}\,K_{\mathbf{q}-\mathbf{q}_1,\omega-\omega_1}\,\delta(\omega_1-\mathbf{q}_1\cdot\mathbf{v}) \tag{47}$$

and

$$\left[-\frac{\mathrm{d}E}{\mathrm{d}x}\right]^2 = -\frac{4}{v}Z_1^3\int\frac{\mathrm{d}\mathbf{q}}{(2\pi)^3}\int_0^\infty\frac{\mathrm{d}\omega}{2\pi}\omega v_{\mathbf{q}}\,\mathrm{Re}\,K_{\mathbf{q},\omega}\,\delta(\omega-\mathbf{q}\cdot\mathbf{v})$$
$$\times\int\frac{\mathrm{d}\mathbf{q}_1}{(2\pi)^4}\int_{-\infty}^\infty\frac{\mathrm{d}\omega_1}{2\pi}H_{\mathbf{q},\omega;-\mathbf{q}_1,-\omega_1}v_{\mathbf{q}_1}\,\mathrm{Re}\,K_{\mathbf{q}_1,\omega_1}v_{\mathbf{q}-\mathbf{q}_1}$$
$$\times\,\mathrm{Re}\,K_{\mathbf{q}-\mathbf{q}_1,\omega-\omega_1}\,\delta(\omega_1-\mathbf{q}_1\cdot\mathbf{v}), \tag{48}$$

where $Y^{\mathrm{TO}}_{\mathbf{q},\omega;\mathbf{q}_1,\omega_1}$ is the time-ordered counterpart of the retarded noninteracting quadratic density-response function $Y^0_{\mathbf{q},\omega;\mathbf{q}_1,\omega_1}$, and

$$H_{\mathbf{q},\omega;\mathbf{q}_1,\omega_1} = 2\pi\,\mathrm{sgn}(\omega)P\int\frac{\mathrm{d}^3\mathbf{k}}{(2\pi)^3}f_{\mathbf{k}}\left[\frac{\delta(\omega+\omega_{\mathbf{k}}-\omega_{\mathbf{k}+\mathbf{q}})}{\omega_1+\omega_{\mathbf{k}}-\omega_{\mathbf{k}+\mathbf{q}_1}}\right.$$
$$\left.+\frac{\delta(\omega-\omega_{\mathbf{k}}+\omega_{\mathbf{k}+\mathbf{q}})}{\omega_2-\omega_{\mathbf{k}}+\omega_{\mathbf{k}+\mathbf{q}_2}}\right], \tag{49}$$

with $\mathbf{q}_2=\mathbf{q}-\mathbf{q}_1$ and $\omega_2=\omega-\omega_1$. Double excitations also contribute, within RPA, to the Z_1^3 stopping power of equation (15), but they are found to be zero in the low- and high-velocity limits and small at intermediate velocities.

The RPA $[-\mathrm{d}E/\mathrm{d}x]^1$ and $[-\mathrm{d}E/\mathrm{d}x]^2$ contributions to the stopping power of a FEG are represented in Fig. 1 by dashed and dashed-dotted lines, respectively. The $[-\mathrm{d}E/\mathrm{d}x]^2$ contribution from losses to two-step single excitations (dashed-dotted line) is very small at high projectile velocities where the velocity distribution of target electrons can be neglected. At high velocities, the surviving $[-\mathrm{d}E/\mathrm{d}x]^1$ contribution approaches the total Z_1^3 stopping power, which is very well reproduced by the second term of equation (20) (dotted line of Fig. 1).

Now we focus on the role that the excitation of e–h pairs and plasmons play in the energy loss process. First, we restrict our calculations to the Z_1^2 (linear) contribution to the stopping power of a FEG. Figure 2 exhibits the separate RPA e–h pair and plasmon contributions to the Z_1^2 stopping power

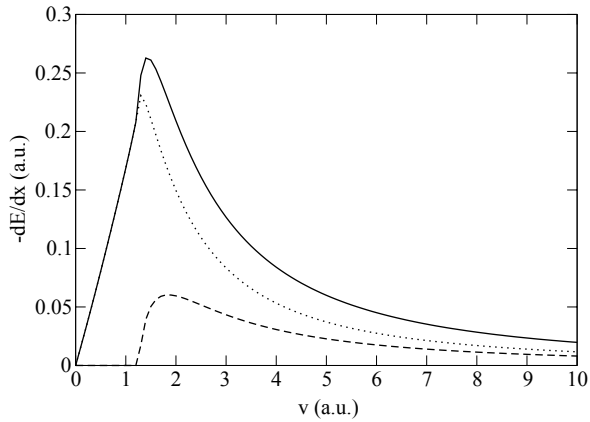

Fig. 2. The solid line represents the RPA Z_1^2 (linear) contribution to the stopping power of equation (15), for $Z_1 = 1$ and $r_s = 2.07$, as a function of the velocity of the probe particle. Dashed and dotted lines represent contributions from the excitation of plasmons and e–h pairs, respectively.

of equation (15). This figure shows that the contribution from losses to plasmons is smaller for all projectile velocities than the contribution from losses to e–h pairs, which is especially true at high electron densities, although both contributions coincide in the high-velocity limit. This is the equipartition rule, which appears straightforwardly in the static-electron gas approximation. In this approximation, plasmon and e–h pair contributions to the energy loss are typically separated according to whether the momentum transfer is below ($q < q_c$) or above ($q > q_c$) the critical momentum q_c where the plasmon dispersion enters the e–h pair excitation spectrum. For an electron gas not at rest, the equipartition rule was formulated by Lindhard and Winther [62].

For a momentum transfer that is smaller than q_c, both plasmon and e–h pair excitations contribute to the full RPA energy loss, though contributions from losses due to the excitation of e–h pairs are very small. For $q > q_c$, however, only e–h pair excitations contribute. This is illustrated in Fig. 3, where the total Z_1^2 stopping power is separated according to whether losses correspond to momentum transfers below ($q < q_c$) or above ($q > q_c$) the critical momentum q_c. In Fig. 4, the total Z_1^2 stopping power is separated according to whether losses come from momentum transfers below ($q < \sqrt{2\omega_p}$) or above ($q > \sqrt{2\omega_p}$) the critical momentum $\sqrt{2\omega_p}$, which is the low-density limit of q_c. In this case, there is exact equipartition for all velocities above the stopping maximum. This equipartition is also found to be exact in the high-velocity limit, by using Coulomb scattering of independent electrons with $q_{min} = \omega_p/v$ or by assuming that independent electrons are

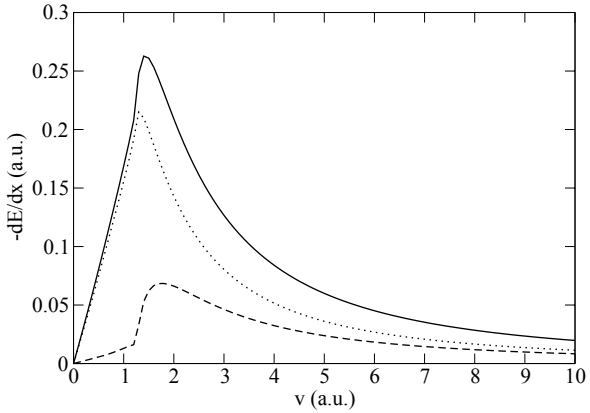

Fig. 3. The solid line represents the RPA Z_1^2 (linear) contribution to the stopping power of equation (15), for $Z_1 = 1$ and $r_s = 2.07$, as a function of the velocity of the probe particle. Dashed and dotted lines represent contributions from momentum transfers below ($q < q_c$) and above ($q > q_c$) the critical momentum q_c where the plasmon dispersion enters the e–h pair continuum.

scattered by a velocity-dependent Yukawa potential with screening length proportional to ω_p/v.

While the RPA $[-dE/dx]^2$ contribution to the Z_1^3 stopping power (see equation (48)) is entirely due to the excitation of e–h pairs, the $[-dE/dx]^1$ contribution to the Z_1^3 stopping power is originated in the excitation of both e–h pairs and plasmons. Hence, we have split $[-dE/dx]^1$ into these

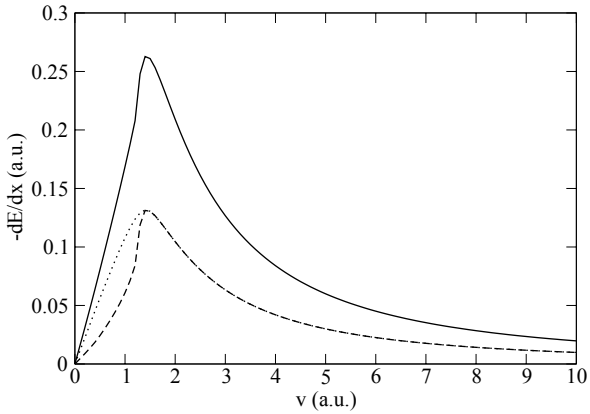

Fig. 4. As in Fig. 3, but with the actual critical momentum q_c replaced by its low-density limit: $q_c \to \sqrt{2\omega_p}$.

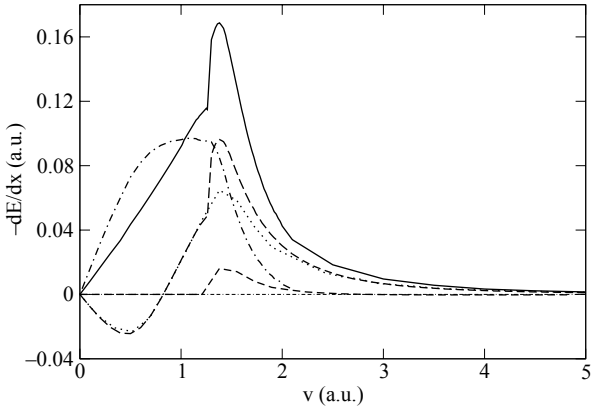

Fig. 5. The solid line represents the RPA Z_1^3 (quadratic) contribution to the stopping power of equation (15), for $Z_1 = 1$ and $r_s = 2.07$, as a function of the velocity of the probe particle. Long-dashed and dashed-dotted lines represent the RPA $[-\mathrm{d}E/\mathrm{d}x]^1$ and $[-\mathrm{d}E/\mathrm{d}x]^2$ contributions to the Z_1^3 stopping power, respectively. Short-dashed and dotted lines represent contributions to $[-\mathrm{d}E/\mathrm{d}x]^1$ from the excitation of plasmons and e–h pairs, respectively.

contributions and have found the result shown in Fig. 5 by dotted and short-dashed lines, respectively. This figure shows that contributions to the Z_1^3 effect coming from losses to plasmons is relatively smaller than in the case of the Z_1^2 term (see Fig. 2), especially at high velocities. Hence, collective excitations appear to be reasonably well described with the use of linearly screened projectile potentials. The equipartition rule, valid within first-order perturbation (linear-response) theory cannot be extended to higher orders in the external perturbation.

In order to account approximately for the Z_1^3 effect coming from both the conduction band and the inner shells, a local-plasma approximation was used in Ref. [16], by assuming that a local Fermi energy can be attributed to each element of the solid. The experimental differences between the stopping power of silicon for high-velocity protons and antiprotons [12] were successfully explained in this way. Proton and antiproton stopping powers of a variety of solid targets have been reported recently for projectile velocities near and below the stopping maximum [13]. A comparison of our theory with these experiments requires the inclusion of charge-exchange processes, xc effects, and higher-order nonlinear terms. Work in this direction is now in progress [63].

3.1.2. Double-plasmon excitation

Single-plasmon contributions to the electron inelastic mean free path of swift electrons have been calculated for many years, both in the high-velocity limit

[64] and in the full RPA [65]. Calculations of the double-plasmon contribution to the electron inverse mean free path have been reported in Refs. [19–21]. Figure 6 shows our full RPA calculation of the double-plasmon inverse mean free path of swift electrons (solid line) interacting with a FEG, as obtained after introducing equation (28) into equation (27). Also shown in this figure is the double-plasmon inverse mean free path of swift positrons (dashed line), as obtained by simply removing the step function of equation (28), and the high-velocity limit dictated by equation (29) multiplied by a factor of 2.16 (dotted line), i.e.,

$$\lambda_{2p}^{-1} \approx 3.13 \times 10^{-3} \frac{\sqrt{r_s}}{v^2}. \tag{50}$$

At high velocities of the projectile the zero-point motion of the target can be neglected. Hence, at these velocities the effect of the Pauli restriction, which only applies to electron probes, is negligible, and the behavior of the double-plasmon inverse mean free path is independent of the particle statistics. On the other hand, it is interesting to notice that the high-velocity formula of equation (50) gives an excellent account of the full RPA result for both probe electrons and positrons in a wide range of projectile velocities. In particular, for Al and a probe-electron energy of 40 keV, equation (50) yields a ratio for the double relative to the single plasmon inverse mean free path of 1.9×10^{-3}, in agreement with experiment [18].

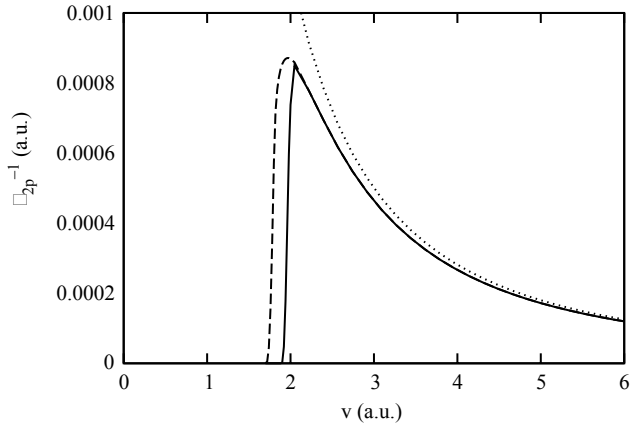

Fig. 6. RPA double-plasmon inverse mean free paths of electrons (solid line) and positrons (dashed line) for $r_s = 2.07$, *versus* the velocity of the projectile, as obtained from equations (27) and (28) by either including (electrons) or excluding (positrons) the step function $\Theta(\omega_{\mathbf{v}-\mathbf{q}} - \varepsilon_{\mathrm{F}})$. The dotted line is the high-velocity limit dictated by equation (50).

3.2. Bounded electron gas

First, we consider a jellium slab of thickness a normal to the z-axis, consisting of a fixed uniform positive background of density

$$n_+(z) = \begin{cases} \bar{n}, & -a \le z \le 0 \\ 0, & \text{elsewhere,} \end{cases} \tag{51}$$

plus a neutralizing cloud of interacting electrons of density $n(z)$. The positive-background charge density $\bar{n}$ is expressed in terms of the Wigner radius r_s [$1/\bar{n} = (4\pi/3)(r_s a_0)^3$], which we take to be $r_s = 2.07$.

To compute the interacting RPA density-response function of equation (32), we follow the method described in Ref. [66]. We first assume that $n(z)$ vanishes at a distance z_0 from either jellium edge [67], and expand the wave functions $\phi_i(z)$ in a Fourier sine series. We then introduce a double-cosine Fourier representation for the density-response function, and find explicit expressions for the stopping power of equation (36) in terms of the Fourier coefficients of the density-response function [57]. We take the wave functions $\phi_i(z)$ to be the eigenfunctions of a one-dimensional local-density approximation (LDA) Hamiltonian with use of the Perdew–Zunger parametrization [68] of the Quantum Monte Carlo xc energy of a uniform FEG [69].

Finally, the stopping power of a semi-infinite FEG is obtained with the use of the following relation

$$-\frac{dE}{dx} = \frac{[-dE/dx](a_n^-) + [-dE/dx](a_n) + [-dE/dx](a_n^+)}{3}, \tag{52}$$

where a_n is the threshold width for which the nth subband for the z motion is first occupied, $a_n^- = a_n - \lambda_F/4$, and $a_n^+ = a_n + \lambda_F/4$, $\lambda_F = 2\pi/(3\pi^2\bar{n})^{1/3}$ being the Fermi wavelength [70]. Converged results have been found with the use of slabs with $n = 12$, for which $a \approx 5-6\lambda_F$.

Figure 7 depicts our full RPA calculation of the stopping power of a semi-infinite FEG, as obtained from equation (36) for protons ($Z_1 = 1$) moving with speed $v = 2v_0$ parallel to the surface. In the interior of the solid, where the electron density is taken to be constant, the stopping power coincides with the Z_1^2 (linear) RPA stopping power of a uniform FEG (see Fig. 1). Outside the solid, the stopping power decreases with the distance z between the surface and the probe-particle trajectory. Also plotted in Fig. 7 is the result of assuming that the stopping power for a charged particle that moves at a distance z from the surface can be approximated by that of a uniform electron gas with the local density $n(z)$ [71]. Figure 7 clearly shows that this often-used LDA yields an inaccurate description of the position-dependent stopping power, due to the intrinsic nature of surface-induced single and collective excitations not present within this approach.

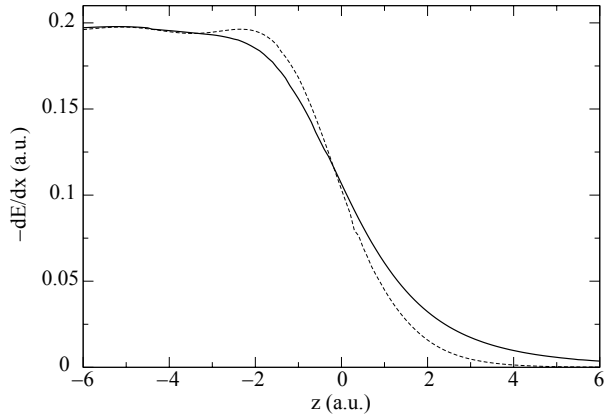

Fig. 7. The solid line represents the RPA stopping power of equation (36) for $Z_1 = 1$, $r_s = 2.07$, and $v = 2v_0$, as a function of the distance z between the surface and the projectile. The solid is in the region $z < 0$. The dashed line represents the LDA stopping power, as obtained by assuming that the actual stopping power of equation (36) can be approximated by that of a uniform FEG with the local density $n(z)$.

As the velocity increases, the energy-loss spectrum of charged particles moving far from the surface into the vacuum is dominated by long-wavelength excitations. In this limit, equation (36) yields the classical stopping power dictated by equation (38). This is illustrated in Fig. 8, where

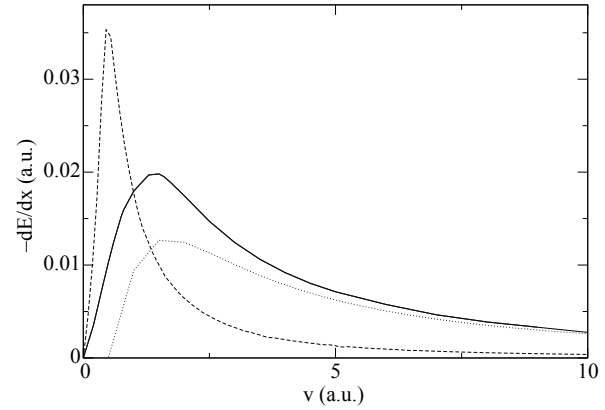

Fig. 8. The solid line represents the RPA stopping power of equation (36) for $Z_1 = 1$, $r_s = 2.07$, and $z = 3a_0 \approx \lambda_F/2$, as a function of the projectile velocity. The dashed line represents the LDA stopping power, as obtained by assuming that the actual stopping power of equation (36) can be approximated by that of a uniform FEG with the local density $n(z)$. The dotted line is the high-velocity limit dictated by equation (38).

the velocity-dependent RPA stopping power of equation (36) is represented together with the classical result (see equation (38)) for a proton ($Z_1 = 1$) moving in the vacuum at a constant distance $z = 3a_0 \approx \lambda_F/2$ from the surface. At low velocities, the energy-loss spectrum is dominated by intermediate- and short-wavelength excitations, even far from the surface into the vacuum, and a combination of the actual electronic selvage at the surface with the intrinsic nature of surface-induced excitations increases the energy loss with respect to that predicted by equation (38). At high velocities, the energy-loss spectrum is dominated by surface-plasmon excitations and the full RPA stopping power nicely converges with the classical result. As in Fig. 7, the LDA is also represented in this figure, showing that this often-used approximation cannot account for the energy loss originated in surface-induced excitations, not even at low velocities where the energy loss is entirely due to the excitation of e–h pairs.

3.3. Periodic crystals

In the case of periodic crystals, we first expand the one-electron $\phi_{\mathbf{k},n}(\mathbf{r})$ eigenfunctions in a plane-wave basis,

$$\phi_{\mathbf{k},n}(\mathbf{r}) = \frac{1}{\sqrt{\Omega}} \sum_{\mathbf{G}} u_{\mathbf{k},n}(\mathbf{G}) e^{i(\mathbf{k}+\mathbf{G})\cdot\mathbf{r}}, \tag{53}$$

with a kinetic-energy cut-off that varies from 12 Ry in the case of Al (~ 100 **G**-vectors) to 16 Ry in the case of Si (~ 300 **G**-vectors). The coefficients $u_{\mathbf{k},n}$ are evaluated by solving the Kohn–Sham equation of DFT in the LDA with use of the Perdew–Zunger parametrization [68] of the Quantum Monte Carlo xc energy of a uniform FEG [69]. The electron–ion interaction is based on the use of an *ab initio* nonlocal, norm-conserving ionic pseudopotential [72]. Then, equation (43) is used to evaluate the Fourier coefficients of the noninteracting density-response function, and a matrix equation (equation (41)) is solved for the Fourier coefficients of the interacting RPA density-response function.

Here we present new calculations for the random stopping power of Al and Si, which represent an extension of existing first-principles calculations [38,40] by allowing transitions with large values of the momentum transfer.

3.3.1. Random stopping power

Figure 9 shows our first-principles first-order (linear-response) RPA calculation of the random stopping power of valence electrons in Al (solid circles) and Si (open circles) for protons and antiprotons ($Z_1^2 = 1$), as obtained from equation (46) [73]. Since the electron density of valence electrons in Al ($r_s = 2.07$) and Si ($r_s = 2.01$) is nearly the same, within

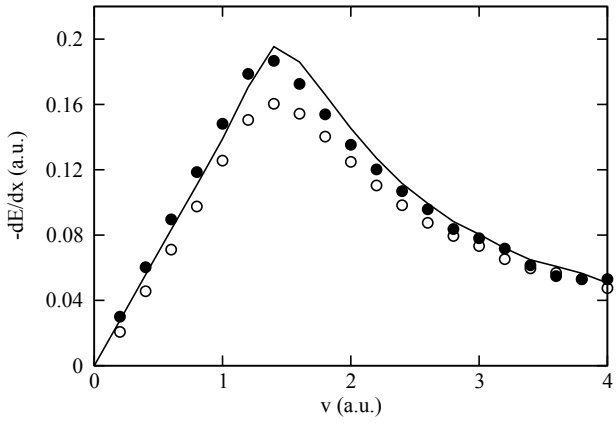

Fig. 9. First-principles RPA calculation of the random stopping power of valence electrons in Al (solid circles) and Si (open circles) for protons and antiprotons ($Z_1^2 = 1$), *versus* the projectile velocity, as obtained from equation (46). These results have been found to be rather insensitive to the choice of the direction of the projectile velocity. The solid line represents the Z_1^2 (linear) stopping power of a uniform FEG with $r_s = 2$.

a FEG model of the solid the stopping powers of Al and Si are expected to coincide (solid line of Fig. 9). Nevertheless, our first-principles calculations indicate that this is not the case. At low-projectile velocities (where only valence electrons contribute to the energy loss of the projectile), the stopping power of Si is considerably smaller than that of Al, in agreement with available measurements of the stopping power of this materials for either protons [74,75] and antiprotons [13]. While the stopping power of Al is found to be slightly larger than in the case of a FEG, the band gap of Si yields a stopping power of this material that is smaller than in the case of a FEG.

At high velocities, well above the stopping maximum, the sum over the frequency ω in equation (46) can be replaced by an integration over all positive frequencies, and the sum rule

$$\int_0^\infty \mathrm{d}\omega\, \omega\, \mathrm{Im}\, K^{-1}_{\mathbf{G},\mathbf{G}'}(\mathbf{q},\omega) = 2\pi^2 n_{\mathbf{G}-\mathbf{G}'} \tag{54}$$

($n_{\mathbf{G}}$ represents the Fourier components of the density, $n_{\mathbf{G}=0}$ being the average electron density n of the crystal) yields a stopping power which depends on n, but not on the details of the band-structure of the target material:

$$\left[-\frac{\mathrm{d}E}{\mathrm{d}x}\right]_{\mathrm{random}} \sim \frac{4\pi Z_1^2}{v^2} n \ln \frac{2v^2}{\omega_{\mathrm{p}}}. \tag{55}$$

Hence, at high velocities the stopping powers of valence electrons in Al and Si both coincide with that of a FEG with the same electron density (see Fig. 9).

While at low velocities the contribution to the total energy loss due to excitation of inner-shell electrons is negligible, at velocities larger than the Fermi velocity it is necessary to allow for this contribution. The cross-sections for the ionization of inner shells in Al were obtained by Ashley *et al.* [76] in the first-Born approximation utilizing atomic generalized oscillator strength functions. By adding the contribution from core electrons to that of valence electrons (this contribution was calculated within a FEG model of the solid) these authors found a nice agreement with experiment. Good agreement with experiment was also shown in Ref. [2] by adding to the valence-electron energy loss of a FEG with $r_s = 2.01$ the energy loss from core electrons in Si as taken from Walske's calculations [77].

4. SUMMARY AND CONCLUSIONS

We have presented a survey of current investigations of various aspects of the interaction of charged particles with solids.

In the framework of many-body perturbation theory, we have studied the nonlinear interaction of charged particles with a free gas of interacting electrons. We have presented general procedures to calculate the nonlinear potential induced by charged particles moving in an inhomogeneous electron system, the Z_1^3 contribution to the stopping power of a FEG, and double-plasmon excitation probabilities.

Our calculations for the RPA stopping power of a FEG indicate that for velocities smaller than the Fermi velocity the stopping power is, up to third order in the projectile charge, a linear function of the velocity of the projectile. Our calculations also indicate that the high-velocity limit dictated by equation (20) gives an excellent account of the full RPA result in a wide range of projectile velocities. By assuming that a local Fermi energy can be attributed to each element of the solid target, the experimental differences between the stopping power of silicon for high-velocity protons and antiprotons [12] were successfully explained in Ref. [16].

New calculations of the various contributions to the second-order stopping power of a uniform FEG coming from the excitation of e–h pairs and plasmons have been reported. We have found that the equipartition rule, valid within first-order perturbation (linear-response) theory, cannot be extended to higher orders in the external perturbation. We have also found that contributions from collective excitations to the Z_1^3 term are small.

New RPA double-plasmon inverse mean free paths of electrons and positrons have been evaluated, with explicit introduction of recoil and probe-particle statistics. The high-velocity limit of equation (50) is found to give

an excellent account of the full RPA double-plasmon inverse mean free paths in a wide range of projectile velocities. This formula (equation (50)) yields for Al and a probe-electron energy of 40 keV a ratio for the double relative to the single plasmon inverse mean free path of 1.9×10^{-3}, in agreement with experiment [18].

We have reviewed existing self-consistent calculations of the energy loss of charged recoiless particles moving parallel to a plane-bounded FEG, in the framework of linear response theory. In the high-velocity limit and for charged particles moving far from the surface into the vacuum the actual stopping power is found to converge with the classical limit dictated by equation (38). However, at low-intermediate velocities substantial changes in the stopping power are observed as a realistic description of the surface response is considered, which leads to the conclusion that a self-consistent description of the surface response is necessary if one is to look at the energy loss of charged particles moving outside a solid surface. Accurate measurements of the energy loss of protons being reflected from a variety of solid surfaces at grazing incidence have been reported [78–80]. A theoretical description of these experiments requires that the ion trajectory $z(t)$ be calculated and energy losses from the excitation of inner shells be taken into account. Work in this direction is now in progress.

Finally, we have extended existing first-principles calculations of the random stopping power of valence electrons in Al and Si by allowing transitions to larger values of the momentum transfer. We have found that at low velocities (where losses from the excitation of inner shells is negligible) the random stopping power of Si is considerably smaller than that of Al, though both Al and Si have nearly the same valence-electron density. At high velocities, band-structure effects become negligible and the random stopping power of valence electrons in Al and Si nearly coincide.

A quantitative comparison of our theory with existing measurements of the energy loss of antiprotons [13] (which unlike protons carry no bound states) in a variety of target materials can be achieved by combining our first-principles calculations of the Z_1^2 (linear-response) stopping power with Z_1^3 corrections in a FEG. Nevertheless, a comparison with experiment still requires the inclusion of losses from the inner shells, xc effects, and higher-order nonlinear terms. Work in this direction is now in progress.

ACKNOWLEDGEMENTS

We acknowledge partial support by the University of the Basque Country, the Basque Unibertsitate eta Ikerketa Saila, and the Spanish Ministerio de Ciencia y Tecnología.

REFERENCES

[1] P. M. Echenique and F. Flores, *Solid State Phys.*, 1990, **43**, 229.
[2] M. A. Kumakhov and F. F. Komarov, *Energy Loss and Ion Rangesin Solids*, Gordon & Breach, New York, 1981.
[3] N. Bohr, *Phil. Mag.*, 1913, **25**, 10; 1915, **30**, 581.
[4] H. A. Bethe, *Ann. Phys. (Leipzig)*, 1930, **5**, 325.
[5] D. Bohm and D. Pines, *Phys. Rev.*, 1951, **82**, 625; D. Pines and D. Bohm, *Phys. Rev.*, 1952, **85**, 338; D. Bohm and D. Pines, *Phys. Rev.*, 1953, **92**, 609; D. Pines, *Phys. Rev.*, 1953, **92**, 626.
[6] J. Lindhard and K. Dan, *Vidensk. Selsk. Mat.-Fys. Medd.*, 1954, **28** (8).
[7] J. Hubbard, *Proc. Phys. Soc. (London)*, 1957, **243**, 336.
[8] K. S. Singwi, M. P. Tosi, R. H. Land and A. Sjolander, *Phys. Rev.*, 1968, **176**, 589; K. S. Singwi, A. Sjolander, M. P. Tosi and R. H. Land, *Phys. Rev. B*, 1970, **1**, 1044; K. S. Singwi and M. P. Tosi, *Solid State Phys.*, 1981, **36**, 177.
[9] S. L. Adler, *Phys. Rev.*, 1962, **126**, 413; N. Wiser, *Phys. Rev.*, 1963, **129**, 62.
[10] N. D. Mermin, *Phys. Rev. B*, 1970, **1**, 2362.
[11] W. H. Barkas, W. Birnbaum and F. M. Smith, *Phys. Rev.*, 1956, **101**, 778; W. H. Barkas, N. J. Dyer and H. H. Heckman, *Phys. Rev. Lett.*, 1963, **11**, 26; W. H. Barkas, N. J. Dyer and H. H. Heckman, *Phys. Rev. Lett.*, 1963, **11**, 138(E).
[12] L. H. Andersen, P. Hvelplund, H. Knudsen, S. P. Moller, J. O. P. Pedersen, E. Uggerhoj, K. Elsener and E. Morenzoni, *Phys. Rev. Lett.*, 1989, **62**, 1731.
[13] S. P. Moller, E. Uggerhoj, H. Bluhme, H. Knudsen, U. Mikkelsen, K. Paludan and E. Morenzoni, *Phys. Rev. A*, 1997, **56**, 2930; S. P. Moller, A. Csete, T. Ichioka, H. Knudsen, U. I. Uggerhoj and H. H. Andersen, *Phys. Rev. Lett*., 2002, **88**, 193201.
[14] J. C. Ashley, R. H. Ritchie and W. Brandt, *Phys. Rev. B*, 1972, **5**, 2393; J. C. Ashley, R. H. Ritchie and W. Brandt, *Phys. Rev. B*, 1974, **10**, 737.
[15] C. C. Sung and R. H. Ritchie, *Phys. Rev. A*, 1983, **28**, 674; C. D. Hu and E. Zaremba, *Phys. Rev. B*, 1988, **37**, 9268; H. Mikkelsen and P. Sigmund, *Phys. Rev. A*, 1989, **40**, 101; H. Esbensen and P. Sigmund, *Ann. Phys.*, 1990, **201**, 152.
[16] J. M. Pitarke, R. H. Ritchie and P. M. Echenique, *Nucl. Instrum. Methods B*, 1993, **79**, 209; J. M. Pitarke, R. H. Ritchie, P. M. Echenique and E. Zaremba, *Europhys. Lett.*, 1993, **24**, 613.
[17] J. C. Spence and A. E. Spargo, *Phys. Rev. Lett.*, 1971, **26**, 895.
[18] P. Schattschneider, F. Fodermayr and D. S. Su, *Phys. Rev. Lett.*, 1987, **59**, 724.
[19] J. C. Ashley and R. H. Ritchie, *Phys. Status Solidi*, 1970, **38**, 425.
[20] J. M. Pitarke and R. H. Ritchie, *Nucl. Instrum. Methods B*, 1994, **90**, 358.
[21] I. Campillo and J. M. Pitarke, *Nucl. Instrum. Methods B*, 1996, **115**, 75. Equation (10) here replaces equation (23) of Ref. [20].
[22] A. Arnau and E. Zaremba, *Nucl. Instrum. Methods B*, 1994, **90**, 32; J. J. Dorado, O. H. Crawford and F. Flores, *Nucl. Instrum. Methods B*, 1994, **93**, 175, erratum, *Nucl. Instrum. Methods B*, 1995, **95**, 144.
[23] J. M. Pitarke, A. Bergara and R. H. Ritchie, *Nucl. Instrum. Methods B*, 1995, **99**, 87; A. Bergara and J. M. Pitarke, *Nucl. Instrum. Methods B*, 1995, **96**, 604; A. Bergara, I. Campillo, J. M. Pitarke and P. M. Echenique, *Phys. Rev. B*, 1997, **56**, 15654.
[24] M. J. Puska and R. M. Nieminen, *Phys. Rev. B*, 1983, **27**, 6121.
[25] P. M. Echenique, R. M. Nieminen and R. H. Ritchie, *Solid State Commun.*, 1981, **37**, 779; P. M. Echenique, R. M. Nieminen, J. C. Ashley and R. H. Ritchie, *Phys. Rev. A*, 1986, **33**, 897; J. C. Ashley, R. H. Ritchie, P. M. Echenique and R. M. Nieminen, *Nucl. Instrum. Methods B*, 1986, **15**, 11.
[26] P. Hohenberg and W. Kohn, *Phys. Rev.*, 1964, **136**, B864; W. Kohn, L. J. Sham, *Phys. Rev*., 1965, **140**, A1133.

[27] E. Zaremba, A. Arnau and P. M. Echenique, *Nucl. Instrum. Methods B*, 1995, 96.
[28] W. Brandt and M. Kitagawa, *Phys. Rev. B*, 1982, **25**, 5631.
[29] J. M. Pitarke, R. H. Ritchie and P. M. Echenique, *Phys. Rev. B*, 1995, **52**, 13883.
[30] F. F. Komarov and M. A. Kumakhov, *Radiat. Effects*, 1974, **22**, 1.
[31] A. Desalvo and R. Rosa, *J. Phys. C*, 1977, **10**, 1595.
[32] H. Esbensen and J. A. Golovchenko, *Nucl. Phys. A*, 1978, **298**, 382.
[33] A. F. Burenkov, F. F. Komarov and M. A. Kumakhov, *Phys. Status Solidi B*, 1980, **99**, 417.
[34] O. H. Crawford and C. W. Nestor, *Phys. Rev. A*, 1983, **28**, 1260.
[35] P. L. Grande and G. Schiwietz, *Phys. Lett. A*, 1992, **163**, 439.
[36] J. J. Dorado and F. Flores, *Phys. Rev. A*, 1993, **47**, 3062.
[37] T. M. H. E. Tielens, G. E. W. Bauer and T. H. Stoof, *Phys. Rev. B*, 1994, **49**, 5741.
[38] I. Campillo, J. M. Pitarke, A. G. Eguiluz and A. García, *Nucl. Instrum. Methods B*, 1998, **135**, 103; I. Campillo, J. M. Pitarke and A. G. Eguiluz, *Phys. Rev. B*, 1998, **58**, 10307.
[39] R. J. Mathar, J. R. Sabin and S. B. Trickey, *Nucl. Instrum. Methods B*, 1999, **155**, 249.
[40] J. M. Pitarke and I. Campillo, *Nucl. Instrum. Methods B*, 2000, **164**, 147; I. Campillo and J. M. Pitarke, *Nucl. Instrum. Methods B*, 2000, **164**, 161.
[41] This approximation is valid for heavy charged particles, e.g., ions, and also for swift electrons moving with velocities that are large compared to those of the electrons in the medium. In the case of electrons, $Z_1 = -1$.
[42] F. Flores and F. García Moliner, *Introduction to the Theory of Solid Surfaces*, Cambridge University Press, Cambridge, 1979.
[43] T. del Río and J. M. Pitarke, *Phys. Rev. B*, 2000, **62**, 6862.
[44] T. del Río and J. M. Pitarke, *J. Phys. A*, 2001, **34**, 7607.
[45] V. U. Nazarov and S. Nishigaki, *Phys. Rev. B*, 2002, **65**, 94303.
[46] M. Petersilka, U. J. Gossmann and E. K. U. Gross, *Phys. Rev. Lett.*, 1996, **76**, 1212.
[47] A. L. Fetter and J. D. Wallecka, *Quantum Theory of Many Particle Systems*, McGraw-Hill, New York, 1964.
[48] R. M. Dreizler and E. K. U. Gross, *Density Functional Theory*, Springer, Berlin, 1990.
[49] F. Aryasetiawan and O. Gunnarsson, *Rep. Prog. Phys.*, 1998, **61**, 237.
[50] M. Nekovee and J. M. Pitarke, *Comput. Phys. Commun.*, 2001, **137**, 123.
[51] In usual practice, all single-particle wave functions and energies are typically obtained by solving the single-particle Kohn–Sham equation of density-functional theory in the so-called local-density approximation (LDA) (see, e.g., Ref. [48]).
[52] R. Cenni and P. Saracco, *Nucl. Phys. A*, 1988, **487**, 279.
[53] C. F. Richardson and N. W. Ashcroft, *Phys. Rev. B*, 1994, **50**, 8170.
[54] G. D. Azevedo, P. L. Grande, M. Behar, J. F. Dias and G. Schiwietz, *Phys. Rev. Lett.*, 2001, **86**, 1482.
[55] The lowest-order double-plasmon Z_1^3 contributions to the inverse mean free path are of third order in the RPA screened interaction $v_{\mathbf{q}} K_{\mathbf{q},\omega}$. Although these contributions to the double-plasmon inverse mean free path are of lower order in $v_{\mathbf{q}} K_{\mathbf{q},\omega}$ than the Z_1^2 contribution of equation (28), which is of fourth order in the RPA screened interaction, they decrease as v^{-5} and are therefore found to be negligible for the velocities of interest.
[56] A. Bergara, J. M. Pitarke and R. H. Ritchie, *Phys. Rev. B*, 1999, **60**, 16176.
[57] A. García-Lekue and J. M. Pitarke, *Phys. Rev. B*, 2001, **64**, 35423; A. García-Lekue and J. M. Pitarke, *Nucl. Instrum. Methods B*, 2001, **182**, 56; A. García-Lekue and J. M. Pitarke, *J. Electron. Spectrosc.*, 2003, **129**, 223.
[58] D. S. Gemmell, *Rev. Mod. Phys.*, 1974, **46**, 129.
[59] R. H. Ritchie, *Phys. Rev.*, 1957, **106**, 874.
[60] A. Liebsch, *Phys. Rev. Lett.*, 1993, **71**, 145; A. Liebsch, *Electronic Excitations at Metal Surfaces*, Plenum Press, New York, 1997.
[61] P. M. Echenique and J. B. Pendry, *J. Phys. C*, 1975, **8**, 2936.

[62] J. Lindhard, A. Winther and K. Dan, *Vidensk. Selsk. Mat.-Fys. Medd.*, 1964, **34** (4).
[63] V. U. Nazarov and J. M. Pitarke, unpublished.
[64] D. Pines, *Phys. Rev.*, 1952, **85**, 931.
[65] C. J. Tung and R. H. Ritchie, *Phys. Rev. B*, 1977, **16**, 4302.
[66] A. G. Eguiluz, *Phys. Rev. Lett.*, 1983, **51**, 1907; A. G. Eguiluz, *Phys. Rev. B*, 1985, **31**, 3303.
[67] z_0 is chosen sufficiently large for the physical results to be insensitive to the precise value employed.
[68] J. Perdew and A. Zunger, *Phys. Rev. B*, 1981, **23**, 5048.
[69] D. M. Ceperley and B. J. Alder, *Phys. Rev. Lett.*, 1980, **45**, 566.
[70] J. M. Pitarke and A. G. Eguiluz, *Phys. Rev. B*, 1998, **57**, 6329; J. M. Pitarke and A. G. Eguiluz, *Phys. Rev. B*, 2001, **63**, 45116.
[71] The use of this local-density approximation, in which one replaces $-(\mathrm{d}E/\mathrm{d}x)(z)$ of equation (36) by the stopping power of a uniform electron gas of density $n(z)$, should not be confused with the use of an LDA xc potential in DFT.
[72] D. R. Hamann, M. Schluter and C. Chiang, *Phys. Rev. Lett.*, 1979, **43**, 1494; D. R. Hamann, *Phys. Rev. B*, 1989, **40**, 2980.
[73] Random stopping powers of valence electrons in Al and Si have been calculated with the integrations over the momentum transfer being extended from 0 to $2.9q_{\mathrm{F}}$ and $2.6q_{\mathrm{F}}$ for Al and Si, respectively.
[74] J. F. Ziegler, J. P. Biersack, U. Littmark, *The Stopping and Range of Ions in Solids*, Pergamon Press, New York, 1985, Vol. 1.
[75] P. Bauer, *Nucl. Instrum. Methods B*, 1990, **45**, 673.
[76] J. C. Ashley, C. J. Tung and R. H. Ritchie, *Surf. Sci.*, 1979, **81**, 409; C. J. Tung, J. C. Ashley and R. H. Ritchie, *Surf. Sci.*, 1979, **81**, 427.
[77] M. C. Walske, *Phys. Rev.*, 1956, **101**, 940.
[78] K. Kimura, M. Hasegawa and M. Mannami, *Phys. Rev. B*, 1987, **36**, 7.
[79] Y. Fuji, S. Fujiwara, K. Narumi, K. Kimura and M. Mannami, *Surf. Sci.*, 1992, **277**, 164; K. Kimura, H. Kuroda, M. Fritz and M. Mannami, *Nucl. Instrum. Methods B*, 1995, **100**, 356.
[80] H. Winter, M. Wilke and M. Bergomaz, *Nucl. Instrum. Methods B*, 1997, **125**, 124.

This Page Intentionally Left Blank

Electronic Stopping and Momentum Density of Diamond from First-Principles Treatment of the Microscopic Dielectric Function

Richard J. Mathar,[1] S. B. Trickey,[2] and John R. Sabin[2]

[1] *Max-Planck Inst. für Astronomie, Heidelberg, Germany*
[2] *Quantum Theory Project, Departments of Physics and Chemistry, University of Florida, Gainesville, FL 32611-8435, USA*

Abstract

We study the dielectric and energy loss properties of diamond *via* first-principles calculation of the (**0**,0)-element ('head' element) of the frequency and wave-vector-dependent dielectric matrix $\varepsilon_{\mathbf{G},\mathbf{G}'}(\mathbf{q}, \omega)$. The calculation uses all-electron Kohn–Sham states in the integral of the irreducible polarizability in the random phase approximation. We approximate the head element of the inverse matrix by the inverse of the calculated head element, and integrate over frequencies and momenta to obtain the electronic energy loss of protons at low velocities. Numerical evaluation for diamond targets predicts that the band gap causes a strong non-linear reduction of the electronic stopping power at ion velocities below 0.2 a.u.

Contents

1. INTRODUCTION

From the beginnings of modern quantum mechanics to the present, scattering methods have played a predominant role. In the case of solids, examples include X-ray diffraction, electron-energy-loss and Auger spectroscopy, angle-resolved photoemission, optical reflectivity and absorption, neutron scattering, and both ion penetration and implantation. The energy loss of ions is particularly interesting. At low incident energies,

ADVANCES IN QUANTUM CHEMISTRY, VOLUME 45
ISSN: 0065-3276 DOI 10.1016/S0065-3276(04)45012-6

the interaction of an ion with a solid is the essence of surface chemistry. At somewhat higher incident energies, implantation takes place. This introduction of structural and/or chemical defects evidently involves at least the lower part of the excited electronic state spectrum of the host material. Further increase of the incident ion energies probes essentially the entire excited spectrum [1–3].

Given both the importance of charged particle scattering in solids and its protean role in the formation of quantum mechanics, it is not surprising that Bohr addressed aspects of the problem several times in his long and illustrious career [4–9]. With respect to this chapter, the first of these is perhaps the most remarkable. For the case of a finite system (atom, molecule, etc.), the energy deposition of an incident ion is determined by the generalized oscillator strength distribution for each state $|n\rangle$

$$f_{0n}(\mathbf{q}) \propto \langle n| \sum_j \mathrm{e}^{\mathrm{i}\mathbf{q}\cdot\mathbf{r}_j} |0\rangle, \tag{1}$$

through the familiar logarithmic mean excitation energy $\ln I = \sum f_{0n} \hbar\omega_n$. As Fano has remarked [10], Bohr managed the remarkable feat – in 1913! – of anticipating the Bethe sum rule for generalized oscillator strengths without having any knowledge of how to calculate them.

Even with the best available methods, for all but the smallest of molecules it is still an almost prohibitively difficult technical task to calculate f_{0n} values over sufficiently large ranges of n and $\mathbf{q}$ to allow one to calculate the proton stopping cross-section [11]. This fact might suggest that detailed first-principles calculation of the proton-stopping cross-section for a periodic solid is unattainable. Such is not the case because, at least in the limit of long-wavelength probes, one can show that $\ln I \propto \int \mathrm{d}\omega\omega(1/\varepsilon(\omega))$ where $\varepsilon(\omega)$ is the frequency-dependent microscopic dielectric function. It is this part of the Bohr tradition of energy-deposition theory that we pursue here by way of modern computational approaches to the microscopic dielectric function.

2. FORMULATION AND METHOD

The specific purpose of this work is to provide a quantitative, first-principles description of the energy deposition by a bare punctiform ion in an insulator. For reasons of scientific as well as technical interest, we pick diamond as the target insulator. The underlying methodological assumptions are the random phase approximation and the use of Kohn–Sham (KS) density functional orbitals as appropriate one-electron functions. A thorough discussion of the underlying approximations (linear response, neglect of channeling and local

field factors, etc.) and details of the implementation are given in Ref. [12]. Here we summarize.

The energy loss per unit path length of a massive, punctiform, charged particle (charge number Z_1) to a target is [12]

$$\frac{\mathrm{d}E}{\mathrm{d}x}(\mathbf{v}) = \frac{(Z_1 e)^2}{4\pi^3 \varepsilon_0 v} \int \mathrm{d}^3 q \, \frac{\mathbf{v}\cdot\mathbf{q}}{q^2} \int_0^\infty \mathrm{d}\omega \, \delta(\omega - \mathbf{q}\cdot\mathbf{v}) \mathrm{Im}\, K_{\mathbf{0},\mathbf{0}}(\mathbf{q}, \omega), \qquad (2)$$

with $\mathbf{v}$ the projectile velocity in the target rest frame, e the elementary charge unit, and ε_0 the vacuum permittivity. For reciprocal lattice vectors $\mathbf{G}$, $K_{\mathbf{0},\mathbf{0}}$ is the $\mathbf{G} = \mathbf{G}' = \mathbf{0}$ ('head') component of the inverse dielectric matrix defined by

$$\sum_{\mathbf{G}'} \varepsilon_{\mathbf{G},\mathbf{G}'}(\mathbf{q}, \omega) K_{\mathbf{G}',\mathbf{G}''}(\mathbf{q}, \omega) = \delta_{\mathbf{G}\mathbf{G}''},$$

with respect to $\varepsilon_{\mathbf{G},\mathbf{G}'}(\mathbf{k}, \omega)$, the wave-vector and frequency-dependent microscopic dielectric matrix. In terms of the irreducible polarizability Π, the dielectric matrix is

$$\varepsilon_{\mathbf{G},\mathbf{G}'}(\mathbf{q}, \omega) = \delta_{\mathbf{G}\mathbf{G}'} - \frac{e^2}{\varepsilon_0 |\mathbf{q} + \mathbf{G}|^2} \Pi(\mathbf{q} + \mathbf{G}, \mathbf{q} + \mathbf{G}', \omega),$$

given in the Random Phase Approximation (RPA) [13] as a sum over all band pairs (ν, ν') and an integral over the first Brillouin zone (BZ)

$$\Pi(\mathbf{q} + \mathbf{G}, \mathbf{q} + \mathbf{G}', \omega) = \sum_{\nu\nu'} \int_{\mathrm{BZ}} \frac{\mathrm{d}^3 k}{(2\pi)^3} \frac{m_{\mathbf{G},\mathbf{q}}^{\nu',\nu^*} m_{\mathbf{G}',\mathbf{q}}^{\nu',\nu} (f_{\nu\mathbf{k}} - f_{\nu'\mathbf{k}+\mathbf{q}})}{\hbar\omega + \mathrm{i}\eta + E_{\nu\mathbf{k}} - E_{\nu'\mathbf{k}+\mathbf{q}}}.$$

$E_{\nu,\mathbf{k}}$ are the band energies, and $f_{\nu,\mathbf{k}}$ are Fermi occupation numbers ($f_{\nu,\mathbf{k}} = 0$ or 2 for $E_{\nu,\mathbf{k}}$ above or below the Fermi energy E_F). The matrix elements in equation (2) are

$$m_{\mathbf{G},\mathbf{q}}^{\nu',\nu} \equiv \langle \nu'\mathbf{k} + \mathbf{q} | \mathrm{e}^{\mathrm{i}(\mathbf{G}+\mathbf{q})\cdot\mathbf{r}} | \nu\mathbf{k} \rangle.$$

We determine the ground-state electronic structure of solids within Density Functional Theory (DFT) and the usual KS variational procedure, all implemented in the computational package GTOFF [14]. The results of the all-electron, full-potential calculations are Bloch eigenfunctions $\varphi_{\nu,\mathbf{k}}(\mathbf{r})$, expressed as linear combinations of Gaussian Type Orbitals (GTOs), and KS eigenvalues $E_{\nu,\mathbf{k}}$.

For convenience in evaluating the required matrix elements, we expand the Bloch functions in a (truncated) plane wave (PW) series,

$$\varphi_{\nu,\mathbf{k}} = \langle \mathbf{r} | \nu\mathbf{k} \rangle = \mathrm{e}^{\mathrm{i}\mathbf{k}\cdot\mathbf{r}} u_{\nu\mathbf{k}}(\mathbf{r}) = \frac{1}{V_\mathrm{UC}} \sum_{\mathbf{G}} \mathrm{e}^{\mathrm{i}(\mathbf{k}+\mathbf{G})\cdot\mathbf{r}} u_{\nu\mathbf{k},\mathbf{G}},$$

Doing so allows representation of $m_{\mathbf{G}}$ as a simple sum over products of expansion coefficients $u_{\nu\mathbf{k},\mathbf{G}}$ [12], where V_{UC} is the volume of a unit cell (UC). The equivalence of the GTO and PW representations is maintained by monitoring the accumulated norm for each $|\nu, \mathbf{k}\rangle$ relative to the exact values,

$$\sum_{\mathbf{G}} |u_{\nu,\mathbf{k},\mathbf{G}}|^2 = V_{\mathrm{UC}}. \tag{3}$$

We subdivide the integration region of the integral (2) into **k**-space tetrahedra. Recursive further subdivision of a given tetrahedron into smaller tetrahedra is done if $f_{\nu\mathbf{k}} - f_{\nu/\mathbf{k}+\mathbf{q}}$ is not constant over all four vertices. Next comes linearization of the product of the matrix elements in the numerator and of the energy denominator inside each tetrahedron for each ω. The resulting approximated integral is evaluated analytically [12].

The product $|\mathbf{q}+\mathbf{G}|^2 \varepsilon_{\mathbf{G},\mathbf{G}'}(\mathbf{q}, \omega)$ is calculated and, in compensation, the term q^2 in the denominator of equation (2) is dropped. The dielectric function is tabulated for **q** commensurate with the uniform mesh of wave vectors used in the underlying GTOFF calculation but covering higher BZs as well as the first. (Values outside the $(\mathbf{q}, \omega)$-meshes are replaced by the vacuum response, $\mathrm{Im}\, K_{\mathbf{0},\mathbf{0}}(\mathbf{q}, \omega) = 0$.) $\mathrm{Im}\, K_{\mathbf{G},\mathbf{G}'}$ is linearized inside each **q**-space tetrahedron. Multiplied by the linear factor $\mathbf{q}\cdot\mathbf{v}$, the integrals (2) over tetrahedra are done analytically, and then summed.

3. DIAMOND

3.1. Basis sets, electron momentum density

We studied diamond at the experimental lattice parameter, $a = 6.74071 a_0$ for the cubic UC (here a_0 denotes 1 bohr). The Moruzzi–Janak–Williams parameterization [15] of the Hedin–Lundqvist local-density approximation (LDA) to the exchange-correlation functional was used. The HL functional combines simplicity with relatively realistic predictions of crystalline properties. Though there are more refined exchange-correlation functionals (e.g., generalized gradient approximations), there is little reason to suppose that they would yield substantially different results.

The choice of basis sets is a particularly important technical issue for this type of calculation. Specifically, the small, highly contracted basis sets such as used in Ref. [16] generally are insufficient to calculate the real parts of dielectric functions and, consequently, the energy loss functions. We started from Partridge's 16s11p set [17], contracted the seven tightest s-functions and the four tightest p-functions, removed the most diffuse s and the two most diffuse p-functions to avoid approximate linear dependencies, and added a full set of three d-functions with exponents equal to those of the

remaining most diffuse p-functions. (Without d-orbitals the total energy would rise by 0.24 eV/atom.) Site centered s- and f-type fitting functions were used with exponents for the s-types as in Ref. [18], and for the f-types $0.5/a_0^2$ and $0.2/a_0^2$ as in Ref. [19]. Space group and lattice type are those of silicon; hence we may refer to a prior GTOFF study [20] for the symmetry properties of the fitting functions.

The density of states (DOS) (see Fig. 1) computed with this 9s6p3d basis (84 basis functions in the primitive UC) is stable up to ≈ 70 eV above the Fermi energy with respect to further de-contraction. Band gaps are too small compared with experiments, as usual for the LDA and known from other DFT calculations on diamond [21]. Note that the error is smaller, roughly 20%, than is often the case and this problem would not be cured by use of a gradient-corrected functional.

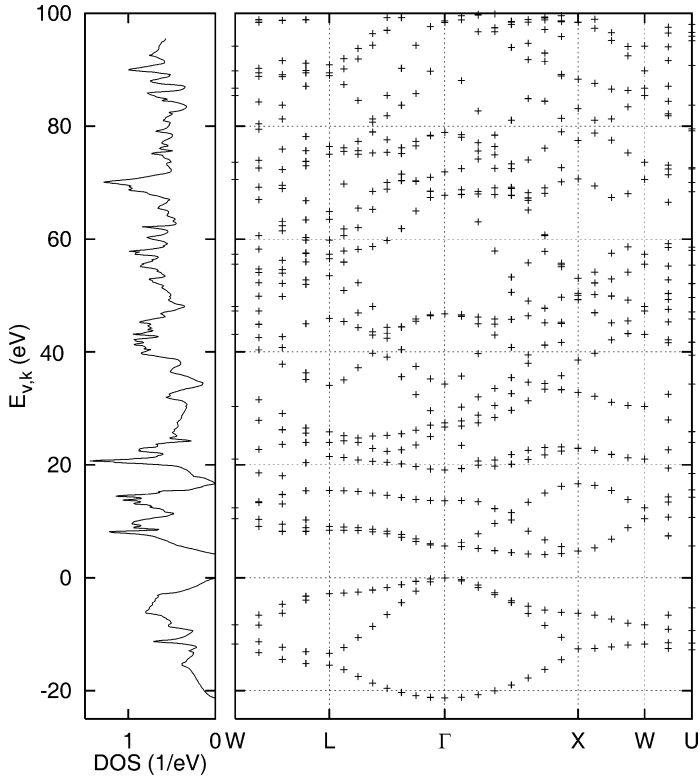

Fig. 1. KS band-structure $E_{\nu,\mathbf{k}}$ using $16 \times 16 \times 16$ **k**-points in the BZ (213 in the IBZ). The direct gap at Γ is 5.59 eV, the indirect gap 4.13 eV, and the width of the four valence bands with eight electrons 21.29 eV. The two bands with four core electrons at -263 eV are not shown [33].

The lowest 24 bands were expanded into 531 PWs, cut off at $|\mathbf{G}| = 7.3/a_0$, with a norm in equation (3) above $0.85V_{\mathrm{UC}}$ for the K-shell electrons (excitations from which were excluded in the subsequent calculations of $\varepsilon_{\mathbf{G},\mathbf{G}'}$ and $\mathrm{d}E/\mathrm{d}x$ anyway), and a norm above $0.98V_{\mathrm{UC}}$ for the remaining 22 bands. The first result is the all-electron momentum density (EMD)

$$\rho(\mathbf{k}+\mathbf{G}) \equiv \frac{1}{V_{\mathrm{UC}}} \sum_{\nu} f_{\nu,\mathbf{k}} |u_{\nu,\mathbf{k},\mathbf{G}}|^2,$$

shown in Fig. 2.

The values near zero momentum $\mathbf{k}+\mathbf{G}=0$ are contributions from the states with long wavelengths and reveal the macroscopic symmetry of

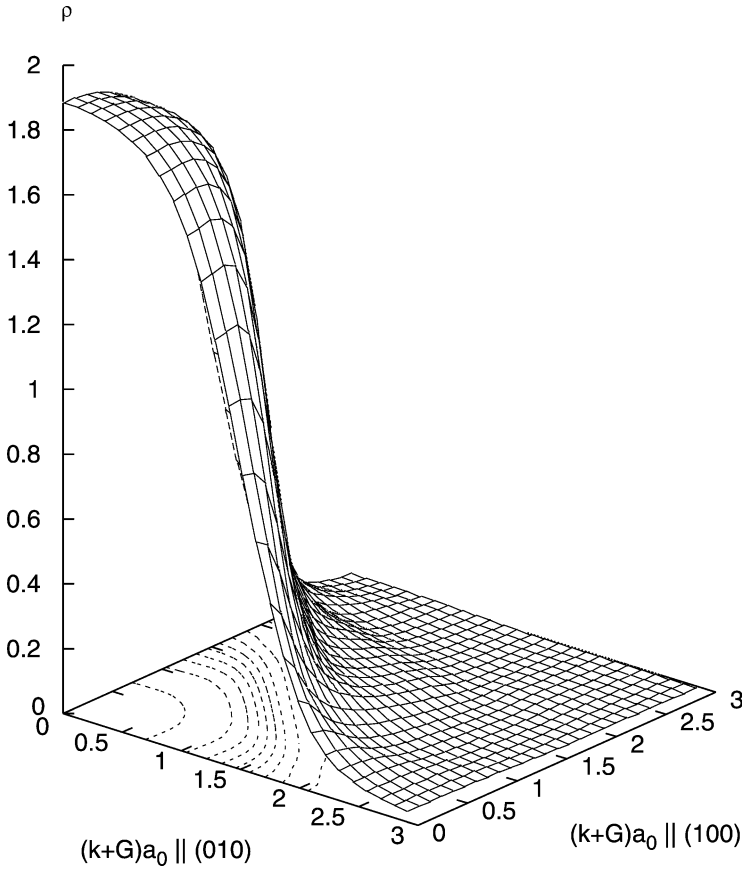

Fig. 2. The EMD as a function of $\mathbf{k}+\mathbf{G}$, which is varied in the plane spanned by (100) and (010). Both momentum components are measured in units of $1/a_0$. Anisotropies of 'projected' positron-EMDs are discussed in Ref. [34].

the crystal system, here, the 4-fold axis of the cubic system. If $|\mathbf{k}+\mathbf{G}|$ is of the order of half a reciprocal lattice vector, the interference with the next-nearest neighbors in the lattice becomes visible; the eight foothills (one full and two halves in the figure) may be interpreted as a projection of the four corners of a carbon tetrahedron onto the (001) plane complemented by the inversion [22]

$$u_{\nu-\mathbf{k},-\mathbf{G}} = u^*_{\nu\mathbf{k},\mathbf{G}}.$$

If $|\mathbf{k}+\mathbf{G}|$ is large, the spherical symmetry of the core states prevails.

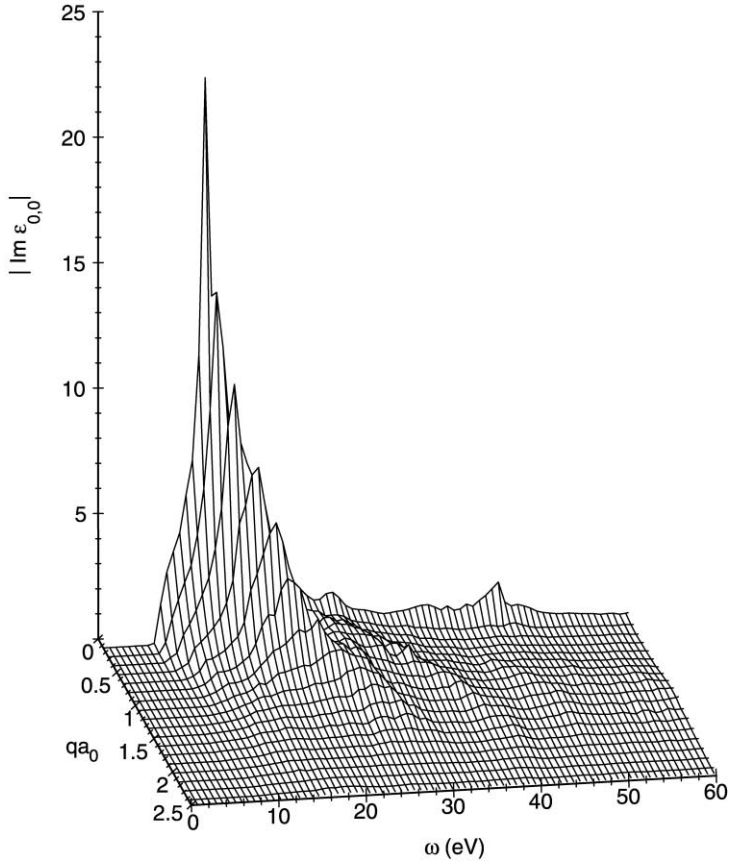

Fig. 3. Calculated Im $\varepsilon_{\mathbf{G},\mathbf{G}'}$ for $\mathbf{G} = \mathbf{G}' = \mathbf{0}$ and $\mathbf{q}\|(\bar{1}11)$. The underlying DFT calculation is based on a $12 \times 12 \times 12$ mesh of $\mathbf{k}$-points in the BZ (98 points in the IBZ), which creates for this particular $\mathbf{q}$-direction commensurate values at $|\mathbf{q}| = (j/12)2\pi\sqrt{3}/a$ as shown here for $j = 2, 3, \ldots$

3.2. Dielectric function

The $\varepsilon_{\mathbf{0},\mathbf{0}}(\mathbf{q},\omega)$ element of the dielectric matrix is shown in Fig. 3. The main absorption peak at 11 eV for $|\mathbf{q}| \to 0$ corresponds to direct transitions from the top of the valence to the bottom of the conduction band at X and L [23].

Local Field Effects (LFEs) are illustrated in Fig. 4. Im $\varepsilon_{\mathbf{0},\mathbf{0}}$ reproduces some values from Fig. 3. For comparison, Im$[1/K_{\mathbf{0},\mathbf{0}}]$ includes an estimate of the local field obtained by calculating $K_{\mathbf{G},\mathbf{G}'}$ as the inverse of a 9×9 dielectric matrix which contains $\mathbf{G} = 0$ and the eight vectors of the closest shell in the bcc reciprocal lattice. The reduction of the values without LFE ($|\mathrm{Im}\ \varepsilon_{\mathbf{0},\mathbf{0}}|$, open symbols) compared to those with LFE ($|\mathrm{Im}(1/K_{\mathbf{0},\mathbf{0}})|$, filled symbols) is of the order reported by Van Vechten and Martin [24] (without their 'dynamical correlations'). The different sign of the effect for frequencies above and below the peak has been noticed before [25]. The differences are even smaller for the energy loss function. Hence the energy loss reported in the next paragraph was calculated from $\varepsilon_{\mathbf{0},\mathbf{0}}(\mathbf{q},\omega)$ alone.

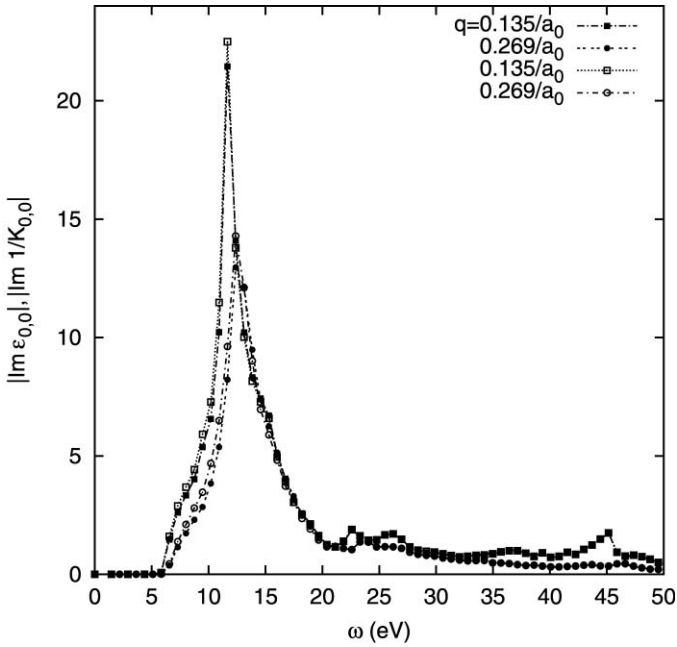

Fig. 4. The absolute value of Im $\varepsilon_{\mathbf{0},\mathbf{0}}(\mathbf{q},\omega)$ (open symbols) and of Im $1/K_{\mathbf{0},\mathbf{0}}(\mathbf{q},\omega)$ (filled symbols). $\mathbf{q}$ is parallel to $(\bar{1}11)$ with $qa_0 = 0.135$ ($j = 1$, squares) and $qa_0 = 0.269$ ($j = 2$, circles) as in Fig. 3. Note that Refs. [24,25,35] refer to the optical limit $q = j = 0$.

3.3. Computed electronic energy loss

To integrate the energy loss function as described by equation (2), the BZ mesh was reduced to $8 \times 8 \times 8$ points, i.e., 35 points in the irreducible Brillouin zone (IBZ). The result is shown in Fig. 5. In the case of the velocity-triplet with smaller cross-sections S, the stopping power was integrated on a $30 \times 30 \times 30$ mesh in $\mathbf{q}$-space (parallelopiped all three edges of length $6.1/a_0$), and in the case of the triplet with larger values over the superset of all $\mathbf{q}$-values obtained from these *via* point group operations with Seitz symbol $\{\mathcal{O}|\mathbf{w}\}$,

$$K_{\mathbf{G},\mathbf{G}'}(\mathbf{q}, \omega) = \mathrm{e}^{\mathrm{i}\mathcal{O}(\mathbf{G}-\mathbf{G}')\cdot\mathbf{w}} K_{\mathcal{O}\mathbf{G},\mathcal{O}\mathbf{G}'}(\mathcal{O}\mathbf{q}, \omega).$$

Our results are about 0–15% lower than the three experimental results [26] for $v \approx 1 \rightarrow 1.3v_0$ which are shown in Fig. 6. ($v_0 \approx 2.19 \times 10^6$ m/s is 1 a.u. of velocity.) Within the framework of linear dielectric response an

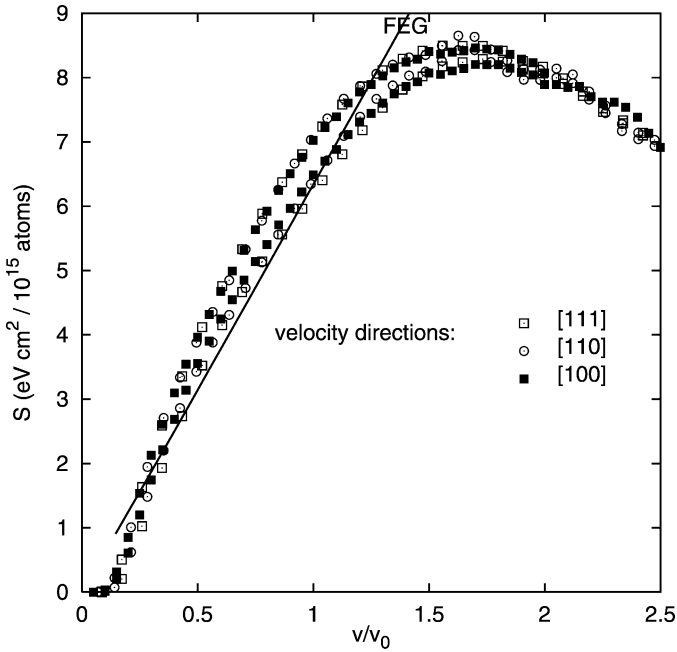

Fig. 5. Electronic stopping cross-section of diamond. The stopping power was integrated on a mesh with 72 points on the ω-axis (0–103 eV). The lowest 28 bands were included in the sum over band-pairs in equation (2). The line is the result for the free electron gas [36] with a density equivalent to four electrons per diamond atom.

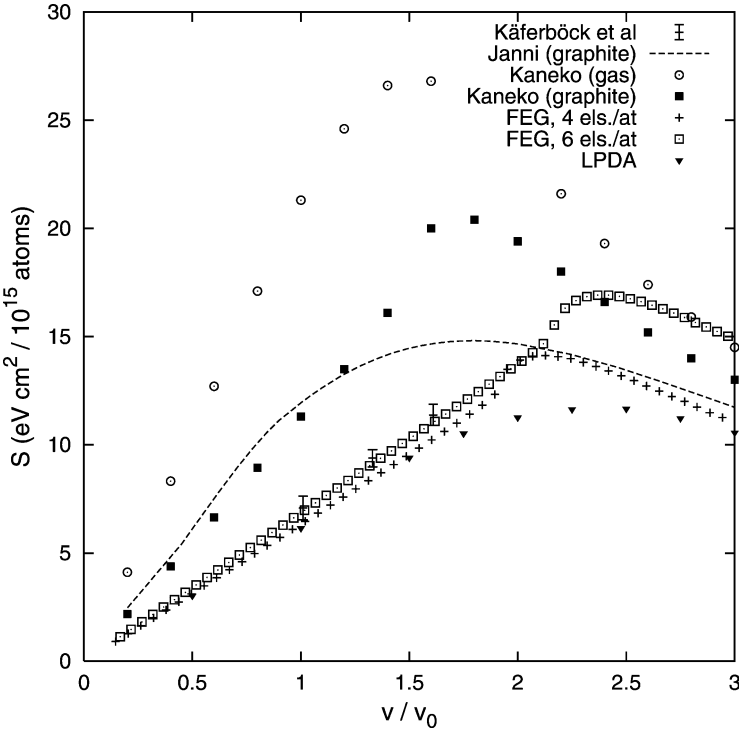

Fig. 6. Experimental proton stopping cross-section of diamond by Käferböck *et al*. [26] and of graphite by Janni [37], compared with calculated values for gaseous carbon and solid graphite from Kaneko's theory [38], and RPA free electron gas (FEG) values [36] with a homogeneous density equivalent to four or six electrons per diamond atom (Fermi velocity $1.457v_0$ or $1.668v_0$) as shown. Values within the LPDA represent intgrals of the all-electron density of GTOFF Fitting Functions weighted with the stopping number of the FEG in the RPA.

underestimation is appropriate though, because terms of $\mathcal{O}(Z_1^3)$ will add about 15% to $S(v)$ at $v \approx 1.5v_0$ [27].

The present results are also consistent with the graphite experimental data, since one would expect the semi-metallic band structure of graphite to correspond to a screened dielectric response, hence a larger inverse dielectric function.

A new result is the 'ionic' band gap, the non-linear suppression of $S(v)$ for $v < 0.2v_0$, which is approximately the value extracted from [12,28]

$$v < \frac{v_0}{2}\sqrt{\hbar\omega_g/E_0}, \tag{4}$$

for a band gap of $\hbar\omega_g = 4$ eV (E_0 is one rydberg).

In contrast, calculations within the local-plasma-density approximation usually integrate over volume elements in real space that are parameterized by the homogeneous electron gas [29], and inevitably yield $S(v) \propto v$ at low velocities. However, an attempt at experimental verification of this reduction of the energy loss in a relatively wide-gap material would be handicapped by the nuclear energy loss, neglected here. It has an estimated maximum of $S \approx 0.8 \times 10^{-15}$ eV cm^2/atom at $v \approx 0.08 v_0$ [30]. Note that equation (4) predicts contributions from K-shell excitations, which are not included here, to start at $v \approx 2.2 v_0$. They have been estimated to shift the maximum to higher velocities by about $0.2 v_0$ [31], and to grow until $v \approx 5.3 v_0$ [32].

ACKNOWLEDGEMENTS

This work was supported in part by grant DAA-H04-95-1-0326 from the US Army Research Office. SBT also was supported in part by grant DMR-0218957 from the US National Science Foundation. JRS also was supported in part by grant N0014-96-1-0707 from the US Office of Naval Research.

REFERENCES

[1] H. Bethe, *Ann. Phys. (Leipzig)*, 1930, **5**, 325.
[2] M. Inokuti, *Rev. Mod. Phys.*, 1971, **43**, 297.
[3] M. Inokuti, Y. Itikawa and J. E. Turner, *Rev. Mod. Phys.*, 1978, **50**, 23.
[4] N. Bohr, *Phil. Mag.*, 1913, **25**, 10.
[5] N. Bohr, *Phil. Mag.*, 1915, **30**, 581.
[6] N. Bohr, *Phys. Rev.*, 1940, **58**, 654.
[7] N. Bohr, *Phys. Rev.*, 1941, **59**, 270.
[8] N. Bohr, *Mat. Fys. Medd. Dan. Vidensk. Selsk.*, 1948, **18** (8).
[9] N. Bohr and J. Lindhard, *Mat. Fys. Medd. Dan. Vidensk. Selsk.*, 1954, **28** (7).
[10] U. Fano, *Ann. Rev. Nucl. Sci.*, 1963, **13**, 2, see footnote 7, page 8.
[11] E. H. Mortensen, J. Oddershede and J. R. Sabin, *Nucl. Instrum. Methods B*, 1992, **69**, 24.
[12] R. J. Mathar, S. B. Trickey and J. R. Sabin, *Nucl. Instrum. Methods B*, 1999, **155**, 249, see also 17th Werner Brandt Workshop on Charged Particle Penetration Phenomena, May 8–9, 1997, Charlottesville, VA.
[13] S. L. Adler, *Phys. Rev.*, 1962, **126**, 413, equations (2.11)–(2.12) are inconsistent with equations (2.7)–(2.10). Either fields ϕ must be replaced by charge densities ρ in equations (2.11)–(2.12), or all factors of squared wavenumbers be dropped.
[14] S. B. Trickey, J. A. Alford and J. C. Boettger, in *Computational Materials Science*, *Theoretical and Computational Chemistry* (ed. J. Leszczynski), Elsevier, Amsterdam, 2003, Vol. 8, in press; see also J. C. Boettger, *Phys. Rev. B*, 2000, **62**, 7809; J. C. Boettger and S. B. Trickey, *J. Mol. Struct. (TheoChem)*, 2000, **501/502**, 285; J. C. Boettger, *Int. J. Quantum Chem.*, 1995, **S29**, 197; U. Birkenheuer, J. C. Boettger and N. Rösch, *J. Chem. Phys.*, 1994, **100**, 6826; J. C. Boettger, *Int. J. Quantum Chem.*, 1993, **S27**, 147; J. C. Boettger and S. B. Trickey, *J. Phys. Condens. Matter*, 1989, **1**, 4323; J. W. Mintmire, J. R. Sabin and S. B. Trickey, *Phys. Rev. B*, 1982, **26**, 1743.

[15] V. L. Moruzzi, J. F. Janak and A. R. Williams, *Calculated Electronic Properties of Metals*, Pergamon Press, New York, 1978.
[16] D. Ayma, J. P. Campillo, M. Rérat and M. Causà, *J. Comput. Chem.*, 1997, **18**, 1253; D. Ayma, M. Rérat and A. Lichanot, *J. Phys. Condens. Matter*, 1998, **10**, 557.
[17] H. Partridge, *National Aeronautics and Space Administration (NASA) Technical Memorandum 1.15:101044*, Ames Research Center, Moffet Field, 1989.
[18] S. B. Trickey, F. Müller-Plathe and G. H. F. Diercksen, *Phys. Rev. B*, 1992, **45**, 4460.
[19] Because no bond-centered basis functions are used, the charge fitting functions do not reproduce the quasi-forbidden (222) X-ray reflex Z. W. Lu, A. Zunger and M. Deutsch, *Phys. Rev. B*, 1993, **47**, 9385; M. A. Spackman, *Acta Crystallogr. Sect. A*, 1991, **47**, 420; T. Takama, K. Tsuchiya, K. Kobayashi and S. Sato, *Acta Crystallogr. Sect. A*, 1990, **46**, 514.
[20] J. C. Boettger, *Int. J. Quantum Chem.*, 1996, **60**, 1345.
[21] S. Fahy, X. W. Wang and S. G. Louie, *Phys. Rev. Lett.*, 1988, **61**, 1631; M. R. Salehpour and S. Satpathy, *Phys. Rev. B*, 1990, **41**, 3048; A. Onodera, M. Hasegawa, K. Furuno, M. Kobayashi, Y. Nisida, H. Sumiya and S. Yazu, *Phys. Rev. B*, 1991, **44**, 12176; M. P. Surh, S. G. Louie and M. L. Cohen, *Phys. Rev. B*, 1992, **45**, 8239; S. Logothetidis, J. Petalas, H. M. Polatoglou and D. Fuchs, *Phys. Rev. B*, 1992, **46**, 4483.
[22] D. S. Falk, *Phys. Rev.*, 1960, **118**, 105.
[23] G. S. Painter, D. E. Ellis and A. R. Lubinsky, *Phys. Rev. B*, 1971, **4**, 3610.
[24] J. A. Van Vechten and R. M. Martin, *Phys. Rev. Lett.*, 1972, **28**, 446, [1972, 28, 646(E)].
[25] V. I. Gavrilenko and F. Bechstedt, *Phys. Rev. B*, 1996, **54**, 13416.
[26] W. Käferböck, W. Rössler, V. Necas, P. Bauer, M. Peñalba, E. Zarate and A. Arnau, *Phys. Rev. B*, 1997, **55**, 13275, Note that their theoretical values are already multiplied with charge state fractions; the H^+ curve in their Fig. 1 is not the analogue of our results.
[27] J. D. Jackson and R. L. McCarthy, *Phys. Rev. B*, 1972, **6**, 4131.
[28] R. J. Mathar, J. R. Sabin and S. B. Trickey, *18th Werner Brandt Workshop on Charged Particle Penetration Phenomena*, June 4–5, 1998, Gainesville, FL.
[29] Recent examples are: P. W. L. van Dijk, L. J. van IJzendoorn, M. de Koning, P. Bobbert, W. van Haeringen and M. J. A. de Voigt, *Nucl. Instrum. Methods B*, 1994, **85**, 551; J. A. Nobel, J. R. Sabin and S. B. Trickey, *Nucl. Instrum. Methods B*, 1995, **99**, 632; J. Calera-Rubio, A. Gras-Martí and N. R. Arista, *Nucl. Instrum. Methods B*, 1994, **93**, 137; K. M. Klein, C. Park and A. F. Tasch, *Appl. Phys. Lett.*, 1990, **57**, 2701; S. T. Nakagawa, *Phys. Status Solidi B*, 1993, **178**, 87; K. Lenkheit, Ch. Trikalinos, L. L. Balashova, N. M. Kabashnik and V. I. Shulga, *Phys. Status Solidi B*, 1990, **161**, 513; D. Cai, N. Grønbech-Jensen, C. M. Snell and K. M. Beardmore, *Phys. Rev. B*, 1996, **54**, 17147; W. Neng-ping and H. Yu-kun, *Phys. Rev. A*, 1995, **52**, 3953; P. Vargas, J. E. Valdés and N. R. Arista, *Phys. Rev. A*, 1996, **53**, 1638; P. Vargas, J. E. Valdés and N. R. Arista, *J. Phys. B*, 1996, **29**, 47.
[30] U. Littmark and J. F. Ziegler, *Phys. Rev. A*, 1981, **23**, 64.
[31] J. R. Sabin and J. Oddershede, *Nucl. Instrum. Methods B*, 1987, **24/25**, 339.
[32] H. Paul and J. Sacher, *Atom. Data Nucl. Tables*, 1989, **42**, 105.
[33] The experimental value is −285 eV: J. Nithianandam and J. C. Rife, *Phys. Rev. B*, 1993, **47**, 3517; Y. Ma, N. Wassdahl, P. Skytt, J. Guo, J. Nordgren, P. D. Johnson, J.-E. Rubensson, T. Boske, W. Eberhardt and S. D. Kevan, *Phys. Rev. Lett.*, 1992, **69**, 2598.
[34] R. W. N. Nilen, S. H. Connell, D. T. Britton, C. G. Fischer, E. J. Sendezera, P. Schaaff, W. G. Schmidt, J. P. F. Sellschop and W. S. Verwoerd, *J. Phys. Condens. Matter*, 1997, **9**, 6323.
[35] M.-Z. Huang and W. Y. Ching, *Phys. Rev. B*, 1993, **47**, 9449.
[36] J. Lindhard, A. Winther and K. Dan, *Vidensk. Selsk. Mat. Fys. Medd.*, 1964, **34** (4).
[37] J. F. Janni, *Atom. Data Nucl. Data Tables*, 1982, **27**, 147.
[38] T. Kaneko, *Phys. Status Solidi B*, 1989, **156**, 49; T. Kaneko, *Phys. Rev. A*, 1989, **40**, 2188; T. Kaneko, *Atom. Data Nucl. Data Tables*, 1993, **53**, 271.

Subject Index